STRUCTURAL CHARACTERIZATION OF FERROIC MATERIALS BY ADVANCED SPECTROSCOPY TECHNIQUES

Jaru Jutimoosik

A Thesis Submitted in Partial Fulfillment of the Requirements for the

Degree of Doctor of Philosophy in Physics

Suranaree University of Technology

Academic Year 2015

การหาลักษณะเฉพาะเชิงโครงสร้างของวัสดุเฟร์โรอิกโดยใช้เทคนิคสเปกโทรสโกปีขั้นสูง

นายจารุ จุติมูสิก

มหาวิทยาลัยเทคโนโลยีสุรนารี

วิทยานิพนธ์นี้เป็นส่วนหนึ่งของการศึกษาตามหลักสูตรปริญญาวิทยาศาสตรดุษฎีบัณฑิต
สาขาวิชาฟิสิกส์
มหาวิทยาลัยเทคโนโลยีสุรนารี
ปีการศึกษา 2558

STRUCTURAL CHARACTERIZATION OF FERROIC MATERIALS BY ADVANCED SPECTROSCOPY TECHNIQUES

Suranaree University of Technology has approved this thesis submitted in partial fulfillment of the requirements for the Degree of Doctor of Philosophy.

Thesis Examining Committee

_____
(Asst. Prof. Dr. Worawat Meevasana)
Chairperson

_____
(Assoc. Prof. Dr. Rattikorn Yimnirun)
Member (Thesis Advisor)

_____
(Dr. Saroj Rujirawat)
Member

_____
(Prof. Dr. Santi Maensiri)
Member

_____
(Assoc. Prof. Dr. Chitnarong Sirisathitkul)
Member

_____
(Dr. Amitesh Paul)
Member

_____	_____
(Prof. Dr. Sukit Limpijumnong)	(Prof. Dr. Santi Maensiri)
Vice Rector for Academic Affairs and Innovation	Dean of Institute of Science

มหาวิทยาลัยเทคโนโลยีสุรนารี

จารุ จุติมูสิก : การหาลักษณะเฉพาะเชิงโครงสร้างของวัสดุเฟร์โรอิกโดยใช้เทคนิคสเปกโทรสโกปีขั้นสูง (STRUCTURAL CHARACTERIZATION OF FERROIC MATERIALS BY ADVANCED SPECTROSCOPY TECHNIQUES) อาจารย์ที่ปรึกษา : รองศาสตราจารย์ ดร.รัตติกร ยิ้มนิรัญ, 209 หน้า.

วิทยานิพนธ์นี้มุ่งศึกษาวัสดุเฟร์โรอิกซึ่งมีสมบัติโดดเด่นคือบิสมัทเฟร์ไรต์ซึ่งเจือด้วยแมงกานีส ($BiFe_{1-x}Mn_xO_3$) และฟิล์มบางแบบหลายชั้น Co/CoO/Au เนื่องจากสามารถนำไปประยุกต์ใช้ในอุปกรณ์สปินทรอนิกส์ (spintronics device) และการจัดเก็บข้อมูล ในงานวิจัยนี้โครงสร้างเฉพาะบริเวณและการเกิดเฟสปลอมปนของสารประกอบอื่นใน $BiFe_{1-x}Mn_xO_3$ และ Co/CoO/Au ถูกศึกษาโดยใช้เทคนิคสเปกโทรสโกปีการดูดกลืนรังสีเอกซ์ (XAS) และการสะท้อนของโพลาไรซ์นิวตรอน (PNR) นอกจากนี้เทคนิค PNR ยังถูกนำมาใช้ตรวจสอบการฟื้นคืนสภาพของ untrained state ในฟิล์มบางแบบหลายชั้น Co/CoO/Au หลังจากที่ได้ทำการวัดวงวนฮิสเทอรีซิสเสร็จสิ้นไปแล้ว 2 รอบ ซึ่งการฟื้นคืนสภาพในลักษณะดังกล่าวนี้ คาดว่าเป็นผลมาจากการจ่ายสนามแม่เหล็ก (reorientation field, H_{RE}) ในทิศทางซึ่งทำมุมต่างๆ (orientation angle, Ω_{RE}) กับทิศทางเดิมของสนามแม่เหล็กที่ใช้ระหว่างการลดอุณหภูมิในตอนเริ่มต้น

ในระบบของ $BiFe_{1-x}Mn_xO_3$ เมื่อทำการวิเคราะห์โครงสร้างโดยรอบของอะตอมแมงกานีสโดยทำการวัดสเปกตรัมการดูดกลืนรังสีเอกซ์ในช่วงโครงสร้างบริเวณใกล้ขอบการดูดกลืน (XANES) ที่ขอบการดูดกลืน K ของอะตอมแมงกานีส พบว่าในสารตัวอย่างที่มีปริมาณแมงกานีสต่ำๆ อะตอมแมงกานีสส่วนใหญ่เข้าไปแทนที่ตำแหน่งอะตอมของเหล็กในบิสมัทเฟร์ไรต์ และเมื่อปริมาณแมงกานีสเพิ่มขึ้น จะทำให้เกิดเฟสปลอมปนของ $BiMnO_3$ และ $BiMn_2O_5$ ในสารตัวอย่าง ซึ่งผลที่ได้สอดคล้องกับผลการคำนวณสเปกตรัมโดยโปรแกรม FEFF8.2

ในระบบของ Co/CoO/Au เมื่อทำการวิเคราะห์โครงสร้างโดยรอบของอะตอมโคบอลต์ โดยทำการวัดสเปกตรัมการดูดกลืนรังสีเอกซ์ในช่วงโครงสร้างบริเวณใกล้ขอบการดูดกลืน (XANES) ที่ขอบการดูดกลืน K ของอะตอมโคบอลต์ พบว่ามีเฟสปลอมปน Co_3O_4 เกิดขึ้นบริเวณชั้นฟิล์มบางชั้นคู่ Co/CoO และจากการวิเคราะห์โดยใช้เทคนิค linear combination fitting ทำให้สามารถหาค่าปริมาณเฟสปลอมปน Co_3O_4 ที่มีอยู่ในสารตัวอย่างได้ ซึ่งปริมาณเฟสปลอมปนดังกล่าวยังถูกนำมาใช้ในการจำลองสเปกตรัมการดูดกลืนรังสีเอกซ์ทางทฤษฎี โดยการใช้โปรแกรม FEFF 8.2 ซึ่งผลที่ได้สอดคล้องเป็นอย่างดีกับผลจากการทดลอง สำหรับการวิเคราะห์วงวนฮิสเทอรีซิสของแม่เหล็กที่วัดโดยใช้เทคนิค SQUID พบว่ามีการฟื้นคืนสภาพของ untrained state ที่ Ω_{RE} = 45 องศา และ 90 องศา ซึ่งสอดคล้องกับผลการวิเคราะห์วงวนฮิสเทอรีซิสของแม่เหล็กที่วัดโดยใช้เทคนิค

PNR นอกจากนี้ผลการวิเคราะห์ข้อมูลจาก PNR ยังพบว่าลักษณะการฟื้นคืนสภาพของ untrained state จะเกิดขึ้นได้ดีที่สุดเมื่อ Ω_{RE} = 45 องศา และ H_{RE} มีค่าอยู่ระหว่าง 3.0 kOe ถึง 10 kOe สำหรับ Ω_{RE} = 135 องศา จะไม่มีการฟื้นคืนสภาพของ untrained state เกิดขึ้น

สาขาวิชาฟิสิกส์ ลายมือชื่อนักศึกษา_____

ปีการศึกษา 2558 ลายมือชื่ออาจารย์ที่ปรึกษา_____

ลายมือชื่ออาจารย์ที่ปรึกษาร่วม_____

JARU JUTIMOOSIK : STRUCTURAL CHARACTERIZATION OF FERROIC MATERIALS BY ADVANCED SPECTROSCOPY TECHNIQUES. THESIS ADVISOR : ASSOC. PROF. RATTIKORN YIMNIRUN, Ph.D. 209 PP.

BISMUTH FERRITE/MULTILAYER/X-RAY ABSORPTION SPECTROSCOPY / POLARIZED NEUTRON REFLECTIVITY

In this work, the materials of interest are $BiFe_{1-x}Mn_xO_3$ ceramic and Co/CoO/Au multilayer due to their potential applications in data storage and spintronics devices. The Synchrotron-based X-Ray Absorption Spectroscopy (XAS) and Polarized Neutron Reflectivity (PNR) techniques were employed to investigate the structural properties of $BiFe_{1-x}Mn_xO_3$ ceramic and Co/CoO/Au multilayer, especially to study the local structure of Mn in $BiFe_{1-x}Mn_xO_3$ ceramic and to verify the formation of secondary phase in Co/CoO/Au multilayer. In addition, the Co/CoO/Au multilayer was examined to explore the degree of recovery of the untrained state after the first two field cycles. Such a recovery was expected by field cycling a reorientation field (H_{RE}) along a direction of orientation angle (Ω_{RE}) away from the initial field cooling direction.

In Mn-doped $BiFeO_3$ system, the measured Mn *K*-edge X-ray Absorption Near Edge Structure (XANES) spectra showed that Mn atoms substituted in Fe sites in $BiFeO_3$ at low Mn content, which corresponded well with the calculated XANES spectra by FEFF8.2 program. Both the experimental and calculated XANES results

indicated that an increase of Mn content in $BiFeO_3$ led to the formation of second phases of $BiMnO_3$ and $BiMn_2O_5$.

In Co/CoO/Au multilayer system, the results of the Co K-edge XANES spectra indicated that the presence of Co_3O_4 in Co/CoO bilayers within the multilayer corresponded well with the calculated linear combination of XANES spectra by FEFF8.2 program. The analysis of SQUID magnetization hysteresis loops demonstrated the recovery of untrained state for Ω_{RE} = 45° and 90°, which corresponded with the PNR data. Furthermore, the results of PNR data analysis revealed that the best recipe for the recovery occurred at Ω_{RE} = 45°, which could be achieved partially with H_{RE} = 3.0 kOe and remained significant even with H_{RE} = 10.0 kOe. For any other higher angles of orientation (e.g., Ω_{RE} = 135°), no recovery of the untrained state arose.

มหาวิทยาลัยเทคโนโลยีสุรนารี

School of Physics

Academic Year 2015

Student's Signature_____

Advisor's Signature_____

Co-advisor's Signature_____

ACKNOWLEDGEMENTS

There are many people, to whom I would like to express my sincere words of acknowledgments:

First of all, I would like to express my sincere gratitude to Assoc. Prof. Dr. Rattikorn Yimnirun, my thesis advisor, for his great advisory, kind patience, guidance, and inspiring me the way to be a good researcher. He supervised this work in all steps, from the very first experiments, new ideas, data processing as well as the final proof reading of the manuscripts. Not only his scientific expertise, but also his optimism and trust were a great help and motivation throughout my work.

I am also very grateful to my co-advisor Dr.Saroj Rujirawat for introducing me to the field of synchrotron x-ray absorption spectroscopy. He provides friendship and kind support for me.

I would like to thank Dr. Amitesh Paul for giving me the opportunity to be a member of his multilayer group at the Institute for Experimental Physics E21, Technical University of Munich (TUM), Garching, Germany and for providing me an excellent experience research condition, especially Polarized Neutron Reflectivity (PNR). I would like to thank him not only for the professional support but also for the good time that he offered me during my visit at TUM.

I would like to thank Prof. Dr. Santi Maensiri for providing Mn-doped $BiFeO_3$ samples and for being on my thesis committee.

I would also like to thank Assoc. Prof. Dr. Chitnarong Sirisathitkul and Asst. Prof. Dr. Worawat Meevasana for being on my thesis committee.

I am grateful to all staff members at XAS beamlines, Synchrotron Light Research Institute, and all graduate students and staff members at School of Physics, Suranaree University of Technology, for their friendship and sincerity. Moreover, I am deeply grateful to SUT-PhD Scholarship Program of Suranaree University of Technology through the Higher Education Research Promotion and National Research University Project of Thailand for the financial support.

Finally, I would like to express appreciation to my parents and sisters for great support, encouragement and good advices to me over the years of my life, and Miss Ausanee Changpratis for her love and encouragement.

Jaru Jutimoosik

มหาวิทยาลัยเทคโนโลยีสุรนารี

CONTENTS

Page

ABSTRACT IN THAI I

ABSTRACT IN ENGLISH III

ACKNOWLEDGEMENTS V

CONTENTS VII

LIST OF TABLES XII

LIST OF FIGURES XIV

LIST OF ABBREVIATIONS XXIV

CHAPTER

I INTRODUCTION 1

1.1 Background 1

1.2 Bismuth ferrite 3

1.3 Cobalt/cobalt oxide exchange-coupled system 6

1.4 Scope and limitations of the study 9

II THEORY 11

2.1 X-ray absorption 11

2.1.1 X-ray interaction with matter 11

2.1.2 Absorption coefficients and cross-sections 12

2.1.3 Absorption edges 14

2.1.4 X-ray Absorption Spectroscopy (XAS) 16

2.1.5 X-ray Absorption Near Edge Structure (XANES) 17

CONTENTS (Continued)

Page

2.1.6 Extended X-ray Absorption Fine Structure (EXAFS) 23

2.2 Neutron reflectivity 27

2.2.1 Reflectivity on non-magnetic system 27

2.2.1.1 Reflection on a homogeneous medium 30

2.2.1.2 Parratt formalism 34

2.2.2 Polarized Neutron Reflectivity (PNR) on magnetic system 36

2.2.3 Coherence volume and resolution 43

2.3 Magnetism 46

2.3.1 Atom in a magnetic field 49

2.3.2 Magnetization 50

2.3.3.1 Diamagnetism 51

2.3.3.2 Paramagnetism 51

2.3.3 Magnetic order 53

2.3.3.1 Ferromagnetism 53

2.3.3.2 Antiferromagnetism 54

2.3.3.3 Ferrimagnetism 56

2.4 Magnetic interaction 57

2.4.1 Magnetic dipole interaction 57

2.4.2 Exchange interaction 57

2.4.2.1 Origin of exchange 58

2.4.2.2 Direct exchange 60

CONTENTS (Continued)

Page

2.4.2.3 Indirect exchange: superexchange 60
2.4.2.4 Indirect exchange: RKKY 60
2.4.2.5 Double exchange 61
2.4.3 Spin-orbit coupling 61
2.5 Magnetic anisotropy 63
2.5.1 Magnetocrystalline anisotropy 63
2.5.2 Shape anisotropy 65
2.5.3 Surface anisotropy 66
2.5.4 Strain anisotropy 67
2.6 Magnetic Domains 68
2.7 Magnetization reversal 73
2.7.1 Magnetization reversal via domain wall motion 73
2.7.2 Magnetization reversal via coherent magnetization rotation 75
III RESEARCH METHODOLOGY 79
3.1 X-ray techniques 79
3.1.1 Synchrotron radiation 79
3.1.2 X-ray Absorption Spectroscopy (XAS) experimental set up 82
3.1.2.1 Transmission mode 82
3.1.2.2 Fluorescence mode 85
3.1.2.3 Electron yield 88
3.1.3 X-ray absorption spectrum calculation 88

CONTENTS (Continued)

Page

3.1.4 Linear combination analysis 92
3.2 SQUID magnetometer 93
3.2.1 Principle of SQUID operation 94
3.2.2 Josephson junction 96
3.3 Neutron technique 97
3.3.1 Neutron source 98
3.3.1.1 Fission source 98
3.3.1.2 Spallation source 99
3.3.2 Neutron Reflectometry 99
3.4 DC magnetron sputtering 103
3.5 Precipitation method 104
IV XANES STUDY OF MANGANESE-DOPED BISMUTH FERRITE AND COBALT-COBALT OXIDE EXCHANGE-COUPLED SYSTEM 105
4.1 XANES measurement of Mn-doped $BiFeO_3$ 105
4.2 XANES measurement of Co/CoO/Au multilayers 106
4.3 XANES analysis 107
4.3.1 Identification of Mn site in $BiFeO_3$ 107
4.3.2 Determination of secondary phase in Mn-doped $BiFeO_3$ 113
4.3.3 Determination of secondary phase in Co/CoO/Au multilayers 115

CONTENTS (Continued)

Page

V SQUID AND PNR STUDY OF RECOVERY OF THE UNTRAINED STATE IN COBALT-COBALT OXIDE EXCHANGE-COUPLED SYSTEM 121

5.1 SQUID measurement of Co/CoO/Au multilayer 121

5.2 PNR measurement of of Co/CoO multilayer 122

5.3 SQUID analysis 123

5.4 PNR analysis 134

5.4.1 First and second field cycles 134

5.4.2 Fourth field cycle with $\Omega_{RE} = 45°$ 140

5.4.3 Fourth field cycle with $\Omega_{RE} = 90°$ 145

5.4.4 Discussion on the rotational sense 148

VI CONCLUSIONS AND SUGGESTION 152

REFERENCES 155

APPENDIX 166

CURRICULUM VITAE 209

LIST OF TABLES

Table **Page**

4.1 Proportion of $BiMnO_3$ and $BiMn_2O_5$ in Mn-doped $BiFeO_3$ samples.. 113

4.2 Proportion of Co metal, CoO and Co_3O_4 in the Co/CoO/Au MLs …..... 117

5.1 The integrated areas under the main peaks A1 (decreasing branch) and A2 (increasing branch) corresponding to the derivatives of the first, second, fourth and fifth hysteresis loops for various fields H_{RE} for Ω_{RE} = 45°... 129

5.2 The integrated areas under the main peaks A1 (decreasing branch) and A2 (increasing branch) corresponding to the derivatives of the first, second, fourth and fifth hysteresis loops for various fields H_{RE} for Ω_{RE} = 90°... 129

5.3 The integrated areas under the main peaks A1 (decreasing branch) and A2 (increasing branch) corresponding to the derivatives of the first, second, fourth and fifth hysteresis loops for various fields H_{RE} for Ω_{RE} = 135°.. 130

5.4 The ratio of integrated areas under the main peaks A1 (decreasing branch) and A2 (increasing branch) corresponding to the derivatives of the first, second, fourth and fifth hysteresis loops for various fields H_{RE} for Ω_{RE} = 45°.... 130

LIST OF TABLES (Continued)

Table **Page**

5.5 The ratio of integrated areas under the main peaks A1 (decreasing branch) and A2 (increasing branch) corresponding to the derivatives of the first, second, fourth and fifth hysteresis loops for various fields H_{RE} for Ω_{RE} = 90°... 131

5.6 The ratio of integrated areas under the main peaks A1 (decreasing branch) and A2 (increasing branch) corresponding to the derivatives of the first, second, fourth and fifth hysteresis loops for various fields H_{RE} for Ω_{RE} = 135°... 131

5.7 Fit parameters extracted from the PNR results at saturation. Here ρ_n and ρ_m designate the nuclear and magnetic scattering length densities, respectively..... 137

LIST OF FIGURES

Figure **Page**

1.1 Crystal structure of BFO (hexagonal setting).. 4

2.1 Schematic view of x-ray absorption measurement in transmission mode..... 13

2.2 Log-log plot of the semi-empirical X-ray absorption cross section for platinum versus X-ray energy. The *K*, $L_{I,II,III}$ and *M* edges are shown, while the fine structure is not shown (Bunker, 2010)..... 14

2.3 Schematics of the atomic energy levels and the symbol used to label the X-ray absorption edges of the elements. Transitions occur to all empty states above the Fermi level that exhibit appropriate symmetry governed by the dipole selection rules (Adapted from Als-Nielsen and MaMorrow, 2001) 15

2.4 Normalized Co *K*-edge absorption spectra classified into two regions; XANES and EXAFS..... 17

2.5 The muffin-tin potential consists of non-overlapping spherical regions (Kodre, 2002)..... 19

2.6 Single scattering (left), double scattering from different atoms (middle), and double scattering from the same atom (right). (b) Graphical representation of the *T*-operator (Kodre, 2002).. 22

2.7 Interference of outgoing and backscattered photoelectron wave responsible for XAFS oscillation (Hippert *et al*., 20060)..... 24

LIST OF FIGURES (Continued)

Figure **Page**

2.8 Speccular reflectivity geometry (Adapted from Zabel *et al*., 2007).... 28

2.9 The reflectivity transmittivity and the transmission coefficient for scattering at single flat surface for normalized scattering vector (Zabel, 1994). 32

2.10 The film with a double layer of thickness d_1 and d_2 and total periodicity Λ (Adapted from Zabel *et al*., 2007). 34

2.11 Parratt's recursion scheme showing reflection and transmission of waves for different media with different electron densities (Zabel, 1994)..... 36

2.12 (a) PNR geometry with magnetic field $\vec{H}$ along Y-axis and magnetization $\vec{M}$ at an angle ϕ_A. The scattering plane is the XZ plane, with polarization either parallel or anti-parallel to the Y-axis. (b) Kinematics of polarized neutron reflection. For specular conditions $\alpha_i = \alpha_f = \alpha,$ the scattering vectors $\vec{p}_i = \vec{p}_f = \vec{p}_0.$ In presence of magnetic field the Zeeman splitting leads to different components of the refracted beam, $\vec{p}_+$ for up neutrons and $\vec{p}_-$ for down neutrons (Adapted from Zabel *et al*., 2007). 38

2.13 Magnetic domains with magnetization lying in-plane are shown with the arrows. (a) The coherence ellipse is smaller than the domain size, so the reflectivity over the total coherence ellipse is the same. (b) Coherence ellipse spanning many domains. The reflectivity is averaged over the

LIST OF FIGURES (Continued)

Figure **Page**

mean potential and may lead to off specular intensity (Adapted from Zabel *et al.*, 2007).. 45

2.14 Demonstration of the magnetic moment associated with (a) an orbiting electron and (b) a spinning electron (Adapted from Coey, 2009). 47

2.15 The temperature dependence of susceptibility for an AF (Adapted from Blundell, 2007). 56

2.16 Double exchange interaction between octahedrally coordinated Fe^{2+} and Fe^{3+} in Fe_3O_4 (a) Electron hopping is allowed from Fe^{2+} to Fe^{3+} in ferromagnetic alignment. (b) Forbidden electron hopping in case of antiferromagnetic alignment. (Adapted from Blundell, 2007) 62

2.17 Hypothetical infinitely thin 180° wall (Adapted from Bedanta, 2004). 69

2.18 Rotation of the magnetization vector between two adjunct domains through a thin 180° wall in a infinite uniaxial material. Two different rotation modes are shown, (a) a Bloch wall and (b) a Néel wall. (c) Schematic of the angle (ϕ) between two adjacent spins. (Adapted from Hubert and Schäfer, 2000). 71

2.19 A typical magnetic hysteresis loop (Adapted from Bedanta, 2004). 74

2.20 Coordinate system for magnetization reversal process in a single domain particle. An externally applied field at an angle ϕ relative to the easy

LIST OF FIGURES (Continued)

Figure **Page**

axis causes a net magnetization to lies at some angle θ relative to the easy axis (Bedanta, 2004). 76

2.21 Hysteresis curves of a spherical single domain particle for different angles between anisotropy axis and external field in the framework of Stoner-Wohlfarth model (Stoner and Wohlfarth, 1948). 78

3.1 Schematic of synchrotron radiation from different sources. Radiation from (a) Bending magnet (b) Wiggler and (c) Undulator (Attwood, 2007). 80

3.2 Schematic of polarization of radiation from undulators with (a) linearly polarized and (b) circularly polarized x-rays (Attwood, 2007). 81

3.3 The excited state (a) x-ray fluorescence and (b) the Auger effect (Adapted from Koningsberger and Prins, 1988). 83

3.4 The three modes of XAS measurement (a) transmission mode, (b) fluorescence mode and (c) electron yield (Adapted from Bunker, 2010)..... 83

3.5 Schematic illustration of the experimental setup of transmission-mode X-ray absorption spectroscopy (Adapted from Stern and Heald, 1983)..... 84

3.6 XAS experimental set up at the Siam Photon Laboratory, Synchrotron Light Research Institute, Nakhon Ratchasima, Thailand..... 84

3.7 Detail of an atoms.inp input file to generate “feff.inp” for FEFF calculation 89

LIST OF FIGURES (Continued)

Figure **Page**

3.8 Detail of a “feff.inp” input file of CoO with Co as center atom for FEFF calculation 90

3.9 (a) Gradiometer coil with sample and the superconducting magnets (b) The response curve fitted with a point dipole approximation. (c) Schematic of the SQUID magnetometry (Bedanda, 2006)..... 95

3.10 Schematic of the neutron scattering geometry from different perspectives. Specular reflectivity geometry; off-specular scattering plane, corresponding to the incident plane (dotted plane); GISANS scattering plane (dashed plane), perpendicular to the incident plane (Adapted from Paul, 2012). 100

3.11 Schematic diagram of AMOR reflectometer at PSI (Gupta *et al*., 2004). 103

4.1 Schematic of layer structure of the Co MLs 106

4.2 Normalized Fe *K*-edge XANES spectra of $BiFeO_3$ and Mn-doped $BiFeO_3$ ceramics with the different Mn concentrations and comparison to the Fe_2O_3 standard sample 108

4.3 XANES spectra of Mn *K*-edge of Mn-doped $BiFeO_3$ ceramics with comparison to the Mn_2O_3 standard sample. Inset presents the broadening and increasing of p_1 , and p_2 peaks 109

4.4 (a) Perovskite crystal structure of $BiFeO_3$. [(b)-(c)] Schematic illustrations of Mn on Fe site, Mn on Bi site, and interstitial Mn. [(d)-(e)]

LIST OF FIGURES (Continued)

Figure **Page**

show the crystal structure of $BiMnO_3$ and $BiMn_2O_5$, respectively..... 111

4.5 The measured Mn *K*-edge XANES spectra of Mn-doped $BiFeO_3$ ceramics compared with the calculated Mn *K*-edge XANES spectra of the different Mn lattice locations (Mn_{Fe}, Mn_{Bi}, and Mn_i). 112

4.6 (a) Comparison of the extrapolated $BiMnO_3$ and $BiMn_2O_5$ spectra obtained from Yoneda *et al*. and Shukla *et al.*, respectively, and the measured Mn K-edge XANNES spectra of Mn doped BFO samples. Also included are the linear combination of Mn *K*-edge XANES spectra with various proportions of $BiMnO_3$ and $BiMn_2O_5$. (b) The calculated Mn *K*-edge XANES spectra of $BiMnO_3$ and $BiMn_2O_5$. The fitted linear combination XANES spectra are also plotted 114

4.7 Normalized Co *K*-edge XANES spectra of the Co MLs with the different Au layer thickness with comparison to the Co metal, Co_3O_4, and CoO standard sample..... 116

4.8 (a) Comparison of the measured Co *K*-edge normalized XANES spectra of the Co/CoO MLs (open symbols) and their fits (lines) using the LCA method. Also included are the reference spectra for CoO, Co_3O_4 and Co metal. (b) The *ab initio* calculated XANES spectra for the reference materials are generated using the FEFF 8.2 code. A weighted proportion of the species, with various proportions of Co metal, Co_3O_4, and CoO as

LIST OF FIGURES (Continued)

Figure **Page**

obtained from the fits are used to calculate the ML spectra, is also plotted 118

4.9 The ratio RS from the Co *K*-edge spectra obtained from two possible scenarios for the AF layer (i) with CoO + Co_3O_4 content and (ii) only with CoO 119

5.1 Illustration of the neutron scattering geometry. H_a along the +*y* axis is shown to be antiparallel to H_{FC}. M_{FM} is the FM magnetization making an angle ϕ_A with respect to the field axis. The reorientation field H_{RE} along the –*x* axis (for $\Omega_{RE} = 90°$) is also shown along with two other orientations ($\Omega_{RE} = 45°$ and $\Omega_{RE} = 135°$) in the sample plane 123

5.2 SQUID magnetization hysteresis loops for different field cycles measured at 10 K and for various reorientation fields H_{RE} along Ω_{RE} = 45° in the sample plane. The stars mark the applied field values H_a for the neutron measurement along the respective branch of the loops 125

5.3 SQUID magnetization hysteresis loops for different field cycles measured at 10 K and for various reorientation fields H_{RE} along Ω_{RE} = 90° in the sample plane. The stars mark the applied field values for the neutron measurement along the respective branch of the loops 126

5.4 SQUID magnetization hysteresis loops for different field cycles measured at 10 K and for various reorientation fields H_{RE} along Ω_{RE} =

LIST OF FIGURES (Continued)

Figure **Page**

135° in the sample plane 127

5.5 The field derivative of magnetization χ_{mag} as a function of field measured at a reorientation field H_{RE} = 0.5 kOe and along different Ω_{RE} in the sample plane. The Gaussian fits to the peaks are in line 128

5.6 The normalized integrated area ratios C1n = X1/X*n* (*n*=2,4,5) with respect to the initial training for various reorientation field H_{RE} and along different orientations Ω_{RE} in the sample plane. Here *n* is the number of loop cycle. The symbol sizes are typical of their error bars..... 132

5.7 The ratio of normalized integrated area corresponding to the fourth field cycle with respect to the trained state during the second field cycle (C14/C12) for various reorientation field H_{RE} and along different Ω_{RE} in the sample plane. The symbol sizes are typical of their error bars..... 134

5.8 Specular reflectivity patterns (solid symbols) along with their best fits (open symbols) as a function of Q_z for the NSF [R_{--} (square) R_{++} (circle)] and SF [R_{-+} (triangle)] channels measured at (a) close to the coercive field H_a = -2.0 kOe, (b) a slightly higher field H_a = -2.0 kOe, (c) a saturation field H_a = -10.0 kOe during the first field cycles, and (d) at H_a = -1.55 kOe during the second field cycle 136

5.9 FM layers switching sequence during the first field cycle at H_a = -2.07

LIST OF FIGURES (Continued)

Figure **Page**

kOe and during the second field cycle at H_a = -1.55 kOe. The arrows indicate that the M_{FM} orientations in the respective layers. The applied field H_a is along the –*y* axis 138

5.10 (a) SF specular reflectivity [R_{-+}] patterns as a function of Q_z measured during the first field cycle at H_a = -2.07 and -10.0 kOe and during the second field cycle at H_a = -1.55 kOe. (b) Plot of the corresponding corrected SF signals as a function of Q_z 139

5.11 Specular reflectivity patterns (solid symbols) along with their best fits (open symbols) as a function of Q_z for the NSF [R_{--} (square) R_{++} (circle)] and SF [R_{-+} (triangle)] channels measured at (a) H_a = -1.43 kOe, (b) H_a = -1.67 kOe, and (c) H_a = -1.73 kOe during the fourth field cycle for different H_{RE} (= 0.5, 3.0, and 10.0 kOe, respectively) values when Ω_{RE} = 45°. 141

5.12 FM layers switching sequence during the first field cycle at H_a = -1.44 kOe (H_{RE} = 0.5 kOe), -1.67 kOe (H_{RE} = 0.5 kOe), and -1.73 kOe (H_{RE} = 0.5 kOe) when Ω_{RE} = 45°. The arrows indicate that the M_{FM} orientations in the respective layers. The applied field H_a is along the –*y* axis..... 143

5.13 (a) SF specular reflectivity [R_{-+}] patterns as a function of Q_z measured during the fourth for Ω_{RE} = 45° at H_a = -1.44, -1.67, and -1.73 kOe for

LIST OF FIGURES (Continued)

Figure **Page**

H_{RE} = 0.5, 3.0, and 10.0 kOe, respectively. (b) Plot of the corresponding corrected SF signals as a function of Q_z 144

5.14 Specular reflectivity patterns (solid symbols) along with their best fits (open symbols) as a function of Q_z for the NSF [R_{--} (square) R_{++} (circle)] and SF [R_{-+} (triangle)] channels measured at (a) H_a = -1.73 kOe, and (b) H_a = -1.65 kOe during the fourth field cycle for different H_{RE} (= 2.0 and 10.0 kOe, respectively) values when Ω_{RE} = 90°..... 146

5.15 FM layers switching sequence during the different fourth field cycles at H_a = -1.73 kOe (H_{RE} = 2.0 kOe), and -1.65 kOe (H_{RE} = 10.0 kOe) when Ω_{RE} = 90°. The arrows indicate that the M_{FM} orientations in the respective layers. The applied field H_a is along the $-y$ axis..... 147

5.16 (a) SF specular reflectivity [R_{-+}] patterns as a function of Q_z measured during the fourth for Ω_{RE} = 90° at H_a = -1.73 kOe, and -1.65 kOe for H_{RE} = 2.0 kOe and 10.0 kOe, respectively. (b) Plot of the corresponding corrected SF signals as a function of Q_z 148

LIST OF ABBREVIATIONS

Å	Angstrom
AF	Antiferromagnet
AMR	Anisotropic Magnetoresistence
Au	Gold
BFO	Bismuth Ferrite
BL8	Beamline 8
Co	Cobalt
CoO	Cobalt oxide
DC	Direct Current
EXAFS	Extended X-ray Absorption Fine Structure
eV	electron-volt
FEFF	Effective Scattering Amplitude
FM	Ferromagnet
FMS	Full Multiple Scattering
GISANS	Grazing Incident small angle X-ray Scattering
GMR	Giant magnetoresistance
H_a	Applied Field
H_{EB}	Exchange Bias Field
H_{FC}	Cooling Field (Cooled)
H_{RE}	Reorientation Field
K	Kelvin

LIST OF ABBREVIATIONS (Continued)

LCF	Linear Combination Fitting
M	Magnetization
M_{FM}	Ferromagnet Magnetization
ML	Multilayer
MT	Muffin Tin
Mn	Manganese
NSF	Non-spin flip
Oe	Oersteds
Ω_{RE}	Orientation angle
PNR	Polarized Neutron Reflectivity
PSI	Paul Scherrer Institute
PVD	Physical Vapor Deposition
RF	Radio Frequency
RSMS	Real Space Multiple-Scattering
RT	Room Temperature
SCF	Self-Consistent Field
SINQ	Swiss Spallation Neutron Source
SF	Spin flip
SLRI	Synchrotron Light Research Institute
SLD	Scattering Length Density
SQUID	Superconducting Quantum Interference Device
TOF	Time of Flight

LIST OF ABBREVIATIONS (Continued)

T_C	Curie Temperature
T_N	Neél Temperature
XANES	X-ray Absorption Near Edge Structure
XAS	X-ray Absorption Spectroscopy
XRD	X-ray Diffraction
ρ_n	Nuclear Scattering Length Density
ρ_m	Magnetic Scattering Length Density

มหาวิทยาลัยเทคโนโลยีสุรนารี

CHAPTER I

INTRODUCTION

1.1 Background

Magnetic materials and magnetic devices play major roles in modern science and technology. Yet in the late 1980s, the association of ferromagnetic and non-ferromagnetic thin layers in a multilayered material leads to the discovery of the Giant magnetoresistance (GMR) effect (Baibich *et al*., 1988). This property represents an important breakthrough in science and opens the way for building up new sensors and magneto storage devices. GMR based exchange biased magnetic tunnel junctions and spin valves have useful properties for forming magnetic memory elements in novel device architecture (Parkin *et al*., 1999).

The exchange bias phenomenon is associated with the direct exchange coupling at the interface between a ferromagnet (FM) and an antiferromagnet (AF), resulting in a unidirectional magnetic anisotropy that causes a shift of the hysteresis loop to negative field values. The magnitude of the field shift is called the exchange bias field (H_{EB}). Usually, the exchange bias shift occurs after cooling the system with a saturated FM below the Néel temperature of the AF. Over the last decade many salient features of the exchange bias effect have been clarified. It turns out that only a very small percentage of moments at the AF interface are pinned while the rest of the moments rotate rigidly with the FM. It also turns out that it is energetically favorable

to form domains in the antiferromagnet. They account for the lowering of the energy cost associated with the reversal of the FM that determines the strength of the H_{EB}. Exchange bias is also related to many salient features such as coercivity enhancement (Stiles and McMichael, 1999; Gruyters and Schmitz, 2008), asymmetry hysteresis loops (Paul *et al*., 2006), and training effect (Paul and Mattauch, 2009).

Despite four decades of research since the exchange bias effect was discovered (Meiklejohn and Bean, 1957) and the commercially available magnetic sensor devices, the microscopic understanding of the exchange bias effect is still not fully established. Therefore, the researches of many salient features which affect to the exchange bias effect have been widely studied.

Furthermore, there has been considerable recent interest in developing multifunctional materials in which two or more useful properties are combined in a single compound. Perhaps the most widely studied class of multifunctional materials are the dilute magnetic semiconductor, where interaction between magnetic field and electronic degrees of freedom allows both charge and spin to be manipulated by applied homogeneous electric fields (Ohno, 1998). These and other related materials having spin-dependent electronic properties are being explored for spintronic applications (Wolf *et al*., 2001). However, another class of materials, the so-called multiferroics (Schmid, 1994), is also growing importance. Multiferroic materials have simultaneous ferromagnetic, ferroelectric and/or ferroelastic ordering. Coupling between the magnetic and ferroelectric order parameters can lead to magnetoelectric effects, in which the magnetization can be turned by an applied electric field and vice versa. Besides scientific interest in their physical properties, multiferroic materials

have potential for application as actuators, switches, magnetic field sensors or new types of electronic memory devices.

$BiFeO_3$ is unique among various multiferroic materials, as its ferroelectric and magnetic transition temperatures are well above the room temperature. This raises the possibility of developing potential devices based on magnetoelectric coupling at the room temperature. Many research groups have tested substitution of the other elements for the Bi- and/or Fe-site to enhance the ferroelectric and magnetic orderings (Lee *et al*., 2005; Wang and Nan, 2006). As a typical result, $BiFeO_3$ thin films have greatly increased their remnant electric polarization by doping with Mn (Singh, Ishiwara and Maruyama, 2006). However, the mechanism has not yet been clarified and, moreover, the doping effect on the magnetic ordering is left an open question. Thus, an investigation of the exact local structure of Mn in $BiFeO_3$ has been extensively studied.

1.2 Bismuth ferrite

Bismuth ferrite ($BiFeO_3$; BFO) is considered as a prototype multiferroic material and is probably the most studied multiferroic materials due to its most promising potentials for realizing multiferroic device. BFO, which exhibits the simultaneous existence of ferroelectric (FE) and antiferromagnetic (AFM) orders, has received great attention, due to its high Curie point (T_C ~ 1103 K) and Neél temperature (T_N ~ 643 K), (Michel, 1996). BFO has a distorted perovskite structure with rhombohedral symmetry which belongs to the *R3C* space group (the hexagonal setting is used in this thesis). The lattice constants determined at room temperature are a_{hex} = 5.5810 Å and c_{hex} = 13.8757 Å (Sosnowska, 2002), as shown in Figure 1.1.

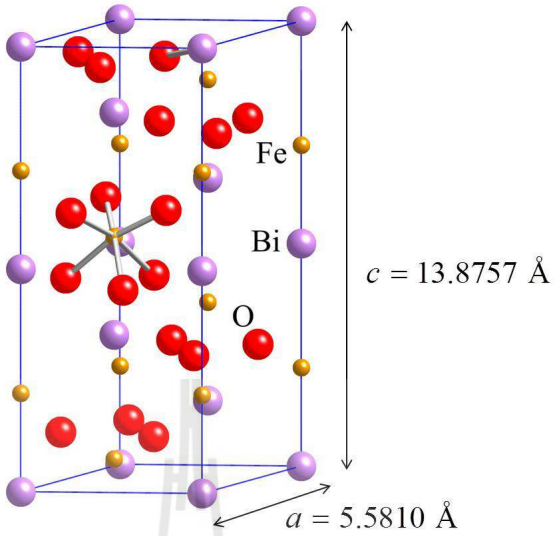

Figure 1.1 Crystal structure of BFO (hexagonal setting).

However, the small room temperature spontaneous polarization and magnetization, as well as large leakage current, are the obstruction of the commercial applications of BFO ceramics. Fortunately, the electrical and magnetic properties of BFO can be improved by doping of other ions or by making low-dimensional structures.

Recently, some research groups have modified BFO nanostructures by doping a small amount of impurities at *A* or *B* site (in ABO_3 perovskite structure) which offer great potential to enhance the physical properties of BFO. For example, the partial substitution of Tb at A-site can enhance both ferroelectric and magnetic properties of BFO (Palkar *et al*., 2004). On the other hand, some research groups have attempted B-site substitution by high valence state such as Zr^{4+} and Ti^{4+} to improve ferroelectric reliability (Wang *et al*., 2006). Recently, One dopant that has been the subject of interest is Mn. Based on X-ray diffraction (XRD) and transmission electron

microscopy (TEM) characterization, Fukumura *et al*. have reported the synthesis of single-phase Mn-doped $BiFeO_3$ nanoparticles with Mn concentration up to 2 at.%. With increasing Mn content, the samples showed anomalous behavior at around ≈ 3%, suggesting a lattice distortion from the rhombohedral structure to a monoclinic or tetragonal structure occurred (Fukumura *et al*., 2009).

Moreover, Ablat *et al*. have investigated the electronic structure of $BiFe_{1-x}Mn_xO_3$ ($0 \leq x \leq 3$) thin films by using X-Ray Absorption Spectroscopy (XAS). They found that XRD patterns of these films illustrated a single phase and have a rhombohedral crystalline structure. From the Fe L_3-edge and O *K*-edge XAS Spectra, they also observed that the increasing of Mn content reduces the charge transfer between the Fe 3*d* and O 2*p* and leads to the bond inhomogeneity in the Fe-O-Mn chains (Ablat *et al*., 2012). By using the first-principle calculation, Wang have reported that the effect of Mn substitution for Fe in multiferroic BFO leads to the enhancement of the spontaneous magnetization of the system (Wang, Huang and Wang, 2010).

Interestingly, most previous works on Mn-doped BFO materials focus on the improvement methods of nanostructure formation and the enhancement of the physical properties of these materials. There has been no direct experimental determination of Mn-site in BFO structure and examination of the formation of the secondary phase. Since the site preference of Mn ions in BFO structure and secondary phase play a critical role in determining the electric and magnetic properties of Mn-doped BFO materials as reported in prior theoretical and experimental investigations (Unruan *et al*., 2012), it is thus important to identify the exact local structure of Mn in BFO lattice and verify the amount of secondary phase.

1.3 Cobalt/cobalt oxide exchange-coupled system

A polycrystalline Co (ferromagnet, FM)/CoO (antiferromagnet, AF) has served as a prototypical exchange bias system, due to its large biasing field (Paul, Schneider, and Stahn, 2007), very distinct asymmetry of magnetization reversal (Gierlings *et al*., 2002), and large enough training effects. Most interestingly, the AF moment configuration of this system can also be frozen in a variety of ways during the process of field cooling (Paul *et al*., 2011) without affecting the overall structure as the AF ordering temperature is far below room temperature.

In general, it may be noted that exchange bias system are frequently coated with a nonmagnetic metallic spacer such as Cu or Au film, in order to protect them against further oxidation (Laureti *et al*., 2012). Moreover, Au is often used as metallic leads for spin-valve structures. Therefore, the Au /FM (or AF) interfaces and their effect on exchange bias cannot be ignored. Based on reflection high energy electron diffraction (RHEED) and Cross-sectional transmission electron microscopy (XTEM) characterization, Miltényi *et al*. have reported an increased defect density ($Co_{1-x}O$) gives to stronger exchange bias in Co/CoO bilayers, even when the defects are located at distance from the interface to the exchange-biased FM layer (Miltényi *et al*., 2000). Recently, researchers have found that increasing of H_{EB} can originate from the formation of defects within the antiferromagnetic Co_xO_y layer or from deviations in the stoichiometry during the route of oxidation of Co to CoO (Paul *et al*., 2004) leading to a stronger pinning of the domain walls at the defect sites. However, most previous works on the formation of defects in the exchange bias system cannot identify the type of defects by using RHEED and XTEM. Thus, in order to verify the formation of such defect sites that can be inadvertently related to the degree of

oxidation of the Co layer (few nanometers), the proportion and stoichiometry of the CoO layers in the system are necessary to be investigated. Such a detailed examination of the chemical species can be effectively done by XAS.

One of the interesting problems in the exchange-coupled system is the training effect, the distinction between subsequent (partial) magnetization reversal loops. The training effect can be linked to a deviation of the average interfacial magnetization vector of the AF CoO grains with respect to the initial field cooling direction. Even though the microscopic origin of the training effect is still ambiguous, it is generally agreed to be due to the rearrangement of interfacial AF spin structure, which can be considered as a rotatable hysteretic grains (rotatable anisotropy) particularly in polycrystalline specimens (Paul, Schneider and Stahn, 2007; Brems, Temst and Haesendonck, 2007).

Generally, a relatively large training can be seen between the first and second hysteresis loops, and a comparatively small effect can be seen for the subsequent higher number of loops. The strong training behavior between the first and second hysteresis loops is usually attributed to some initial nonequilibrium arrangement or metastable state of the AF (Paul *et al*., 2006; Fecioru-Morariu *et al*., 2007). The exact mechanism for the initial AF spin arrangement is still a matter of debate. However, it is perceived that the metastable state can somehow be rearranged to reinduce the original state. By using the anisotropy magnetoresistence (AMR) analysis, Breme *et al*. have reported that the orientation of the interfacial magnetization of the AF grains can be largely rotated back to the initial orientation after field cooling (i.e., the untrained state) by a moderate magnetic field which is applied perpendicular ($\perp^r$) to the initial cooling field in a Co/CoO bilayer system (Breme *et al*., 2007). The

possibility of the recovery of the untrained state strongly depends on the magnitude of a moderate magnetic field. Furthermore, the simulated AMR for a hysteresis loop along the cooling field, after first applying a hysteresis loop with a perpendicular field, has indicated that the reinduction of the untrained state depends on the amplitude and direction of a moderate magnetic field (Breme *et al*., 2005).

Recently, Breme *et al*. reported that the AMR effect with a specific choice of the measurement geometry (with an angle of 45° between current and magnetic field) can be used to reliably monitor the average rotation sense of the magnetization vector of a 20 nm Co layer upon magnetization reversal in a similar CoO/Co bilayer system (Breme *et al*., 2013). However, their inference on the rotational sense relies upon the AMR single measured along 45° with respect to the cooling field and also the $\perp^r$ field direction. Therefore, it may be noted that the AMR measurements rely on the current distribution within the sample and are difficult to infer on any reinduction of the untrained state within a multilayered system, particularly when domains are involved. AMR values are weak when a sample comprises of different domains of equal proportions that can rotate clockwise or counterclockwise. Moreover, the direction of the reorienting magnetic fields (with different magnitudes) in the works of Brems *et al*. were always restricted along or opposite to the direction $\perp^r$ to the initial cooling field.

Based on depth sensitive polarized neutron reflectivity (PNR) analysis, Paul *et al*. have reported the magnetization angles, which are extracted from the specular reflectivity patterns, for the layers in the stack of antiferromagnetically coupled Fe/Si multilayer (Paul *et al*., 2008). Very recently, Paul and Buchmeier reported that a partial restoration of the untrained state was indeed possible even within a

Co/CoO/Au multilayer (Paul, 2010; Paul and Buchmeier, 2013). Although the bilayers of the multilayer were separated by a thick nonmagnetic Au layer at each AF-FM interface, it was expected to behave as a repeated stack of independent Co/CoO bilayers. Interestingly, the PNR data illustrated that the $\perp^r$ field cycling has inflicted an additional modification at the Co/CoO interface magnetization. One may note that PNR is sensitive to each and every interface along the depth of the entire multilayer stack and to the direction of the parallel magnetic moment (though not to the directional sense of the perpendicular magnetic moment). However, such a conclusion on interface magnetism in the work of Paul *et al*. suffered two shortcomings. First, the PNR data were limited to a relatively low value of the accessible scattering vector (0.05 $Å^{-1}$) and second, the particular specimen was subjected to a single field value along the $\perp^r$ direction. In fact, there are no experimental studies on the impact of the strength and orientations of the applied field on the recovery of the untrained state. The aim of this study is, therefore, to investigate of the reinduction of the untrained state in a Co/CoO/Au multilayer using different values of the applied field with respect to the cooling and along different orientations

1.4 Scope and limitations of the study

This study aims to investigate the valence state and the local structure of the Mn atoms atom in $BiFe_{1-x}Mn_xO_3$ ceramic samples using the low energy region of X-ray absorption spectroscopy (XAS), which called X-ray Absorption Near Edge Structure (XANES). XANES will also be employed to examine the formation of the secondary phase in $BiFe_{1-x}Mn_xO_3$ ceramic samples as well as the Co/CoO/Au multilayers. FEFF 8.2 code, which is based on *ab initio* multiple scattering, will be used to simulate the

XANES spectra of $BiFe_{1-x}Mn_xO_3$ and Co/CoO/Au multilayers to compare with the experimental results obtained from XAS beamline at SLRI, Nakhon Ratchasima, Thailand. The linear combination analysis (LCA) method will be used to quantify the proportion of oxidized and poorly oxidized Co layer in the Co/CoO/Au multilayers (ML).

Furthermore, the reinduction of the untrained state in a Co/CoO/Au multilayered system using different values of the reorientation field (H_{RE}) and along different orientation angles (Ω_{RE}) with respect to the cooling field direction will be explored by SQUID magnetization hysteresis loops and depth sensitive Polarized Neutron Reflectivity (PNR).

มหาวิทยาลัยเทคโนโลยีสุรนารี

CHAPTER II

THEORY

2.1 X-ray absorption

2.1.1 X-ray interaction with matter

X-rays are a type of electromagnetic radiation with energies in the range 120 eV to 120 keV. They were discovered by Röntgen in 1985 (Stanton, 1896) and have become an invaluable tool to study the structure of matter. X-rays, like any other electromagnetic radiation, can be treated as either a wave or a particle. This wave-particle duality is described by the *Einstein relation*

$$E = h\nu = \frac{hc}{\lambda_{ph}}, \tag{2.1}$$

where E is the energy of the photon with h being Planck's constant. ν and λ_{ph} are the frequency and the wavelength of the wave, respectively. Likewise, electrons possess the wave-particle duality. The wavelength and the momentum of an electron are related by the *de Broglie equation*

$$\lambda_{\mathrm{el}} = \frac{h}{p_{\mathrm{el}}} = \frac{2\pi}{k_{\mathrm{el}}}, \tag{2.2}$$

And the kinetic energy of electron is given by

$$E_{\mathrm{el}} = \frac{h^2}{2m_e\lambda_{\mathrm{el}}^2}, \tag{2.3}$$

where m_e is the electron mass.

In general, an X-ray photon can be interacted with an atom either scattered or absorbed (Als-Nielsen and MaMorrow, 2001). In scattering, the X-ray photons are deflected from their original direction of propagation, either Compton scattering or Rayleigh scattering (without loss of energy), by collision with an electron or an atom. In the X-ray absorption process, the energy of the X-ray photon is used to expel an electron from the atom, leaving the atom ionized. The excess photon energy is transferred as kinetic energy to the electron. The process is called photoelectric absorption which was first rigorously described by Einstein in 1905 (Einstein, 1905).

2.1.2 Absorption coefficients and cross-sections

The equation of absorption was explained by Lambert-Beer law, the intensity of the beam after pass through the sample decreases according to exponential equation with the intensity of the incoming x-ray beam, as

$$I = I_0 e^{-\mu x} \tag{2.4}$$

where I_0 is the intensity of the incoming x-ray beam, I is the intensity of the beam after pass through the sample, x is the thickness of the sample and μ is the absorption coefficient as shown in Figure 2.1. According to Equation (2.4), for the x-ray absorption measurement, the measured absorption signal can be defined by the following:

$$\mu x = \ln\left(\frac{I_0}{I}\right) \tag{2.5}$$

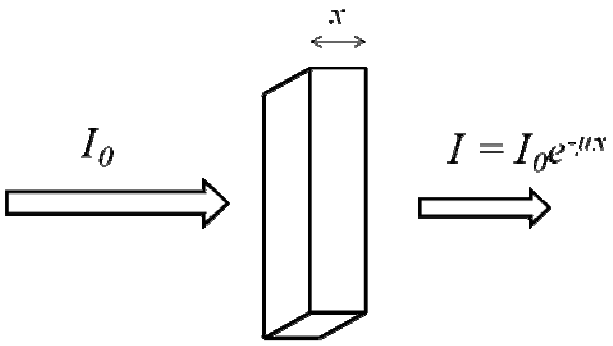

Figure 2.1 Schematic view of x-ray absorption measurement in transmission mode.

The linear absorption coefficient and the absorption cross-section σ_a, are related by

$$\mu = \rho_a \sigma_a = \left(\frac{\rho_m N_A}{A} \right) \sigma_a , \tag{2.6}$$

where N_A, ρ_a, ρ_m, and A are Avogadro's number, the atomic density, the mass density and the atomic mass number, respectively.

The absorption cross section has a distinct dependence on the photon energy. An example is shown in Figure 2.2 for the element platinum. The double-logarithmic plot illustrates that the absorption cross section is approximately proportional to $1/E^3$ below and above discontinuities. The latter, which well known as the absorption edges, occur at characteristic energies for which the X-ray has enough energy to expel an electron from an atomic core level giving rise to a sudden increase of the absorption cross section.

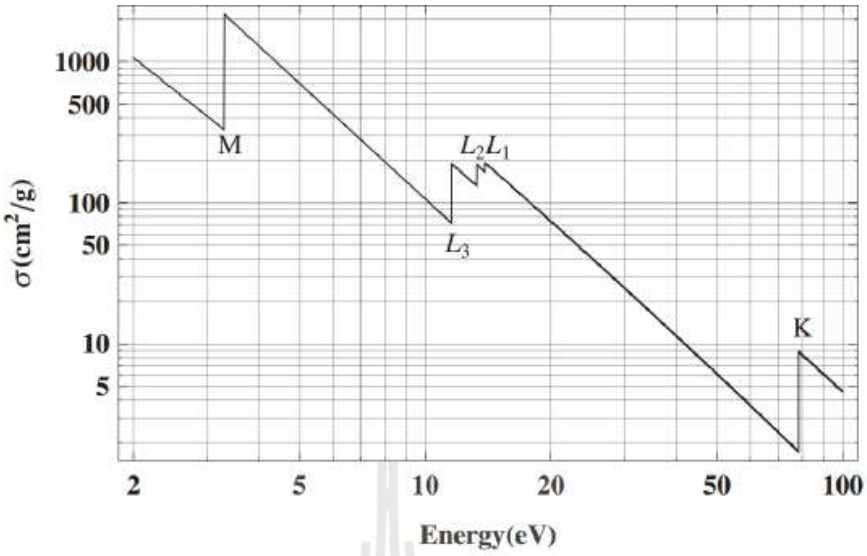

Figure 2.2 Log-log plot of the semi-empirical X-ray absorption cross section for platinum versus X-ray energy. The *K*, $L_{I,II,III}$ and *M* edges are shown, while the fine structure is not shown (Bunker, 2010).

2.1.3 Absorption edges

The shells of the electron in an atom are classified as *K*, *L*, *M*, etc. according to the values of their principle quantum number n = 1, 2, 3,…respectively. However, the degeneracy is lifted into subshells due to interelectron repulsion and coupling between spin and angular momentum. The subshell can thus be labeled as $(nl_j)^{2j+1}$ where n, l and j are the principal, orbital angular momentum, and total angular momentum quantum numbers, respectively, of the single-electron states ($2j$+1 is the multiplicity).

An X-ray absorption edge occurs if the photon energy matches the energy necessary to excite an atomic core-level electron in one of the shells into an unoccupied level above the Fermi energy E_F. In general, the electrons transition is

followed by the selection rules. For the transition of an atomic core-level electron to a valence orbital (in this case a bound-bound transition occurs), the optical dipole selection rules ($\Delta j = 0, \pm 1$, $\Delta m = 0, \pm 1$; ignoring spin) can be applied. The Orbital Rule ($\Delta l = \pm 1$), the difference electron's orbital angular momentum must be equal -1 or 1 only, will be used when an atomic core-level electron are expelled to final continuum states. The symbol used to label the X-ray absorption edges is given in Figure 2.3. For instance, the L_{I}, L_{II} and L_{III} edges arise for absorption from the $(2s)^2$, $(2p_{1/2})^2$ and $(2p_{3/2})^4$ subshells, respectively. The energies of the edges are unique to the type of atom that absorbs the X-ray. The absorption edges are therefore signatures of the atomic species present in a material.

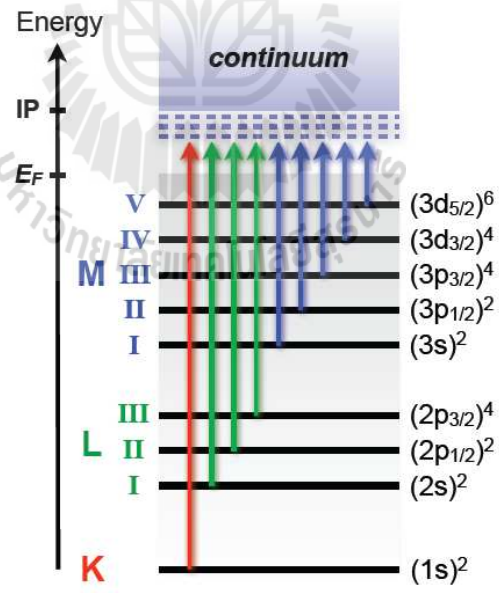

Figure 2.3 Schematics of the atomic energy levels and the symbol used to label the X-ray absorption edges of the elements. Transitions occur to all empty states above the Fermi level that exhibit appropriate symmetry governed by the dipole selection rules (Adapted from Als-Nielsen and MaMorrow, 2001).

2.1.4 X-ray Absorption Spectroscopy (XAS)

The X-ray absorption spectroscopy (XAS), sometime also known as X-ray absorption fine structure (XAFS), is an absorption spectroscopy technique that refers to a modulation of the absorption coefficient as a function of the incident photon, typically by a few percent, around and above the absorption edge. This fine structure is a unique signature of a given material due to it depends on the detailed atomic structure and electronic properties of the material.

The X-ray absorption spectrum is typically divided into two regions differing in the energy of the photoelectron and the information content of the fine structure (1) the X-ray Absorption Near Edge Structure (XANES) which includes features approximately 80-100 eV above the absorption edge and (2) the Extended X-ray Absorption Fine Structure (EXAFS) typically extending to 1,000 eV above the absorption edge as shown in Figure 2.4. The XANES region (including the pre-edge region) contains the information about the local geometry of the absorbing atom. The edge position also contains information about the charge (oxidation state) on the absorber. According to the overlapping contributions of many electronic and structural effects and the approximations necessary for its theoretical description, the XANES is frequently only qualitatively interpretable. The EXAFS spectrum is more directly related to the structure around the absorbing atom. Electronic effects play a reduced role making the interpretation of the EXAFS spectrum straight-forward.

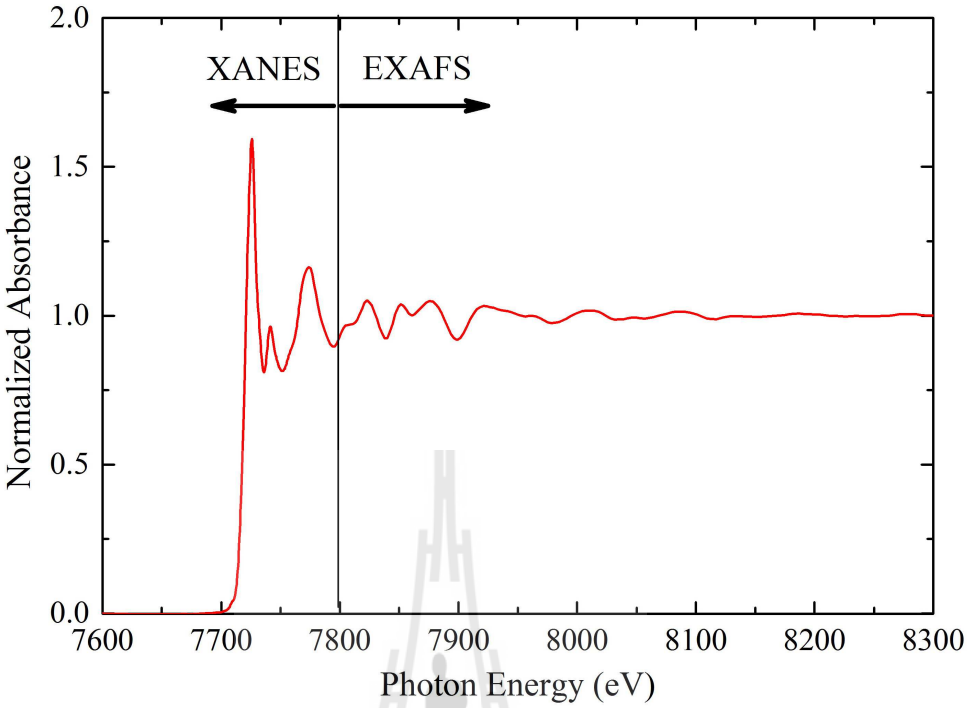

Figure 2.4 Normalized Co *K*-edge absorption spectra classified into two regions; XANES and EXAFS.

2.1.5 X-ray Absorption Near Edge Structure (XANES)

The X-ray absorption cross section, which is related to the absorption coefficient via the equation (2.6), can be written using the Fermi's Golden rule of one electron approximation (Sakurai, 1967; Ankoudinov, 1996)

$$\sigma(\omega) = \frac{2\pi}{\hbar\Phi_0}\sum_f \left|\langle f \left| \vec{r}\cdot\hat{\varepsilon}e^{i\vec{k}\cdot\vec{r}} \right| i\rangle\right|^2 \delta(E_i - E_f + \hbar\omega), \qquad (2.7)$$

where $|i\rangle, |f\rangle$, E_i and E_f denote the initial and final stats and their energies; $\vec{k}$ is wave vector, Φ_0 is the x-ray photon flux, $\hbar\omega$ is the energy of x-ray photon energy, $\hat{\varepsilon}$ is the x-ray polarization vector and $\delta(E)$ is the Dirac delta function.

According to equation (2.7), the absorption coefficient can therefore be written in form of the Dipole operator (*D*) as

$$\mu(E) \propto \sum_f \left| \langle f | \vec{D} | i \rangle \right|^2 \delta\left(E_i - E_f + \hbar\omega\right), \tag{2.8}$$

which can easily understand that the absorption coefficient is proportional to the transition rate of photoelectron form $|i\rangle$ to next $|f\rangle$ state corresponding to the photon energy incident in the Dirac delta function and amplitude relate dipole transition in inner atom. However, the absorption spectrum in XANES region is dominated by multiple scattering of low kinetic energy of the photoelectron. The wave associated with the photoelectron propagates from the absorbing atom as a spherical wave. The oscillation extends for a several hundred eV above the edge, due to the back scattering of the outgoing spherical wave by neighboring atom.

The scattering process of the photoelectron can be described by spherical potential approximation, known as *muffin-tin approximation* (Rehr and Albers, 2000; Kodre, 2002). In this approximation, the photoelectron suffers a potential *V*, which is sum of single contribution in non-overlapping spherical region of finite radius.

$$V = \sum_n v_n(\vec{r}), \tag{2.9}$$

where $v_n(\vec{r})$ is the single atom contribution to the muffin-tin potential. Then the muffin-tin potential consists of non-over lapping well-defined spherical regions. The muffin-tin potential is sketched in Figure 2.5. The potential outside the spherical regions or interstitial regions is set to zero. The scattering amplitude and phase shifts parameters are determined separately for each scatterer and are thus pure atomic quantities.

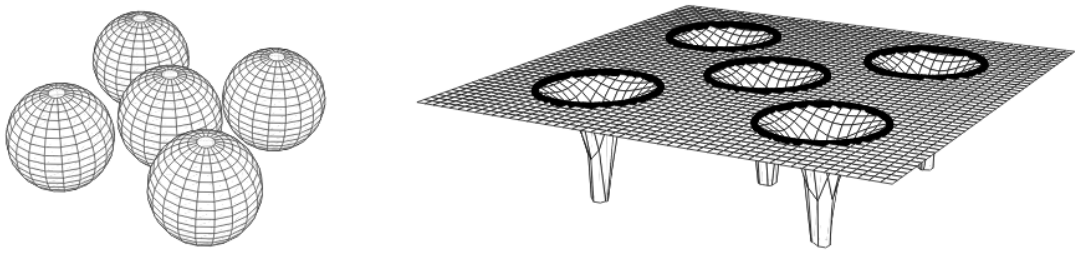

Figure 2.5 The muffin-tin potential consist of non-overlapping spherical regions (Kodre, 2002).

Propagation of the photoelectron in such muffin-tin potential V is described by the Hamiltonian

$$H = H_0 + V, \tag{2.10}$$

where H_0 is the unperturbed contribution, consisting of only kinetic-energy operator. In order to obtain the eigenstate $|\psi\rangle$ of the Hamiltonian operator H, The Schrodinger equation is considered

$$H|\psi\rangle = E|\psi\rangle, \tag{2.11}$$

substituting equation (2.11) into (2.10), obtaining

$$(E - H_0)|\psi\rangle = V|\psi\rangle. \tag{2.12}$$

The term of $(E - H_0)|\psi\rangle$ is free-electron wave function. Therefore, the solution of the homogeneous part of equation free-electron wave function can be defined in a coordinate representation as $\langle \vec{r}\,|\phi\rangle$, giving

$$(E - H_0)\langle \vec{r}\,|\phi\rangle = 0. \tag{2.13}$$

The free-electron Green's function G_0 is defined with relation

$$(E - H_0)G_0(\vec{r}, \vec{r}'; E) \equiv (\nabla^2 + k^2)G_0(\vec{r}, \vec{r}'; E) = \delta(\vec{r} - \vec{r}'). \tag{2.14}$$

Consequently, the general solution of equation (2.12) is given as a sum of the solution of homogeneous part and the Green's function for the muffin-tin potential part

$$\langle \vec{r} | \psi \rangle = \langle \vec{r} | \phi \rangle + \int d^3\vec{r}' G_0(\vec{r}, \vec{r}'; E) \langle \vec{r}' | V | \psi \rangle. \quad (2.15)$$

If the photoelectron is only weakly scattered by the potential *V*, the solution $\langle \vec{r} | \psi \rangle$ is closed to the free-electron solution $\langle \vec{r} | \phi \rangle$. In order to solve the equation (2.15), the formal solution of the operator equation (2.12) is given by the Lippman-Schwinger equation (Meszbacher, 1970)

$$| \psi \rangle = | \phi \rangle + \frac{1}{E - H_0 \pm i\eta} V | \psi \rangle. \quad (2.16)$$

According to its singularity, an imaginary term is modified in the operator $1/(E - H_0)$ by $\pm i\eta$, where η is infinitesimally small for identify direction of spherical wave electron.

To demonstrate the equation (2.15), $\langle \vec{r} |$ is used to multiply the equation (2.16) and can be written as

$$\psi(\vec{r}) = \langle \vec{r} | \psi \rangle = \langle \vec{r} | \phi \rangle + \langle \vec{r} | \frac{1}{E - H_0 \pm i\eta} V | \psi \rangle \quad (2.17)$$

By introducing the closed relation $\int d\vec{r}' | \vec{r}' \rangle \langle \vec{r}' | = 1$ in the above equation, we can write the equation as

$$\psi(\vec{r}) = \langle \vec{r} | \psi \rangle = \langle \vec{r} | \phi \rangle + \int d\vec{r}' \langle \vec{r} | \frac{1}{E - H_0 \pm i\eta} | \vec{r}' \rangle \langle \vec{r}' | V | \psi \rangle \quad (2.18)$$

Comparing the equation (2.15) to equation (2.18), the Green's function can be written in form

$$G_0^{\pm}(\vec{r}, \vec{r}'; E) = \langle \vec{r} | \frac{1}{E - H_0 \pm i\eta} | \vec{r}' \rangle \quad (2.19)$$

and

$$G_0^{\pm} = \frac{1}{E - H_0 \pm i\eta} \tag{2.20}$$

Obviously, G_0^+ and G_0^- describe how outing and incoming spherical waves propagate in free space, respectively. For solving the Lippman-Schwinger equation, the transition operator *T* is introduced (Sakurai, 1967; Merzbacher, 1970)

$$V|\psi\rangle = T|\phi\rangle. \tag{2.21}$$

If we define the propagator *G* of the entire system as

$$G(E) = (E - H_0 - V + i\eta) = \left([G_0]^{-1} - V\right)^{-1}, \tag{2.22}$$

$$G(E) = (1 - VG_0)^{-1} G_0 . \tag{2.23}$$

By using the Taylor series expression, the equation (2.23) can be written as

$$G(E) = G_0 + G_0 V G_0 + G_0 V G_0 V G_0 + ... = G_0 + G_0 V[G_0 + G_0 V G_0 + ... \tag{2.24}$$

$$G(E) = G_0 + G_0 V G. \tag{2.25}$$

The relationship between the transition operator *T* and the muffin-tin potential V is given by

$$G_0 T = GV. \tag{2.26}$$

By substituting the equation (2.25) in (2.26), the transition operator can be written as

$$T = V + V G_0 V + V G_0 V G_0 V + ... = V + V G_0 T. \tag{2.27}$$

The following important relationships from the equation (2.26) are

$$G = G_0 + G_0 T G_0 ; \quad T = V + VGV. \tag{2.28}$$

Since we consider the muffin-tin potential as a sum of single spherical potentials, each act in a well-defined non-overlapping region of the space.

Therefore, the transition operator of individual atom can be written in form

$$t^i = v^i + v^i G_0 t^i . \tag{2.29}$$

However, the transition operators T and t is not explicit the physical meaning, but we can explain in the meaning of the weak-scattering expansions by substituting the equation (2.29) into (2.27), (2.28), respectively, we obtain

$$T = \sum_i t^i + \sum_i \sum_{i_1 \neq i} t^{i1} G_0 t^i + \sum_i \sum_{i_1 \neq i} \sum_{i_2 \neq i_1} t^{i2} G_0 t^{i1} G_0 t^i + \ldots \tag{2.30}$$

$$t^i = v^i + v^i G_0 v^i + v^i G_0 v^i G_0 v^i \tag{2.31}$$

$$\begin{aligned} G &= G_0 + \sum_i G_0 v^i G_0 + \sum_{i,i_1} G_0 v^{i_1} G_0 v^i G_0 + \ldots \\ &= G_0 + \sum_i G_0 t^i G_0 + \sum_i \sum_{i_1 \neq i} G_0 t^{i_1} G_0 t^i G_0 + \ldots \end{aligned} \tag{2.32}$$

Their series equations are called Dyson's expansion (Ankudinov *et al*., 1998). The transition operator *T* can explain by the order of scattering process of the photoelectron wave. The first term corresponds to the no scattered wave propagation, while the second term is the scattered wave from the *i*th atom due to the potential v^i and then heads forward again as shown in Figure 2.6(a)-left. In the same way, the third term describes double scattering of the incident wave as shown in Figure 2.6(a)-middle and right.

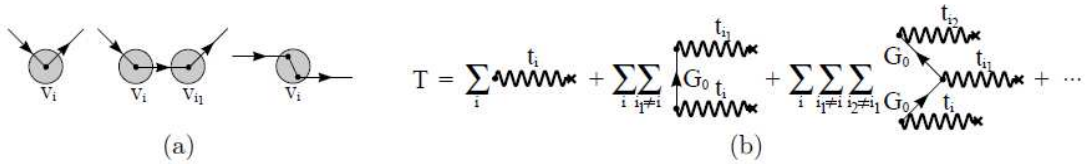

Figure 2.6 Single scattering (left), double scattering from different atoms (middle), and double scattering from the same atom (right). (b) Graphical representation of the *T*-operator (Kodre, 2002).

2.1.6 Extended X-ray Absorption Find Structure (EXAFS)

The EXAFS refers to the oscillating part of the x-ray absorption spectrum starting at approximately 80 eV above the absorption edge and extending up to about 1,000 eV. Above the absorption edge, the energy of X-ray photon is used to excite an electron into the continuum and any remaining energy is given to photoelectron in the form of kinetic energy.

The photoelectron can be described as spherical waves propagating from the absorber atoms. If the other atoms are located in the vicinity of the absorber atoms, the photoelectron is scattered by the neighbouring atoms and then return to the absorber atoms contribute to the EXAFS signal (Groot *et al.*, 1994; Hench and West, 1990). The incoming and the scattered waves may interfere, as indicated in Figure 2.7. Each atom at the same radial distance from the absorber contributes to the same component of the EXAFS signal. This group of the atoms is called a shell. The phase of the EXAFS signal change with the wavelength of the photoelectron depends on the distance between the absorber and backscattering atom. The variation of the backscattering strength as a function of energy of the photoelectron depends on the type of atom doing the backscattering. Thus EXAFS contains information on the atomic surroundings of the center atom.

In the EXAFS measurement, the oscillatory part of the x-ray absorption spectrum above a given absorption edge are considered. Therefore, an experimental EXAFS function can be defined by

$$\chi(E) = \frac{\left[\mu(E) - \mu_{\circ}(E)\right]}{\Delta\mu_{\circ}}. \qquad (2.33)$$

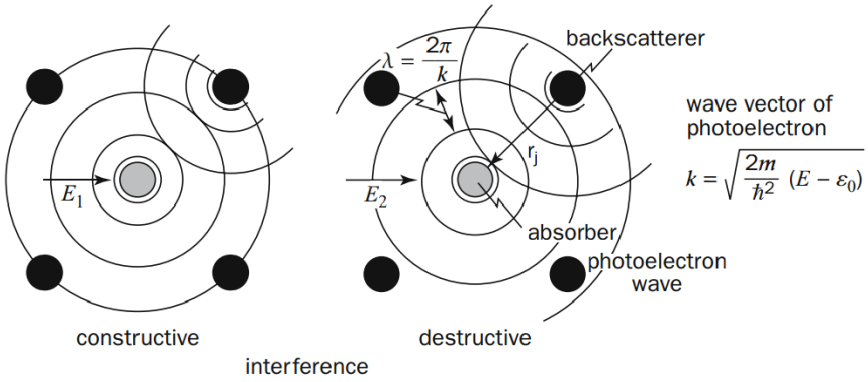

Figure 2.7 Interference of outgoing and backscattered photoelectron wave responsible for XAFS oscillation. $E = \hbar\omega$ is the incoming photon energy (Hippert *et al*., 20060).

where μ_0 is the background absorption coefficient. $\Delta\mu_0(E)$ is the absorption edge jump. The EXAFS function is usually expressed as a function of the photoelectron wave number *k* instead that on the incoming X-ray photon energy. The simple relation between the two quantities is

$$k = \sqrt{\frac{2m_e(E - E_0)}{\hbar^2}}, \tag{2.34}$$

where E_0 is the edge energy. Also, E_0 is defined as the energy at the first maximum of the derivation of the measured X-ray absorption spectrum (G. Bunker, 2010). Then the EXAFS function can be converted from $\chi(E)$ to $\chi(k)$ for general purpose.

The $\chi(k)$ can be understood in term of the EXAFS equation. In theoretical procedure, the EXAFS equation can be written in term of a sum of the contribution from all scattering path of the photoelectron (Stern and Heald, 1983):

$$\chi(k) = \sum_j \chi_j(k) \tag{2.35}$$

$$\chi(k) = \sum_j \frac{S_\circ^2 N_j}{k R_j^2} \left| f_j(k,\pi) \right| \sin\left[2kR_j + \varphi_j(k)\right] e^{-2\sigma_j^2 k^2} e^{-2R_j/\lambda(k)}, \tag{2.36}$$

The EXAFS equation is easiest to understand for a single scattering path. Each of the terms in the EXAFS equation is described below.

$(S_0^2 N_j)$: These terms modify the amplitude of the EXAFS signal. The subscript *j* indicates that this value can be difference for each path of the photoelectron. For single scattering, N_j is the number of coordinating atoms with a particular shell. For multiple scattering, N_j is the number of identical paths. $S_\circ^2(k)$ is the amplitude reduction term, due to many-body effect, usually has a value between 0.7 and 1.0 (Li *et al.*, 1995). $S_\circ^2(k)$ is different for different elements, but the value is generally transferable between different species from the same element and the same edge.

$f_j(k,\pi)$: This term is the effective scattering amplitude. For the single scattering path, it is the atomic scattering factor. For a multiple scattering, $f_j(k,\pi)$ is the effective scattering amplitude written in terms of the single scattering formalism (Rehr and Albers, 1990). This term describes the element sensitivity of EXAFS.

$1/R_j^2$: This term represents the contribution from a shell of atoms at a distance decreases with increasing distance from the absorber.

$\sin\left[2kR_j + \varphi_j(k)\right]$: This term account for the oscillations in the EXAFS signal with a phase given by $2kR_j + \varphi_j(k)$. The path of the photoelectron is described by $2R_j$ (the distance to the neighboring atom and then back to the absorber atom), which is multiplied by the photoelectron wave number *k* to determine the phase. $\varphi_j(k)$ is a

phase shift of the photoelectron caused by the interaction of the photoelectron with the nuclei of the absorber atom and the interaction with the nuclei of the coordinating atoms of the photoelectron path.

$e^{-2\sigma_j^2 k^2}$: Due to all of the coordinating atoms in a shell are not fixed at positions of exactly a distance R_j from the central absorber atom, σ^2 represents the disorder in the interatomic distance. σ^2 is the mean-square displacement of the bond length between the absorber atom and the coordinating atoms in a shell. This term has contributions from dynamic (thermal) disorder as well as static disorder (structural heterogeneity).

$e^{-2R_j/\lambda(k)}$: This exponential term depends on $\lambda(k)$, the mean free path of the photoelectron, which is the mean distance that a photoelectron travels after excitation.

Therefore, analyses of the EXAFS spectrum provide information about the number, species and inter-atomic distances of the neighbors from the absorption atom. However, in the EXAFS analysis $\chi(k)$ can be a Fourier transform (FT) in R-space and expressed by

$$\chi(R) = \frac{1}{2\pi}\int_0^\infty k^2 \chi(k) W(k) e^{i2kR} dk, \qquad (2.37)$$

To process and enhance the EXAFS with the high k region, the plot $\chi(k)\times k^2$ is considered and windowed using a Hanning window $W(k)$.

2.2 Neutron reflectivity

Neutron can be reflected on surface in the same way as X-ray or electron. So the scatter of neutrons from a surface or interface is quite similar to the X-ray. Neutron being charge neutral, primarily interact with the nuclear potentials. A neutron reflectivity provides the same information as X-ray reflectivity, which making the formalisms developed for x-ray reflectivity can be transposed to neutron reflectivity. In addition to that, neutrons also interact with the local magnetic induction $\vec{B}$ in the sample due to the magnetic moment $\vec{\mu}$. If the sample is magnetic and polarized neutrons are used, they reveal the magnetic depth profile of the film or multilayer (Zabel *et al*., 2007).

2.2.1 Reflectivity on non-magnetic system

Considering a collimated neutron beam impinges at a glancing angle α_i onto a surface from air (n=1) and then the reflected beam leaves the surface sample (with an refractive index *n*) under a glancing angle α_f, as shown in Figure 2.8, in case of specular reflection, the angle of reflection equals to the angle of incidence $(\alpha_i = \alpha_f = \alpha)$. The projection of the scattering vector Q_z on the *z*-axis (perpendicular to the surface) is given by

$$Q_z = 2k \sin\alpha = \frac{4\pi}{\lambda_n} \sin\alpha, \tag{2.38}$$

where $k = 2\pi / \lambda_n$ is the magnitude of the incident wave vector $\left|\vec{k}_i\right|$ which equal to the magnitude of the scattered wave vector $\left|\vec{k}_f\right|$ in the vacuum, and λ_n is the neutron wavelength.

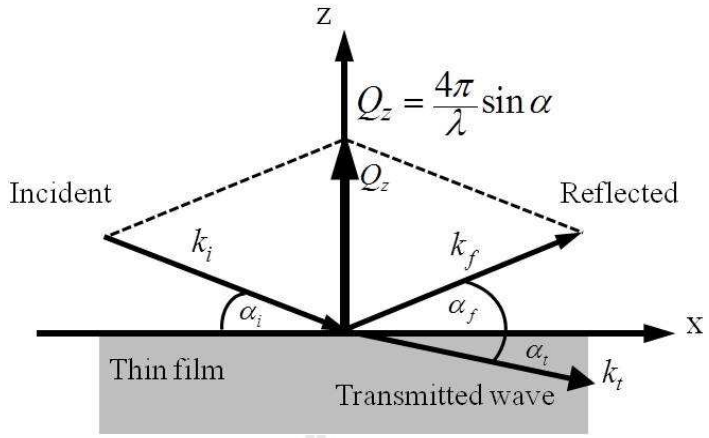

Figure 2.8 Specular reflectivity geometry (Adapted from Zabel *et al*., 2007).

In vacuum, the energy of neutron corresponding to the direction of neutron propagate in the *z*-direction is given by

$$E = \frac{\hbar^2 k^2}{2m_n} = \frac{h^2}{2m_n \lambda_n^2}, \tag{2.39}$$

where m_n is the electron mass. At the interface between vacuum and sample surface the neutrons experience a nuclear potential given by

$$V_n(r) = \frac{2\pi\hbar^2}{m_n} N b_n, \tag{2.40}$$

where N is the atomic density and b_n is the coherent nuclear scattering length of neutron. It depends on the nuclear angular momentum and hence is different for different isotopes. The product Nb_n is referred to as the scattering length density (SLD).

In the absence of any magnetic field, the Schrödinger equation can be written as

$$\frac{\hbar^2}{2m}\frac{d^2\psi}{dr^2} + \left[E - V_n(r)\right]\psi = 0. \tag{2.41}$$

The above equation can also be written in the form of a Helmholtz propagation equation as

$$\frac{d^2\psi}{dr^2} + k_t^2\psi = 0, \tag{2.42}$$

with

$$k_t^2 = \frac{2m}{\hbar^2}\left[E - V_r(r)\right]. \tag{2.43}$$

We define the refractive index as follows:

$$n^2 = \frac{k_t^2}{k^2} \tag{2.44}$$

The refractive index *n* can be written as

$$n^2 = 1 - \frac{V_n(r)}{E} = 1 - \frac{\lambda^2}{\pi} Nb_n. \tag{2.45}$$

It is in most cases smaller than 1. The quantity $1-n$ is of the order of 10^{-5} and thus *n* can be written as

$$n \approx 1 - \frac{\lambda^2}{2\pi} Nb_n. \tag{2.46}$$

At the interface between two media, the Snell's law applies:

$$\cos\alpha = n\cos\alpha_t. \tag{2.47}$$

For angle $\alpha \le \alpha_c$, there is a total reflection of the incident wave like in the case of x-ray reflection. The critical angle α_c is given by the condition $\alpha_t = 0$. So the reflection index can be written as

$$\cos\alpha_c = n. \tag{2.48}$$

Since α_c is very small and a Taylor expansion is applied to the Equation (2.48). Then comparing the Equation (2.46) and (2.48) the expression of α_c is given by

มหาวิทยาลัยเทคโนโลยีสุรนารี

$$\alpha_c = \sqrt{\frac{Nb_n}{\pi}}\lambda. \tag{2.49}$$

The corresponding critical scattering vector for the total reflection can be expressed as

$$\left|\vec{Q}_c\right| = Q_c = \frac{4\pi \sin\alpha_c}{\lambda} = \sqrt{16\pi Nb_n}\ . \tag{2.50}$$

It shows that the critical scattering vector $\vec{Q}_c$ does not depend on the wavelength. Normally the value of $\vec{Q}_c$ for most of the material lies below 1°. Below the critical angle an evanescent wave propagates parallel to the sample surface and decreases exponentially from the surface to the bottom of the sample.

2.2.1.1 Reflection on a homogeneous medium

For incident neutron $\psi_I = A_I e^{i\vec{k}_i\cdot\vec{r}}$, reflected wave $\psi_R = A_R e^{i\vec{k}_f\cdot\vec{r}}$ and transmitted wave $\psi_T = A_T e^{i\vec{k}_t\cdot\vec{r}}$, with incident reflected and transmitted wave vectors $\vec{k}_i$, $\vec{k}_f$ and $\vec{k}_t$ and amplitude A_I, A_R and A_T, respectively (See Figure 2.8). The reflectance and transmittance can be derived by imposing the boundary conditions that the wave and its derivative are continuous at the interface $z = 0$. Therefore, the relationship between the amplitudes are related by

$$A_I + A_R = A_T \tag{2.51}$$

and

$$A_I\vec{k}_i + A_R\vec{k}_r = A_T\vec{k}_t. \tag{2.52}$$

The wave number in vacuum is denoted by $k = \left|\vec{k}_i\right| = \left|\vec{k}_f\right|$ and in the sample it is $nk = \left|\vec{k}_t\right|$. By taking the components of $\vec{k}$ parallel and perpendicular to the sample surface, obtaining

$$A_I k\cos\alpha + A_R k\cos\alpha = A_T (nk)\cos\alpha_t \tag{2.53}$$

$$-(A_I - A_R)k\sin\alpha = -A_T (nk)\sin\alpha_t \tag{2.54}$$

Substituting equation (2.51) into (2.54)

$$\frac{A_I - A_R}{A_I + A_R} = n\frac{\sin\alpha_t}{\sin\alpha} \approx \frac{\alpha_t}{\alpha}. \tag{2.55}$$

The reflectivity and transmittivity calculated by using the Snell's law and continuity equation are given by

$$r = \frac{A_R}{A_I} = \frac{\alpha - \alpha_t}{\alpha + \alpha_t} \tag{2.56}$$

$$t = \frac{A_T}{A_I} = \frac{2\alpha}{\alpha + \alpha_t}. \tag{2.57}$$

The transformation to Q-space is obtained by the relation $Q = 2k\sin\alpha \approx 2k\alpha$, $Q_c = 2k\sin\alpha_c \approx 2k\alpha_c$ and is given as

$$r(q) = \frac{q - q_t}{q + q_t} \tag{2.58}$$

$$t(q) = \frac{2q}{q + q_t}, \tag{2.59}$$

where,

$$q = \frac{Q}{Q_c} = \frac{2k}{Q_c}\alpha \;\; ; \;\; q_t = \frac{Q_t}{Q_c} = \frac{2k}{Q_c}\alpha_t$$

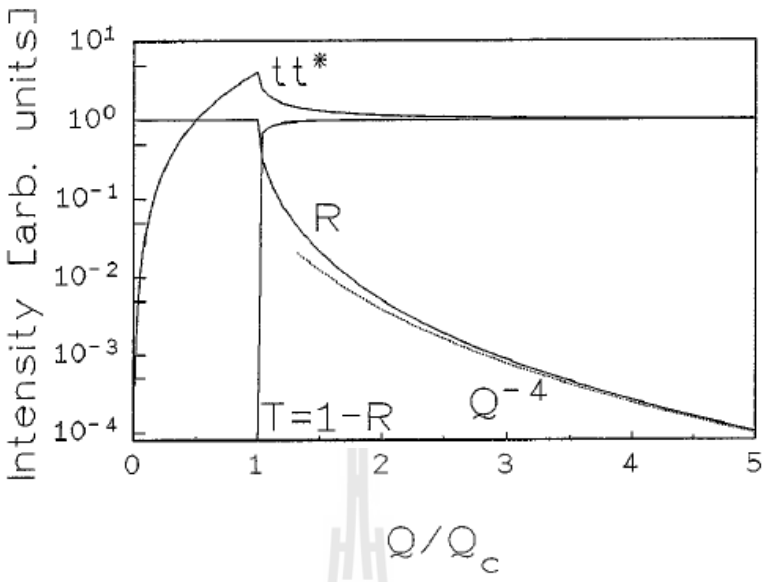

Figure 2.9 The reflectivity transmittivity and the transmission coefficient for scattering at single flat surface for normalized scattering vector (Zabel, 1994).

The Fresnel reflectivity (R_F) and transmittivity (T_F) or the reflected and transmitted intensities are given by

$$R_F = rr^* = r^2 \tag{2.60}$$

$$T_F = tt^* \frac{q_t}{q}. \tag{2.61}$$

where, as usual, $R_F + T_F = 1$. Two extreme cases will be considered. First, when $q >> 1,$ then $q^2 - q_t^2 = 1$ and $q + q_t \approx q$. Thus the reflectivity becomes

$$R_F \propto q^{-4} \approx Q^{-4} \tag{2.62}$$

$$T_F = 1. \tag{2.63}$$

This is known as the Fresnel reflectivity. The reflected wave is in phase with the incident wave. The intensity reflectivity falls off as $R_F \approx Q^{-4}$, there is almost

complete transmission. For the second limiting case, when $q << 1$, the reflected wave is out of phase with the incident wave. So the transmitted wave becomes very weak and propagates along the surface with a minimal penetration dept of $1/Q_c$. The plot of reflectivity and transmittivity against the normalized wave vector Q/Q_c is shown in Figure 2.9. It can be clearly seen that the transmittance increase with increasing Q until Q_c and then becomes unity. The reflectivity shows the Q^{-4} dependence at large Q values.

In case of reflection from a film supported on a substrate, the system will be consisted of two interfaces; between vacuum and the film and the other between film and substrate. The phase differences between the reflected intensities from the two interfaces are varied by changing the incident angle. So an interference pattern is created between the two reflected intensities, which give rise to oscillations in the reflectivity measurement known as Kiessing oscillations. The oscillation period is related to the film thickness (d) and is given by

$$\frac{2\pi}{d} = Q_{z2} - Q_{z1}, \tag{2.64}$$

where Q_{z1} and Q_{z2} are the position of two consecutive maxima or minima. By using the conversion $Q_z = 2k\sin\alpha = (4\pi/\lambda)\sin\alpha \approx (4\pi/\lambda)\alpha$, the film thickness can be written as

$$d = \frac{2\pi}{\Delta Q_z} = \frac{\pi}{k\Delta\alpha} = \frac{\lambda}{2\Delta\alpha}, \tag{2.65}$$

where $\Delta\alpha$ is the difference between the two maxima or minima in radian. To consider the film contain two different layers of thicknesses d_1 and d_2 and this double layer is repeated several times. The combined periodicity is given by $\Lambda = d_1 + d_2$.

Such the film is shown in Figure 2.10. The corresponding reflectivity displays some enhanced Kiessing fringes. They appear with a periodicity defined by $2\pi/\Lambda$. The thickness oscillations according to d_1 and d_2 will also be visible. The position of the Bragg peak appears at

$$Q_z^n = \sqrt{Q_c^2 + \left(\frac{2\pi n}{\Lambda}\right)^2} \tag{2.66}$$

where n is the order of the Bragg peak.

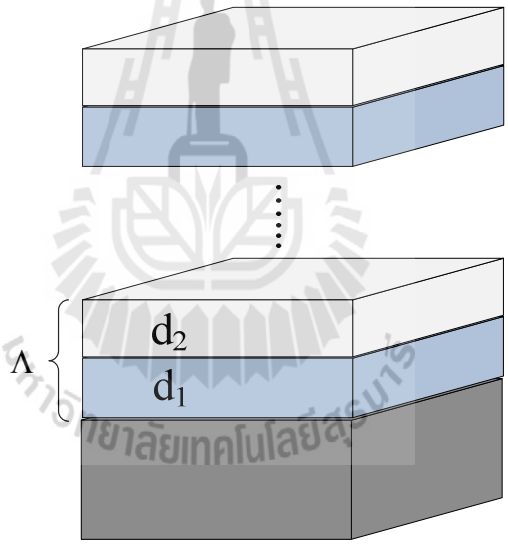

Figure 2.10 The film with a double layer of thickness d_1 and d_2 and total periodicity Λ (Adapted from Zabel *et al*., 2007).

2.2.1.2 Parratt formalism

In order to calculate the exact reflectivity for multiple layers, the boundary condition must be matched at each individual interface. Parratt

formulated a recursive scheme to add all the reflected and transmitted beam amplitudes to the total reflected beam (Parratt, 1954). The situation of Parratt's recursion scheme is shown in Figure 2.11.

The amplitudes of reflected and transmitted neutron in medium m of thickness d_m are r_m and t_m respectively. The phase factor at the middle of the layer between two interfaces $m-1$ and m is defined by

$$a_m = e^{iQ_m d_m/2} , \tag{2.67}$$

where Q_m is the scattering vector in the medium m. Continuity of the transverse component of the neutron at the interface between m, $m-1$ requires:

$$t_{m-1}a_{m-1} + r_{m-1}a_{m-1}^{-1} = t_m a_m^{-1} + r_m a_m \tag{2.68}$$

and continuity of the neutron gradient

$$(t_{m-1}a_{m-1} - r_{m-1}a_{m-1}^{-1})Q_{m-1}/2 = (t_m a_m^{-1} - r_m a_m)Q_m/2 . \tag{2.69}$$

Solution of these two equations leads to the following expression for reflectance:

$$\Re_{m-1} = a_{m-1}^4 \frac{R_{m-1,m} + \Re_m}{R_{m-1,m}\Re_m + 1} , \tag{2.70}$$

where the generalized Fresnel reflectivity for the interface between m and $m+1$ and the Fresnel coefficient between $m-1$ and m, respectively, are

$$\Re_m = a_m^2 \frac{r_m}{t_m} \tag{2.71}$$

$$\Re_{m-1,m} = \frac{Q_{m-1} - Q_m}{Q_{m-1} + Q_m} \tag{2.72}$$

In case of a single flat layer the equation reduce to the Fresnel reflectivity. For deriving the reflected intensity of multiply layers, the Parratt recursion scheme start

with the lowest layer M, which is assumed to be infinitely thick so that $\Re_M = 0$, and then working up to the top of the surface.

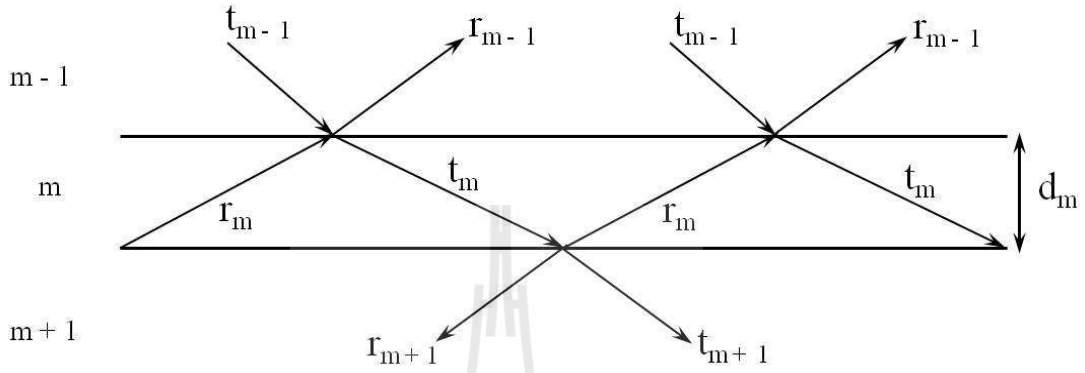

Figure 2.11 Parratt's recursion scheme showing reflection and transmission of waves for different mediums with different electron densities (Zabel, 1994).

2.2.2 Polarized Neutron Reflectivity (PNR) on magnetic system

When neutrons strike a surface from air or vacuum, they encounter a nuclear potential given by Equation (2.40). Neutrons carry a magnetic moment $\vec{\mu}_n$, whose operator

$$\hat{\mu} = \gamma_n \mu_N \hat{\sigma} \tag{2.73}$$

where $\hat{\sigma}$ represents the operator associated with the Pauli-spin matrices. γ_N is the neutron gyromagnetic ratio and μ_N is the nuclear magnetron. The neutron magnetic moment $\vec{\mu}_n$ interacts with the magnetic induction $\vec{B}$ providing a magnetic (Zeeman) potential for the neutron. The corresponding magnetic potential is given by

$$V_m = -\vec{\mu}_n \cdot \vec{B} \,. \tag{2.74}$$

In general, the magnetic induction inside the sample can be written as

$$\vec{B} = \mu_0(\vec{H} + \vec{M}), \tag{2.75}$$

where $\vec{H}$ is the external field. μ_0 is the permeability of free space and $\vec{M}$ is the magnetization inside the sample. The magnetic field is normally applied parallel to the sample plane and for thin films the magnetization $\vec{M}$ lies along the sample plane. The neutrons only see the step $\mu_0\vec{M}$ due to the magnetization.

For polarized neutrons, the magnetic moment is either parallel or anti-parallel to the applied field. This condition is usually satisfied according to the geometry of the PNR experiment as shown in Figure 2.12(a). The magnetic field is applied along the Y-axis. The neutron polarization is either parallel or anti-parallel to the applied field $\vec{H}$. The parallel component will be represented as *up neutron* and anti-parallel component will be termed as *down neutron*. The magnetization lies in the plane of sample. For the saturation, the magnetization should be parallel to the applied field $\vec{H}$. The total potential for two different neutron polarization is given by

$$V_T = V_n \pm V_m = \frac{2\pi\hbar^2}{m_n} N(b_n \pm b_m), \tag{2.76}$$

where Nb_m is the magnetic scattering length density (MSLD). The (+) sign stands for the spin up, that is for neutrons polarized along, and the (-) sign stands for the spin down states, that is for the neutrons polarized opposite to the (small) ambient field guiding the polarization directed along the Y-axis.

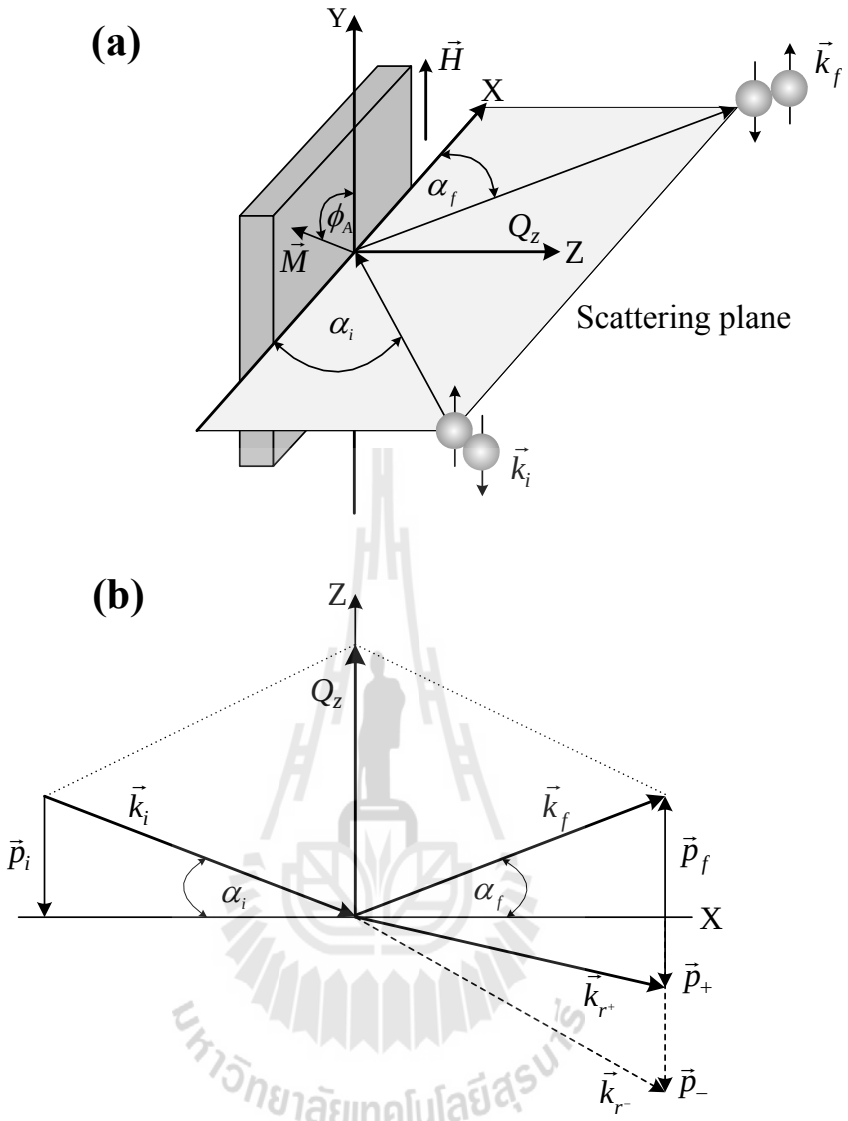

Figure 2.12 (a) PNR geometry with magnetic field $\vec{H}$ along Y-axis and magnetization $\vec{M}$ at an angle ϕ_A. The scattering plane is the XZ plane, with polarization either parallel or anti-parallel to the Y-axis. (b) Kinematics of polarized neutron reflection. For specular conditions $\alpha_i = \alpha_f = \alpha$, the scattering vectors $\vec{p}_i = \vec{p}_f = \vec{p}_0$. In presence of magnetic field the Zeeman splitting leads to different components of the refracted beam, $\vec{p}_+$ for up neutrons and $\vec{p}_-$ for down neutrons (Adapted from Zabel *et al*., 2007).

The 3-dimensional Schrödinger equation can be written as

$$\left\{-\frac{\hbar^2}{2m}\nabla^2+\hat{V}(z)-E\right\}\left|\psi(\vec{r})\right\rangle=0, \tag{2.77}$$

where $E=\hbar^2k^2/2m$ is the energy of neutron. It is conserved for elastic scattering. The potential $\hat{V}(z)$ depends only on the transverse coordinate z and thus the wave function can be factorized into two components. First, the lateral component, which remains unchanged after scattering due to elastic scattering and retains the plane wave characteristics is represented by $e^{i\kappa\rho}$, where κ is the lateral component of the wave vector $\vec{k}$ and ρ is the lateral component of the radius vector $\vec{r}$. The neutron wave function for *up* and *down neutron* is represented as

$$\left|\psi(z)\right\rangle=\begin{pmatrix}\psi_+(z)\\ \psi_-(z)\end{pmatrix}. \tag{2.78}$$

The column matrix represents the two-dimensional spin state of the neutron. The total wave function can be written as

$$\left|\psi(\vec{r})\right\rangle=e^{i\kappa\rho}\left|\psi(z)\right\rangle. \tag{2.79}$$

The corresponding potential matrix can be expressed as

$$\begin{pmatrix}V_{++} & V_{+-}\\ V_{-+} & V_{--}\end{pmatrix}=\frac{2\pi\hbar^2}{m_n}N\left[\begin{pmatrix}b_n & 0\\ 0 & b_n\end{pmatrix}+\begin{pmatrix}b_y & b_x\\ b_x & -b_y\end{pmatrix}\right]. \tag{2.80}$$

It is clearly seen that the first matrix of the formulation stands for nuclear potential, while the second one correspond to the magnetic potential. If the magnetization $\vec{M}$ makes an angle ϕ_A against the Y-axis (or the applied field $\vec{H}$). The

elements $V_{\pm\mp} \propto b_x$, where $b_x = b_m \sin\phi_A$ is proportional to the component of the magnetic induction perpendicular to the polarization axis. The other two elements $V_{\pm\pm} \propto (b_n \pm b_y)$ depend on $b_y = b_m \cos\phi_A$, that is on the inductance component parallel to the Y-axis. For magnetization parallel to the applied field, the matrix also becomes diagonal.

Using the equation (2.78) and (2.80) the Schrödinger equation in the matrix form equation (2.77) can be explicitly written as a system of two coupled equation

$$\frac{\partial^2 \psi_+(z)}{\partial z^2} + \left[p_0^2 - \frac{2m}{\hbar^2} V_{++}(z) \right] \psi_+(z) - \frac{2m}{\hbar^2} V_{+-}(z) \psi_-(z) = 0 \qquad (2.81)$$

$$\frac{\partial^2 \psi_-(z)}{\partial z^2} + \left[p_0^2 - \frac{2m}{\hbar^2} V_{--}(z) \right] \psi_-(z) - \frac{2m}{\hbar^2} V_{-+}(z) \psi_+(z) = 0, \qquad (2.82)$$

where $p_0 = Q_z / 2 = k \sin\alpha$ is the z-component of the neutron wave vector. The conservation of energy at elastic reflection leads to

$$\frac{\hbar^2 k^2}{2m_n} = \frac{\hbar^2 p_0^2}{2m_n} + \frac{\hbar^2 \kappa^2}{2m_n}, \qquad (2.83)$$

$$p_0^2 = k^2 - \kappa^2. \qquad (2.84)$$

The couple of linear differential equations lead to two consequences important from experimental point of view. If $V_{\pm}$ and $V_{\mp}$ are zero, then the neutrons maintain their spin state upon interaction with the sample. This is known as the *non spin flip* (NSF) scattering which happens when the magnetization vector $\vec{M}$ is oriented parallel to the Y-axis. Alternatively, if $V_{++} = V_{--} = 0$, then the spin state of the neutron is flipped with equal efficiency after scattering and this is knows as spin flip (SF) scattering. This occurs when $\vec{M}$ is aligned parallel to the X-axis. Thus, by distinguishing between NSF and SF scattering, a quantitative analysis of PNR data

yields the x and y component of $\vec{M}$, which combine to the magnitude and orientation of the magnetization vector $\vec{M}$ in the sample plane. Not that in the configuration shown in Figure 2.12(a) only the magnitude of M_x, but not its direction, can be determined. So it is difficult to distinguish the orientation of the $\vec{M}$ with respect to the polarization (Y) axis. The several important points should also be noted as down (Zabel *et al*., 2007)

- The effective potential V_{++} and V_{--} contain the nuclear and magnetic contributions.

- The effective potential V_{+-} and V_{-+} are solely of magnetic origin.

- PNR is not sensitive to any magnetization component parallel to the scattering vector (Z-component).

- The spin and orbital parts, which contribute to the total magnetization of the sample, cannot be distinguished.

According to the total potential for *up* and *down neutrons* are different, this leads to two critical angles for total reflection;

$$p_{c\pm} = k \sin \alpha_{c\pm} = \sqrt{4\pi N(b_n \pm b_m)}. \tag{2.85}$$

The magnetization inside the sample shows two different critical angles. The *up neutrons* have a higher critical angle compared to the *down neutrons*. The reflectivity corresponding to four different potential can be determined by matching the boundary conditions for the wave function and its derivative with respect to z at z = 0. The Fresnel reflection coefficients (reflectance amplitudes) are given by

$$R_{\pm} = R_{\pm}^{F} = \frac{p_0 - \sqrt{p_0^2 - p_{c\pm}^2}}{p_0 + \sqrt{p_0^2 - p_{c\pm}^2}}. \tag{2.86}$$

Where, $p_0 = k\sin\alpha_i$ is the z-component of the scattering vector and $p_{c\pm} = k\sin\alpha_{c\pm}$ is the scattering vector at critical angles.

With PNR, it is possible to measure independently the NSF and SF reflectivities. So the NSF reflectivities are given by

$$R^{++} = \frac{1}{4}\left|R_+(1+\cos\phi_A) + R_-(1-\cos\phi_A)\right|^2 \tag{2.87}$$

$$R^{--} = \frac{1}{4}\left|R_+(1-\cos\phi_A) + R_-(1+\cos\phi_A)\right|^2. \tag{2.88}$$

The SF reflectivities are

$$R^{+-} = R^{-+} = \frac{1}{4}\left|R_+ - R_-\right|^2 \sin^2\phi_A\ . \tag{2.89}$$

A simplified version of PNR is often used which no analysis of the final spin states of the reflected neutron beam. The measured quantities are obtained as

$$R^+ = R^{++} + R^{+-} = \frac{1}{2}\left\{\left|R_+\right|^2(1+P\cos\phi_A) + \left|R_-\right|^2(1-P\cos\phi_A)\right\} \tag{2.90}$$

$$R^- = R^{--} + R^{-+} = \frac{1}{2}\left\{\left|R_+\right|^2(1-P\cos\phi_A) + \left|R_-\right|^2(1+P\cos\phi_A)\right\}, \tag{2.91}$$

where P is the polarization of the neutron beam. For fully polarized beam $P = 1$.

Another quantity called spin asymmetry (*SA*) can be used to determine the magnitude of magnetization in the sample. It is defined as

$$SA = \frac{R^+ - R^-}{R^+ + R^-} = \frac{\left|R_+\right|^2 - \left|R_-\right|^2}{\left|R_+\right|^2 + \left|R_-\right|^2}\cos\phi_A\,. \tag{2.92}$$

2.2.3 Coherence volume and resolution

Both specular and Bragg reflections from X-ray source are coherent phenomena, which result from the constructive interference of coherently scattered x-ray from electrons. On the other hand, the neutron source is an incoherent source owing to the random emissions of the neutron. However, the experimental set up with monochromatization and collimation systems ensures that only neutrons with a close phase relations impinge on the sample. The emissions of neutrons from a small area known as "source coherence volume" also convince that the plane wave approximation is valid at the sample surface. The resolution also influences on the coherency of the neutron waves. The resolution is determined by the slit size defined for the incoming beam and the resolution of the detector. For most of the experiments with horizontal scattering plane, the height of the neutron beam which opening along the Y-axis is much larger than the width (opening along the Z-axis). The resolution in *q*-space along Y-axis and X-axis are given by, respectively,

$$\Delta q_y \approx \frac{2\pi}{\lambda\left(\Delta\theta_y\right)} \tag{2.93}$$

$$\Delta q_x \approx \frac{\pi}{\lambda\sqrt{\alpha_i\left(\Delta\alpha_i^2\right)+\alpha_f\left(\Delta\alpha_f^2\right)}}, \tag{2.94}$$

where $\Delta\theta_y$ and $\Delta\alpha_i$ are determined by the incoming beam divergence and $\Delta\alpha_f$ is defined by the detector resolution. As the divergence is much larger than the other two divergences, the q resolution $\Delta q_y >> \Delta q_x$. The corresponding coherence area on the sample is defined by the parameters $l_x = 1/\Delta q_x$ and $l_y = 1/\Delta q_y$, so that $l_y << l_x$. This asymmetric area forms a coherence ellipse on the sample (Zabel *et al*., 2007.)

The coherence area usually covers only a small fraction of the sample surface illuminated by the neutron beam. Therefore, an experimentally recorded a reflected intensity is actually an incoherence averaging of intensities coherently reflected from different small areas of the sample. If the sample is homogeneous over the illuminated area then the reflected intensity from different coherence areas are similar. But the situation could be different for a magnetic sample with domains or for a nanostructured surface. Figure 2.13(a) illustrates the image of magnetic domains of the sample, where the size of each domain (D_m) is much larger than the coherence lengths, $D_m >> l_x$. The reflectivity has to be calculated for different magnetic domains with different magnetization vectors and finally averaged over all domain orientations. Such averaging would not affect the intensity of unpolarized neutron reflection, while only PNR delivers the information on the magnetization distribution over the reflected surface. In this case, the sample is homogeneous over the coherence area and hence the reflected intensities from different coherence areas can be simply added up.

The averaging equation (2.92) gives information about the mean value $\langle \cos\phi_A \rangle$ from measurements of the spin asymmetry. This mean value is proportional to the mean value of magnetization projection on to the polarization analysis axis but it does not allow to discriminate between coherent rotation of the net magnetization for the angle γ and magnetization reduction due to random domains. For example, *SA* cannot distinguish between total demagnetized state and rotational of magnetization perpendicular to the polarization direction, because in both cases $\langle \cos\phi_A \rangle = 0$. More information can be obtained by measuring the NSF and SF reflectivities. Indeed, averaging of the equations (2.87 - 2.89) gives information about not only the mean

value $\langle \cos\phi_A \rangle$, but also to the mean square $\langle \sin^2\phi_A \rangle$. One can determine the parameter $\langle \cos^2\phi_A \rangle = 1 - \langle \sin^2\phi_A \rangle$. In case of a random distribution of domains the dispersion $\Delta = \langle \cos^2\phi_A \rangle - \langle \cos\phi_A \rangle^2$ is usually non zero and positive which represents a demagnetized state. If Δ is zero then the sample is in saturation state.

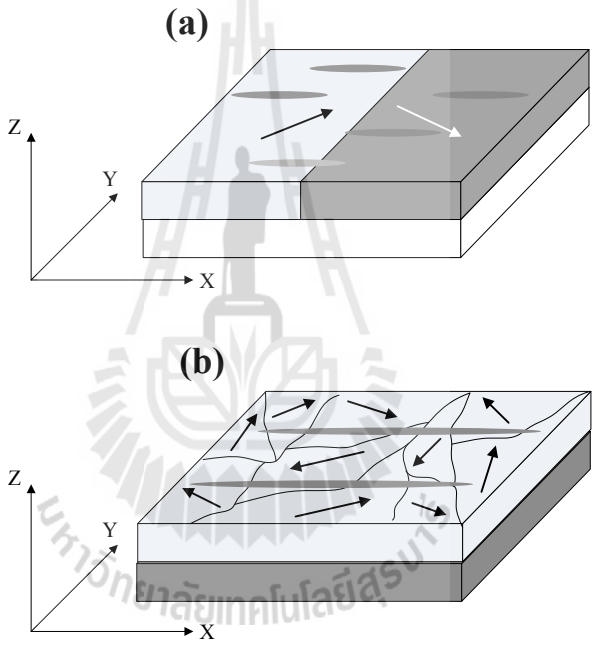

Figure 2.13 Magnetic domains with magnetization lying in-plane are shown with the arrows. (a) The coherence ellipse is smaller than the domain size. So the reflectivity over the total coherence ellipse is same. (b) Coherence ellipse spanning many domains. The reflectivity is averaged over the mean potential and may lead to off specular intensity (Adapted from Zabel *et al*., 2007).

In case of the system is in multidomain state as shown in Figure 2.13(b), then a vector polarization analysis is required. If the coherence length $l_x > D_m$, the neutron wave is not only reflected from and transmitted through the mean optical potential, but also scattered in off-specular directions $\alpha_i = \alpha_f$. The off-specular intensity will be a Bragg peak if the inhomogeneities are periodic as in nanostructures or will form diffuse scattering if the inhomogeneitie are random.

2.3 Magnetism

The macroscopic magnetic properties of materials are a consequence of magnetic moments associated with individual electrons. Electrons carry a magnetic moment. They have an intrinsic magnetic moment, which does not have any classical analogue. Electrons orbiting around a nucleus in an atom also have an orbital angular momentum. The classical analogue is similar to the flow of current *I* in a loop of area $\left|d\vec{S}\right|$. The magnetic moment is,

$$d\vec{\mu} = Id\vec{S}. \tag{2.95}$$

For a finite size loop, all the infinitesimally small magnetic moments are summed up to get the total magnetic moment,

$$\mu = \int d\vec{\mu} = I\int d\vec{S}. \tag{2.96}$$

In this case of an electron of charge *e* and mass m_e moving in an orbit of radius r with a speed of *v* around the nucleus, a moving electron may be considered to be a small current loop which generating a very small magnetic field and having a magnetic moment along its axis of rotation, as schematically illustrated in Figure 2.14(a). Therefore the magnetic moment in term of the angular momentum is given by

$$\mu_L = \pi r^2 I = -\frac{e}{2m_e} L \tag{2.97}$$

where, the current is replaced by

$$I = -\frac{e}{\tau} = -\frac{ev}{2\pi r} \tag{2.98}$$

and the angular momentum by

$$L = m_e v r . \tag{2.99}$$

The proportionality between the magnetic moment and angular momentum is a general result,

$$\mu_L = \gamma L \tag{2.100}$$

where the proportionality factor γ is known as the gyromagnetic ratio. For orbital motion of electron, γ is $-(e/2m_e)$; the minus sign means that μ_L and L are oppositely directed because of the negative charge.

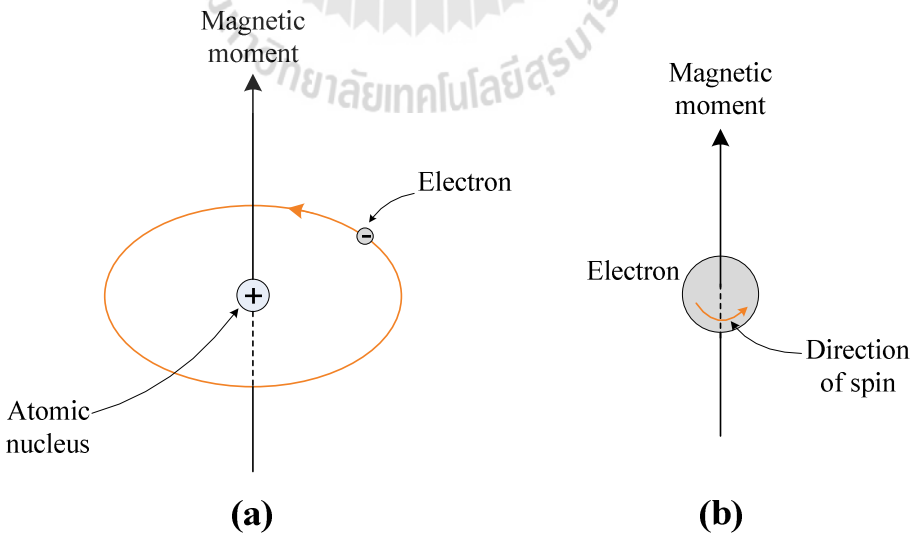

Figure 2.14 Demonstration of the magnetic moment associated with (a) an orbiting electron and (b) a spinning electron (Adapted from Coey, 2009).

In quantum mechanical terms, the angular momentum is conserved. So the magnetic moment can be written as

$$\mu_L = -g\frac{e\hbar}{2m_e}\sqrt{l(l+1)}. \tag{2.101}$$

For the *z*-direction, the magnetic moment becomes

$$\mu_{L_z} = -g\frac{e\hbar}{2m_e}m_l = -gm_l\mu_B, \tag{2.102}$$

where $\mu_B = e\hbar/2m_e$ is known as the Bohr magnetron. This represents the smallest unit of atomic magnetic moment and has a value 9.274×10^{-24} J/T. The factor g is known as the g-factor of the electron and is a dimensionless quantity. The approximate value of g is 2. Here $m_l = 0, \pm1, \pm2,...$ is the magnetic quantum number. Similarly the magnetic moment due to electron spin *s*, which is directed along the spin axis as shown in Figure 2.50(b), is given by

$$\mu_S = -g\mu_B\sqrt{s(s+1)} \tag{2.103}$$

$$\mu_{S_z} = -g\mu_B m_s, \tag{2.104}$$

where $s=\frac{1}{2}$ is the spin quantum number and $m_s=\pm\frac{1}{2}$ is the spin magnetic quantum number. The energy of the electron in a magnetic field B can be written as

$$E = g\mu_B m_s B. \tag{2.105}$$

This is known as Zeeman splitting in presence of a magnetic field.

2.3.1 Atom in a magnetic field

The total angular momentum of *Z* electrons orbiting around a nucleus is

$$\hbar\vec{L} = \sum_{i=1}^{Z} \vec{r}_i \times \vec{p}_i \,, \tag{2.106}$$

where $\vec{r}_i$ is the position vector and $\vec{p}_i$ is the momentum vector of the i^{th} electron.

The Hamiltonian operator of the atom is given by

$$\hat{H}_0 = \sum_{i=1}^{Z} \left(\frac{p_i^2}{2m_e} + V_i \right) \tag{2.107}$$

where $p_i^2 / 2m_e$ is the kinetic energy and V_i is the potential energy of the i^{th} electron. A magnetic field $\vec{B}$ is applied to the system.

$$\vec{B} = \vec{\nabla} \times \vec{A} \tag{2.108}$$

The magnetic potential can be expressed in a gauge form

$$\vec{A}_r = \frac{\vec{B} \times \vec{r}}{2} \tag{2.109}$$

The momentum term can be replaced by a canonical momentum $\left(p_i + e\vec{A} \right)^2$. Thus the Hamiltonian operator of atom in a magnetic field can be written as

$$\hat{H} = \sum_{i=1}^{Z} \left(\frac{\left[p_i^2 + e\vec{A}(\vec{r}_i) \right]^2}{2m_e} + V_i \right) + g\mu_B \vec{B} \cdot \vec{S} \tag{2.110}$$

$$\hat{H} = \sum_{i=1}^{Z} \left(\frac{p_i^2}{2m_e} + V_i \right) + \mu_B (\vec{L} + g\vec{S}) \cdot \vec{B} + \frac{e^2}{8m_e} \sum_{i=1}^{Z} (\vec{B} \times \vec{r}_i^{\,2}) \tag{2.111}$$

$$\hat{H} = \hat{H}_0 + \mu_B (\vec{L} + g\vec{S}) \cdot \vec{B} + \frac{e^2}{8m_e} \sum_{i=1}^{Z} (\vec{B} \times \vec{r}_i^{\,2}) \tag{2.112}$$

The second term is the dominant contribution and is known as paramagnetic term. The last term, $e^2/8m_e\sum_{i=1}^{Z}(\vec{B}\times\vec{r}_i^{\,2})$ is known as the diamagnetic term.

2.3.2 Magnetization

A magnetic solid consists of many atoms with magnetic moments. The magnetization is defined as the magnetic moment per unit volume.

$$\vec{M} = \frac{\vec{\mu}}{V} \tag{2.113}$$

In presence of an external field $\vec{H}$ the magnetic induction $\vec{B}$ induced inside a material with magnetization $\vec{M}$ are related.

$$\vec{B} = \mu_0(\vec{H} + \vec{M}) \tag{2.114}$$

In a vacuum,

$$\vec{B} = \mu_0\vec{H} \tag{2.115}$$

where μ_0 is the permeability of a vacuum. The magnitude of magnetization is proportional to the external field as follows:

$$\vec{M} = \chi_m\vec{H} \tag{2.116}$$

and χ_m is called the magnetic susceptibility. χ_m is a dimensionless quantity and the value of χ_m basically distinguishes three types of magnetic materials.

$$\chi_m \begin{cases} < 0, \text{ diamagnetic} \\ > 0, \text{ paramagnetic} \\ >> 1, \text{ ferromagnetic} \end{cases} \tag{2.117}$$

2.3.2.1 Diamagnetism

All materials show some degree of diamagnetism, which is weak and negative. For a diamagnetic substance, an applied magnetic field induces a magnetization, which opposes the applied field. Lenz's law is the analogous classical explanation of this property. But diamagnetism is entirely quantum mechanical effect.

Using the first order perturbation theory, the expression of the diamagnetic susceptibility is given by (Blundell, 2007)

$$\chi_{dia} = -\frac{Ne^2\mu_0}{6Vm_e}\sum_{i=1}^{Z}\left\langle r^2\right\rangle. \tag{2.118}$$

The diamagnetic susceptibility is largely temperature independent. It is important for determining the size of atoms and molecules in chemistry.

2.3.2.2 Paramagnetism

Paramagnetism corresponds to a positive susceptibility, which is the applied magnetic field induces a magnetization along the direction of the applied field. The magnetic moment aligns parallel to the applied magnetic field. This is observed in materials with unpaired electron. However, the susceptibility is very small and depends on the strength of the applied magnetic field. Without an applied magnetic field, these magnetic moments point in randomly direction because the magnetic moments on neighbouring atoms interact only very weakly with each other and can be assumed to be independent.

At finite temperature usually the spins are randomly oriented due to thermal fluctuation. There is no interaction between the atomic moments. The magnetization depends on the total angular momentum $\vec{J}$, which is given by

$$\vec{J} = \vec{L} + \vec{S}. \tag{2.119}$$

Brillouin Function: The susceptibility function can be derived by using the general approach to solve the Brillouin function for any arbitrary value of *J*, which can be integer or half integer. The magnetization in term of the Brillouin function B_J is expressed as

$$M = M_s B_J(y), \tag{2.120}$$

where the saturation magnetization is given by

$$M_s = n g_J \mu_B J, \tag{2.121}$$

where *n* is the number of ions with total angular momentum J and g_J is known as the Lande's g-factor.

$$g_J = \frac{3}{2} + \frac{S(S+1) - L(L-1)}{2J(J+1)}. \tag{2.122}$$

The Brillouin function is given by

$$B_J(y) = \frac{2J+1}{2J} \coth\left(\frac{2J+1}{2J} y\right) - \frac{1}{2J} \coth\frac{y}{2J}, \tag{2.123}$$

where $y = \dfrac{g_J \mu_B JB}{k_B T}$ and k_B is the Boltzmann factor. The Brillouin function has the appropriate limits. So, two limiting cases will be considered.

In case of $J = \infty$, it is equivalent to the Langevin function.

$$B_\infty(y) = L(y) = \coth y - \frac{1}{y} \tag{2.124}$$

where, $y = \mu B / k_B T$.

For $J = 1/2,$ it reduces to the tanh function.

$$B_{1/2}(y) = \tanh(y) \tag{2.125}$$

For low magnetic fields the susceptibility is given by

$$\chi = \frac{M}{H} \approx \frac{\mu_0 M}{B} = \frac{n\mu_0 \mu_{eff}^2}{3k_B T}\,, \tag{2.126}$$

where $\mu_{eff} = g_J \mu_B \sqrt{J\left(J+1\right)}$ and the above equation looks like a classical Curie law.

2.3.3 Magnetic order

A magnetic solid can show long rang magnetic order which depends on the interaction between the magnetic moment. The ordering can lead to a spontaneous magnetization known as ferromagnetism. The alternate magnetic moment can be in opposite direction and lead to antiferromagnetism.

2.3.3.1 Ferromagnetism

A ferromagnet has a spontaneous magnetization even in the absence of the applied field. All the magnetic moments are aligned parallel to each other. This effect arises due to exchange interaction, which will be described in more detail in the next section. For a ferromagnet in an applied magnetic field $\vec{B}$, the appropriate Hamiltonian to be solved is

$$\hat{H} = -\sum_{ij} \mathrm{J}_{ij} \vec{S}_i \cdot \vec{S}_j + g\mu_B \sum_j \vec{S}_j \cdot \vec{B}. \tag{2.127}$$

The first term on the right hand is known as the Heisenberg exchange energy. J_{ij} is the exchange constant and for ferromagnets is positive. The second term on the right is the Zeeman energy in presence of a field.

The origin of FM was developed by Weiss. The Weiss model of ferromagnet assumed that each magnetic moment experiences a mean field or molecular field given by

$$\vec{B}_{mf} = \lambda \vec{M}, \tag{2.128}$$

where λ is a constant known as Weiss coefficient and $\vec{M}$ is the magnetization. The internal molecular field is responsible for the parallel alignment of the magnetic moments. In order to find a solution, the following Brilloin functions have to be solved.

$$M = M_s B_J(y). \tag{2.129}$$

$$y = \frac{g_J \mu_B J(B+\lambda) M}{k_B T}. \tag{2.130}$$

Without the λM term due to the molecular field, these equations reduce to the ones for paramagnetism. The second equation represents the temperature dependence of the magnetization. For zero field and below a critical temperature T_C, the solution show the spontaneous magnetization. The susceptibility is given by

$$\chi \propto \frac{1}{T - T_C}. \tag{2.131}$$

The above equation is known as the Curie-Wiess laws.

2.3.3.2 Antiferromagnetism

For an antiferromagnet, the magnetic moments are aligned antiparallel to the next nearest neighbour. The exchange interaction is negative in this case, J < 0. In many case of antiferromagnetism it can be considered as a two interpenetrating sublattice system, where the magnetic moments in one sublattice points up and in the other points down. The Weiss model of an antiferromagnetism is

also used to find out the solution for Curie temperature. This model assumes that the molecular field experienced by one sublattice is proportional to the magnetization of the other sublattice. So the molecular fields on two sublattices are given by

$$B_{+} = -|\lambda| M_{-} \tag{2.132}$$

$$B_{-} = -|\lambda| M_{+} \tag{2.133}$$

where λ is the molecular field constant which is now negative. The magnetization can be written as

$$M_{\pm} = M_s B_J \left(-\frac{g_J \mu_B J |\lambda| M_{\mp}}{k_B T} \right). \tag{2.134}$$

The sublattices magnetizations are equal and have opposite direction. Thus

$$|M_{+}| = |M_{-}| \equiv M \tag{2.135}$$

The Brillouin function is similar to the one for FM. The molecular field disappears above a critical temperature known as the Néel temperature T_N. The magnetic susceptibility can be written as

$$\chi \propto \frac{1}{T + T_N}. \tag{2.136}$$

When a magnetic field is applied to an antiferromagnet at temperature below T_N it is important to know the direction of the applied field with respect to the sublattice magnetization direction. If the field is applied parallel to the magnetization direction of one of the sublattices, a small term is added or subtracted to the local field of each sublattices. Since both sublattices are already saturated, the net magnetization in an antiferromagnet is zero so that the susceptibility is zero ($\chi_{\parallel}$). If instead the small magnetic field is applied perpendicular to the magnetization direction of one of

sublattices, the magnetization of both sublattices to tilt slightly so that a component of magnetization is produced along the applied magnetic field. Thus the susceptibility is non zero ($\chi_{\perp}$). The variation of these two susceptibility with temperature is shown in Figure 2.15.

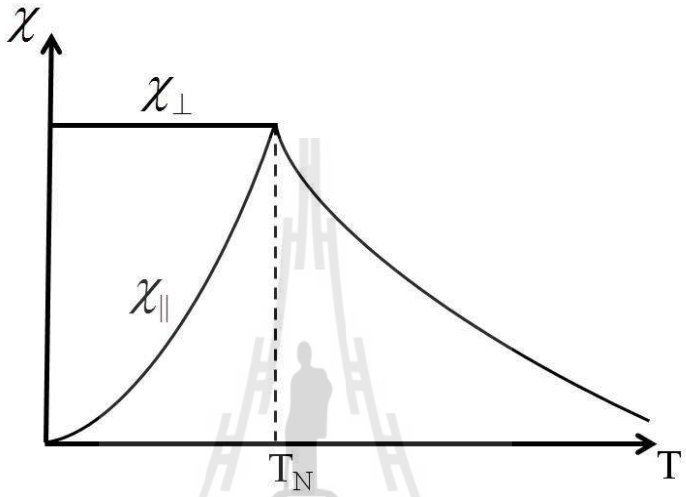

Figure 2.15 The temperature dependence of susceptibility for an AF (Adapted from Blundell, 2007).

When the field is applied parallel to the magnetization direction for very strong fields a spin-flop transition is observed, where the sublattice with opposite moments becomes parallel to the applied fields. The Zeeman energy dominates and can overcome the exchange interaction. Such spin-flop transitions are observed for very high values of applied fields, which are usually the experimentally accessible field ranges.

2.3.3.2 Ferrimagnetism

In case of the magnetization of the two sublattices, which described in the anfiferromagnet, may not be equal and opposite. Therefore they do

not cancel out and have a net magnetization. This phenomenon is known as Ferrimagnetism. It depends on the crystal structure of the material.

$$|M_+| \neq |M_-| \tag{2.137}$$

2.4 Magnetic interaction

The interaction between the magnetic moments could lead to different long range ordering like FM, AF etc. These interaction energy will be considered and discussed briefly in this section.

2.4.1 Magnetic dipole interaction

Magnetic moment can be considered as magnetic dipoles and can have dipole-dipole interaction among them. The dipolar interaction energy between two magnetic dipoles $\vec{\mu}_1$ and $\vec{\mu}_2$ separated by $\vec{r}$ is given by

$$E_d = \frac{\mu_0}{4\pi r^3}\left[\vec{\mu}_1 \cdot \vec{\mu}_2 - 3(\vec{\mu}_1 \cdot \hat{r})(\vec{\mu}_2 \cdot \hat{r})\right]. \tag{2.138}$$

The dipolar interaction energy depends on the separation and the degree of orientation in case of magnetic moments align parallel to each other the interaction energy is repulsive, whereas for antiparallel alignment it is attractive. For atomic moments, the ordering temperature is usually of the order of 1 K, which is very small to influence any long range order.

2.4.2 Exchange interaction

The internal molecular field responsible for long range magnetic ordering as calculated from the Weiss law is of the order of 10^7 gauss. This enormous field cannot be explained by the dipolar interactions. The origin of exchange can be explained by taking into account the electrostatic interaction between electrons.

2.4.2.1 Origin of exchange

For a two electron system, the combined wave function of the state can be written as $\psi_a(\vec{r}_1)\psi_b(\vec{r}_2)$, where $\psi_a(\vec{r}_1)$ and $\psi_b(\vec{r}_2)$ are the wave functions of individual electrons at position vectors $\vec{r}_1$ and $\vec{r}_2$ respectively. However this product state does not follow the exchange symmetry. The wave function has to be consistent under the particle exchange and hence has to a linear combination of $\psi_a(\vec{r}_1)\psi_b(\vec{r}_2)$ and $\psi_a(\vec{r}_2)\psi_b(\vec{r}_1)$.

For electrons the overall wave function is antisymmetric (fermion). The wave function can be separated into a spatial part and the spin part. If the spin part is antisymmetric single state χ_S, then the spatial state would be symmetric. Whereas when the spin part is symmetric triplet state χ_T, then the spatial state would be antisymmetric. Therefore the two electron wave functions in a single and a triplet can be written as, respectively, (Blundell, 2007)

$$\psi_S = \frac{1}{\sqrt{2}}[\psi_a(\vec{r}_1)\psi_b(\vec{r}_2) + \psi_a(\vec{r}_2)\psi_b(\vec{r}_1)]\chi_S \tag{2.139}$$

$$\psi_T = \frac{1}{\sqrt{2}}[\psi_a(\vec{r}_1)\psi_b(\vec{r}_2) - \psi_a(\vec{r}_2)\psi_b(\vec{r}_1)]\chi_T \tag{2.140}$$

The energies of the two possible states are

$$E_S = \int \psi_S^* \hat{H} \psi_S^* \, d\vec{r}_1 d\vec{r}_2 \tag{2.141}$$

$$E_T = \int \psi_T^* \hat{H} \psi_T^* \, d\vec{r}_1 d\vec{r}_2 \tag{2.142}$$

with the assumption that the spin parts of the wave function χ_S and χ_T are normalized. The difference between the two energies is

$$E_S - E_T = 2\int \psi_a^*(\vec{r}_1)\psi_b^*(\vec{r}_2)\hat{H}\,\psi_a^*(\vec{r}_2)\psi_b^*(\vec{r}_1)d\vec{r}_1 d\vec{r}_2 . \tag{2.143}$$

The exchange constant (or exchange integral) is defined as

$$\mathrm{J} = \frac{E_S - E_T}{2} = \int \psi_a^*(\vec{r}_1)\psi_b^*(\vec{r}_2)\hat{H}\,\psi_a^*(\vec{r}_2)\psi_b^*(\vec{r}_1)d\vec{r}_1 d\vec{r}_2 . \tag{2.144}$$

The Hamiltonian operator can be written down as

$$\hat{H} = \frac{1}{4}(E_S + 3E_T) - (E_S - E_T)\vec{S}_1 \cdot \vec{S}_2 . \tag{2.145}$$

The spin part of the Hamiltonian is

$$\hat{H}^{spin} = -2\mathrm{J}\vec{S}_1 \cdot \vec{S}_2 . \tag{2.146}$$

If $\mathrm{J} > 0$, $E_S > E_T$ and the triplet state is favored. If $\mathrm{J} < 0$, $E_S < E_T$ and the singlet state is favored. For many electrons the Hamiltonian can be written as

$$\hat{H} = -\sum_{ij} \mathrm{J}_{ij}\vec{S}_1 \cdot \vec{S}_2 , \tag{2.147}$$

where J_{ij} is the exchange constant between the i^{th} and j^{th} spins. The factor of 2 is omitted because double counting is automatically included in the summation. It is often possible to take J_{ij} to be equal to constant J for nearest neighbors and to be zero otherwise. The exchange integral has some general features. If the two electrons are on the same atom, the exchange integral is positive and the triplet state is favored with antisymmetric spatial state. This minimizes the coulomb energy by keeping them apart, which is consistent with the Hund's rule.

When the two electrons belong to different atoms, then it is favorable that the two electron states are shared by the two atoms, which lead to the formation of bonds. Instead of considering the atomic orbitals, the molecular orbitals are considered. The molecular orbitals can be bonding (spatially symmetric) or antibonding (spatially antisymmetric) with the antibonding state having higher energy compared to bonding state. This leads to a singlet spin state and the exchange integral is negative.

2.4.2.2 Direct exchange

The interaction is known as direct exchange, when two magnetic orbitals overlap directly. However this situation is quite rare because the magnetic orbitals are usually localized in case of rare-earth materials (4f electrons). For transition metals, such as Fe, Co and Ni, the d electrons are also localized and the band structure should also be taken into account to explain the exchange interaction.

2.4.2.3 Indirect exchange: superexchange

Most magnetic materials display an indirect exchange interaction. Normally in ionic solids such as MnO and MnF_2 the direct overlap is impossible. The magnetic ions interact via a non magnetic ion like oxygen. The exchange interaction is given by

$$J \sim -\frac{t^2}{U}, \tag{2.148}$$

where t is known as the hopping integral and *U* is the coulomb energy. The energy will be minimized if the unpaired electrons are shared by the metal-oxygen-metal bond. If the metal is magnetic (single electron), then AF coupling has a lower kinetic energy compared to FM orientation. Importantly, the hopping does not involve spin-flip. Therefore the super exchange would lead to an AF system. The bond angle also plays a role in the interaction energy.

2.4.2.4 Indirect exchange: RKKY

In metals the exchange interaction between magnetic ions can be mediated by the conduction electrons. The localized magnetic ion polarizes the conduction electron, which is then coupled to another localized magnetic ion and influences its magnetic state. The exchange interaction is thus indirect because it does

not involve direct coupling between magnetic moments. This kind of indirect exchange is called Ruderman, Kittel, Kasuya and Yosida (RKKY) interaction. The coupling depends on distance and is given by

$$J_{RKKY}(r) \propto \frac{\cos(2k_F r)}{r^3}, \tag{2.149}$$

where r is the distance and k_F is the radius of the Fermi surface. The interaction is long range and has oscillatory dependence on the distance between magnetic moments. Hence depending on the separation it can be either FM or AF. The wavelength of oscillation is π / k_F.

2.4.2.5 Double exchange

If the magnetic ions are in mixed valence state then it is possible to have a FM exchange interaction among the ions. This is known as Double exchange. It could be understood by considering the interaction between Fe^{3+} and Fe^{2+} ions on the octahedral sites of Fe_3O_4 (magnetite). Due to crystal field splitting, in octahedral environment the d-orbital splits into t_{2g} and e_g level with the latter having higher energy than the former. The t_{2g} level composes of the d_{xy}, d_{xz} and d_{yz} orbitals and e_g level composes of the d_{z^2} and $d_{x^2-y^2}$ orbitals. The situation for Fe^{3+} and Fe^{2+} are shown in Figure 2.16. The hopping of the electron between Fe^{3+} and Fe^{2+} is possible if they have FM interactions. FM interaction lowers the energy of the system.

2.4.3 Spin-orbit coupling

In general, the orbital and spin angular momenta are coupled weakly which leads to perturbation in the Hamiltonian and is known as spin-orbit interaction. This leads to fine structure splitting of the electronic energy level.

The Hamiltonian is given by

$$\hat{H}_{SO} = \lambda \vec{L} \cdot \vec{S}, \tag{2.150}$$

where λ is a constant. The spin-interaction also lead to exchange interaction between excited state of one ion and ground state of the other ion. This is known as Dzyaloshinsky-Moriya or anisotropic exchange interaction.

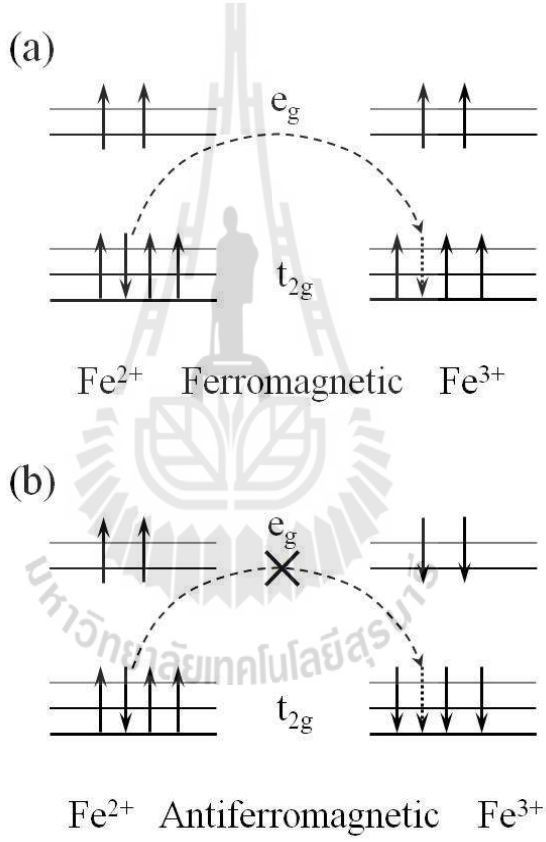

Figure 2.16 Double exchange interaction between octahedrally coordinated Fe^{2+} and Fe^{3+} in Fe_3O_4 (a) Electron hopping is allowed from Fe^{2+} to Fe^{3+} in ferromagnetic alignment. (b) Forbidden electron hopping in case of antiferromagnetic alignment (Adapted from Blundell, 2007).

2.5 Magnetic anisotropy

The term magnetic anisotropy is used to describe the dependence of the internal energy on the direction of the spontaneous magnetization in a magnetic material. It separates two different directions in the material known as easy axis and hard axis. The total magnetization of a system will prefer to lie along the easy axis. During a reversal process, smaller field is required to align the sample along the easy axis compared to the hard axis. The microscopic origin of magnetic anisotropy arises from the spin-orbit coupling and long range dipolar interaction between the magnetic moments (Blundell, 2007). The spin-orbit coupling is responsible for the intrinsic (magnetocrystalline) anisotropy, surface anisotropy and magnetostriction, while the shape anisotropy is a dipolar contribution. In bulk materials, magnetocrystalline and magnetostatic anisotropy are the main source of anisotropy whereas in thin films and nanostructures, other kinds of anisotropy such as shape and surface anisotropy are relevant in addition to these usual anisotropies (Bedanta and Kleemann, 2009).

2.5.1 Magnetocrystalline anisotropy

Magnetic anisotropy is meant as the dependence of the internal energy on the direction of spontaneous magnetization. An energy term of this kind is called as magnetic anisotropy energy. In general the magnetic anisotropy energy term possesses the crystal symmetry of the material, and known as crystal magnetic anisotropy or magnetocrystalline anisotropy (Chikazumi, 1999). Some crystallographic directions are preferred over others for the orientation of magnetization due to spin-orbit interaction or quenching of the orbital angular momentum.

The simplest forms of crystal anisotropies are the uniaxial anisotropy. For example, hexagonal cobalt shows uniaxial anisotropy, which makes the stable direction of internal magnetization (or easy direction) parallel to the *c* axis of the crystal at room temperature. The energy associated with uniaxial symmetry is given by

$$E_a^{uni} = K_1 V \sin^2\theta + K_2 V \sin^4\theta + ... \quad (2.151)$$

where K_1 and K_2 are the anisotropy constants, V is the particle volume and θ is the angle between the magnetization direction and the symmetry axis. The anisotropy constants are dependent on temperature, but at temperature much lower than the Curie temperature of the material they can be considered as constant. Normally in case of ferromagnetic materials K_2 and other higher coefficients are negligible in comparison with K_1 and many experiments may be analyzed by using the first term only. For single domain particles with uniaxial anisotropy, the magnetocrystalline anisotropy energy can be written as

$$E_a^{uni} = KV \sin^2\theta, \quad (2.152)$$

where K is usually considered as the uniaxial anisotropy constant. This expression corresponds to two local energy minima for $\theta = 0$ and π separated by an energy barrier KV. This has significant consequences for studying the temperature dependence of single domain particles.

For a cubic system the cubic anisotropy leads to a complicated expression for the energy (Blundell, 2007).

$$E_a^{cubic} = K_1\left(\frac{1}{4}\sin^2\theta\sin^2 2\phi + \cos^2\theta\right)\sin^2\theta + \frac{K_2}{16}\sin^2 2\phi \sin^2 2\theta \sin^2\theta + ... \quad (2.153)$$

where θ is the angle between the magnetization and the Z-axis and ϕ is the azimuthal angle.

2.5.2 Shape anisotropy

The shape of material also creates an additional anisotropy due to the demagnetizing energy. A uniformly magnetized single domain spherical particle has no shape anisotropy, because the demagnetizing factors are isotropic in all direction. However in case of an ellipse, the demagnetizing energy is smaller if the magnetization lies along the major axis. In this case the induced poles are further apart compared to the minor axis case. The shape anisotropy energy of a uniform magnetized ellipsoid is given by

$$E_a^{shape} = \frac{1}{2}\mu_0 V(N_x M_x^2 + N_y M_y^2 + N_z M_z^2), \tag{2.154}$$

where M_x, M_y and M_z are the components of magnetization and N_x, N_y and N_z are the demagnetization factors relative to the *X*, *Y*, and *Z* axes, respectively and they satisfy the condition $N_x + N_y + N_z = 1$.

Taking the magnetocrystalline anisotropy into account for a uniaxial anisotropy the total energy can be written as

$$E_a^{uni} = KV\sin^2\theta, \tag{2.155}$$

where *K* is the anisotropy constant, in case of shape anisotropy, is modified as

$$K = \frac{1}{2}\mu_0 M_s^2 (N_x - N_z). \tag{2.156}$$

If $K > 0$ an easy axis type anisotropy is obtained, whereas for $K < 0$ an easy plane type anisotropy is obtained. The shape anisotropy of thin films is given by (Bedanta and Kleemann, 2009)

$$E_{shape}^{thin\ film} = \frac{1}{2}\mu_0 M_s^2 \cos^2\theta, \tag{2.157}$$

where θ is the angle between the film normal and the magnetization. Thus for thin films, the easy axis is along the film plane.

2.5.3 Surface anisotropy

The surface anisotropy is caused by the breaking of the symmetry and a reduction of the nearest neighbour coordination. Surface effects in small magnetic nanoparticles are a major source of anisotropy (Garanin and Kachkachi, 2003). When particle sizes are decreased, the magnetic contributions from the surface will eventually become more important than those from the bulk of the particle and the surface anisotropy will dominate over the magnetocrystalline anisotropy and magnetostatic energies. Therefore, the change in symmetry of atoms at the surface of a thin film has a impact on the magnetic anisotropy and the easy direction of magnetization.

To lowest order, the anisotropy energy of a ferromagnetic can be written as

$$E_{an} = K\sin^2\theta, \tag{2.158}$$

where θ is the angle between the magnetization and surface normal and K is the effective anisotropy constant. Typically, the effective anisotropy can be described as the sum of three terms

$$K = \frac{2K_s}{t} + K_v - \mu_0 M^2, \tag{2.159}$$

where t is the thickness of the film, K_s is the surface contribution, and K_v is the volume anisotropy consisting of magnetocrystalline and shape anisotropy. The expression of the effective magnetic anisotropy of small spherical particles with diameter d can be written as

$$K_{eff} = K_v + \frac{S}{V}K_s = K_v + \frac{6}{d}K_s, \tag{2.160}$$

where $S = \pi d^2$ and $V = \frac{1}{6}\pi d^3$ are the surface and volume of the particle respectively (Bodker *et al*., 1994).

2.5.4 Strain anisotropy

Strain anisotropy is essentially a magnetostrictive effect. Due to magnetostriction, strains are effective in the magnetization direction. This kind of anisotropy is usually described by a magnetostatic energy term

$$E_a^{strain} = -\frac{3}{2}M_s \sigma S \cos^2 \theta', \tag{2.161}$$

where σ is the strain value by surface unit, S is the particle surface, and θ' the angle between magnetization and the strain tensor axis.

2.6 Magnetic Domains

A ferromagnet of macroscopic size contains many regions called “magnetic domains” in the demagnetized state. Within each domain, all the atomic moments are aligned in one of the easy direction leading to spontaneous magnetization. However, the direction of spontaneous magnetization varies from domain to domain so as to minimize the total magnetic energy of the system. The magnetostatic energy or the volume energy is given by

$$E_{MS} = \frac{1}{2}\mu_0 N M_s^2 V, \tag{2.162}$$

where N is the demagnetizing factor, M_s is the saturation magnetization and V is the volume. The magnetostatic energy increases with increase in the volume. To

minimize this energy the material breaks into domains, so that the demagnetization energy is minimized. On a purely statistical basis, all available easy directions will be used equally in the material. For example, if there are *n* domains of approximately equal volume in a demagnetized iron specimen, the number of domains spontaneously magnetized in each of the six <100> easy directions will be *n*/6. Therefore the whole specimen will not show a net magnetization in the absence of an applied field. Several factors affecting domain distribution and magnetic behavior may be listed as follows:

- magnetocrystalline anisotropy, which determines the natural easy axis of the crystallites;
- induced anisotropy, produced by strain which creates an easy axis over-riding the magnetocrystalline contribution;
- shape anisotropy, in which the easy axis is determined by minimization of magnetostatic energy (this applied to small particles);
- size and orientation of the crystallite composing the specimens.

The orientation of magnetization in each domain and the domain size are determined by magnetostatic, crystal anisotropy, magnetoelastic and domain wall energy. All domain structure calculations involve minimization of the appropriately selected energies.

Domains are associated with domain walls. Domain walls are interfaces between regions in which the spontaneous magnetization has different directions. At the wall the magnetization must change direction. A simple picture of a domain which makes an abrupt change between two domains is shown in Figure 2.17. For this ferromagnetic specimen the easy axis is $\pm y$ and a row of atoms is shown parallel to *x*-axis, with the $180°$ domain wall lying in the *y*-*z* plane. In this case the domain wall

will have a large exchange energy associated with it because the spins adjacent to the wall are antiparallel and the exchange energy in a ferromagnet is a minimum only when adjacent spins are parallel. To calculate the exchange energy, the minimized structure of a domain is considered.

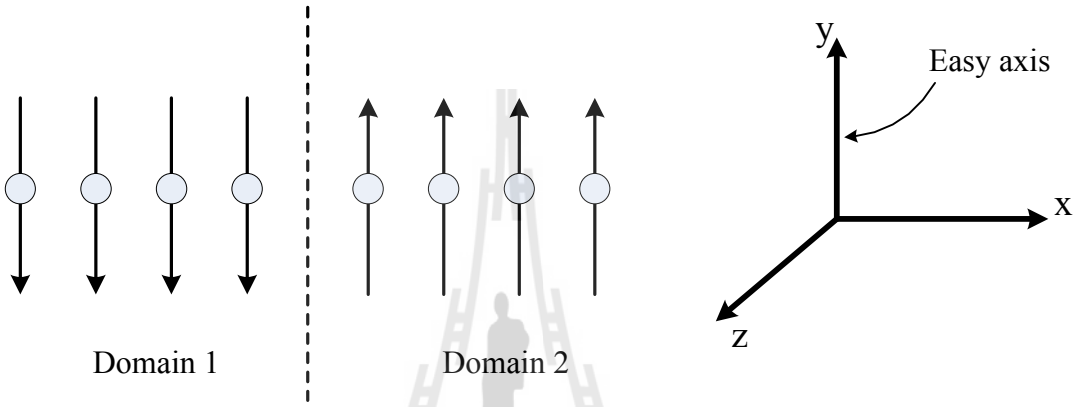

Figure 2.17 Hypothetical infinitely thin 180° wall (Adapted from Bedanta, 2004).

The exchange energy for a pair of atoms with the same spin *S* is given by

$$E_{ex} = -2JS^2 \cos\phi, \tag{2.163}$$

where *J* is an exchange integral and ϕ is the angle between adjacent spins as shown in Figure 2.18(c). The series expansion of $\cos\phi$ is

$$\cos\phi = 1 - \frac{\phi^2}{2} + \frac{\phi^2}{24} - ..... \tag{2.164}$$

Due to ϕ is very small, the term in ϕ^4 and higher power can be ignored. So the exchange energy can be written as

$$E_{ex} = JS^2\phi^2 - 2JS^2. \tag{2.165}$$

The second term in Equation (2.165) is independent of angle and has the same value within a domain as within the wall, and it can therefore be dropped. The extra exchange energy per spin pair existing within the wall is given by the first term, $JS^2\phi^2$.

In order to decrease the exchange energy, a 180° change in spin direction occur gradually over *N* atoms is necessary so that the ϕ angle between adjacent spins will be π / N. Then the total exchange energy is reduced because, from equation (2.165), it varies as ϕ^2 rather than as ϕ. Figure 2.18 shows the two simplest cases of a 180° domain wall, (a) a Bloch wall and (b) a Néel wall, in both of which the magnetization rotates from one domain to other in different ways.

In case of the wall plane contains the anisotropy axis, the domain magnetizations are parallel to the wall and there will be no global magnetic charge, meaning that the component of magnetization perpendicular to the wall is the same on both sides of the wall. However if the magnetization rotates parallel to the wall (*y*-*z* plane in Figure 2.18(a)), there will be no charges inside the wall too. Then the stray field energy will suppose its minimum zero value. This wall mode, first proposed and calculated by Landau and Lifshitz (Landau and Lifshitz, 1935) and the first theoretical examination of the structure of a domain wall was made by Felix Bloch (Bloch, 1932) in 1932, and domain walls are accordingly called as *Bloch walls*.

In ultrathin films where the film thickness becomes comparable to the wall width, Block walls cannot occur. Because with decrease of sample thickness, the magnetostatic energy of the wall that extends through the thickness of sample increase as a result of the free poles at the top and bottom of the wall. The spins inside the wall may perform their 180° rotation in such a way as to minimize their magnetostatic

energy. If the spins will rotate in the plane of the surface, a smaller magnetostatic energy at the internal face of the wall is accepted as the price for removing the large magnetostatic energy at the top surface. Such a wall is called *Néel wall* in which the magnetization rotates in a plane perpendicular to the plane of the wall (see Figure 2.18(b)).

The spins within the wall of Figure 2.18 are not pointing in easy directions so that the crystal anisotropy energy within the wall is higher than it is in the adjoining domains. While the exchange energy tries to make the wall as wide as possible in order to make the ϕ angle between adjacent spins as small as possible. Meanwhile the anisotropy tries to make the wall thin so that to reduce the number of spins which are not pointing in the easy direction. As a result of this competition, the wall has a certain finite width and a certain structure.

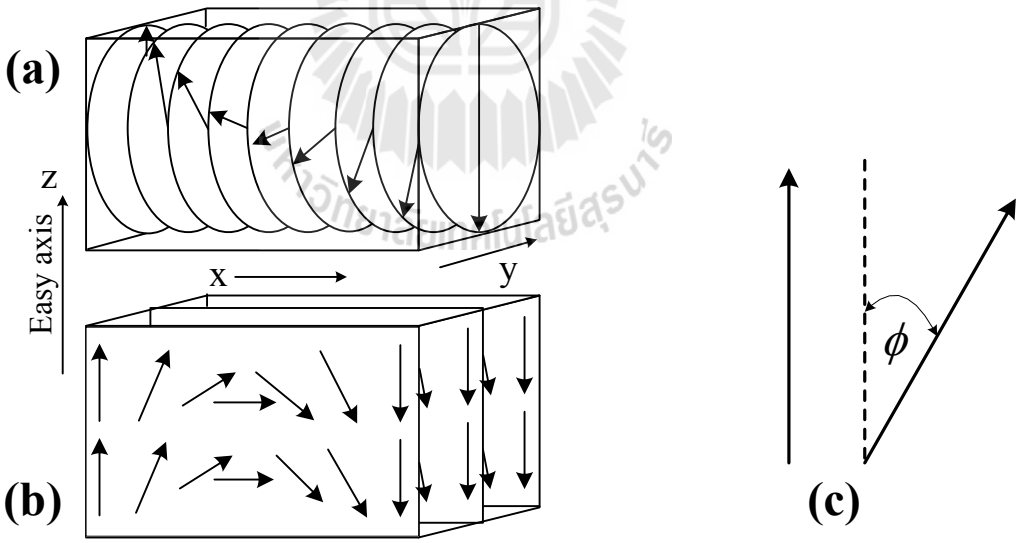

Figure 2.18 Rotation of the magnetization vector between two adjunct domains through a thin 180° wall in a infinite uniaxial material. Two different rotation modes are shown, (a) a Bloch wall and (b) a Néel wall. (c) Schematic of the angle (ϕ) between two adjacent spins (Adapted from Hubert and Schäfer, 2000).

The classical definition of domain wall width introduced by Lilley is given by

$$W_L = \pi\sqrt{AK_u}\,, \tag{2.166}$$

where $A \propto \mathrm{J}$ is called the exchange stiffness and K_u is the uniaxial anisotropy.

When the volume of the magnetic material is reduced, the magnetostatic energy is also reduced. For a critical radius it is possible that the magnetostatic energy is smaller than the domain wall energy. Below that radius the system would prefer to stay in a single domain state. The critical radius r_c, for which the single domain state is stable compared to multidomain state, is given by (ÓHandley, 2000)

$$r_c \approx 9\frac{\sqrt{AK_u}}{\mu_0 M_s^2}. \tag{2.167}$$

Typical values for r_c are about 15 nm for Fe and 35 for Co particles. The magnetization reversal of single domain particles can occur by various mechanisms such as Curling, Buckling, Coherent rotation of the moments and so on. The coherent rotation of the moments in unison is a simple model and is quite handy in describing many experimental observations (ÓHandley, 2000). The Stoner-Wohlfarth model can be used to explain the coherent rotation of the magnetization. This model assumed no-interacting particles with uniaxial anisotropy in which the spins are parallel and rotate at unison. In this case one can define a net magnetic moment $\vec{m}_{NP}$ to the nanoparticle, with $\left|\vec{m}_{NP}\right| \approx M_s V$. The large magnetic moment is similar to the atomic moment and is known as *superspin*. It is of the order of $1000\mu_B$. The magnetization reversal of the superspin in presence of field or temperature can be described by theoretical models Stoner-Wohlfarth and Néel-Brown respectively.

2.7 Magnetization reversal

Generally, magnetization reversal process in thin films can occur either via domain wall motion and or via coherent rotation. In this section, we will discuss briefly the magnetization process in bulk thin films and then magnetization via coherent rotation will be discussed using the Stoner-Wohlfath model.

2.7.1 Magnetization reversal via domain wall motion

One important practical characteristic of ferromagnet is the magnetic hysteresis. The magnetization in applied field depends on the history of the field cycle. The hysteresis behavior was first explained by Pierre Weiss by the assumption that ferromagnetic materials consist of domains (Weiss, 1970). These domains are separated by domain walls and try to minimize the net energy of the system. A typical hysteresis loop is shown in Figure 2.19.

If the system is magnetized to the saturation magnetization M_s by an applied field, then reducing the field to zero, the magnetization reduces to the remanent magnetization M_r. A magnetic field equal to the coercive field H_c is needed to switch the magnetization into the opposite direction and to bring the magnetization to zero from remanence. The parameters M_r and H_c can be to characterize a ferromagnet. The previous section has evidenced if a specimen exceeds a certain critical size, it would divide into domains. In each domain all the magnetization M_s is everywhere parallel and separated by domain walls where the direction of M_s varies with position.

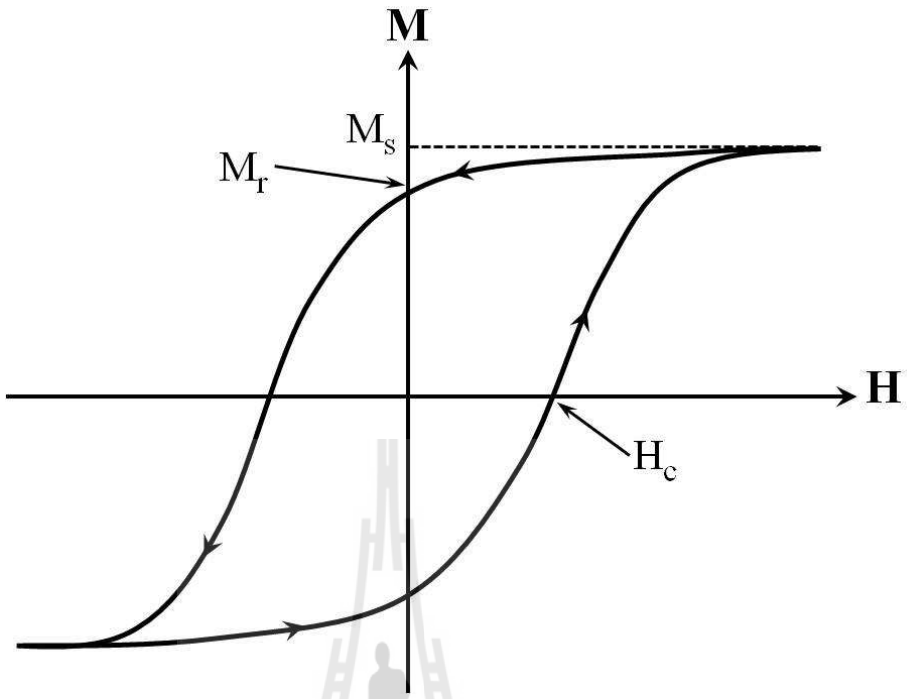

Figure 2.19 A typical magnetic hysteresis loop (Adapted from Bedanta, 2004).

When s demagnetized ferromagnet is magnetized, various processes occur. First the applied field is increased from zero, domain wall motion starts to occur which requires least magnetic energy. In this process, domain are aligned favorably with the magnetic field will grow at the expense of domains which are unfavorably aligned. At small applied fields the domain walls move through small distance and return to their original position on removal of the field; these are termed reversible displacements and correspond to the initial curved part of the magnetization curve. This reversible process is called as *domain-wall bowing* or one can also call it *domain-wall relaxation*. Wall bowing becomes irreversible when the domain wall is sufficiently deformed that expansion continues without further increase of field.

The bending of the wall which begins as reversible can also become irreversible if during this process the wall encounters further pinning sites which prevent it

relaxing once the field is removed. At intermediate to high field amplitudes, there is irreversible mechanism, namely domain rotation can occur in which the anisotropy energy can be outweighed and the magnetization can suddenly rotate away from the original direction of magnetization to the crystallographic easy axis which is nearest to the field direction. The final domain process at highest magnetic fields is coherent rotation of the domains to a direction aligned with the magnetic field, irrespective of the easy and hard axis.

2.7.2 Magnetization reversal via coherent magnetization rotation

The hysteresis curve for single domain particles can be calculated using the Stoner-Wohlfarth (SW) model. Since there are no domains and domain walls, the magnetization reversal can be explained by coherent rotation of the magnetization of single domain particles or superspins. The SW model describes the magnetization curve of an aggregation of single domain particles with uniaxial anisotropyeither as a result of particle shape or from the magnetocrystalline anisotropy. The main assumption curves of the model are: (i) coherent rotation of the magnetization of each particle and (ii) negligible interaction between the particles. In the SW model, the calculations were made for the ellipsoidal particles.

The coordinate system of SW model is illustrated in Figure 2.20. The equilibrium direction of the particle magnetization vector is defined by the easy anisotropy (EA) axis and the direction of the applied field. When a magnetic field H is applied at an angle ϕ to the easy axis of the uniaxial anisotropy of the particle, then the magnetization vector leans with an angle θ relative to the easy axis.

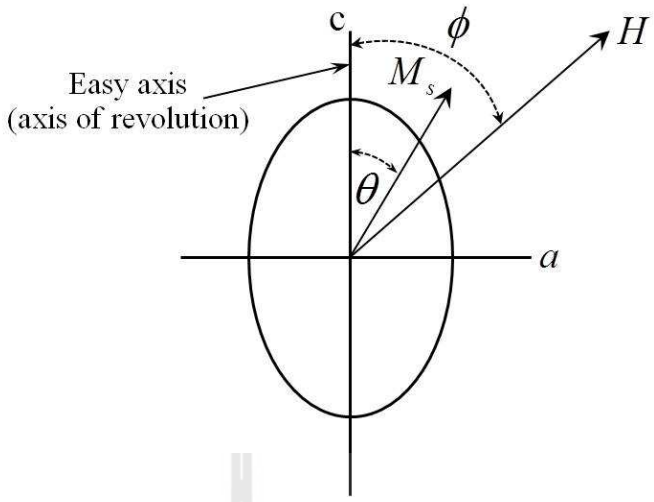

Figure 2.20 Coordinate system for magnetization reversal process in a single domain particle. An externally applied field at an angle ϕ relative to the easy axis causes a net magnetization to lies at some angle θ relative to the easy axis (Adapted from Bedanta, 2004).

The free energy of the system can be written in terms anisotropy energy as

$$E = KV\sin^2\theta - \mu_0 HM_s V\cos(\phi-\theta). \tag{2.168}$$

The equilibrium position of the magnetization M is given by

$$\frac{dE}{d\theta} = 2KV\sin\theta\cos\theta - \mu_0 HM_s V\sin(\phi-\theta) = 0 \tag{2.169}$$

$$2K\sin\theta\cos\theta = \mu_0 HM_s\sin(\phi-\theta) \tag{2.170}$$

The magnetization resolved in the field direction is given by

$$M = M_s\cos(\phi-\theta). \tag{2.171}$$

To consider in the case of a magnetic field is normal to the easy axis, so that ϕ is $90°$. Then the equation (2.170) and (2.171) become

$$2K\sin\theta\cos\theta = \mu_0 HM_s\cos\theta. \tag{2.172}$$

$$M = M_s\sin\theta. \tag{2.173}$$

Let $m = M / M_s$ is the reduced magnetization and substitute the equation (2.173) into (2.172). Then the reduce magnetization can be written as

$$m = \frac{\mu_0 HM_s}{2K}. \tag{2.174}$$

Saturation is achieved when $H = H_k = 2K / M_s =$ anisotropy field. The reduced field is defined by $h = H / H_k$ and can be written as

$$h = \frac{\mu_0 HM_s}{2K} \tag{2.175}$$

Now the equation (2.170) and (2.171) can be expressed as

$$\sin\theta\cos\theta = h\sin(\phi - \theta) \tag{2.176}$$

$$m = \cos(\phi - \theta) \tag{2.177}$$

Analytic solutions are possible for $\phi = 0$ or $\phi = 90°$. When $\phi = 0$ the hysteresis is rectangular and when $\phi = 90°$, the hysteresis passes through the origin and does not show any coercive field as shown in Figure 2.21.

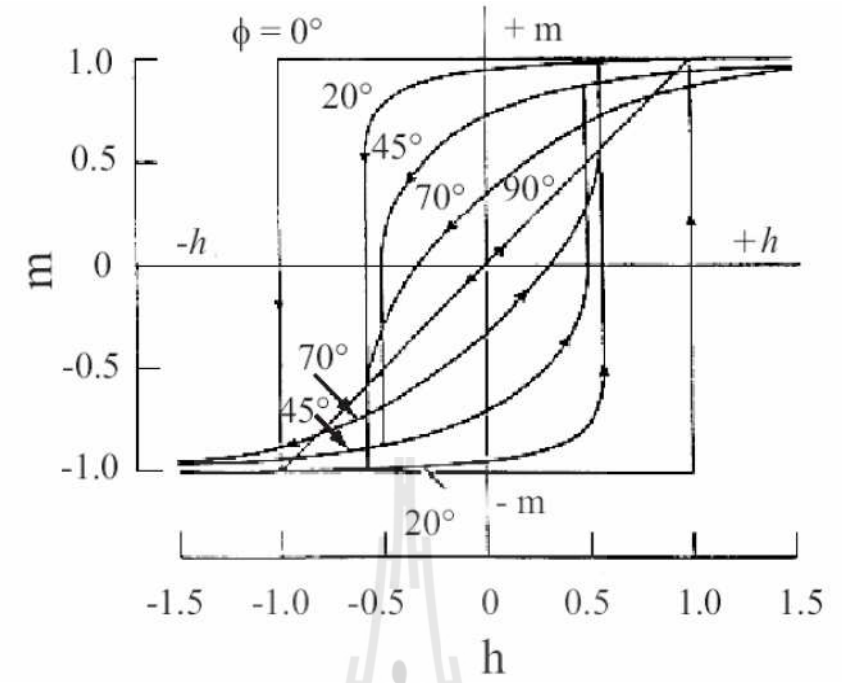

Figure 2.21 Hysteresis curves of a spherical single domain particle for different angles between anisotropy axis and external field in the framework of Stoner-Wohlfarth model (Stoner and Wohlfarth, 1948).

มหาวิทยาลัยเทคโนโลยีสุรนารี

CHAPTER III

RESEARCH METHODOLOGY

3.1 X-ray techniques

3.1.1 Synchrotron radiation

Synchrotron radiation is the electromagnetic radiation emitted by charge particles (electron or positrons) that are moving at speeds close to that of light when their paths are altered, as by a magnetic field. The radiation has a broad energy spectrum from infrared till hard x-ray and the intensity is 10 orders of magnitude higher than conventional x-ray tubes.

There are three forms of synchrotron radiation, depending on the process of generations. The Bending Magnet (BM) is the simplest procedure to provide synchrotron radiation. The radiation emanates in the form of cone with a divergence $1/\gamma$, where $\gamma = 1/\sqrt{1-v^2/c^2} = 1/\sqrt{1-\beta^2}$. It can also be expressed in term of the electron energy as

$$\gamma = \frac{E_e}{m_e c^2} = 1957\, E_e[\text{GeV}]. \tag{3.1}$$

The radiated energy in the electron frame of reference falls in the range of neV, but increases to the x-ray energy range in the laboratory frame of reference. The energy of the emitted photon is given by (Als-NielsenFultz and McMorrow, 2001)

$$E_c = \frac{3e\hbar B\gamma^2}{2m_e} \tag{3.2}$$

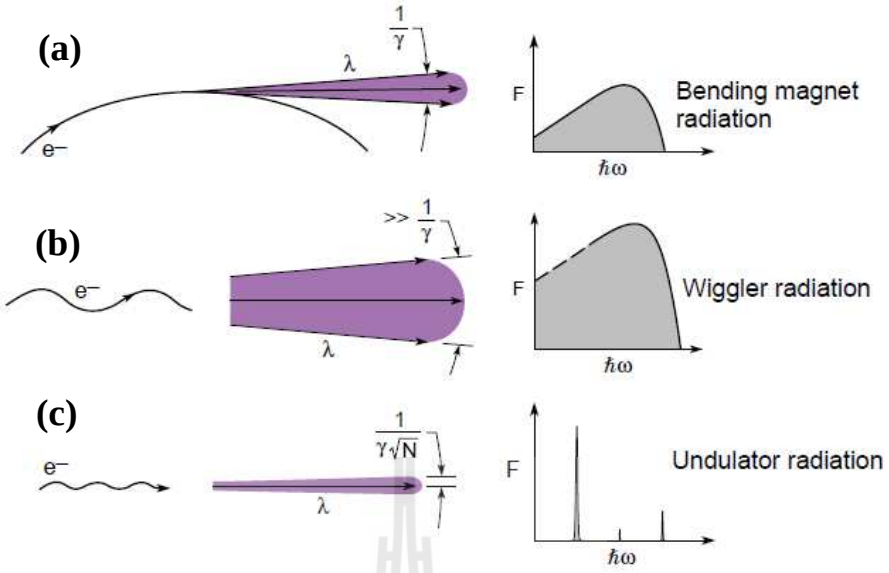

Figure 3.1 Schematic of synchrotron radiation from different sources. Radiation from (a) Bending magnet (b) Wiggler and (c) Undulator (Attwood, 2007).

$$E_c[\text{eV}] = 665 E_c[\text{GeV}] B[T], \tag{3.3}$$

where B is the applied magnetic field. Figure 3.1(a) shows the photon flux versus energy plot of radiation coming out from a BM.

The other two structures, Wiggler and Undulator consist of periodic array of magnets with alternate field direction applied perpendicular to the charge particle motion and are collectively known as Insertion devices. They have higher brilliance than the BM. The difference between these two depends on the parameter, *K*, which is given by

$$K = \frac{e\lambda_u B_0}{2\pi m_e c} = 0.934 \lambda_u[cm] B_0[T], \tag{3.4}$$

where λ_u is the periodicity of the magnets and B_0 is the magnetic field.

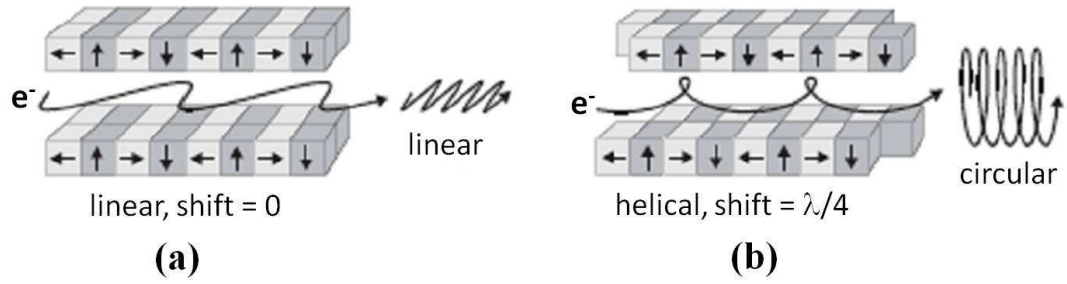

Figure 3.2 Schematic of polarization of radiation from undulators with (a) linearly polarized and (b) circularly polarized x-rays (Attwood, 2007).

For a Wiggler $K >> 1$ and the intensity $I \propto 2N$, where N is the number of periods, while an Undulator $K \leq 1$ and $I \propto N^2$. The undulator produces highest peak brilliance and lowest divergence $1/\gamma\sqrt{N}$. The flux versus energy from a wiggler and undulator is shown in Figure 3.1(b) and (c), respectively. The beam is usually linearly polarized in the plane of the electron orbit. If the two opposite poles of the magnets are periodically shifted the polarization can be adjusted. For a shift by $\lambda_u / 4$ a helical magnetic field is generated and circular polarized photon are obtained. If the shift is $\lambda_u / 2$ then linear polarization along vertical direction is obtained. Figure 3.2(a) and (b) illustrate the undulators producing linear and circularly polarized light, respectively.

Recently also fourth generation synchrotron sources i.e. Free Electron Laser (FEL) are available, which provide fully coherent (transverse and longitudinal) x-ray beam with very high intensity in small pulses.

3.1.2 X-ray absorption spectroscopy (XAS) experimental set up

X-ray absorption spectroscopy (XAS) is one of the powerful techniques to study the electronic structure of materials, formal oxidation state and coordination number and also used to probe local structure. The XAS experiment is generally performed at the synchrotron radiation source, due to high intensity and energy modifiable capability of generated x-ray photon, and the capability to obtain the continuous absorption spectrum over extensive energy range (Koningsberger and Prins, 1988).

In the x-ray absorption phenomena, where x-ray photon knock out an electron from the inner shell an electron from higher energy level will cascade down to fill in the hole and discharging radiation of energy, the discharged energy x-ray photon will be released as demonstrated in Figure 3.3(a) and the fluorescence x-ray can be detected. In addition, de-excitation can cause the Auger effect, where the electron reduces to lower energy state, a second electron can be excited to the continuum state and perhaps go out from the sample as shown in Figure 3.3(b). Therefore to measure the absorption coefficient it is possible to measure: the transmitted intensity, the fluorescence yield and the electron yield (Auger Yield). The schematic illustration of three types of x-ray absorption measurement is shown in Figure 3.4.

3.1.2.1 Transmission mode

This is actually the only real measurement of the absorption coefficient and it gives bulk information the samples. After the energy of x-ray photons being changed by x-ray double crystals monochromator, the intensities of incident x-ray photon beam (I_0) and the transmitted x-ray photon beam (I_t) are measured by ionization chambers as shown in Figure 3.5.

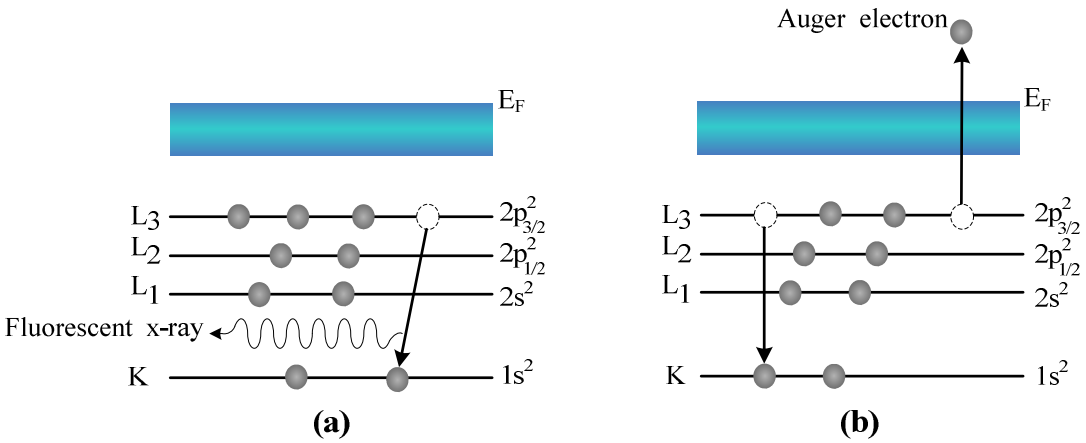

Figure 3.3 The excited state (a) x-ray fluorescence and (b) the Auger effect (Adapted from Koningsberger and Prins, 1988).

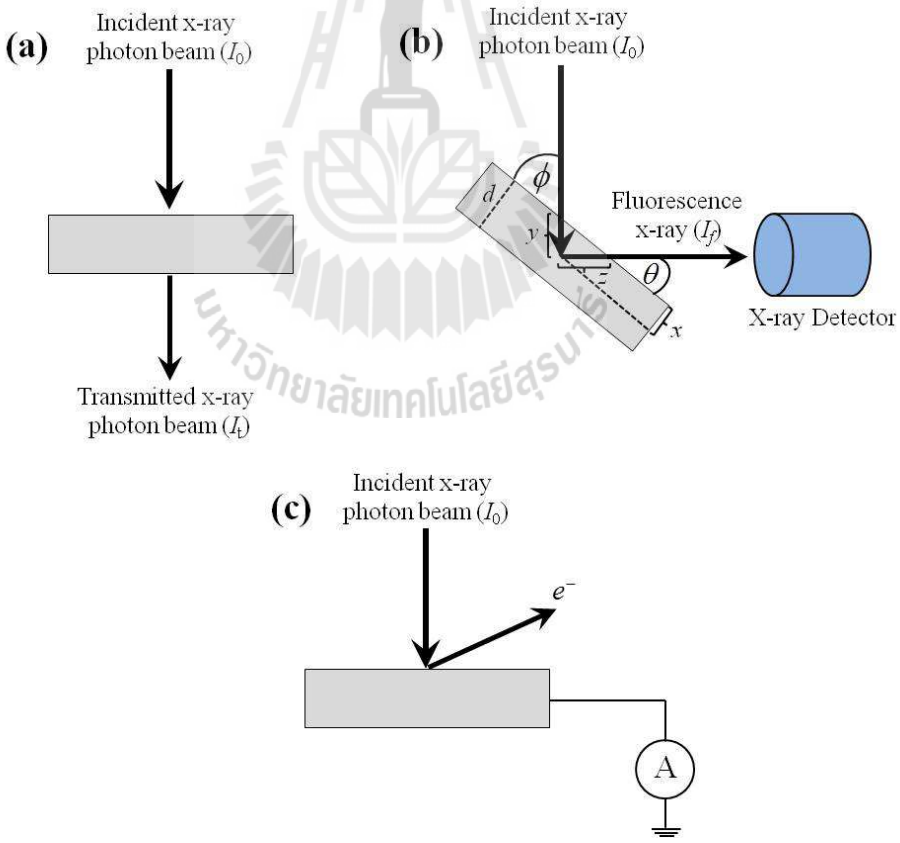

Figure 3.4 The three modes of XAS measurement (a) transmission mode, (b) fluorescence mode and (c) electron yield (Adapted from Bunker, 2010).

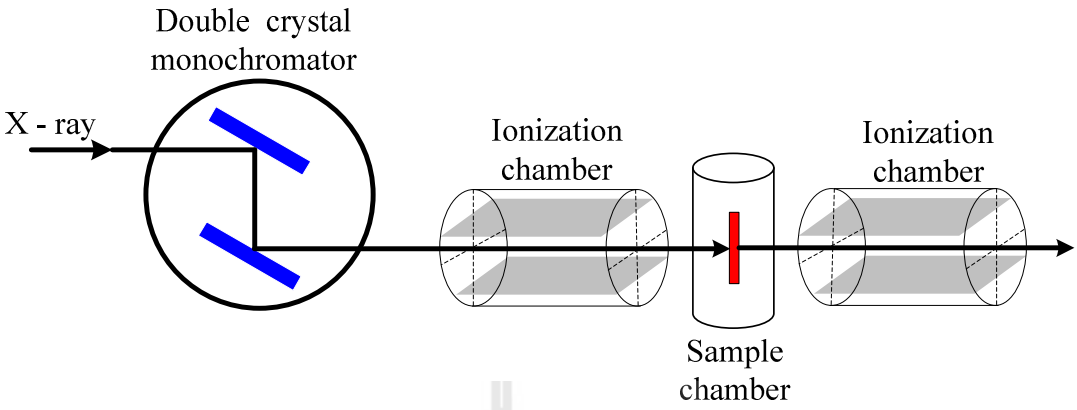

Figure 3.5 Schematic illustration of the experimental setup of transmission-mode X-ray absorption spectroscopy (Adapted from Stern and Heald, 1983).

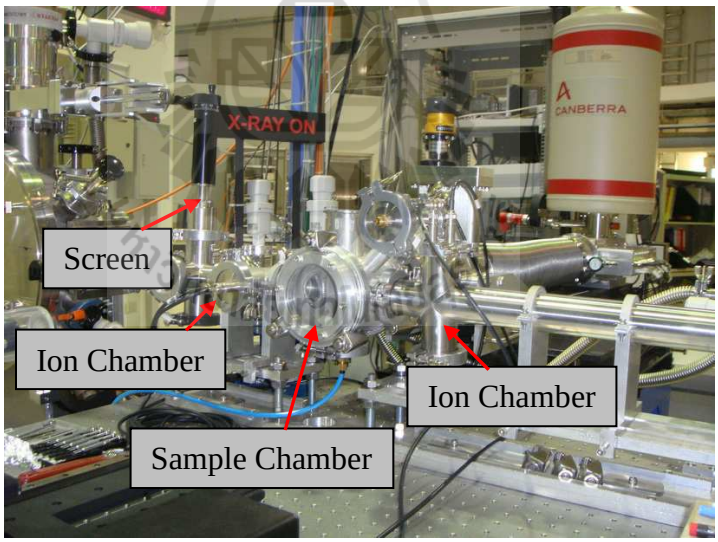

Figure 3.6 XAS experimental set up at the Siam Photon Laboratory, Synchrotron Light Research Institute, Nakhon Ratchasima, Thailand.

In this mode, we make sure the x-ray photon beam is well-aligned on the sample. The x-ray absorption can be extracted based on equation (2.5). During the sample preparation it is important to optimize the thickness of the sample and the concentration of the absorbing specie in order to minimize the saturation of the intense features near the edge. Those parameters are, in first approximation, a function only of the atomic number Z of the absorbing atom and of the chemical composition of the sample. The experimental set up of XAS experimental station at XAS beam line, Siam Photon Laboratory, SLRI is shown in Figure 3.6.

3.1.2.2 Fluorescence mode

In this case the measured quantity is the fluorescence x-ray emitted by the sample. Usually the fluorescence detector is placed at 90° to the incident x-ray photon beam in the horizontal plane, with the sample at an angle (usually 45°) with respect to the beam. Fluctuations in the number of elastically scattered x-ray are a significant source of noise in fluorescence XAS, so the position of the detector is selected to minimize the elastically scattered radiation by exploiting the polarization of the x-ray beam.

In case of fluorescence mode, the measured signal I_f is merely proportional to the absorption coefficient $\mu(E)$, and needs to be corrected for the fluorescence quantum efficiency and geometrical factors. As depicted in Figure 3.4(b), the fluorescence yield at the point of absorption is proportional to the x-ray intensity at the fluorescence efficiency ϵ_A. The incident intensity *I* at a depth *y* will be equal to:

$$I = I_0 e^{-\mu(E)y} \tag{3.5}$$

The fluorescence photon produced following absorption will then have to escape from the sample and reach the detector. Therefore, the measured fluorescence flux I_f at position y within the sample is given by (Tröger *et al*., 1992)

$$I_f = I_0 \mu_A(E) \epsilon_A \cdot e^{-\mu_T(E) y} \cdot e^{-\mu_f(E_f) z}, \tag{3.6}$$

where $\mu_A(E)$ is the absorption coefficient due to a given core excitation of the absorbing atom, e.g. *K*-excitation of Co atom, $\mu_T(E)$ is the total absorption coefficient in the sample: $\mu_T(E) = \mu_A(E) + \mu_{other}(E)$, $\mu_f(E_f)$ is the absorption coefficient at the dominant emission energy, ϵ_A stands for the fluorescence yield efficiency per unit solid angle, E is the incident beam energy and E_f is the line emission energy or fluorescence photon energy. Equation (3.6) applies to particular y and z depths within the samples as shown in Figure 3.5(b). In addition, z and y variables are dependent via the relationship is $y \sin\phi = z \sin\theta = x$. Thus in order to calculate the fluorescence signal for the entire sample thickness, the equation (3.6) can be written as

$$dI_f = I_0 \mu_A(E) \epsilon_A \cdot e^{-\left(\frac{\mu_T(E)}{\sin\phi} + \frac{\mu_f(E_f)}{\sin\theta}\right)x} dx. \tag{3.7}$$

Hence, the integrated fluorescence flux is then obtained by integration over the entire jet thickness *d*:

$$I_f = I_0 \mu_A(E) \epsilon_A \frac{1}{\sin\phi} \int_0^d e^{-\left(\frac{\mu_T(E)}{\sin\phi} + \frac{\mu_f(E_f)}{\sin\theta}\right)x} dx \tag{3.8}$$

$$I_f = \frac{I_0 \mu_A(E) \epsilon_A}{\mu_T(E) + g\mu_f(E_f)} \left\{ 1 - \exp\left[-\left(\frac{\mu_T(E)}{\sin\phi} + \frac{\mu_f(E_f)}{\sin\theta} \right) d \right] \right\}, \tag{3.9}$$

where $g = \sin\phi / \sin\theta$. This above-written equation describes the integrated fluorescence flux at the direction given by the angle $\theta = 45°$ in case of the setup shown in Figure 3.5(b). For this geometry, we approximate $\phi + \theta = 90°$ and the fluorescence intensity can be written as

$$I_f = \frac{I_0 \mu_A(E) \epsilon_A}{\mu_T(E) + \mu_f(E_f)} \left\{ 1 - exp\left[-(\mu_T(E) + \mu_f(E_f))\, d' \right] \right\}, \qquad (3.10)$$

where $g = 1$, $\sin\phi \equiv \sin\theta = 45°$ and $d' = d / \sin(45°)$. The fluorescence intensity is thus directly proportional to the absorption coefficient of the absorber, but in addition, the geometrical factors and the quantum efficiency are now included. Moreover, the equation (3.10) has two interesting limits which are the best cases for XAS measurements in fluorescence mode: (1) the thick sample (Eisebitt *et al*., 1993) and (2) the thin sample (Jaklevic *et al*., 1977) limits.

For the thick sample limit, one assumes that the sample thickness is much larger compared to the absorption length. The fulfillment of this condition implies that $\left[\mu_T(E) + \mu_f(E_f) \right] d' >> 1$, and thus $e^{-\left[\mu_T(E) + \mu_f(E_f)\right] d'} << 1$. Hence, the fluorescence flux coming out of thick sample can be rewritten as

$$I_f \approx I_0 \epsilon_A \frac{\mu_A(E)}{\mu_T(E) + \mu_f(E_f)} \qquad (3.11)$$

In addition, if the element of interest is dilute, then the XAS contribution to the overall absorption from the denominator can be neglected and detected (I_f / I_0) will be practically equal to $\mu_A(E)$.

In the thin sample limit, both the sample thickness and the absorption lengths are small, so that the argument of the exponential term becomes

$\left[\mu_T(E)+\mu_f(E_f)\right]d' \leq 1$ and therefore $exp\left[-\left(\mu_T(E)+\mu_f(E_f)\right)d'\right] \approx 1$. We can then Taylor-expand the exponential term to first-order, thus the equation (3.10) reduces to

$$I_f \approx I_0 \epsilon_A \frac{\mu_A(E)}{\mu_T(E)+\mu_f(E_f)}\left[\mu_T(E)+\mu_f(E_f)\right]d' \approx I_0 \epsilon_A \mu_A(E)\, d' \qquad (3.12)$$

As can be seen in both cases, the resulting x-ray fluorescence can be directly related to the changes in the absorption coefficient of the central absorbing atom and thus it should yield quantitatively the same XAS spectrum, as recorded in x-ray transmission.

3.1.2.3 Electron yield

In this case the measured quantity is the current generated in the sample through an ammeter. Since the mean free path of electrons in a material is very low, thus the total electron yield is surface sensitive technique.

3.1.3 X-ray absorption spectrum calculation

In this thesis, the principle theoretical calculations are performed based on FEFF 8.2 code. This code is developed to primarily calculate x-ray absorption for the FEFF (f_{eff}) project developed by the Department of Physics, University of Washington, Seattle. USA. Apart from XAS spectra calculation, FEFF code can also calculate x-ray natural circular dichroism (XNCD), spin-dependent calculations of x-ray magnetic dichroism (XMCD), nonresonent x-ray emission (XES) and electronic structure including local densities of states (LDOS). FEFF code is written in ANSI FORTRAN 77 with principle investigator John J. Rehr and co-principle investigator Alexei Ankudinov.

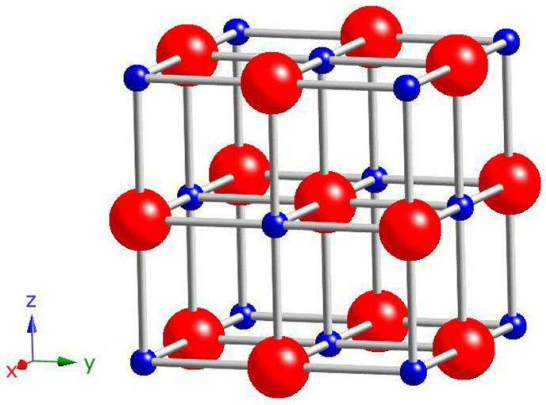


```
Title CoO rock salt structure
Space F m 3 m
a=4.2667
rmax=10
core=Co
atom
Co 0.0000  0.0000  0.0000
O   0.5000  0.5000  0.5000
```

Figure 3.7 Detail of an atoms.inp input file to generate "feff.inp" for FEFF calculation.

FEFF is *ab initio* self-consistent real space multiple-scattering (RSMS) code for simultaneous calculations of x-ray absorption spectra and electronic structure. The input file "feff.inp" can be created directly from ATOMS code via "atoms.inp" as shown in Figure 3.7.

The power of FEFF lies in the relative simplicity of the required input from the user. The suitable commands, parameter and atomic positions for FEFF-XAS spectrum calculations can be edited within the input file named "feff.inp", which is shown in Figure 3.8. This file can be controlled with some details, for instance the generator of input file and the number of atom which is contained in the cluster. The following details describe about various cards used to assign the steps of calculation. The type of atomic potentials and defined atomic symbols are presented in the next part, and eventually with the locations of the created atoms in the system where the location of center atom is placed at (0,0,0) in (x,y,z) coordination.

```
* This feff.inp file generated by ATOMS, version 2.50
 * ATOMS written by and copyright (c) Bruce Ravel, 1992-1999
*      total mu =     1888.7 cm^-1, delta mu =     1632.2 cm^-1
 *      specific gravity =  6.408, cluster contains  437 atoms.
 *      mcmaster corrections:  0.00062 ang^2 and  0.694E-06 ang^4

TITLE   CoO rock salt structure

EDGE     K
S02      1.0

*             pot   xsph  fms   paths genfmt ff2chi
CONTROL   1       1     1      1      1      1
PRINT     1       0     0      0      0      0

*       r_scf   [ l_scf  n_scf  ca ]
SCF     5.0       0     30    0.2

*               ixc  [ Vr  Vi ]
EXCHANGE    0     0   0

*EXAFS
*RPATH    9.38674

*         kmax  [ delta_k  delta_e ]
XANES    4.5       0.07      0.5
*         r_fms     [ l_fms ]
FMS       7.0          0
*
RPATH    0.10000
*          emin  emax  resolution
*LDOS     -20     20      0.1

POTENTIALS
*   ipot   z [ label   l_scmt  l_fms  stoichiometry ]
    0  27   Co          -1       -1       0
    1   8   O           -1       -1       1
    2  27   Co          -1       -1       1

ATOMS
 0.00000      0.00000      0.00000     0    Co          0.00000
 0.00000      2.13335      0.00000     1    O           2.13335
 0.00000      0.00000     -2.13335     1    O           2.13335
 0.00000     -2.13335      0.00000     1    O           2.13335
 2.13335      0.00000      0.00000     1    O           2.13335
-2.13335      0.00000      0.00000     1    O           2.13335
 0.00000      0.00000      2.13335     1    O           2.13335
 2.13335      0.00000      2.13335     2    Co          3.01701
-2.13335      0.00000      2.13335     2    Co          3.01701
-2.13335      2.13335      0.00000     2    Co          3.01701
 2.13335      2.13335      0.00000     2    Co          3.01701
-2.13335     -2.13335      0.00000     2    Co          3.01701
    ⋮            ⋮            ⋮        ⋮    ⋮           ⋮
-2.13335     -8.53340     -4.26670     1    O           9.77624
 -4.26670    -8.53340     -2.13335     1    O           9.77624
 2.13335     -4.26670      8.53340     1    O           9.77624
END
```

Figure 3.8 Detail of a “feff.inp” input file of CoO with Co as center atom for FEFF calculation.

FEFF code aids scientist to approach the XAS spectra by performing the possibly precise Green's function in the absorption coefficient $\mu(E)$. For FEFF 8 series, the developers suggested two main developed features for XAS calculation. The two main advantages are the approaches of self-consistent field (SCF) and full multiple scattering (FMS).

For XAS calculation (especially XANES), the SCF loop are used to compute the electron density and Coulomb potential within RSMS Green's-function framework. The self-consistency allows to redistribute charge in the system in such a way that charge is transferred between atoms based on their chemical electron affinity (i.e., oxidation state). In addition, the SCF calculation provides an accurate *ab initio* estimation of the Fermi energy, which is essential for the correct representation of the intensity of "white lines" (strong absorption features just above the Fermi level).

The SCF loop is initialized by the construction of a so-called muffin tin (MT) potential as an approximation to the real (full) potential. The MT potentials are obtained by placing the free atoms at the positions specified by the feff.inp data. In this scheme, all atoms are treated as spheres and the radii of the spheres are decreased up to a certain level determined by Norman criterion (Norman, 1976), with excess charge placed onto the flat interstitial region. In the next step of the SCF loop, the relativistic Dirac equation is solved for the above MT potentials to obtain photoelectron scattering amplitudes and phases. These quantities are used in turn to construct the Green's function given in Equations (2.32). FMS card will perform the calculation for all possible paths within the defined cluster. XANES calculation can be performed under the defined control cards, most of them are normally used as the defaults, excepting FMS and SCF which are importantly managed.

3.1.4 Linear combination analysis

Linear combination fitting (LCF) is presently the most common approach for quantitative XAS analysis. LCF models the spectrum from a sample of unknown speciation with a linear combination of spectra from standards of known structure and composition that are candidate species within the sample.

The underlying principle of LCF is the additive nature of the absorption from each species in the sample. It can be applied to XANES, derivative XANES, or EXAFS spectra. In principle, the total absorption coefficient μ can be written as a sum of coefficients for all the chemical forms or species in the sample:

$$\mu = \sum_i f_i \mu_i , \tag{3.13}$$

where f_i is the fraction of species i having the absorption coefficient μ_i.

In this thesis, the fractions of secondary phase in the samples are examined using LCF subroutines in Athena (Ravel and Newville, 2005). This program calculates the scaling factor applied to difference standard spectra that provide the best representation of the measured spectrum over a defined energy range. Mathematically,

$$Model = \sum_i f_i \left(\mathrm{STD}_i\right), \tag{3.14}$$

where *Model* represents the least-squares fit to the sample spectrum over a selected energy range, and f_i represents the scaling factors applied to each spectrum of the corresponding standard $\left(\mathrm{STD}_i\right)$ across that energy range of the fit. The scaling factors can be constructed so that they sum to one and are not negative. Ideally, the scaling factor obtained from LCF represents the fractions of each standard species within the unknown sample. The statistical goodness-of-fit parameter is the *R* factor.

The *R* factor is the sum of the squares of the differences between the data and the fit at each data point, divided by the sum of the squares of the data at each corresponding point. The *R* factor is defined by

$$R \text{ factor} = \frac{\sum_i \left(\text{data}_i - \text{fit}_i\right)^2}{\sum_i \text{data}_i^2} . \qquad (3.15)$$

In general, R factor values less than 0.05 are considered to reflect a reasonable fit.

3.2 SQUID magnetometer

Superconducting Quantum Interference Device (SQUID) is a very sensitive magnetometer to measure the magnetization of tiny samples with tiny magnetic moments. The special design of the detection coil and the Josephson junction provides the high sensitivity to these measurements. The sensitivity is of the order of 10^{-8} emu (10^{-11} Am^2). Essentially two modes of operation exist. First, as a magnetometer, it measures the static magnetic moment, μ, at various applied fields, *H*, and temperature, *T*. When normalized to the volume of the sample one obtains the average magnetization, *M*. Second, as an *ac* susceptometer additionally a small alternating magnetic field is applied and the time dependent response $\mu(t)$, is recorded. SQUID magnetometers are used in various field of research such as in the study of superconductors, biological materials, thin films, magnetic nanostructures, magnetic fluids and geological materials.

In this thesis, a commercial SQUID magnetometer, magnetic property measurement system (MPMS) from Quantum Design, was used for the magnetization

measurements. The MPMS system includes several different superconducting components:

- a superconducting magnet to generate large magnetic fields,
- a superconducting detection coil which couples inductively to the sample,
- a Superconducting QUantum Interference Device (SQUID) connected to the detection coil,
- a superconducting magnet shield surrounding the SQUID.

3.2.1 Principle of SQUID operation

In the SQUID device, a Josephson junction detects the magnetization. It is shielded by a magnetic shield from the external magnetic fields and the sample. The SQUID is connected to the detection coils ("pick up" coil) around the sample space by superconducting wires. The detection coil (pick up coil) is a single piece of superconducting wire wound in a set of three coils configured as a second order (second derivative) gradiometer as shown in Figure 3.9(a). The upper coil is a single turn wound clockwise, the center coil comprises two turns wound counter-clockwise, and then the bottom coil is again a single turn wound clockwise. In this configuration the pick up coil is only sensitive to the magnetic stray fields from the sample, whereas any field change outside the coil is not detected. The sample is moved through this pick up coil. The detection coil, the superconducting wire and the SQUID input coil form a closed loop superconducting system. The sample is mounted in a tube of diameter 9 mm and is attached to a rigid sample rod. The sample space is maintained at low pressure and filled with He gas. The detection coil is surrounded by a superconducting magnet (type II), which provides uniform magnetic field over the

sample. The uniformity of the magnetic field changes by 0.01% over a sample displacement of 4 mm.

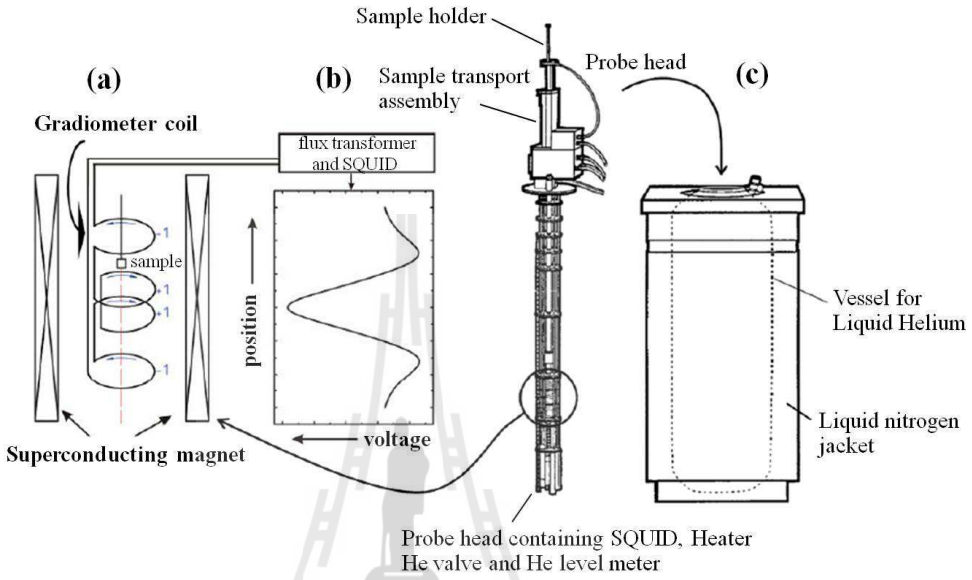

Figure 3.9 (a) Gradiometer coil with sample and the superconducting magnets (b) The response curve fitted with a point dipole approximation. (c) Schematic of the SQUID magnetometry (Bedanda, 2006).

The sample is suspended from a rod mounted at the top of the cryostat to a transport mechanism. When the sample is moved vertically through the detection coil, the magnetization can induces an electric current in the detection coil, which is inductively coupled to the SQUID sensor. As the sample moves through it the magnetic flux changes and the SQUID sensor provides a response curve for voltage versus distance as shown in Figure 3.9(b). This response curve is fitted with the theoretical curve of an ideal dipole and the fit provides the value of the magnetization.

The SQUID magnetometer measures the longitudinal magnetization that means the magnetization component along the direction of the applied magnetic field and parallel to the detection coil. The maximum field that can be achieved is ± 5 T. The temperature at the sample can be set in the range $2 \leq T \leq 400$ K and the temperature stability of magnetometer is better than 50 mK. Figure 3.9(c) shows a schematic of the SQUID magnetometer.

3.2.2 Josephson junction

The SQUID device consists of closed superconducting loop including one or two Josephson junctions in the loop's current path. The SQUID function is a manifestation of two fundamental physical properties: magnetic flux quantization in a superconducting ring and Josephson Effect.

The magnetic flux inside a superconducting ring is quantized (Kittel, 1986). The total magnetic flux in the loop is given by

$$\Phi_T = \int \vec{A} \cdot d\vec{s} = n\Phi_0 \tag{3.16}$$

where $\vec{A}$ is the vector potential n is an integer. The flux quantum is given by

$$\Phi_0 = \frac{h}{2e} \approx 2.07 \times 10^{-15} \ \ Tm^2 \tag{3.17}$$

The superconducting properties are related to a Cooper pair (electron-electron pair) and the wave function can be written as

$$\psi(\vec{r},t) = \psi_0(\vec{r},t)\exp(i\phi(\vec{r},t)), \tag{3.18}$$

where ϕ is the phase factor, which is same for all Cooper pairs.

When two superconductors are separated by a tunnel barrier (can be conducting or insulating), the current density through the barrier can be written as

$$I = I_c \sin \delta_0 , \tag{3.19}$$

where I_c is the critical current density, $\delta_0 = \phi_1 - \phi_2$ is the phase difference.

This junction is called a “weak link” or “Josephson junction”, which plays a crucial role for the detection of magnetic moment. This is achieved without applying any voltage across the junction.

If a voltage V is applied across the junction, then the current density can be expressed as

$$I = I_c \sin \delta \tag{3.20}$$

where δ is given by $\delta = \delta_0 - \omega t$. The current density oscillates with a frequency $\omega = 2eV / \hbar$, which is known as Josephson Effect.

3.3 Neutron technique

The neutron is an uncharged (electrically neutral) subatomic particle with mass $m_n = 1.675 \times 10^{-27}$ kg and spin $s = 1/2$. Neutron possesses a magnetic moment, which is coupled antiparallel to its spin in the order of $\mu = \gamma_N \mu_N$, where $\gamma_N = -1.913$ is the neutron gyromagnetic ratio, and μ_N is the nuclear magneton given by $\mu_N = e\hbar / m_p = 5.501 \times 10^{-27}$ J/T.

Neutrons are stable when bound in an atomic nucleus, while having a mean lifetime of approximately 1000 seconds as a free particle. The neutron wavelength is obtained from the de Broglie relation. The velocity distributions of neutrons are given by Maxwell velocity distribution and are dependent upon the temperature of the moderator. They are detected by nuclear reactions that produce charged using

proportional counters (with ^{3}He) or scintillation counters (^{6}Li). Neutrons are classified according to their wavelength and energy as “epithermal” for short wavelengths ($\lambda \sim$ 0.1 Å), “cold” for long wavelengths ($\lambda \sim 10$ Å). The desired range of wavelengths is obtained by moderation of the neutrons during their production, either in reactors or spallation sources.

3.3.1 Neutron source

Most fundamental neutrons experiments are conducted with slow neutrons for two reasons. First, slower neutrons spend more time in an apparatus. Second, slower neutrons can be more effectively manipulated through coherent interactions with matter and external fields. Free neutrons are usually created through either fission reactions in a nuclear reactor or spallation in accelerator-based neutron sources.

3.3.1.1 Fission source

Neutrons have traditionally been produced by fission in nuclear reactors optimized for high neutron brightness. In this process, thermal neutrons are absorbed by uranium-235 nuclei, which split into fission fragments and evaporate a very high-energy (MeV) constant neutron flux. After the high-energy (MeV) neutrons have been thermalized to meV energies in the surrounding moderator, beams are emitted with a broad band of wavelengths. The energy distribution of the neytrons cab be shifted to higher energy by allowing them to come into thermal equilibrium with a “hot source” or to lower energies with a “cold source” such as liquid deuterium at 25 K. Wavelength selection is generally achieved by Bragg scattering from a crystal monochromator or by velocity selection through a mechanical chopper. In this way

high-quality, high-flux neutron beams with a narrow wavelength distribution are made available for neutron experiments.

3.3.1.2 Spallation source

In these sources neutrons are released by bombarding a heavy-metal target (e.g., tantalum), with high-energy particles (e.g., protons) from a high-power accelerator. The methods of particles acceleration tend to produce short intense bursts of high-energy protons, and hence pulses of neutrons. Spallation releases much less heat per useful neutron than fission (typically 30 MeV per neutron, compared with 190 MeV in fission). The low heat dissipation means that pulsed sources can deliver high neutron brightness with significantly less heat generation in the target.

The main feature that differentiates spallation sources from reactors is the possibility for operation in pulsed mode. At reactor one obtains continuous beams with a thermalized Maxwellian energy spectrum. In a spallation source, neutrons arrive at the experiment while the production source is off, and the frequency of the pulsed source can be chosen so that slow neutron energies can be determined by time-of-flight methods. The lower radiation background and convenient neutron energy information can be advantageous for certain experiments.

3.3.2 Neutron reflectometry

Neutron reflectometry is used to probe the structure of surfaces, thin films or buried interfaces. Polarized neutron reflectometry (PNR) is a technique for studying the magnetization profile near the surface of thin films and magnetic multilayer materials. This technique involves shining a highly collimated beam of neutrons onto an extremely flat surface and measuring the reflected intensity as a function of the scattering vector Q (momentum transfer vector) perpendicular to the

reflecting surface. The exact shape of the reflectivity profile provides detailed information about the structure of surface, including the thickness, density, and roughness of any thin films layered on the substrate.

At grazing incidence, it can be distinguished three scattering geometries, specular reflection, scattering in the incidence plane (off-specular scattering) and scattering perpendicular to the incidence plane (grazing incidence small-angle neutron scattering). The neutron scattering geometry is shown in Figure 3.10.

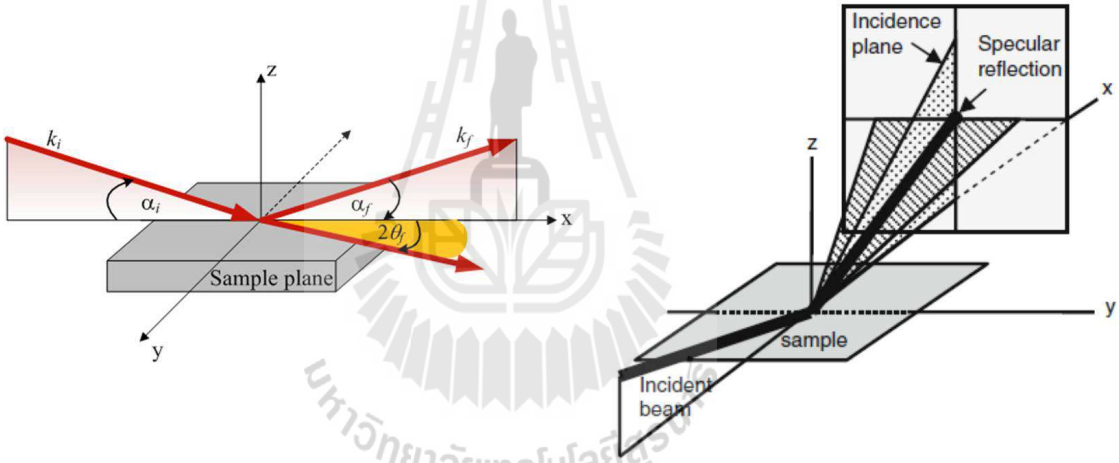

Figure 3.10 Schematic of the neutron scattering geometry from different perspectives. Specular reflectivity geometry; off-specular scattering plane, corresponding to the incident plane (dotted plane); GISANS scattering plane (dashed plane), perpendicular to the incident plane (Adapted from Paul, 2012).

The correlation lengths can be estimated from the three equations of momentum transfers along three different axes due to the scattering geometry for small angles.

$$\vec{Q}_z = \vec{Q}_\perp = \frac{2\pi}{\lambda}\left[\sin(\alpha_i) + \sin(\alpha_f)\right] \approx \frac{2\pi}{\lambda}\left[\alpha_i + \alpha_f\right]. \tag{3.21}$$

$$\begin{aligned}\vec{Q}_x = \vec{Q}_\parallel &= \frac{2\pi}{\lambda}\left[\cos(\alpha_f) + \cos(2\theta_f) - \cos(\alpha_i)\right] \\ &\approx \frac{2\pi}{\lambda}\left[\alpha_i^2 - \alpha_f^2 - \theta_f^2\right].\end{aligned} \tag{3.22}$$

$$\vec{Q}_y = \vec{Q}'_\parallel = \frac{2\pi}{\lambda}\cos(\alpha_f)\sin(2\theta_f) \approx \frac{2\pi}{\lambda}\left[\theta_f\right]. \tag{3.23}$$

As shown in Figure 3.10, the incident wave vector $\vec{k}_i$ making an angle α_i in the *x*-*z* plane while the scattered wave vector $\vec{k}_f$ making an angle α_f in *x*-*z* plane and also $2\theta_f$ in the *x*-*y* plane (relevant for diffuse scattering). Different length scales $\xi = 2\pi / \vec{Q}$ (ranging from nm to μm) can be accessed by using different scattering geometries in most practical cases. Specular reflectivity probes the structure along $\vec{Q}_z$ or in the depth of the film (3 nm $< \xi <$ 1 μm). Off-specular scattering probes surface features along $\vec{Q}_x$ (500 nm $< \xi <$ 50 μm) whereas grazing incidence SANS probes surface features in the range of 3 nm $< \xi <$ 100 μm along $\vec{Q}_y$.

Neutron reflectometry is a specular reflection technique, where the angle of incident beam is equal to the angle of reflected beam. The reflection is usually described in terms of a momentum transfer vector, denoted $\vec{Q}_z$, which describes the change in momentum of neutron after reflecting from the material. Conventionally the *z* direction is defined to be the film normal direction. A typical neutron reflectometry plot displays the reflected intensity (relative to the incident beam) as a function of the

scattering vector $\vec{Q}_z = (4\pi/\lambda)\sin\alpha$. The neutron wavelength used for reflectivity is typically on the order of 0.2 to 1 nm.

The measured reflectivity can be achieved either by using a monochromatic neutron and scanning a large range of incident angles, or by using the broad-band neutron time of flight method with fixed scattering angle. In the case of the time of flight method the fixed sample geometry ensures constant samples illumination and essentially constant Q_z resolution over the available Q_z range. The experimental set up and principle layout of the apparatus for multioptional reflectometry (AMOR) station at the Swiss spallation neutron source SINQ, Paul Scherrer Institute, PSI is shown in Figure 3.11.

The moderated neutrons pass through a dish chopper to select the wavelength range. The beam is coarsely collimated by neutron absorbing jaws before entering the experimental measurement area. Fine collimation is achieved by two slits before the sample which define the illuminated area and resolution at the sample position. The beam intensity is monitored just before reaching the sample using a low efficiency monitor detector. Post sample, the background noise is suppressed by two further slits and shielded detector nose cone. Polarized incident neutrons are obtained by using a polarizer and the polarization of the reflected neutrons is determined using a analyzer crystal. Both polarizer and analyzer are consisting of a multilayer system comprising magnetic and non magnetic layers.

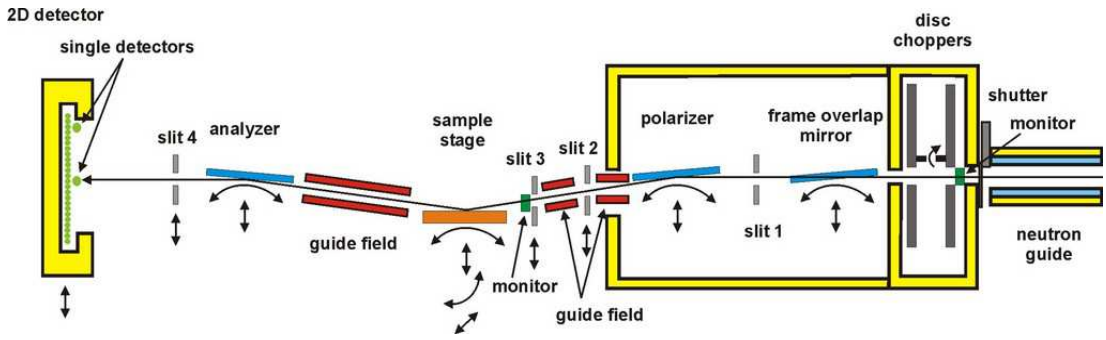

Figure 3.11 Schematic diagram of AMOR reflectometer at PSI (Gupta *et al*., 2004).

3.4 DC magnetron sputtering

Magnetron sputtering is a type of Physical Vapor Deposition (PVD), a process in which a target material is vaporized and deposited on a substrate to create a thin film. Conductive materials can be deposited using a direct current (DC) power supply. For insulating or semiconducting targets, a radio frequency (RF) power supply is required with an automatic. This method is used to prepare multilayers of the composition SiO_2/[Co(13 nm)/CoO(5 nm)/Au(25,30,35)]$_{N=16}$ by the multilayer research group of Dr. Amitesh Paul, Technical University of Munich (TUM) and through collaborations for studying the local structure of Co atoms and the formation of various cobalt oxide forms in these samples by using the X-ray absorption spectroscopy technique as well as studying together on the magnetic properties of these samples using SQUID and PNR measurements. More details of the sample preparation and X-ray diffraction (XRD) are presented elsewhere (Paul and Mattauch, 2004; Paul, Schneider and Stahn, 2007).

3.5 Precipitation method

In this thesis, the $BiFeO_3$ and Mn-doped $BiFeO_3$ samples were prepared by the research group of Prof. Dr. Santi Maensiri and through collaborations for studying the local structure of Fe and Mn atoms in these samples by using the X-ray absorption spectroscopy technique. These samples were prepared by a precipitation method. More details of the sample preparation and X-ray diffraction (XRD) are presented elsewhere (Hunpratub *et al*., 2012; Unruan *et al*., 2012).

มหาวิทยาลัยเทคโนโลยีสุรนารี

CHAPTER IV

XANES STUDY OF MANGANESE-DOPED BISMUTH FERRITE AND COBALT-COBALT OXIDE EXCHANGE-COUPLED SYSTEM

4.1 XANES measurement of Mn-doped $BiFeO_3$

The nominal $BiFe_{1-x}Mn_xO_3$ ceramic compositions (with x = 0, 0.05, 0.10, 0.20, 0.30, and 0.40) used in this study were prepared by a precipitation method (Unruan *et al*., 2012; Hunpratub *et al*., 2012). X-ray diffraction (XRD) measurements were first carried out to verify the *global* crystal structure of the BFO and Mn-doped BFO samples. The *local* structure of the Mn in BFO structure was then determined by XANES technique. The XANES measurements of Fe and Mn *K*-edge were performed in fluorescent mode with 13-component Ge detector (Canbera) at the X-ray absorption spectroscopy beamline (BL-8) of the Siam Photon Source (electron energy of 1.2 GeV with electron currents between 120 mA and 80 mA), Synchrotron Light Research Institute, Thailand. The XANES spectra of all samples were collected at ambient temperature. Double crystal monochromator Ge(111) with an energy resolution ($\Delta E/E$) of 3×10^{-4} was used to scan the synchrotron X-ray with the photon energy step of 0.25 eV in the range of 7090 to 7190 eV and 6520 to 6620 eV, covering the XANES region of Fe and Mn *K*-edges, respectively.

4.2 XANES measurement of Co/CoO/Au multilayers

Multilayers (MLs) of the composition $SiO_2/[Co(11.0\,nm)/CoO(5.0\,nm)/Au(25,30,35\,nm)]_{N=16}$ were prepared by DC magnetron sputtering (Paul *et al*., 2006). During deposition, the Ar pressure in the magnetron sputtering chamber was 3×10^{-3} mbar. The process was started at a base pressure of 1×10^{-7} mbar. An ultraviolet was used to assist oxidation at an O_2 pressure of 200 mbar at 50 °C for 1 h. A schematic of layer structures is shown in Figure 4.1. The Co ML samples are label as Co_25, Co_30 and Co_50. The sample numbers denote the thickness of Au layers.

The Co K-edge measurements were performed in the fluorescence mode with a 13-component Ge detector at the x-ray absorption spectroscopy beamline (BL-8) of the Siam Photon Source (electron energy of 1.2 GeV, beam current 120-180 mA), Synchrotron Light Research Institute, Thailand. A double crystal monochromator Ge (220) was used to scan the energy of the synchrotron x-ray beam with energy steps of 0.30 eV in the range of 7700 to 7785 eV covering the XANES region of Co *K*-edge.

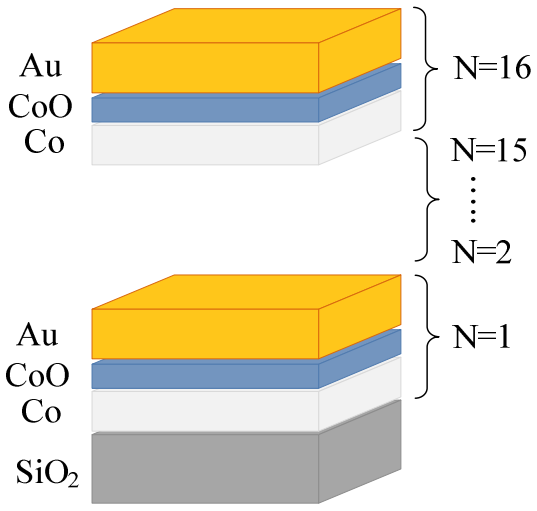

Figure 4.1 Schematic of layer structure of Co/CoO/Au ML.

4.3 XANES Analysis

4.3.1 Identification of Mn site in $BiFeO_3$

The measured Fe and Mn *K*-edge XANES spectra measured for BFO and Mn-doped BFO samples with different Mn contents are compared with standard Fe_2O_3 and Mn_2O_3 powders, as shown in Figure 4.2 and 4.3, respectively. For Fe *K*-edge, the position of absorption edge of all samples resembles that of the Fe_2O_3 standard, showing that the valence of Fe in BFO structure is +3, as expected. This observation also rules out the presence of the other bismuth ferrite secondary phases. Similarly, the Mn *K*-edge spectra of all samples and the Mn_2O_3 standard have similar positions of the absorption edge. This result indicates that the majority of Mn species in Mn-doped BFO is Mn^{3+}. Furthermore, both spectra contain the same main features, implying that the majority of Mn atoms assumes the same lattice locations in these samples. The main feature of the Mn *K*-edge XANES spectra are composed of two shoulders and three peaks labeled as s_1, s_2, p_1, p_2, and p_3 (as shown in inset of Figure 4.3). The pre-edge (s_1) absorption region around 6542 eV is attributed to the electric dipole forbidden transition of a 1*s* electron to an unoccupied 3*d* orbital, which is partially allowed because of electric quadrupole coupling and/or 3*d*-4*p* orbital mixing. The main absorption edge feature (s_2) is assigned to the purely dipole-allowed $1s \rightarrow 4p$ transition. Feature p_1, p_2 and p_3 result from the multiple-scattering contribution of absorbing Mn in MnO_6 octahedra surrounded by Bi.

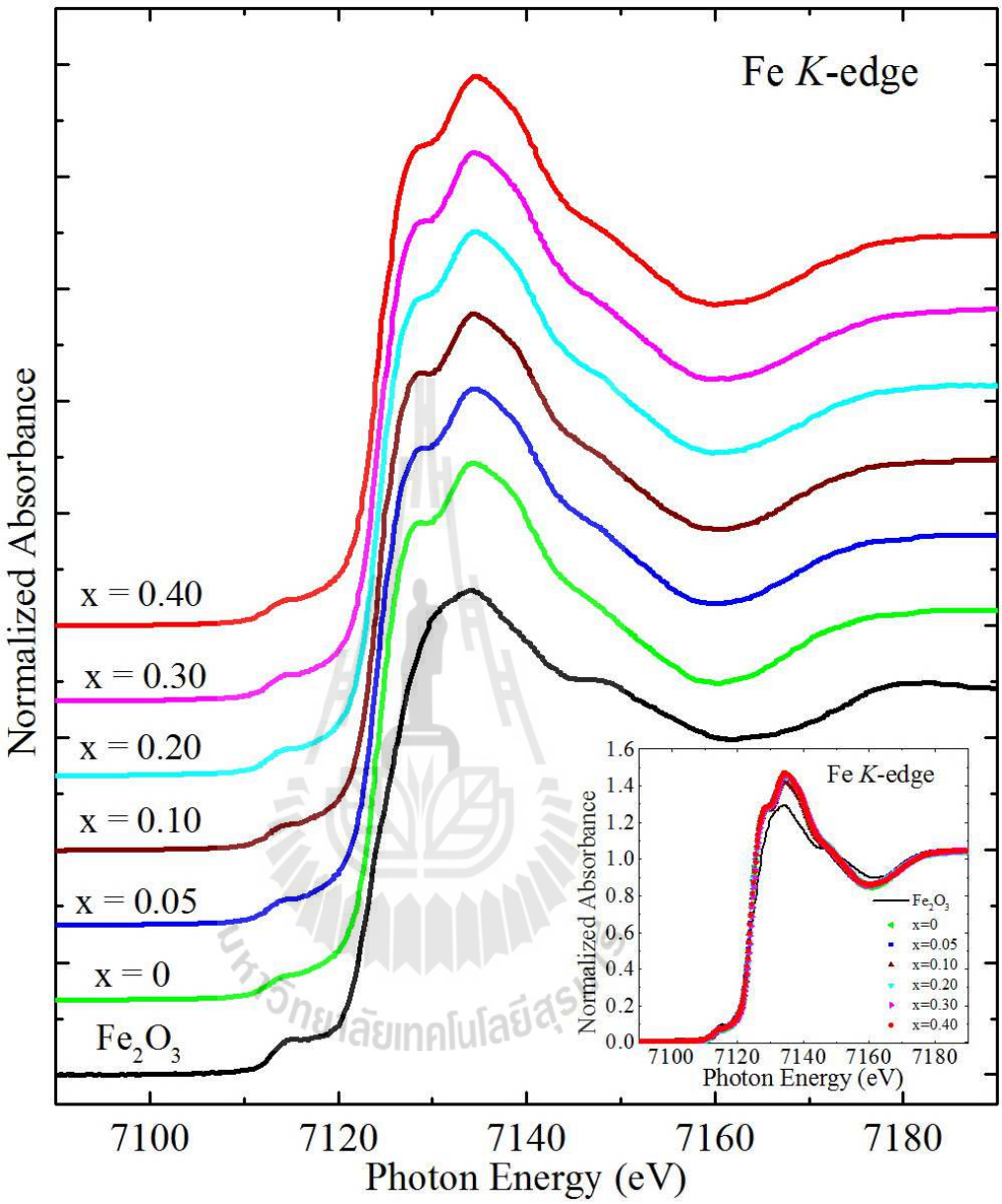

Figure 4.2 Normalized Fe *K*-edge XANES spectra of $BiFeO_3$ and Mn-doped $BiFeO_3$ ceramics with the different Mn concentrations with comparison to the Fe_2O_3 standard sample.

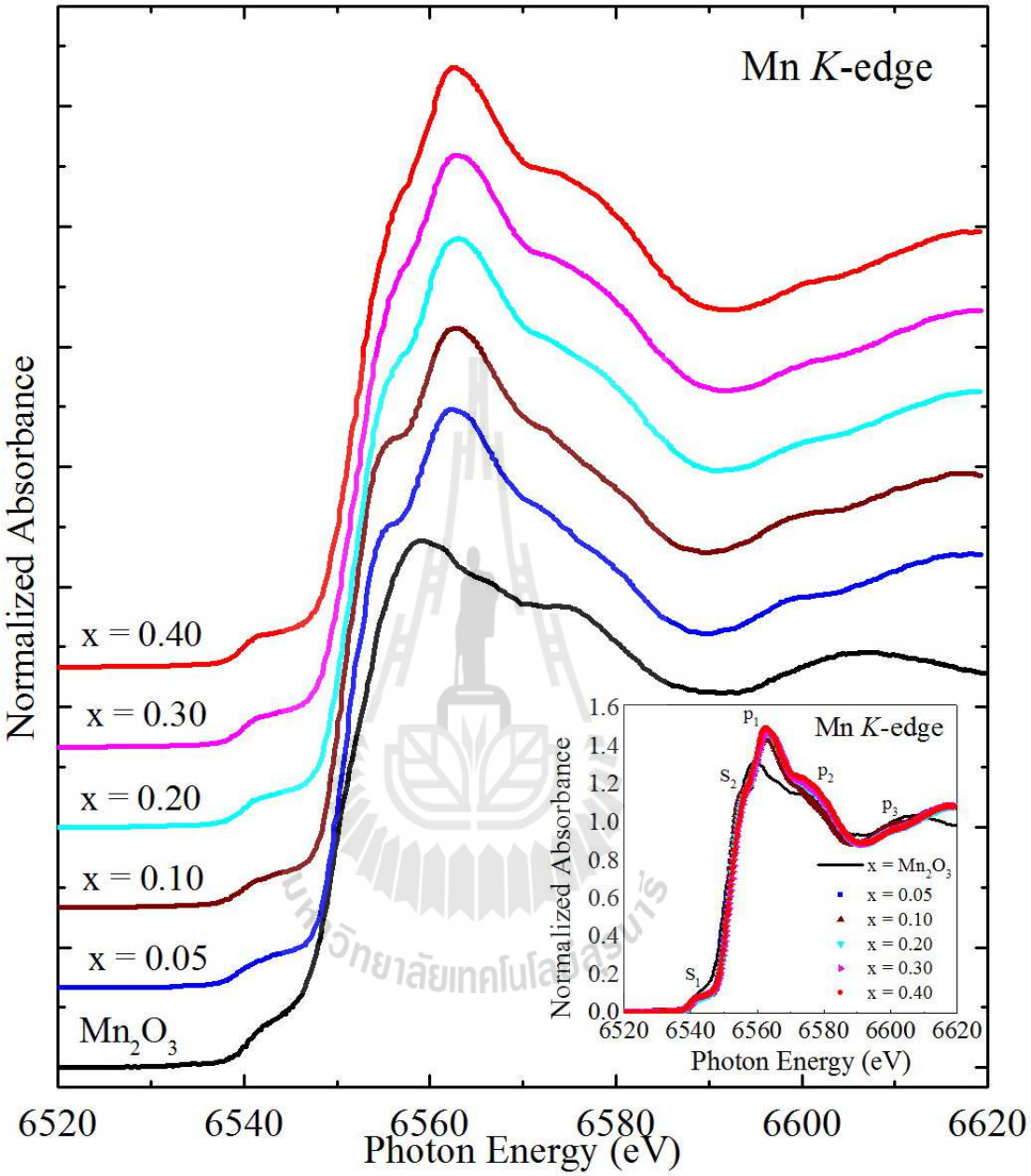

Figure 4.3 XANES spectra of Mn *K*-edge of Mn-doped $BiFeO_3$ ceramics with comparison to the Mn_2O_3 standard sample. Inset presents the broadening and increasing of p_1 , and p_2 peaks.

The features of Mn *K*-edge spectra of all the samples also look similar to those of Fe *K*-edge spectra, indicating that the local structure surrounding Mn atoms in Mn-doped BFO samples is similar to that of Fe atoms, which means Mn substituting for Fe in Mn-doped BFO samples. However, a small shift of the absorption edge to the higher energy and the broadening and increasing of p_1 and p_2 peaks can be observed when Mn concentration increases, as shown in inset of Figure 4.3. These results can be attributed to the formation of secondary phase with $Bi_2Fe_4O_9$ or $BiMn_2O_5$ structure appeared in XRD pattern of high Mn-doped BFO samples (not shown here).

To further identify the lattice location of Mn atoms in BFO structure, *ab initio* XANES calculations of Mn at several lattice locations were carried out using FEFF8.2 code (Ankudinov, 1998). This code utilizes a full multiple scattering approach based on *ab initio* overlapping muffin-tin potentials. The muffin-tin potentials used in FEFF code were obtained using self-consistent calculations with Hedin-Lundqvist exchange-correlation functions. The sphere with 5.5 Å radius (containing approximately 50-atoms) around the absorber Mn atom was used for the self-consistent calculations. The full multiple scattering calculations included all possible paths within a large cluster radius of 7.8 Å (containing approximately 150-atoms). The electronic transitions associated with the XANES measurements must follow the dipole selection rule.

In BFO perovskite structure, as shown in Figure 4.4(a), there are three probable Mn sites: Mn substituting on the Bi site (Mn_{Bi}, Figure 4.4(b)), Mn substituting on the Fe site (Mn_{Fe}, Figure 4.4(c)), and Mn interstitial (Mn_i). The crystal structure of $BiMnO_3$ and $BiMn_2O_5$ are also shown in Figure 4.4(d) and 4.4(e), respectively. In

these lattice settings, Mn_{Bi} and Mn_{Fe} are surrounded by O atoms, while Mn_i is surrounded by O and Bi atoms. The calculated XANES spectra of Mn_{Bi}, Mn_{Fe}, and Mn_i are shown in Figure 4.5. It is clear that the features of calculated Mn_{Fe} XANES spectrum match very well with those of the measured ones. On the other hand, the calculated XANES spectrum of Mn_{Bi} can be clearly ruled out and the Mn_i calculation produces some features with slight similarity to the measured XANES spectra. The results intuitively indicate the lattice location of Mn atoms at B-site (Fe) in the BFO unit cell (Mn_{Fe}).

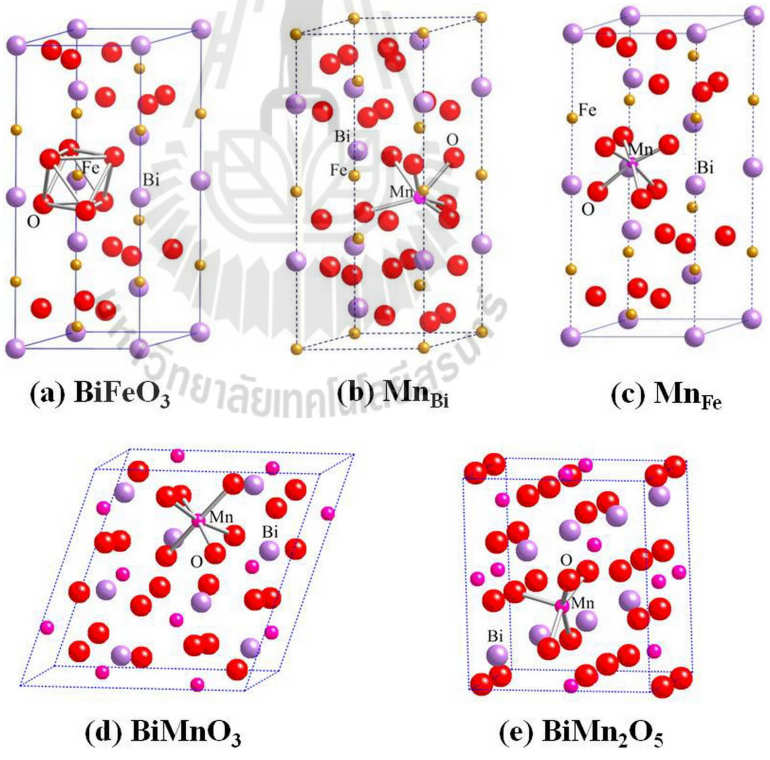

Figure 4.4 (a) Perovskite crystal structure of $BiFeO_3$. [(b)-(c)] Schematic illustrations of Mn on Fe site, Mn on Bi site, and interstitial Mn. [(d)-(e)] show the crystal structure of $BiMnO_3$ and $BiMn_2O_5$, respectively.

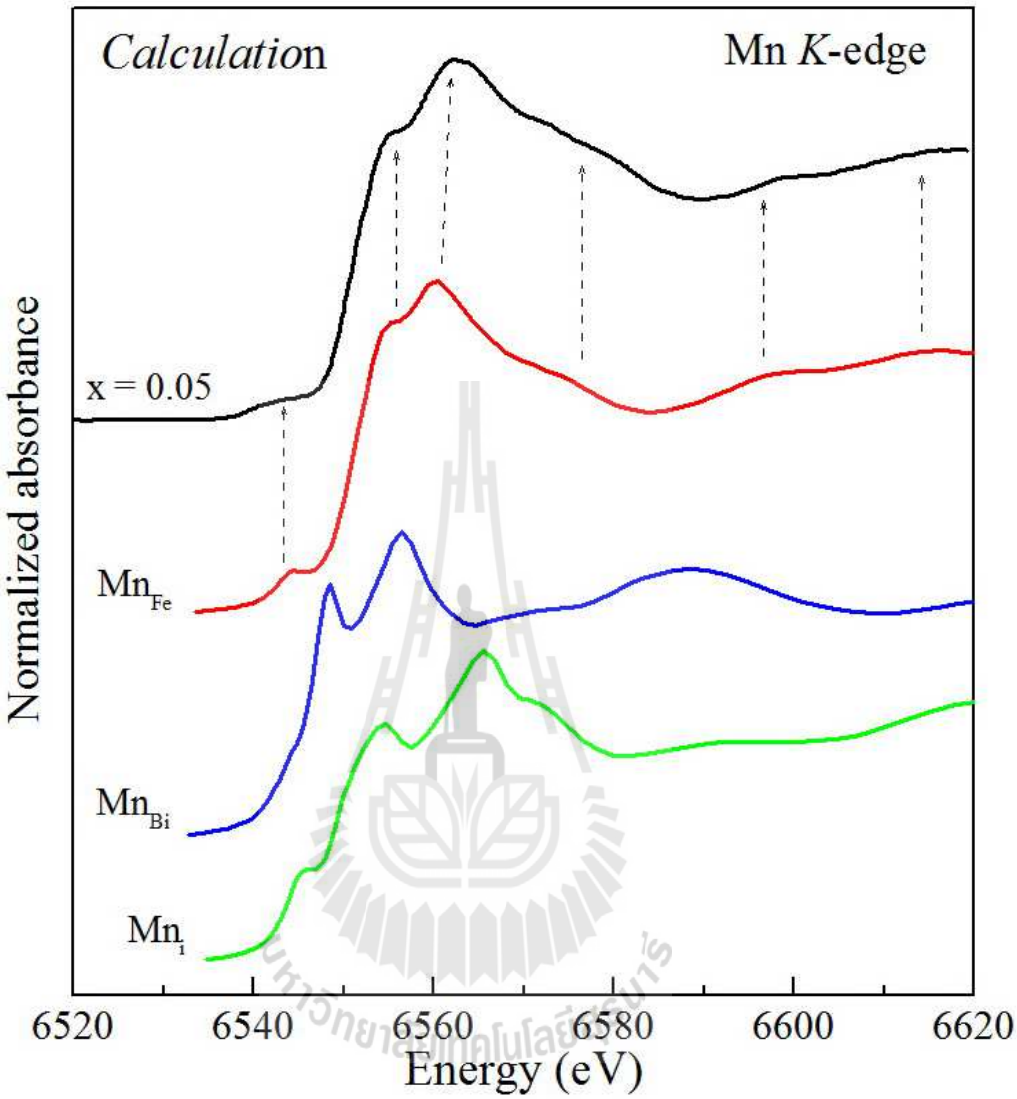

Figure 4.5 The measured Mn *K*-edge XANES spectra of Mn-doped $BiFeO_3$ ceramics compared with the calculated Mn *K*-edge XANES spectra of the different Mn lattice locations (Mn_{Fe}, Mn_{Bi} and Mn_i).

4.3.2 Determination of secondary phase in Mn-doped $BiFeO_3$

In order to clarify a small shift of the absorption edge to the higher energy and the broadening and increasing of p_1 and p_2 peaks, the Mn *K*-edge XANES spectra of pure $BiMnO_3$ and $BiMn_2O_5$ are compared qualitatively with those of Mn-doped BFO samples (as shown in Figure 4.6(a)), as these spectra were obtained by extrapolating the spectra reported by Yoneda *et al*. (Yoneda *et al*., 2012) and Shukla *et al*. (Shukla *et al*., 2008), respectively. It can be clearly observed that the spectrum of low Mn-doped BFO sample (x=0.05) certainly represents the features of pure $BiMnO_3$ XANES spectra, while the spectrum of the high Mn-doped BFO sample (x=0.40) mostly represents the features of pure $BiMn_2O_5$ XANES spectra; an indication of the secondary phase formation. To estimate the quantitative constituent of the secondary phase, the Mn *K*-edge XANES spectra of x=0.05 and x=0.40 are considered as the parent component for creating the linear combination spectra. The proportion of $BiMnO_3$ and $BiMn_2O_5$ obtained from the fits are tabulated in the Table 4.1. The fitted XANES spectra with various proportions of $BiMnO_3$ and $BiMn_2O_5$ are shown as a solid curves superimposed on top of the measured XANES spectra in Figure 4.6(a). To validate this interpretation, the *ab initio* calculation was also performed.

Table 4.1 Proportion of $BiMnO_3$ and $BiMn_2O_5$ in Mn-doped $BiFeO_3$ samples.

Sample ($BiFe_{1-x}Mn_xO_3$)	Proportion of $BiMnO_3$ (x = 0.05)	Proportion of $BiMn_2O_5$ (x = 0.40)	R-factor
x = 0.10	0.967	0.033	0.0004
x = 0.20	0.332	0.668	0.0004
x = 0.30	0.171	0.829	0.0003

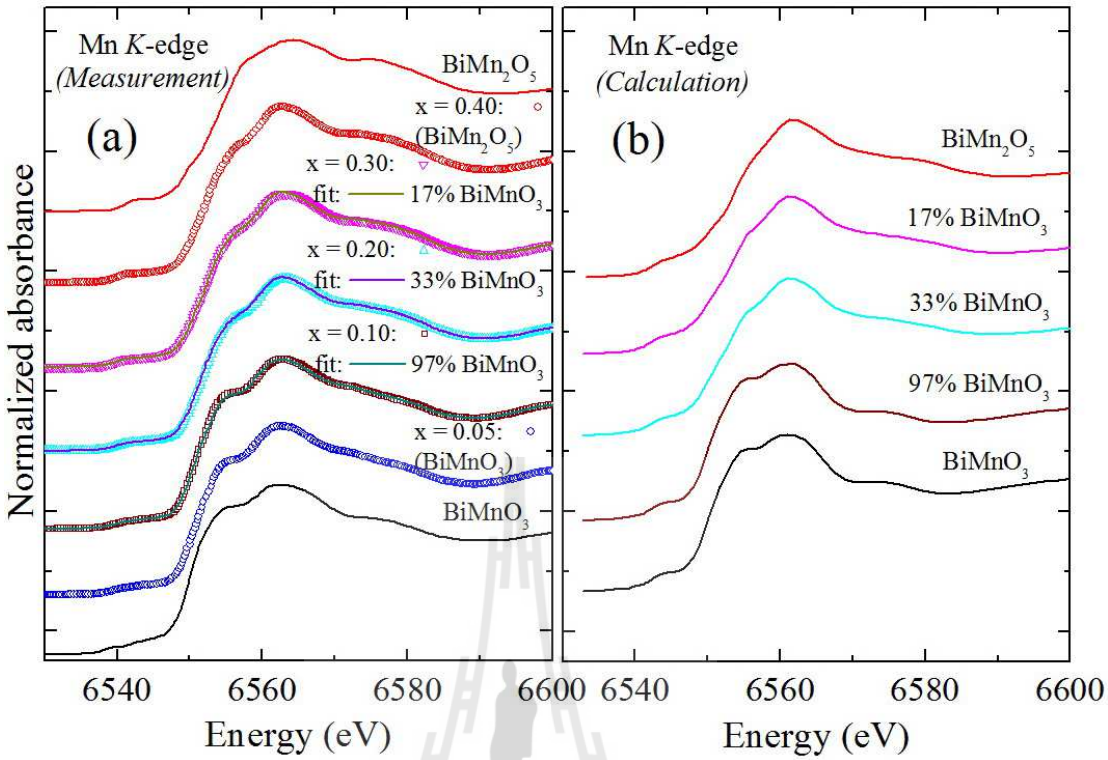

Figure 4.6 (a) Comparison of the extrapolated $BiMnO_3$ and $BiMn_2O_5$ spectra obtained from Yoneda *et al*. and Shukla *et al*., respectively, and the measured Mn K-edge XANES spectra of Mn doped BFO samples. Also included are the linear combination of Mn *K*-edge XANES spectra with various proportions of $BiMnO_3$ and $BiMn_2O_5$. (b) The calculated Mn *K*-edge XANES spectra of $BiMnO_3$ and $BiMn_2O_5$. The fitted linear combination XANES spectra are also plotted.

The FEFF 8.2 code is used to calculate the Mn *K*-edge XANES spectra of $BiMnO_3$ and $BiMn_2O_5$ for ensuring all features of extrapolated XANES spectra. Similarly, the calculated Mn *K*-edge XANES spectra with various compositions can be simulated by using the linear combination of the proportion of $BiMnO_3$ and $BiMn_2O_5$, as shown in Figure 4.6(b). More importantly, the features of the calculated

XANES spectra confirmed the accuracy of extrapolated XANES spectra and are in good agreement with the corresponding measured spectra obtained from Mn-doped BFO samples. This result supports that (1) Mn atoms certainly occupy B-site (Fe) in Mn-doped BFO samples and (2) a small shift of the absorption edge to the higher energy and the broadening and increasing of p_1 and p_2 peaks of Mn *K*-edge XANES spectra of Mn-doped BFO samples probably occur due to the increasing of the formation of $BiMn_2O_5$ as the Mn content are increased, which cannot be revealed by XRD measurement.

4.3.3 Determination of secondary phase in Co/CoO/Au multilayers

The measured Co *K*-edge XANES spectra measured for the MLs are compared with standard Co metal (foil), CoO and Co_3O_4 powders, as shown in Figure 4.7. It can be clearly seen that XANES spectra of all MLs are likely to be the superposition of the standard spectra of Co in many forms. For instance, the pre-edge peak (7715 eV) is quite similar to that of the Co metal and the highest peak (7725-7730 eV) can be the superposition of the highest peak of CoO and the peak of Co metal at around 7730 eV.

In order to determine the weighted proportion of Co_xO_y and Co layers, the linear combination analysis (LCA) are considered. By considering CoO, Co_3O_4 and Co metal as the parent components, the XANES spectra of all Co/CoO/Au MLs are fitted (lines) with a superposition of XANES profiles of the parent components using the LCA method. The fitted was performed using the package ATHENA (Ravel and Newville, 2005) with the LCA tool. The best fits are shown in Figure 4.8(a) together with the measured XANES spectra (solid symbols). In this way, the weighted proportions of Co_xO_y and Co layers can be estimated as shown in Table 4.2.

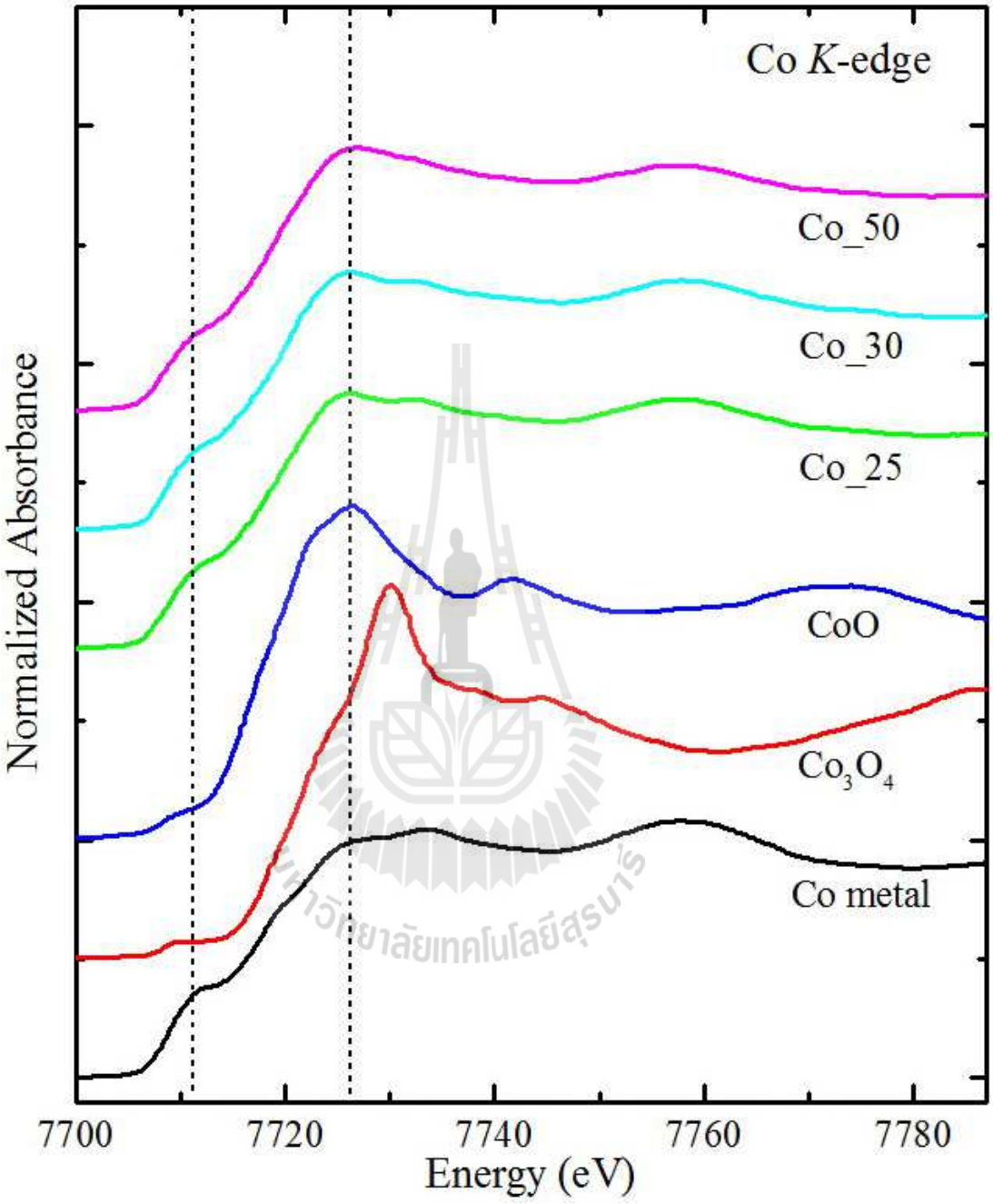

Figure 4.7 Normalized Co *K*-edge XANES spectra of the Co MLs with the different Au layer thickness with comparison to the Co metal, Co_3O_4, and CoO standard samples.

Table 4.2 Proportion of Co metal, CoO and Co_3O_4 in the Co/CoO/Au MLs.

Sample	Proportion of Co metal	Proportion of CoO	Proportion of Co_3O_4	R-factor
Co_25	0.793	0.192	0.015	0.00019
Co_30	0.771	0.212	0.017	0.00025
Co_50	0.738	0.224	0.038	0.00013

Furthermore, to examine the weighted proportions of Co_xO_y and Co metal forms in the Co MLs, the calculated XANES spectra of the Co metal, Co_3O_4 and CoO were performed using FEFF 8.2 code which is based on ab initio multiple scattering calculation (Ankudinov *et al*., 1998). The calculated spectra are shown in Figure 4.8(b). For Co metal (hexagonal), $a = 2.5074$ Å and $c = 4.0699$ Å are used as the lattice parameters, whereas $a = 4.2667$ Å is used for the lattice constant of CoO (rocksalt) structure. For Co(CoO) metal, a cluster of 40(57) atoms [radius of 4.5(5.0) Å] is used to calculate the self-consistent field muffin-tin atomic potentials within the Hedin-Lundqvist exchange potential and a 80-atom cluster with a radius of 6.0 Å is used for full multiple scattering calculations. They include possible paths within a larger cluster radius of 7.0 Å (147 atoms).

The proportions of each of the constituents are varied for generating the calculated (an initio) spectra according to the R-factor obtained from the proportional fits and compare them with measured XANES spectra. One can easily see that the calculated XANES spectra are in very good agreement with the corresponding features in the measured spectra of the MLs in both energy positions and shapes. This confirms the presence of multiple constituents in the MLs from *ab initio* calculations.

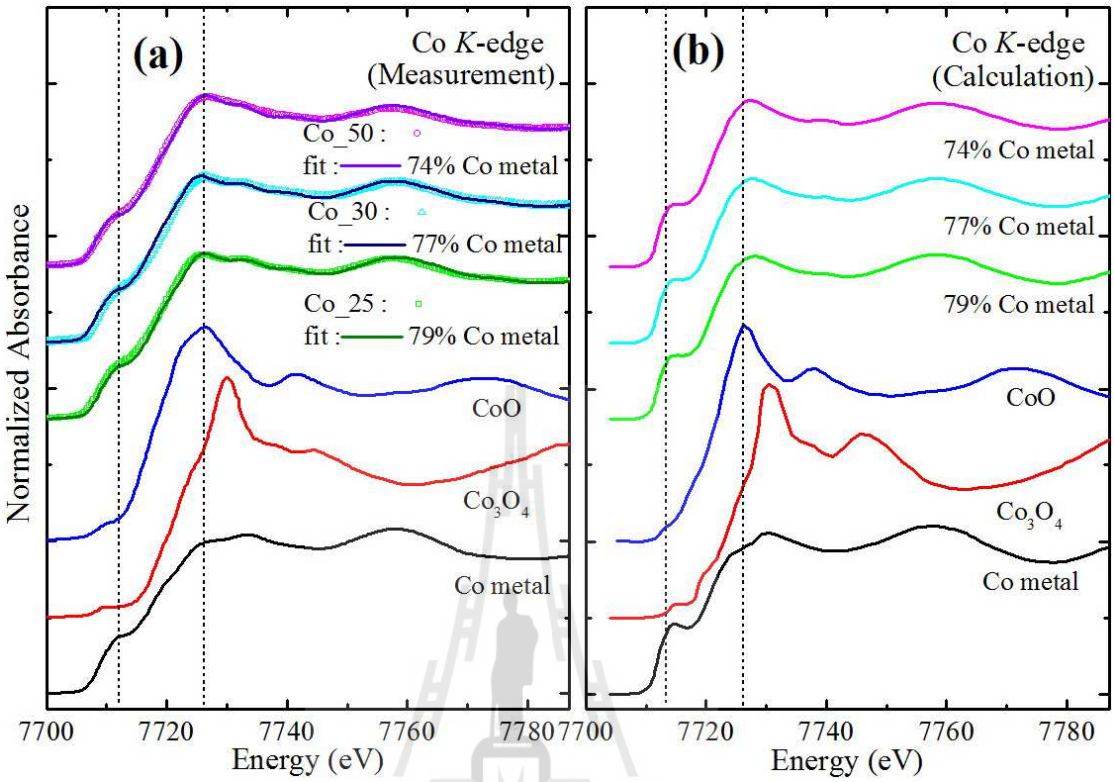

Figure 4.8 (a) Comparison of the measured Co *K*-edge normalized XANES spectra of the Co/CoO MLs (open symbols) and their fits (lines) using the LCA method. Also included are the reference spectra for CoO, Co_3O_4 and Co metal. (b) The *ab initio* calculated XANES spectra for the reference materials are generated using the FEFF 8.2 code. A weighted proportion of the species, with various proportions of Co metal, Co_3O_4, and CoO as obtained from the fits are used to calculate the ML spectra, is also plotted.

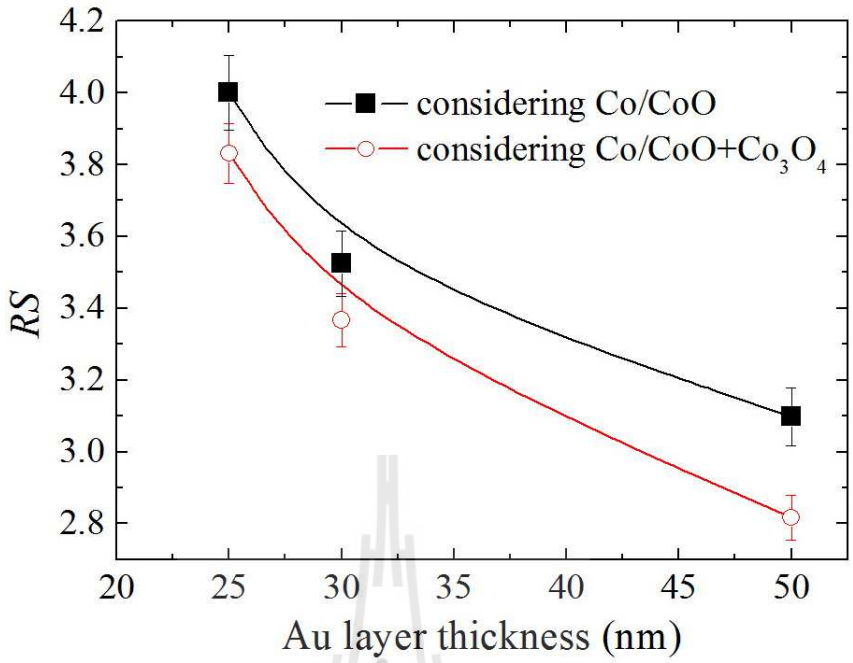

Figure 4.9 The ratio RS from the Co *K*-edge spectra obtained from two possible scenarios for the AF layer (i) with CoO + Co_3O_4 content and (ii) only with CoO.

The ratio of signal, *RS* is determined by evaluating the ratio between the Co-signal and the CoO-or the CoO + Co_3O_4 signal as obtained from the fit. Therefore, two possible circumstances for the AF layer are considered for comparing the ratios (i) with CoO + Co_3O_4 content and (ii) only with CoO content. The plot of the ratio *RS* against the Au spacer layer thickness is shown in Figure 4.9. A better agreement with the data is obtained while considering circumstance (i). The goodness of fit parameter (R-factor) decreases by 5-30%. This indicates that the Co/CoO/Au MLs are composed of phase-separated regions that differ in the proportion of Co metal, Co_3O_4 and CoO.

From the ratio *RS* in Figure 4.9, it is interesting to note that the XANES spectra show an increasing proportion of oxide (AF) material, which is largely compensated by a decreasing proportion of Co in the Co/CoO/Au MLs. A plausible change in the

deposition pressure and temperature, with increasing deposition time (while growing thicker Au layers), might have caused an ≈4% increase the Co_3O_4 content. Co_3O_4 has an ordering temperature (T_N = 40 K) lower than CoO, which can vary depending upon the FM layer in its proximity (Gangopadhyay *et al*., 1993). Coupling of the uncompensated AF spins within the Co_3O_4 proportion may be quite different from that of within the CoO proportion, as they have different anisotropy axes. Therefore, the presence of multiple constituents with different magnetic ordering temperatures will affect the magnetization loop and an increase in the exchange bias field (Girgis *et al*., 2003).

มหาวิทยาลัยเทคโนโลยีสุรนารี

CHAPTER V

SQUID AND PNR STUDY OF RECOVERY OF THE UNTRAINED STATE IN COBALT-COBALT OXIDE EXCHANGE-COUPLED SYSTEM

5.1 SQUID measurement of Co/CoO/Au multilayer

Conventional in-plane magnetization loops are measured using a superconducting quantum interference device (SQUID) MPMS and a physical property measurement system (PPMS) from Quantum Design. All SQUID measurements were done after the sample was cooled down to 10 K from room temperature (RT) in the presence of a well defined cooling field of H_{FC} = +10.0 kOe (along the –*y* axis) provided by a cryomagnet and then it was subjected to two consecutive field cycling (first and second). After the second hysteresis loop we have completed a third hysteresis loop, which starts and ends in the direction (Ω_{RE}) away from the initial field cooling direction, before measuring the hysteresis loop along the fourth and fifth field cycles which is along the same direction as the first and second field cycles. Therefore, all measurements were along the *y* axis except for the third field cycle.

The sample was raised to room temperature and cooled again each time. We choose a different amplitude of the reorientation field H_{FC} and also along a different orientation Ω_{RE} in measuring along the third field cycle. The purpose of the third

field cycle is simply to reorient the spin configuration after the first field cooling. The orientation angles were made possible by using a precision sample rotator attached to the SQUID.

5.2 PNR measurement of Co/CoO/Au multilayer

The neutron scattering experiments were performed at the polarized neutron reflectometer (PNR) with polarization analysis AMOR in a time of flight (TOF) mode at SINQ, Paul Scherrer Institute in Switzerland. The neutron measurements were done following the very same procedure as described for measuring the SQUID data which enabled us to measure along the decreasing branch (applied field opposite to the cooling field). The different orientation angles of the sample with respect to the initial cooling field direction were made possible by using a unique precision sample rotator within the cryomagnet at the sample position of AMOR.

Figure 5.1 shows a sketch of the neutron scattering geometry together with the direction of the magnetic field during the field cycles. Here the applied field H_a along the *y* axis is shown to be antiparallel to the cooling field H_{FC}. The FM magnetization (M_{FM}) is making an angle ϕ_A with respect to the field axis. The reorientation fields are shown along different orientation Ω_{RE} in the sample plane.

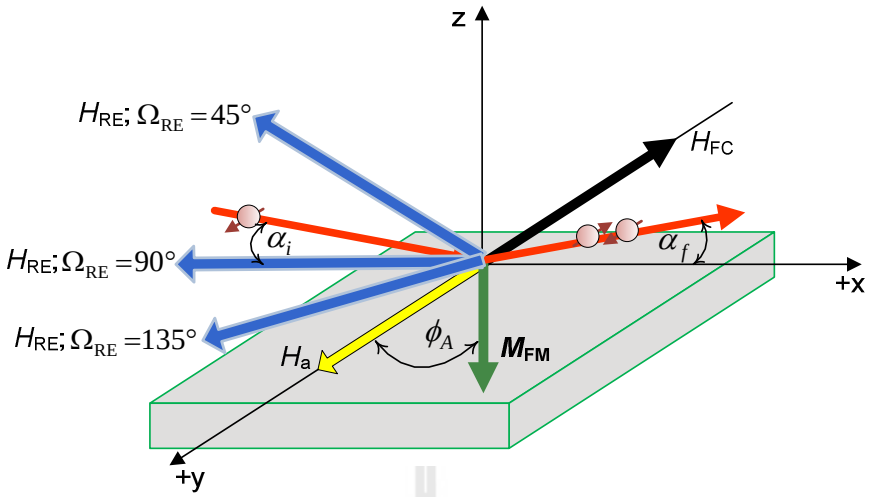

Figure 5.1 Illustration of the neutron scattering geometry. H_a along the +*y* axis is shown to be antiparallel to H_{FC}. M_{FM} is the FM magnetization making an angle ϕ_A with respect to the field axis. The reorientation field H_{RE} along the –*x* axis (for $\Omega_{RE}=90°$) is also shown along with two other orientations ($\Omega_{RE}=45°$ and $\Omega_{RE}=135°$) in the sample plane.

5.3 SQUID Analysis

Figures 5.2, 5.3 and 5.4 show SQUID hysteresis loops measured at 10 K for an in-plane cooling field. The parallel component of magnetizations $\left(M_{FM||}\right)$ were measured for different strengths of the H_{FC} values and for three different orientation angle Ω_{RE}. The usual asymmetry in the magnetization reversal during the first field cycle and the disappearance of the asymmetry during the second field cycle can be clearly seen. We define the exchange bias shift $H_{EB}=\left(H_{C1}+H_{C2}\right)/2$, where H_{C1} and H_{C2} are the coercive fields on the decreasing and increasing branches of the hysteresis loop. Thus, the exchange bias field along the cooling field axis is

approximated to be around -630 Oe and -430 Oe for the first and second field cycles, respectively. This decrease in the bias field is owing to normally observed training. The first hysteresis loop reveals a kink around -1500 Oe along the decreasing branch and at around +100 Oe along the increasing branch. These are typical indications of different oxidation levels in the CoO layers in the stack. Such a variation of oxidation affects the exchange coupling that result in a decrease in the switching fields along the respective branches (Paul *et al*., 2013).

After the first two field cycles, the third hysteresis loop shows the magnetization for different values of H_{RE} while completing a field cycle along Ω_{RE} = 45°, 90°, and 135° in Figure 5.2, 5.3, and 5.4, respectively. At Ω_{RE} = 135° the magnetization goes negative for H_{RE} = 0.5 kOe since it changes its direction. After each third field-cycling process, it was followed by two other consecutive hysteresis loop measurements along the fourth and fifth field cycles, respectively. By comparing the coercive fields of the second and fourth field cycles, one can find that there is indeed a reinduction of the unstrained state. However, during the fifth field cycle the revival is completely lost. The degree of reinduction certainly varies with the strength of the H_{RE} values and with the orientation angle Ω_{RE}.

To further analyze the SQUID data, we have plotted the derivative of the magnetization $\chi_{mag} = dM / dH_a$ as a function of field corresponding to the different loops as shown in Figure 5.5 for H_{RE} = 0.5 kOe , as an example. The two peaks on either branch of the hysteresis loops indicate multiple switching fields. We ignore the smaller peak and concentrate on the main peaks A1 and A2 on the decreasing and the increasing branch, respectively, which represents most of the magnetization (from majority of the layers) within the layer stack.

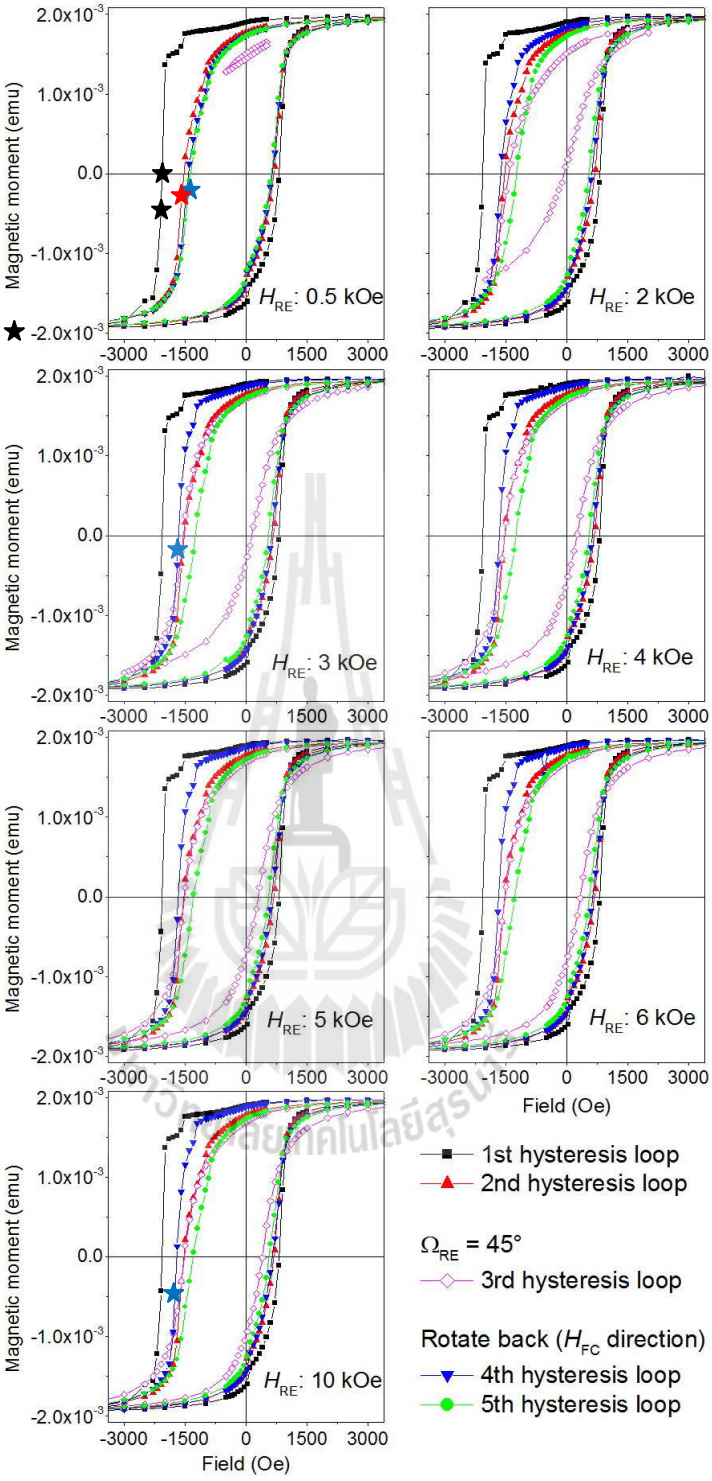

Figure 5.2 SQUID magnetization hysteresis loops for different field cycles measured at 10 K and for various reorientation fields H_{RE} along Ω_{RE} = 45° in the sample plane. The stars mark the applied field values H_a for the neutron measurement along the respective branch of the loops.

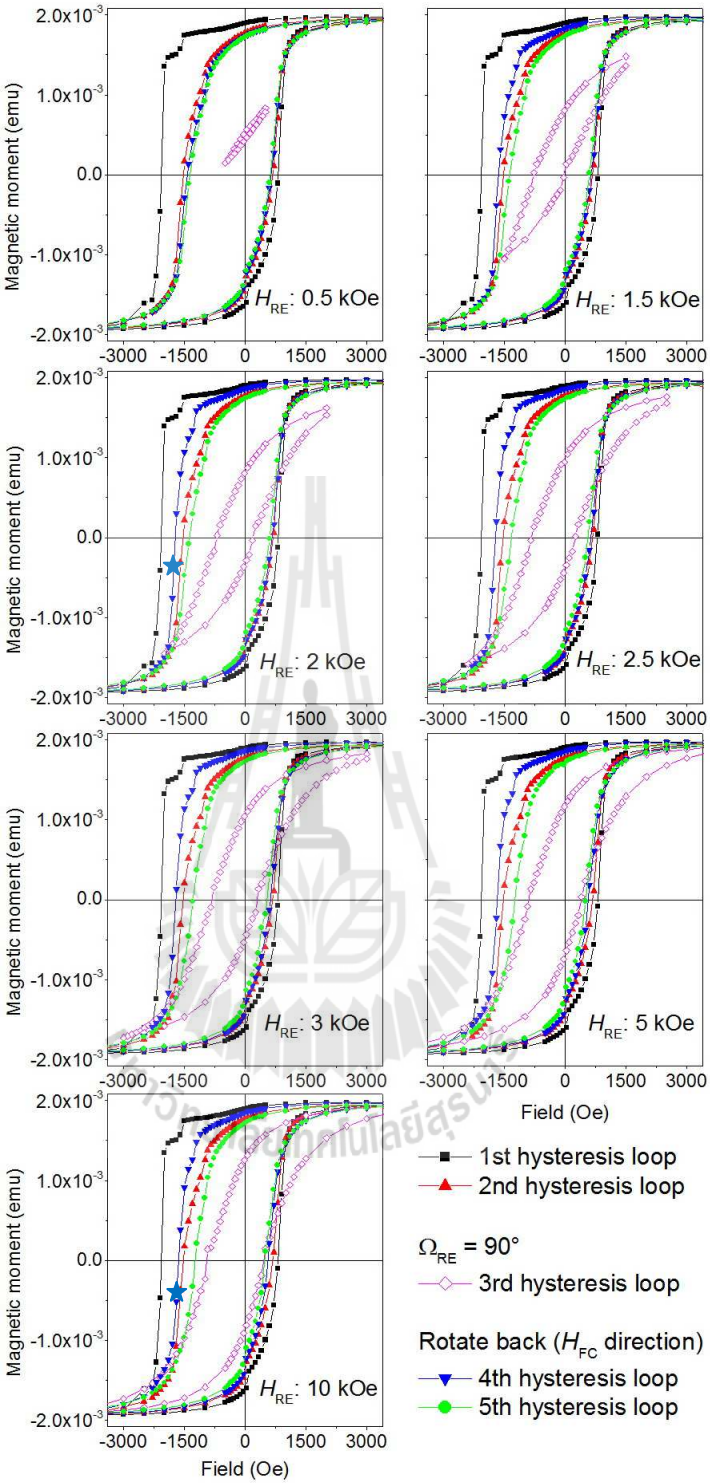

Figure 5.3 SQUID magnetization hysteresis loops for different field cycles measured at 10 K and for various reorientation fields H_{RE} along Ω_{RE} = 90° in the sample plane. The stars mark the applied field values H_a for the neutron measurement along the respective branch of the loops.

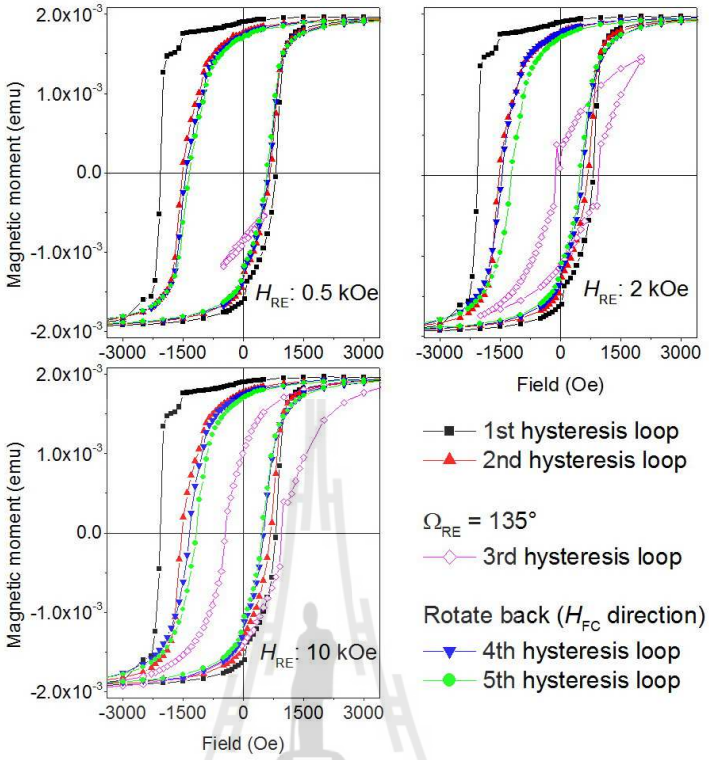

Figure 5.4 SQUID magnetization hysteresis loops for different field cycles measured at 10 K and for various reorientation fields H_{RE} along Ω_{RE} = 135° in the sample plane.

In order to quantify the degree of reinduction of the untrained state, we have taken the following path. Firstly, we calculate the integrated areas under each peak from a Gaussian fit to each and every peak A1 and A2 for each field cycle shown in Figure 5.5 Secondly, we approximate the degree of asymmetry by defining a parameter X1 for the first hysteresis loop as X1 = $Hys1_{A1}/Hys1_{A2}$. A similar procedure was selected for the second, fourth, and fifth hysteresis loops as we estimate X2 = $Hys2_{A1}/Hys2_{A2}$, X4 = $Hys4_{A1}/Hys4_{A2}$, and X5 = $Hys5_{A1}/Hys5_{A2}$. Here $Hys1_{A1,A2}$, $Hys2_{A1,A2}$, $Hys4_{A1,A2}$, and $Hys5_{A1,A2}$ are the integrated areas under the

peaks corresponding to the derivatives of the first, second, fourth and fifth hysteresis loops, respectively, as shown in Table 5.1, 5.2 and 5.3 for various fields H_{RE} for Ω_{RE} = 45°, 90° and 135°, respectively. Finally, we defined the ratio of the integrated areas under each peak as C12 = X1/X2, C14 = X1/X4, and C15 = X1/X5, and are tabulated along with the parameter X*n* (n = 1, 2, 4, 5) in Table 5.4, 5.5 and 5.6 for various fields H_{RE} for Ω_{RE} = 45°, 90° and 135°, respectively.

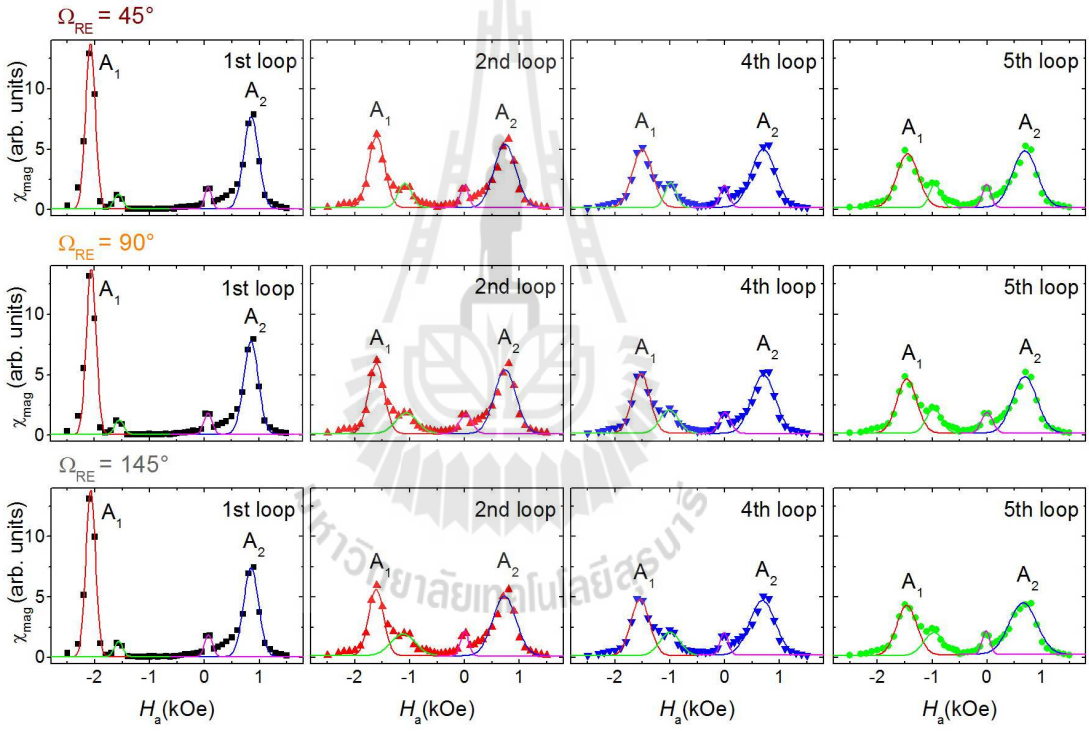

Figure 5.5 The field derivative of magnetization χ_{mag} as a function of field measured at a reorientation field H_{RE} = 0.5 kOe and along different Ω_{RE} in the sample plane. The Gaussian fits to the peaks are in lines.

Table 5.1 The integrated areas under the main peaks A1 (decreasing branch) and A2 (increasing branch) corresponding to the derivatives of the first, second, fourth and fifth hysteresis loops for various fields H_{RE} for Ω_{RE} = 45°.

H_{RE} (kOe)	$Hys1_{A1}$	$Hys1_{A2}$	$Hys2_{A1}$	$Hys2_{A2}$	$Hys4_{A1}$	$Hys4_{A2}$	$Hys5_{A1}$	$Hys5_{A2}$
0.5	210.87	318.89	315.58	460.95	389.30	518.32	407.54	504.85
2	212.48	315.43	333.25	452.53	333.43	563.05	755.51	589.92
3	207.69	318.36	357.27	482.00	291.04	544.78	796.48	584.18
4	212.46	316.58	349.33	467.57	305.34	550.77	809.28	591.47
5	213.00	313.58	347.25	460.04	308.70	555.57	771.18	597.11
6	212.91	315.78	348.32	460.24	300.77	561.67	800.85	609.33
10	211.64	310.36	324.25	463.99	284.85	572.20	732.66	638.40

Table 5.2 The integrated areas under the main peaks A1 (decreasing branch) and A2 (increasing branch) corresponding to the derivatives of the first, second, fourth and fifth hysteresis loops for various fields H_{RE} for Ω_{RE} = 90°.

H_{RE} (kOe)	$Hys1_{A1}$	$Hys1_{A2}$	$Hys2_{A1}$	$Hys2_{A2}$	$Hys4_{A1}$	$Hys4_{A2}$	$Hys5_{A1}$	$Hys5_{A2}$
0.5	207.35	317.54	316.25	469.22	382.80	509.72	426.61	515.91
1	211.16	311.29	323.18	465.69	321.83	503.83	413.86	527.75
1.5	205.97	330.01	339.06	474.12	299.93	523.28	487.33	558.19
2	212.48	316.54	321.47	452.66	272.90	514.73	462.94	559.42
2.5	210.36	339.97	320.36	456.12	300.25	549.32	584.12	572.97
3	211.26	316.29	359.62	467.09	333.96	548.60	511.12	602.53
5	207.76	318.92	319.52	472.64	303.03	537.43	474.31	563.62
10	207.68	316.18	312.38	475.45	302.38	516.74	496.31	575.19

Table 5.3 The integrated areas under the main peaks A1 (decreasing branch) and A2 (increasing branch) corresponding to the derivatives of the first, second, fourth and fifth hysteresis loops for various fields H_{RE} for Ω_{RE} = 135°.

H_{RE} (kOe)	$Hys1_{A1}$	$Hys1_{A2}$	$Hys2_{A1}$	$Hys2_{A2}$	$Hys4_{A1}$	$Hys4_{A2}$	$Hys5_{A1}$	$Hys5_{A2}$
0.5	205.76	321.47	321.99	504.34	401.00	554.07	449.32	582.90
2	208.86	314.75	308.34	465.30	546.37	544.18	699.26	596.25
10	210.08	324.43	319.57	478.43	623.48	515.11	724.54	525.23

Table 5.4 The ratio of integrated areas under the main peaks A1 (decreasing branch) and A2 (increasing branch) corresponding to the derivatives of the first, second, fourth and fifth hysteresis loops for various fields H_{RE} for Ω_{RE} = 45°.

H_{RE} (kOe)	X1	X2	X4	X5	C12	C14	C15
0.5	0.6613	0.6846	0.7511	0.8072	0.9659	0.8804	0.8192
2	0.6736	0.7364	0.5922	1.2807	0.9148	1.1376	0.5260
3	0.6524	0.7412	0.5342	1.3634	0.8801	1.2211	0.4785
4	0.6711	0.7471	0.5544	1.3683	0.8983	1.2106	0.4905
5	0.6792	0.7548	0.5556	1.2915	0.8999	1.2224	0.5259
6	0.6742	0.7568	0.5355	1.3143	0.8909	1.2591	0.5130
10	0.6819	0.6988	0.4978	1.1477	0.9758	1.3698	0.5942

Table 5.5 The ratio of integrated areas under the main peaks A1 (decreasing branch) and A2 (increasing branch) corresponding to the derivatives of the first, second, fourth and fifth hysteresis loops for various fields H_{RE} for Ω_{RE} = 90°.

H_{RE} (kOe)	X1	X2	X4	X5	C12	C14	C15
0.5	0.6530	0.6740	0.7510	0.8269	0.9689	0.8695	0.7897
1	0.6784	0.6940	0.6388	0.7842	0.9775	1.0620	0.8650
1.5	0.6241	0.7151	0.5732	0.8731	0.8728	1.0889	0.7149
2	0.6712	0.7102	0.5302	0.8275	0.9452	1.2661	0.8111
2.5	0.6188	0.7024	0.5466	1.0195	0.8810	1.1321	0.6070
3	0.6679	0.7699	0.6088	0.8483	0.8675	1.0972	0.7874
5	0.6515	0.6760	0.5638	0.8416	0.9637	1.1554	0.7741
10	0.6569	0.6570	0.5852	0.8629	0.9997	1.1225	0.7613

Table 5.6 The ratio of integrated areas under the main peaks A1 (decreasing branch) and A2 (increasing branch) corresponding to the derivatives of the first, second, fourth and fifth hysteresis loops for various fields H_{RE} for Ω_{RE} = 135°.

H_{RE} (kOe)	X1	X2	X4	X5	C12	C14	C15
0.5	0.6401	0.6384	0.7237	0.7708	1.0026	0.8844	0.8303
2	0.6636	0.6627	1.0040	1.1728	1.0014	0.6609	0.5658
10	0.6476	0.6680	1.2104	1.3795	0.9695	0.5350	0.4694

Finally, we plot in Figure 5.6 the ratio of the integrated areas under each peak for different strengths of the H_{RE} values and for three different orientation angle Ω_{RE}. Thus C12 (up-triangles) lies close to unity and defines the initial degree of training with respect to the state where H_{RE} = 0 Oe and Ω_{RE} = 0°. This is compared with the case every time we heat the ML sample up to room temperature and cool down again to 10 K in H_{FC} = +10 kOe as we set for a different value of H_{RE} and Ω_{RE}. The slight variation of C12 from unity with increasing H_{RE} redefines the initial trained state.

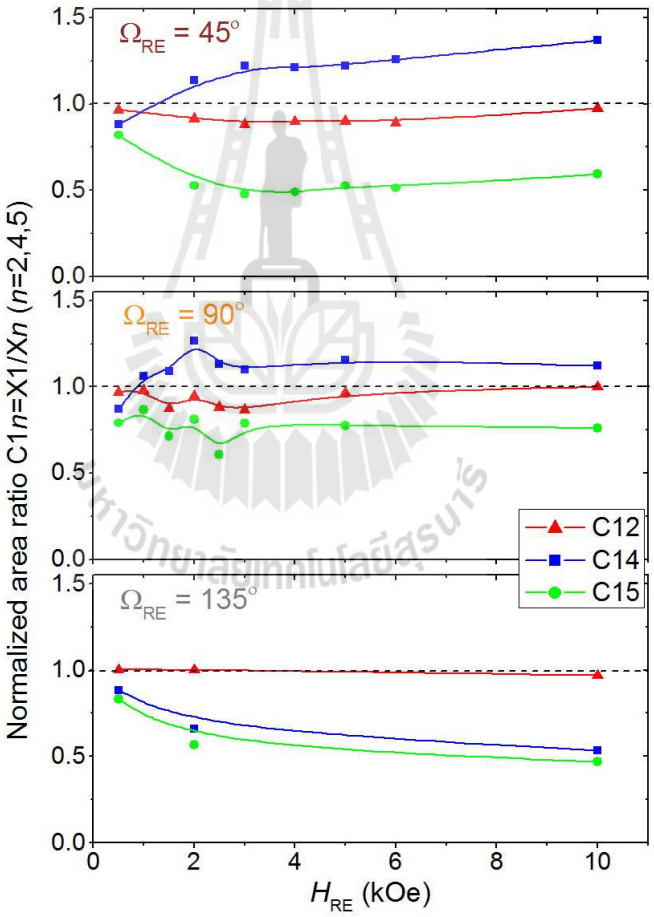

Figure 5.6 The normalized integrated area ratios C1n = X1/X*n* (*n* = 2,4,5) with respect to the initial training for various reorientation field H_{RE} and along different orientations Ω_{RE} in the sample plane. Here *n* is the number of loop cycle. The symbol sizes are typical of their error bars.

Here some specific cases are considered and discussed. It may be noted that C14 seems clearly higher than C12, C15 is always lower. This is true for Ω_{RE} = 45° and Ω_{RE} = 90° and for all H_{RE} with an exception for H_{RE} = 0.5 kOe, where C14 is also lower. On the other hand, for Ω_{RE} = 135°, C14 and C15 are always lower than C12. Following these plots one can deduce on the fact that a reinduction of the training has plausibly occurred where C14 is higher than C12. The plot of C15 indicates that the reinduction of training is ultimately lost after such a revival.

To drive the point on the degree of reinduction/recovery further, we summarize our finding in Figure 5.7 where we plot the ratio of the normalized integrated areas C14 with respect to C12 for the three Ω_{RE} values. These ratio (C14/C12) reveal that the reinduction is most efficient (~42%) for Ω_{RE} = 45° and attains a fairly constant value after H_{RE} = 3.0 kOe. For Ω_{RE} = 90°, one can see that a maximum of the reinduction is reached around H_{RE} = 2.0 kOe. Note that this is very similar to the value reported by Brems et al. as well for the Ω_{RE} = 90° case. Furthermore, it agrees with their observation that the amplitude of reorientation $(\perp)$ field needs to be sufficiently large (~1.9 kOe) in order to realize a maximum in reinduction (Brems *et al.*, 2013). Interestingly, unlike that in the Ω_{RE} = 45° case, here we find a decrease (from 35% to 10%) in the reinduction for any further increase in H_{RE}. However, in the case when Ω_{RE} = 135° there is no indication of reinduction.

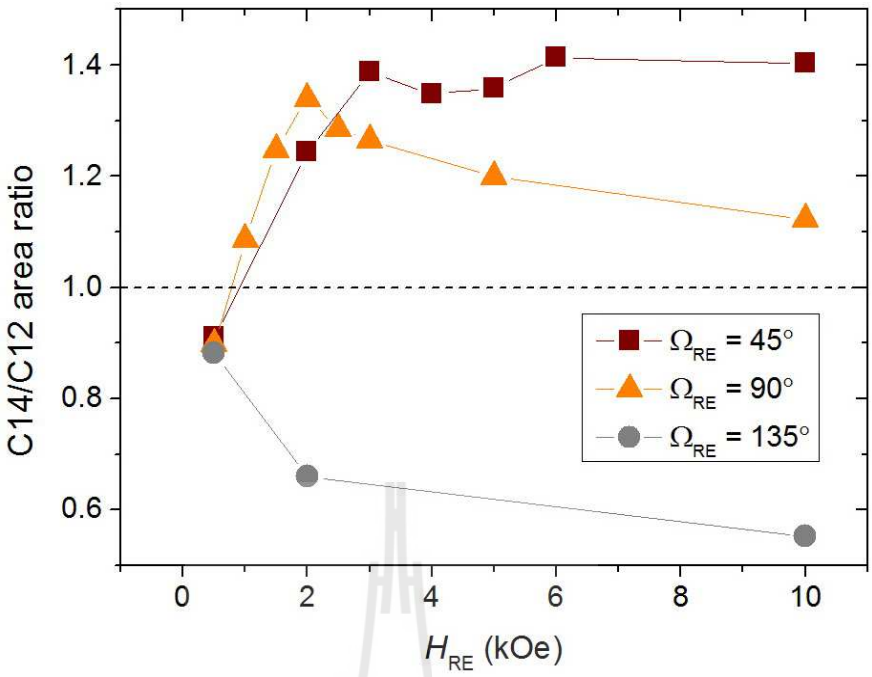

Figure 5.7 The ratio of normalized integrated area corresponding to the fourth field cycle with respect to the trained state during the second field cycle (C14/C12) for various reorientation field H_{RE} and along different Ω_{RE} in the sample plane. The symbol sizes are typical of their error bars.

5.4 PNR Analysis

5.4.1 First and second field cycles

Figure 5.8 shows the specular NSF and SF scattering signals measured at 10 K after the system has been cooled down in the presence of H_{FC} = +10.0 kOe. The data display at least four orders of magnitude drop in intensity at Q_z = 0.11 Å^{-1}. We first concentrate on the data that was measured at a saturation field of H_a = -10.0 kOe [Figure 5.8(c)] during the first field cycle. The black star markers in Figure 5.2 show the field measurement. We do not expect any SF signal to be present in the data which were measured at saturation. Thus, the intensities in the SF channel are from the small

contribution of the NSF intensities which appears in the SF channels due to nonideal efficiencies of the polarizer and analyzer which amounts to polarization efficiency factor $P \approx 94\%$.

The layer thickness, nuclear ρ_n and magnetic ρ_m scattering length density (SLD) can be obtained by fitting the saturation data. For Co layers in the stack, we get the information on $\rho_n \approx 3.0\times10^{-6}$ Å^{-2} and $\rho_m \approx 3.0\times10^{-6}$ Å^{-2}. For Au and CoO layers, $\rho_n \approx 4.5\times10^{-6}$ Å^{-2} was obtained. The thicknesses and the SLD values of the individual layers in the multilayer are found to be close to their nominal values and they are tabulated along with the nuclear and magnetic SLDs in the Table 5.7. Note that since $R_{--} > R_{++}$ (as H_a is negative), we expect a complete alignment of the Co moments along the field direction at -10 kOe. This means that $\phi_A = 0°$.

Next, we examine the data measured at a coercive file of H_a = -2.0 kOe [Figure 5.8(a)] and H_a = -2.07 kOe [Figure 5.8(b)] during the first field cycle (marker by the blue stars in Figure 5.2). The fit to the data set reveal that the magnetization reversal is via domain wall and/or nucleation (DW) process. The identification of the reversal process via DW or rotational reversal from the SF was demonstrated more than a decade earlier (Gierlings *et al.*, 2002). Here in our model we have considered eight of the Co layers to have flipped ($\phi_A = 0°$) along the field direction while the other eight layers have not ($\phi_A = 180°$). However, due to the fact that the net magnetization in the system at this field is close to zero ($R_{++} \approx R_{--}$ since $\bar{M}_{\mathbf{FM}} = 0$) it is not possible to determine the preferential directional sense of M_{FM} the with respect to the H_{FC} direction.

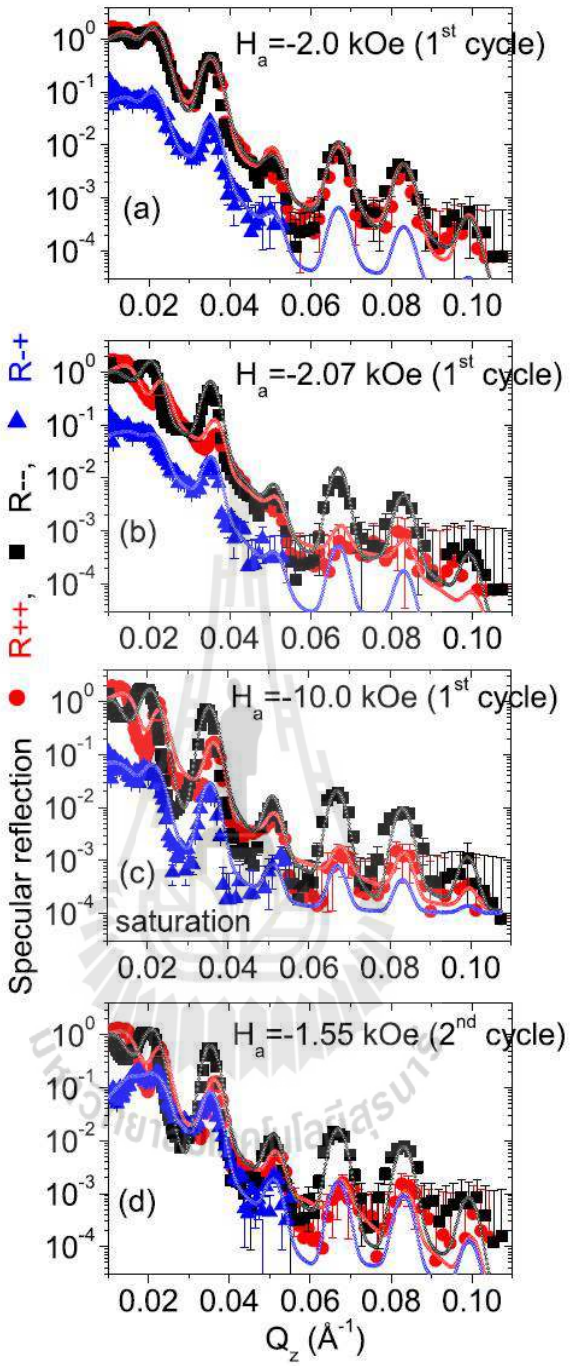

Figure 5.8 Specular reflectivity patterns (solid symbols) along with their best fits (open symbols) as a function of Q_z for the NSF [R_{--} (square) R_{++} (circle)] and SF [R_{-+} (triangle)] channels measured at (a) close to the coercive field H_a = -2.0 kOe, (b) a slightly higher field H_a = -2.0 kOe, (c) a saturation field H_a = -10.0 kOe during the first field cycles, and (d) at H_a = -1.55 kOe during the second field cycle.

Table 5.7 Fit parameters extracted from the PNR results at saturation. Here ρ_n and ρ_m designate the nuclear and magnetic scattering length densities, respectively.

Multilayer	Au	CoO	Co	Error
Thickness (nm)	20.0	5.1	10	$\pm$ 0.2
$\rho_n \left(\times 10^{-6}\ \text{Å}^{-2}\right)$	4.5	4.5	3.0	$\pm$ 0.2
$\rho_n \left(\times 10^{-6}\ \text{Å}^{-2}\right)$	0.0	0.0	1.0	$\pm$ 0.2

When the sample is measured at a slightly higher coercive field, the directional sense of the FM layers can be clearly sensed. This is due to the imbalance in the torque on the magnetic layers that would be exerted on the layers at a field higher than the coercive field. Here at H_a = -2.07 kOe [Figure 5.8(b)], since $R_{--} > R_{++}$, it can deduce from the fit to the data that more numbers of the FM layers (14 out of 16) have flipped ($\phi_A = 0°$) towards the H_a direction while the bottommost layer ($\phi_A = 180°$) has not. The top/bottom FM layer ($\phi_A = 17°$) has a different turn angle which can be ascribed to a loosely coupled state of the FM layer. The alteration in coupling strength is due to the asymmetric sequence of the layers in the stack. The difference between the top or bottom layer upon their interchange in magnetization angle is not very clear. It may be note that the SF signals at the two measuring fields (H_a = -2.0 and -2.0 kOe) did not show significant differences owing to negligible variation in the perpendicular components of the respective layer magnetizations.

Next we examine the data measured at H_a = -1.55 kOe [Figure 5.8 (d)] during the second field cycle. The red star in Figure 5.2 shows the field of measurement. In this case, the fits to the data reveal that almost all the FM layers (14) in the stack are

undergoing a simultaneous rotational reversal process with $\phi_A = 30°$. While the topmost and the bottommost layer have slightly different turn angles ($\phi_A = 50°$) from the rest.

Figure 5.9 shows the layer switching sequences for H_a = -2.07 kOe during the first field cycle and H_a = -1.55 kOe during the second field cycle. The reversal is dominated by DM process and by the rotational reversal process, respectively. The rotational senses of M_{FM} for all the layers are seen to be preserved. Here the rotational senses of the layers are indicated towards the H_a direction as $R_{--} > R_{++}$. One may recall that apart from a decrease in the coercive field, rotational reversal process of the layers is also a strong signature of training in Co/CoO systems where the untrained-state reversal mechanism during the first field cycle is usually via a DW reversal process.

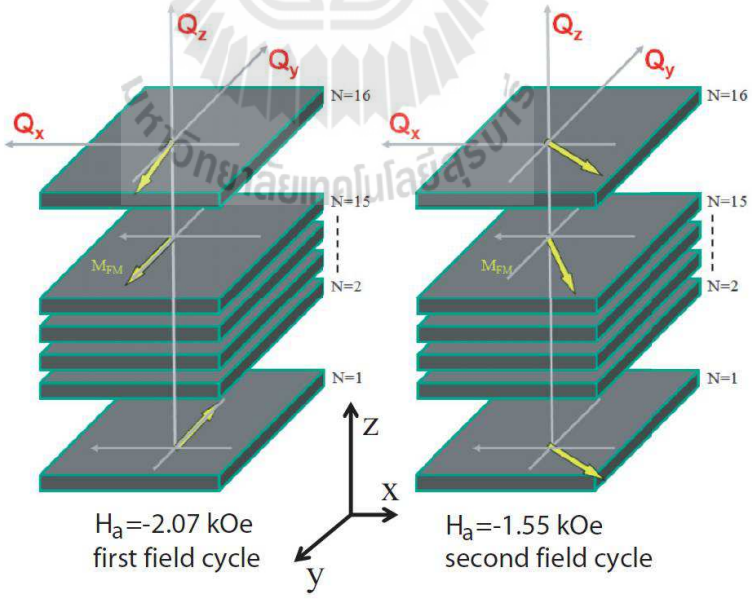

Figure 5.9 FM layers switching sequence during the first field cycle at H_a = -2.07 kOe and during the second field cycle at H_a = -1.55 kOe. The arrows indicate that the M_{FM} orientations in the respective layers. The applied field Ha is along the –*y* axis.

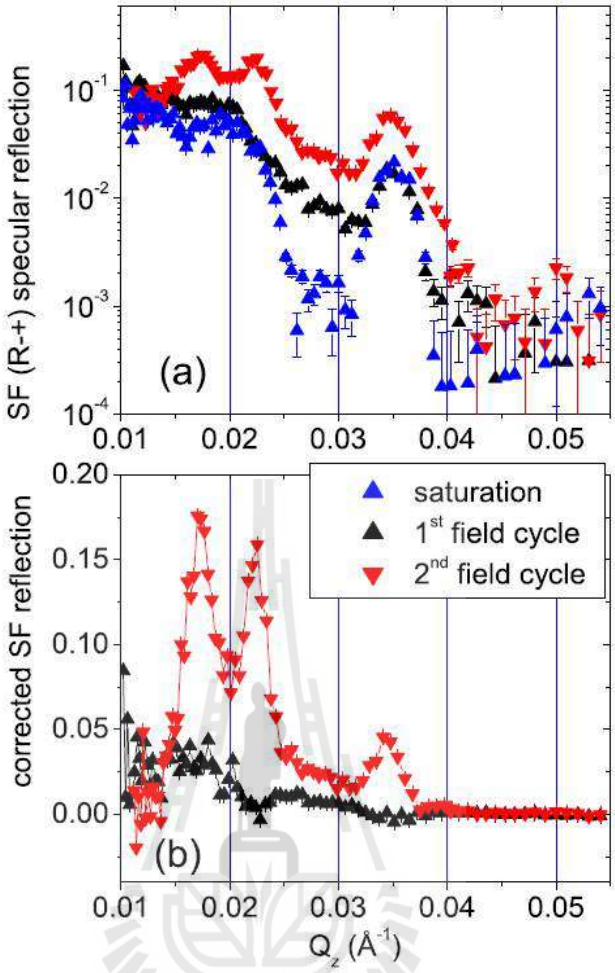

Figure 5.10 (a) SF specular reflectivity [R_{-+}] patterns as a function of Q_z measured during the first field cycle at H_a = -2.07 and -10.0 kOe and during the second field cycle at H_a = -1.55 kOe. (b) Plot of the corresponding corrected SF signals as a function of Q_z.

We compare the measured SF scattering signals (perpendicular component of M_{FM}) measured at 10 K and at a field of H_a = -2.07 and -10 kOe (at saturation) during the first field cycle and -1.55 kOe during the second field cycle, as shown in Figure 5.10(a). The corrected SF signal in Figure 5.10(b) is the subtracted-off SF signal at saturation. This can be estimated as the net SF signal assuming no SF signal to be

appeared at saturation (neutron polarization is collinear with the magnetization direction). However, the small increase in the corrected SF signal during the first field cycle, which is unexpected during a DW reversal process, is owing to some instability within one of the unflipped layer of 16 layers (Paul *et al*., 2011). During the second field cycle we find a significant increase in the corrected SF intensity. This increase is related to a rotational reversal process and therefore leads to training (Gierlings *et al*., 2002).

5.4.2 Fourth field cycle with Ω_{RE} = 45°

PNR measurements during the fourth field cycles were performed keeping Ω_{RE} = 45°. The blue star markers in Figure 5.2 show the fields of measurements. The specular NSF and SF scattering signals measured at 10 K and at H_a = -1.44, -1.67, and -1.73 kOe during the fourth field cycles are shown in Figure 5.11(a), (b) and (c), respectively. The respective H_a values were chose slightly higher than the coercive field which are corresponding to three different respective values of H_{RE} (= 0.5, 3.0, and 10.0 kOe). Notice that each time we chose to select for a different H_{RE} value during the third field cycle, we have used a different H_a value during the fourth field cycle. This was done in accordance with the measured SQUID data.

To consider H_{RE} = 0.5 kOe, the fits to the data reveal magnetization reversal via rotation of the FM magnetization majority of the layers with $\phi_A = 35°$. We also could find that almost all layers (14 out of 15 the layers) in the stack are rotating simultaneously with the exception of the top ($\phi_A = 55°$) and the bottom ($\phi_A = 65°$) layers which have different turn angles. The rotational sense of M_{FM} for all the layers are seen to be preserved since ϕ_A lies in between 0° and 180°.

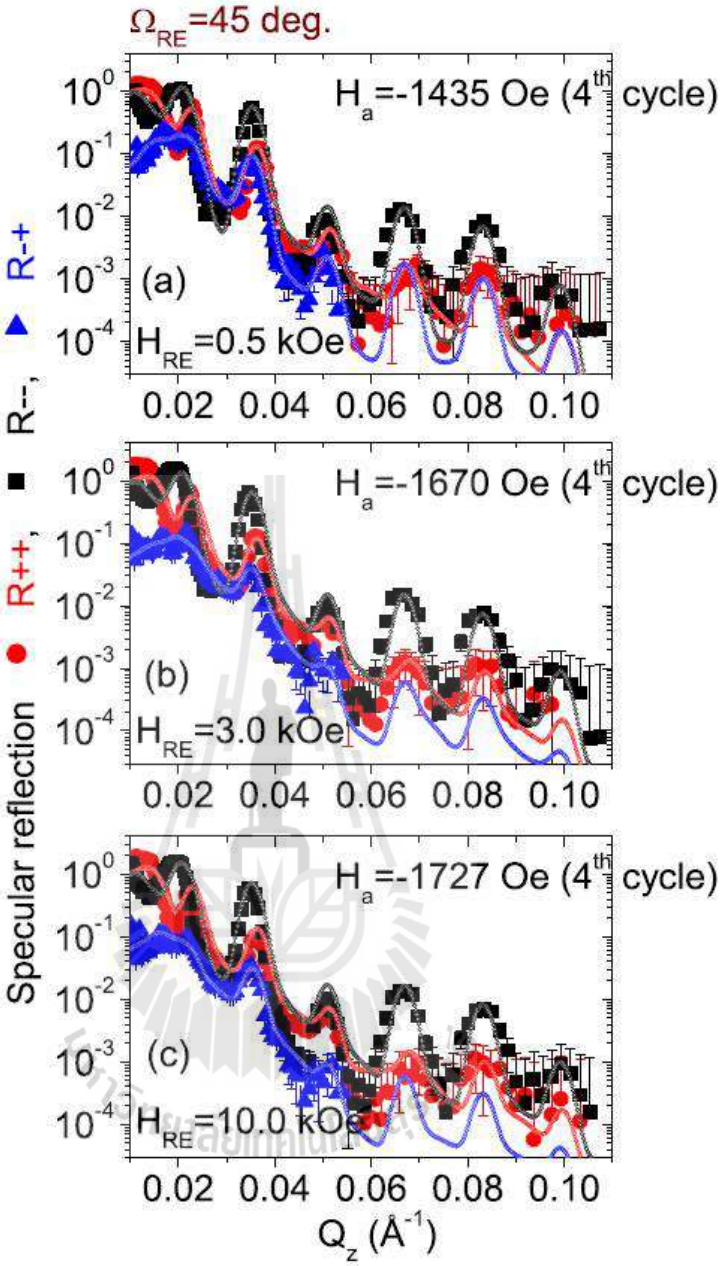

Figure 5.11 Specular reflectivity patterns (solid symbols) along with their best fits (open symbols) as a function of Q_z for the NSF [R_{--} (square) R_{++} (circle)] and SF [R_{-+} (triangle)] channels measured at (a) H_a = -1.43 kOe, (b) H_a = -1.67 kOe, and (c) H_a = -1.73 kOe during the fourth field cycle for different H_{RE} (= 0.5, 3.0 and 10.0 kOe, respectively) values when Ω_{RE} = 45°.

In the case of H_{RE} = 3.0 kOe, the fits to the data reveal magnetization reversal process of the multilayer is via both a DW (flipping) and rotational process. In this case, 12 out of 16 the layers with $\phi_A = 0°$ have flipped while the bottommost did not flip ($\phi_A = 180°$). A layer above the bottommost layer ($\phi_A = 40°$) and two layers from the top ($\phi_A = 25°$) are found to be rotating. Therefore, we have a combination of rotation and flipping, depending upon the degree of coupling of the layers.

For H_{RE} = 10.0 kOe, a distinct layer-by-layer flipping scenario are occurred. The scenario is close to the case during the first field cycle. Here, 13 out of the 16 layers have flipped ($\phi_A = 0°$), while the bottommost layer remain unflipped ($\phi_A = 180°$). The top layer has a turn angle of around $\phi_A = 25°$.

The layer switching sequences for H_a = -1.44, -1.67, and -1.73 kOe during the respective fourth field cycles is shown in the Figure 5.12. It can be seen that a gradual transition of the reversal process from being dominated by rotational reversal process followed by a mixed process of DW and rotational reversal and finally taken over by a pure DW process.

Figure 5.13(a) shows the measured SF scattering signals (perpendicular component of M_{FM}) measured at 10 K and at fields of H_a = -1.44, -1.67, and -1.73 kOe during the respective fourth field cycles compare with H_a = -10.0 kOe (at saturation) during the first field cycle. The corrected SF signals in Figure 5.13(b) is the subtracted-off SF signal at saturation. One can see that a gradual decrease in the corrected SF signals with increasing H_{RE}. The significant decrease in ϕ_A (= 0° or 180°) for a majority of the layers in the case of H_{RE} = 3.0 and 10.0 kOe as compared to that ($\phi_A = 35°$) for H_{RE} = 0.5 kOe, is mainly responsible for the decrease in the

respective corrected SF signal. It may be noted that in the case H_{RE} = 0.5 kOe, there is no flipping of the layers. Thus it cannot attribute this to reversal via a DW process. Since the rotational reversal process is a signature of training, it can readily infer that in this case there is no revival of the untrained state. This was also expected following the analysis of the SQUID data.

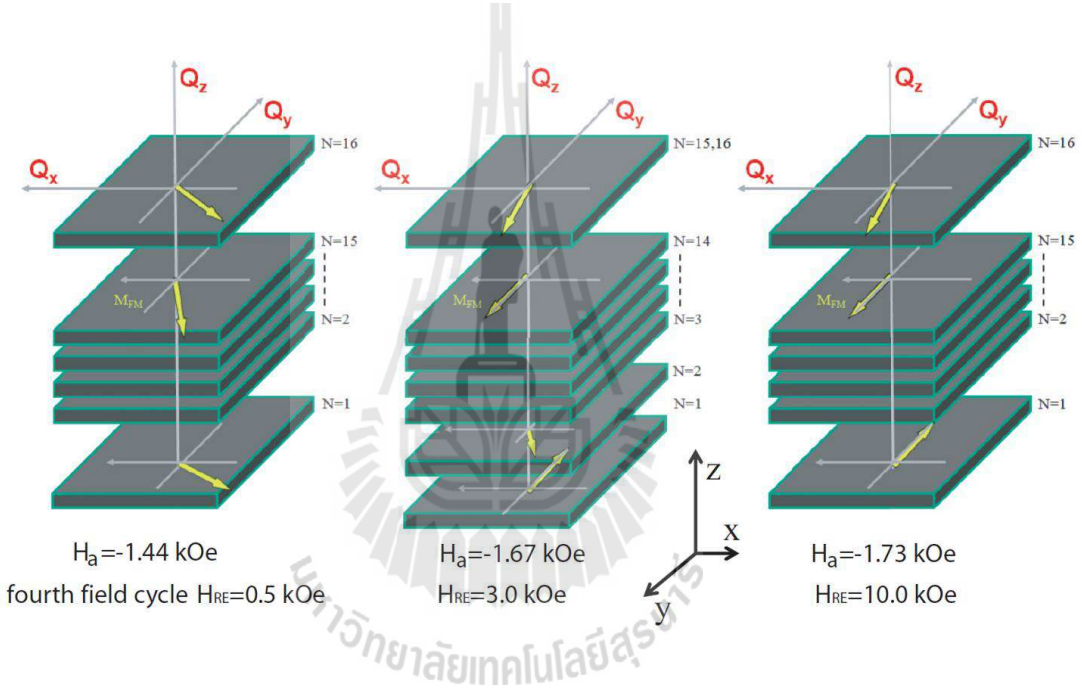

Figure 5.12 FM layers switching sequence during the first field cycle at H_a = -1.44 kOe (H_{RE} = 0.5 kOe), -1.67 kOe (H_{RE} = 0.5 kOe), and -1.73 kOe (H_{RE} = 0.5 kOe) when Ω_{RE} = 45°. The arrows indicate that the M_{FM} orientations in the respective layers. The applied field H_a is along the –*y* axis.

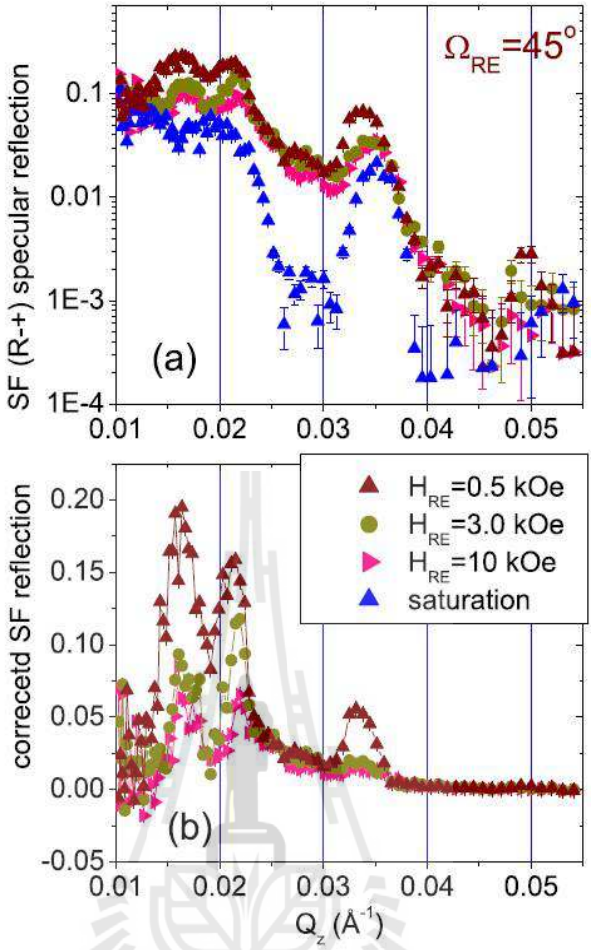

Figure 5.13 (a) SF specular reflectivity [R_{-+}] patterns as a function of Q_z measured during the fourth for Ω_{RE} = 45° at H_a = -1.44, -1.67 and -1.73 kOe for H_{RE} = 0.5, 3.0 and 10.0 kOe, respectively. (b) Plot of the corresponding corrected SF signals as a function of Q_z.

When H_{RE} = 3.0 kOe, the decrease in the SF signal is due to the flipping of the layers which indicates a DW reversal mechanism for majority of the layers. However, the remaining SF intensities are due to the rotation of one or two top and bottom layers. Even though the reversal mechanism for majority of the layers is via a DW process, for minority of the layers is recognized as rotation. Therefore it can infer that the sample has signature of mixed reversal processes.

Interestingly, in case of H_{RE} = 10.0 kOe, the reversal process is fully dominated via the DW process. Here, it can conclude that a significant revival of the untrained state has indeed take place. Moreover, it may also note that the M_{FM} orientation of the do not depend upon the strength of H_a, but upon the H_{RE} strength. Thus the degree of revival of the untrained state has been shown to depend upon the H_{RE} strength.

5.4.3 Fourth field cycle with $\Omega_{RE} = 90°$

PNR measurements during the fourth field cycles were performed keeping Ω_{RE} = 90°. The blue star markers in Figure 5.3 show the fields of measurements. Figure 5.14(a) and (b) show the specular NSF and SF scattering signals measured at 10 K and at H_a = -1.73, and -1.65 kOe, respectively, during the respective fourth field cycles corresponding to the two different representative values of H_{RE} (= 2.0 and 10.0 kOe). Note that also each time we chose to select for a different H_{RE} value during the third field cycle, we have used a different H_a value during the fourth field cycle. This was done again in accordance with the measured SQUID data.

The layer switching sequences for H_a = -1.73, and -1.65 kOe during the respective fourth field cycles is shown in Figure 5.15. It can see that for H_{RE} = 2.0 kOe the situation is typical of a magnetization reversal via the DW process. However, for H_{RE} = 10.0 kOe the situation is greatly more complicated. There is a mixture of DW and rotational reversal processes. This is consistent with the earlier observations in similar system by Brems *et al*. (Brems, Temst, and Van Haesendonck, 2007) as we can see that with further increase in the H_{RE} strength, the recovery of the untrained state is reduced.

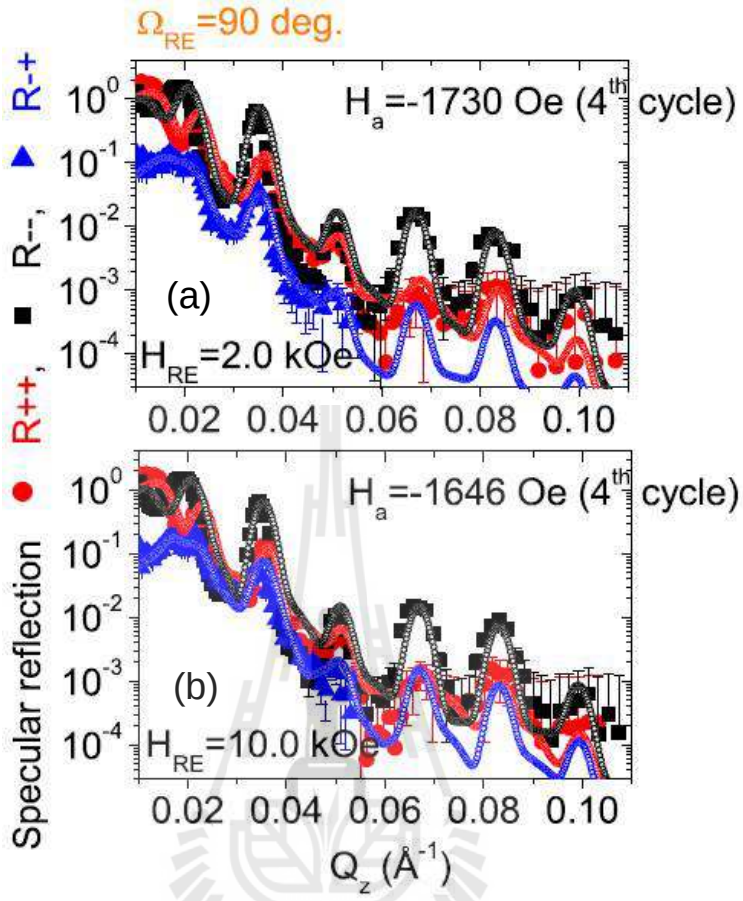

Figure 5.14 Specular reflectivity patterns (solid symbols) along with their best fits (open symbols) as a function of Q_z for the NSF [R_{--} (square) R_{++} (circle)] and SF [R_{-+} (triangle)] channels measured at (a) H_a = -1.73 kOe, and (b) H_a = -1.65 kOe during the fourth field cycle for different H_{RE} (= 2.0 and 10.0 kOe, respectively) values when Ω_{RE} = 90°.

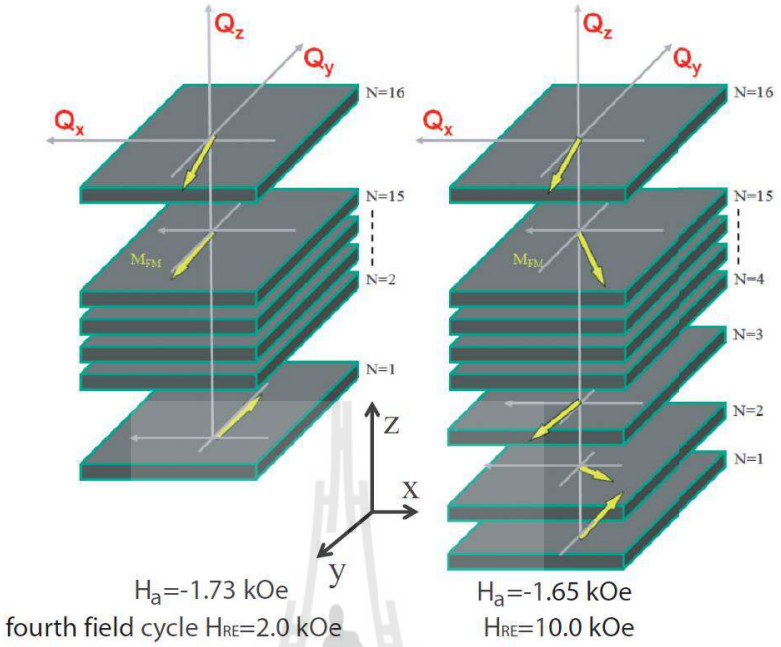

Figure 5.15 FM layers switching sequence during the different fourth field cycles at H_a = -1.73 kOe (H_{RE} = 2.0 kOe), and -1.65 kOe (H_{RE} = 10.0 kOe) when Ω_{RE} = 90°. The arrows indicate that the M_{FM} orientations in the respective layers. The applied field H_a is along the –*y* axis.

In Figure 5.16(a), we compare the measured SF scattering signals (perpendicular component of M_{FM}) measured at 10 K and at fields of H_a = -1.73 and -1.65 kOe during the respective fourth field cycles compare with H_a = -10.0 kOe (at saturation) during the first field cycle. The corrected SF signals, which is the subtracted-off SF signal at saturation, is shown in Figure 5.16(b). The corrected SF signals can also be regarded as signatures of recovery or nonrecovery of the untrained state.

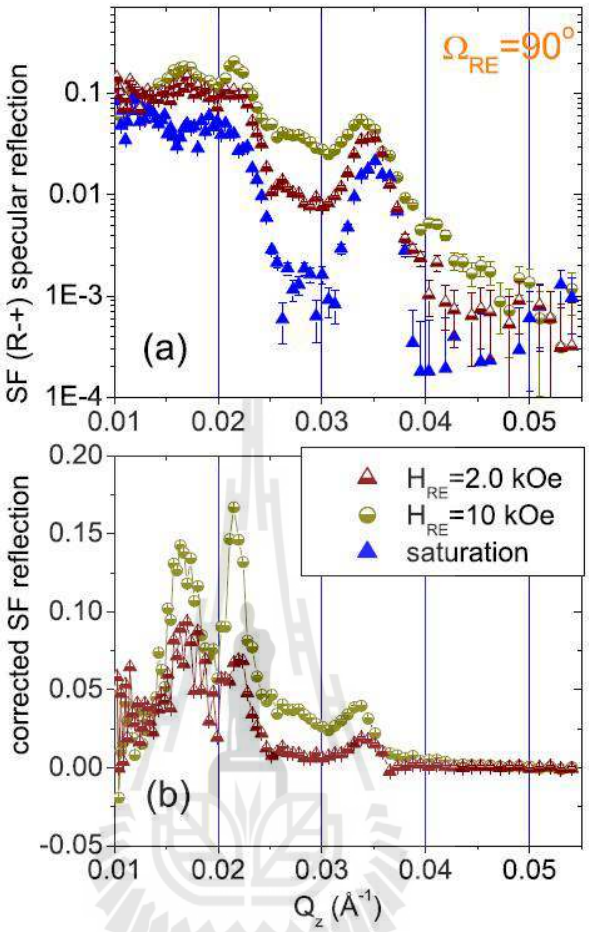

Figure 5.16 (a) SF specular reflectivity [R_{-+}] patterns as a function of Q_z measured during the fourth for Ω_{RE} = 90° at H_a = -1.73 kOe, and -1.65 kOe for H_{RE} = 2.0 kOe and 10.0 kOe, respectively. (b) Plot of the corresponding corrected SF signals as a function of Q_z.

5.4.4 Discussion on the rotational sense

We can explain our experimental observations within the extended Fulcomer-Charap model (Fulcomer and Charap, 1972), where a single ferromagnetic domain (FM magnetization) exchange coupled with multiple AF grains with rotatable (responsible for training) and/or nonrotatable (responsible for bias field) moments but

without any direct exchange coupling between the grains (Gredig, Krivorotov and Dahlberg, 2002; Miao *et al*., 2005).

Brems *et al*. (Brems *et al*., 2013) have shown the results of changing the sense of direction during field cycling, for instance, along +*x* and –*x* direction. The recovery of the untrained state depends upon the direction of the average uncompensated magnetization vector $\vec{m}_{\mathrm{AF}}$ of the antiferromagnetic grains. The directional sense of $\vec{m}_{\mathrm{AF}}$ was related to the directional sense of the FM magnetization. The whole sample magnetization was found rotating in the negative direction during the initial hysteresis loop which was accounted for in the initial negative direction of $\vec{m}_{\mathrm{AF}}$ as well (Mino *et al*., 2010).

The rotational sense of magnetization can be determined by following the trend of the angle ϕ_A with respect to the cooling field direction along the –*y* axis for increasing measurement fields along the +*y* axis. When the angle is positive (negative), the system experiences a positive (negative) rotational sense. Generally, more is the angular direction of $\vec{m}_{\mathrm{AF}}$ oriented away from the cooling field direction, more is the torque acting o the FM moments. The torque in turn leads to magnetization reversal via rotation instead of the DW reversal process.

In principle, the rotational sense of $\vec{m}_{\mathrm{AF}}$, which remains unknown from our experimental data can be evaluated by energy minimization of the total energy in the system. The total energy is given by

$$E = \sum A^i k_{\mathrm{AF}} t_{\mathrm{AF}} \sin^2\left(\phi^i - \alpha\right) - J_{\mathrm{int}} A^i \cos\left(\theta - \phi^i\right) - H_a M_{\mathrm{FM}} t_{\mathrm{FM}} \cos\left(\chi - \theta\right) \sum A^i. \quad (5.1)$$

Here the uniaxial anisotropy energy constant of CoO and Co are $k_{AF} = 2.5 \times 10^8$ erg/cm^{-3} and $k_{FM} = 1.5 \times 10^6$ erg/cm^{-3}, respectively. J_{int} is the interfacial exchange energy which involves the coupling constant between the FM and AF grains and $t_{FM}\left(t_{AF}\right)$ is the FM (AF) thickness. The angles are the respective angles made by $\vec{m}_{AF}\left(\phi^i\right)$, AF easy axis (α), FM magnetization (θ), and $H_a\left(\chi\right)$ with H_{FC} along the –*y* axis. A^i is the area of every noninteracting AF grain coupled to a single FM domain $\sum A^i$. We have considered 100 such AF grains coupled to one FM grain. The term corresponding to k_{FM} can be neglected due to it is smaller by 2 orders of magnitude when compared with the value of k_{AF}. From the value of ρ_m we approximate M_{FM} =1051 erg/cm^3 or 1.25 μB/atom, which gives $J_{int}\left(= H_{eb} M_{FM} t_{FM}\right)$ = 0.86 erg/cm^2.

For the first field cycling case, we can consider $\alpha = 0°$ assuming the AF easy to be coinciding with the H_{FC} axis after field cooling. Using the stability conditions $dE/d\phi^i = 0$ and $dE/d\theta = 0$ we are lead to a system of two equations:

$$k_{AF} t_{AF} \sin 2\left(\phi^i\right) + J_{int} \sin\left(\theta - \phi^i\right) = 0, \tag{5.2}$$

$$H_a M_{FM} t_{FM} \sin\left(\chi - \theta\right) + J_{int} \sin\left(\theta - \phi^i\right) = 0. \tag{5.3}$$

In our case, since we always measures along the axis of H_{FC}, so we can consider $\chi = 0°/180°$ (parallel or antiparallel to the cooling axis). For finding the coercive fields we have used $\theta = \chi + \pi/2$, considering the magnetization of the FM

is zero across the easy axis which gives $\sin\phi^i = \frac{-J_{\text{int}}}{2k_{\text{AF}}t_{\text{AF}}}$ or $\phi^i = -0.33°$ from equation (5.2) during the first field cycle. Note that using a similar model, the average magnetization vector was calculated to be at -0.6° away from the cooling field direction by Brems *et al*. (Brems *et al*., 2007), signifying a negative sense of rotation.

In our case, using PNR alone, we cannot discriminate the rotational sense of the FM magnetization. However, following the systematic variation of the magnetization direction (during the fourth field cycles) with applied fields H_a we could figure out that the rotational sense has not changed with the change in the H_{RE} values along a particular direction. This unchanged FM rotational sense can be due to the fact that H_{RE} in our case always starts and end in the –*x* direction (at least for $\Omega_{\text{RE}} = 90°$). This implies that in spite of an unchanged rotational sense of the FM magnetization, a well pronounced recovery of the untrained state is possible.

มหาวิทยาลัยเทคโนโลยีสุรนารี

CHAPTER VI

CONCLUSIONS AND SUGGESTION

In this work, the powerful techniques based on synchrotron X-ray absorption near edge structure (XANES) was used to examine the local structure of Mn atoms in $BiFe_{1-x}Mn_xO_3$ ceramic compositions. XANES was also employed to determine the formation of trace secondary phase(s) in $BiFe_{1-x}Mn_xO_3$ ceramic compositions and the Co/CoO/Au MLs. Systematic magnetization measurements by a superconducting quantum interference device (SQUID) magnetometry along with depth-sensitive vector magnetometry by polarized neutron reflectivity (PNR) were used for exploring the degree of recovery of the untrained state in an exchange-coupled Co/CoO/Au ML.

In Mn-doped $BiFeO_3$ system, both the experimental and calculated XANES results showed that the majority of Mn atoms occupied the Fe site or B-site in BFO lattice. By a linear combination of the calculated Mn *K*-edge XANES spectra of various $BiMnO_3$ and $BiMn_2O_5$ contents, it was found that the increase of Mn content led to the formation of $BiMn_2O_5$.

In Co/CoO/Au MLs system, the XANES result indicated the formation of Co_3O_4 in the [Co/CoO] bilayers within the multilayer. By a linear combination analysis of both the measured and calculated XANES spectra, the proportions of Co metal, Co_3O_4 and CoO were obtained for all Co/CoO/Au MLs.

For the investigations of the magnetic interaction between exchange-coupled stacked CoO and Co bilayers, the parallel component of magnetization measurements

by SQUID indicated the recovery of the untrained state for two orientation angles, namely Ω_{RE} = 45° and Ω_{RE} = 90° along the –*x* direction. PNR measurements, which simultaneously involved parallel as well as perpendicular components of magnetization, revealed that for Ω_{RE} = 45° it was necessary to apply at least H_{RE} = 3.0 kOe to achieve a significant recovery. For a higher value of H_{RE} (up to ≈10.0 kOe), the recovery saturated while for a lower value, a partially recovery was only achieved. For Ω_{RE} = 90°, it demonstrated a peak in the recovery even with H_{RE} = 2.0 kOe. However, with higher fields, the recovery gradually decreased and only a partial recovery was possible. For any other higher angles of orientation (e.g., Ω_{RE} = 135°), no recovery of the untrained state occurred.

This study has clearly demonstrated the combination of XANES measurements and ab initio XANES calculations is a very powerful tool for determining the formation of trace secondary phase(s), not detected by a conventional XRD technique, in ferroic materials. Furthermore, for Co/CoO/Au MLs system, we suggest that the degree of recovery of the untrained state after the first two field cycles can be regulated not only with H_{RE} values but also with the Ω_{RE} values below 90°.

However, from the results obtained in this work, there are some important points that are not well understood and further study is needed. In Mn-doped $BiFeO_3$ system, we should consider synthesizing this system with the whole range of Mn contents ($0 \leq x \leq 1$) as well as $BiMnO_3$ and $BiMn_2O_5$ standards because characterizing these compounds would allow more understanding on the detailed phase composition of $BiMnO_3$/ $BiMn_2O_5$. Moreover, we should explore a possible

change in the directional sense of the untrained state by applying H_{RE} along the $+x$ direction in Co/CoO/Au MLs system.

REFERENCES

REFERENCES

Ablat, A., Muhemmed, E., Cheng, S., Wang, J., Quian, H., Wu, R., Zhang, N., Rong, W. and Ibrahim, K. (2012). Electronic structure of $BiFe_{1-x}Mn_xO_3$ thin films investigated by x-ray absorption spectroscopy. **J. Nanomater.** 7: 123438.

Als-NielsenFultz, J. and McMorrow, D. (2001). **Elements of Modern X-ray Physics**. Chichester: John Wiley & Sons.

Ankoudinov, A. L. (1996). Relativistic spin-dependent X-ray absorption theory. PhD Thesis, University of Washington.

Ankudinov, A. L., Ravel, B., Rehr, J. J. and Conradsan, S. D. (1998). Real-space multiple-scattering calculation and interpretation of X-ray-absorption near-edge structure. **Phys. Rev. B.** 58: 7565.

Attwood, D. (2007). Synchrotron radiation for materials science application. (Online). Available: www.coe.berkeley.edu/AST/srms, UC Berkeley, California.

Baibich, M. N., Broto, J. M., Fert, A., Nguyen Van Dau, F., Petroff, F., Etienne, P., Creuzert, G., Friederich, A. and Chazelas, J. (1988).Giant magnetoresistance of (001)Fe/(001)Cr magnetic superlattaces. **Phys. Rev. Lett.** 61: 2472.

Bedanta, S. (2006). Supermagnetism in magnetic nanoparticle systems. PhD Thesis, Universität Duisburg-Essen.

Bedanta, S. and Kleemann, W. (2009). Supermagnetism, **J. Phys. D: Appl. Phys.** 42: 013001.

Bloch, F. (1932). Zur Theorie des austauschproblems und der remanenzerscheinung der ferromagnetika. **Z. Phys.** 74: 295.

Blundell, S. (2007). **Magnetism in Condensed Matter.** New York: Oxford University Press.

Bodker, F., Morup, S. and Linderoth, S. (1994). Surface effects in metallic iron nanoparticles. **Phys. Rev. Lett.** 72: 282.

Brems, S., Buntinx, D., Termst, K., Van Haesendonck, C., Radu, F. and Zabel, H. (2005). Reversing the training effect in exchange biased CoO/Co bilayers. **Phys. Rev. Lett.** 95: 157202.

Brems, S., Liu, H., Termst, K. and Van Haesendonck, C. (2013). Rotation sense of the magnetization in the Co/CoO exchange-bias system probed with anisotropic magnetoresistance measurement. **Phys. Rev. B.** 88: 214427.

Brems, S., Termst, K. and Van Haesendonck, C. (2007). Origin of the training effect and asymmetry of the magnetization in polycrystalline exchange bias system. **Phys. Rev. Lett.** 99: 067201.

Bunker, G. (2010). **Introduction to XAFS: A Practical Guide to X-ray Absorption Fine Structure Spectroscopy.** Cambridge: Cambridge University Press.

Chikazumi, S. (1999). **Physics of Ferromagnetism.** New York: Oxford University Press.

Coey, J. M. D. (2009). **Magnetism and Magnetic Materials.** Cambridge: Cambridge University Press.

Depla, D. and Mahiey, S. (2008). **Springer Series in Materials Science: Reactive Sputter Deposition.** New York: Springer.

Dormann, L. L, Fiorani, D. and Tronc, E. (1997). **Magnetic Relaxation in Fine-Particle System (Advance in Chemical Physics).** New York: John Wiley & Sons.

Dredig, T., Krivorotov, I. and Dahlberg, E. (2002). Magnetization reversal in exchange biased Co/CoO probed with anisotropic magnetoresistance. **J. Appl. Phys.** 91: 7760.

Eisebitt, S., Böske, T., Rubensson, J. E. and Eberhardt, W. (1993). Determination of absorption coefficients for concentrated samples by fluorescence detection. **Phys. Rev. B.** 47: 14103.

Einstein, A. (1905). On a heuristic viewpoint concerning the production and trans formation of light. **Ann. Phys.-Berlin.** 17: 132.

Fecioru-Morariu, M., Ali, S. R., Papusoi, C., Sperlich, M. and Güntherodt, G. (2007). Effect of Cu dilution in IrMn on the exchange bias of Co/FeIrMn bilayers. **Phys. Rev. Lett.** 99: 097206.

Fukumura, H., Matsui, S., Tonari, N., Nakamura, T., Hasuike, N., Nishio, K., Isshiki, T. and Harima, H. (2009). Synthesis and characterization of Mn-doped $BiFeO_3$ nanoparticle. **Acta. Phys. Plo. A.** 116: 47.

Fulcomer, E. and Charap, S. H. (1972). Thermal fluctuation aftereffect model for some systems with ferromagnetic-antiferromagnetic coupling. **J. Appl. Phys.** 43: 4190.

Fultz, B. and Howe, J. M. (2008). **Transmission Electron Microscopy and Diffractometry of Materials.** New York: Springer.

Gangopadhyay, S., Hadjipanayis, G. C., Sorensen, C. M. and Klabunde, K. J. (1993). Exchange anisotropy in oxide passivated Co fine particles. **J. Appl. Phys.** 73: 6964.

Garanin, D. A. and Kachkachi, H (2003). Surface contribution to the anisotropy og magnetic nanoparticles. **Phys. Rev. Lett.** 90: 065504.

Gierlings, M., Prandolini, M. J., Fritzsche, H., Gruyters, M. R. and Riegel, D. (2002). Change and asymmetry of magnetization reversal for a Co/CoO exchange-bias system. **Phys. Rev. B.** 65: 092407.

Girgis, E., Portugal, R. D., Loosvelt, H., Van Bael, M. J., Gordon, I., Malfait, M., Termst, K., Van Haesendonck, C., Leunissen, L. H. A. and Jonckheere, R. (2013). Enhanced asymmetric magnetization reversal in nanoscale Co/CoO arrays: competition between exchange bias and magnetostatic coupling. **Phys. Rev. Lett.** 91: 187202.

Groot, d., F., F. M., Hu, Z. W., Lopez, M. F., Kaindl, G., Guillot, F. and Tronc, M. (1994). Differences between L_3 and L_2 X-ray absorption spectra of transition metal compounds. **J. Chem. Phys.** 101: 6570.

Gruyters, M. R. and Schmita, D. (2008). Microscopic nature of ferro- and antiferromagnetic interface coupling of uncompensated magnetic moments in exchange bias systems. **Phys. Rev. Lett.** 100: 077205.

Gupta, M., Gutberlet, T., Stahn, J. and Clemens, D. (2004). AMORE-the time of flight neutron reflectometer at SINQ/PSI. **Pramana J. Phys.** 63: 57.

Hench, L. L. and West, J. K. (1990). **Principles of Electronic Ceramics.** New York: John Wiley & Sons.

Hippert, F., Geissler, E., Hodeau, J. L., Leliévre-Berna, E. and Regnard, J. R. (2006). **Neutron and X-ray Spectroscopy.** Netherlands: Springer.

Hubert, A. and Schäfer, R. (2000). **Magnetic Domains**, Berlin: Springer.

Hunpratub, S., Thongbai, P., Yamwong, T., Yimnirun, R. and Maensiri, S. (2012). Effects of Mn doping on the dielectric relaxations and dielectric response in multiferroic $BiFeO_3$ ceramics. **J. Supercond. Novel Magn.** 25: 1619.

Jaklevic, J., Kirby, J. A., Klein, M. P., Robertson, A. S., Brown, G. S. and Eisenberger, P. (1977). Fluorescence detection of EXAFS: Sensitivity enhancement for dilute species and thin films. **Solid State Commun.** 23: 679.

Kittel, C. (1986). **Introduction to Solid State Physics**. New York: John Wiley & Sons.

Kodre, A. (2002). **XANES spectroscopy.** (Online). Available: http://www.ung.si/~arcon/xas/xanes/xanes-theory.pdf.

Koningsberger, D. C. and Prins, R. (1998). **X-ray Absorption: Principles, Applications, Techniques of EXAFS, SEXAFS and XANES.** New York: John Wiley & Sons.

Landau, L. D. and Lifshitz, E. (1935). On the theory of the dispersion of magnetic permeability in ferromagnetic bodies. **Phys. Z. Sowjetunion.** 8(153): 101.

Laureti, S., Suck, S. Y., Haas, H., Prestat, E., Bourgeois, O. and Givord, D. (2012). Size dependence of exchange bias in Co/CoO nanostrutures. **Phys. Rev. B** 108: 077205.

Lee, D., Kim, M. G., Ryu, S. and Jang, H. M. (2005). Epitaxially grown La-modified $BiFeO_3$ magnetoferroelectric thin films. **Appl. Phys. Lett.** 86: 222903.

Miao, B. F., Ai, J. H., Sun, L., You, B., Hu, A. and Ding, H. F. (2010). Recovery of the training effect in exchange bias systems within a coherent rotation model. **Phys. Rev. B.** 82: 134442.

Michel, C., Moreau, J. M., Achenbach, G. D., Gerson, R. and James, W. J. (1969). The atomic structure of $BiFeO_3$. **Solid State Commun.** 7: 701.

Miltényi, p., Gierlings, J., Keller, J., Beschoten, B. and Güntherodt, G. (2000). Diluted antiferromagnets in exchange bias: Proof of the domain state model. **Phys. Rev. Lett.** 84: 4224.

Meiklejohn, W. H. and Bean, C. P. (1957). New magnetic Anisotropy. **Phys. Rev.** 105: 904.

Merzbacher, E. (1970). **Quantum Mechanics.** Chichester: John Wiley & Sons.

Néel, L. (1951). Le trainage magnetique. **J. Phys. Radium** 12: 339.

Norman, J. G. (1976). Non-empirical versus empirical choices for overlapping-sphere radii ratios in SCF-Xα-SW calculations on ClO_4-and SO_2. **Molecular Physics.** 34(4): 1191.

ÓHandley, R, C. (2000). **Modern Magnetic Materials: Principles and Application.** New York: John Wiley & sons.

Ohno, H. (1998). Making nonmagnetic semiconductors ferromagnetic. **Science** 281: 951.

Palkar, V. R., Kumara, K. G. and Malik, S. K. (2004). Observation of room-temperature magnetoelectric coupling in pulsed-laser-deposited $Bi_{0.6}Tb_{0.3}La_{0.1}FeO_3$ thin films. **Appl. Phys. Lett.** 84: 2856.

Parkin, K. K., Roche, K. P., Samant, M. G., Rich, P. M., Beyers, R. B., Scheuerlein, R. E., ÓSullivan E. J., Browm, S. L., Wanner, R. A. and Gallagher, W. J. (1999). Exchange-biased magnetic tunnel junctions and application to nonvolatile magnetic random access memory. **J. Appl. Phys.** 85: 5828.

Parratt, L. G. (1954). Surface studies of solids by total reflection of x-rays. **Phys. Rev.** 95: 359.

Paul, A. (2012). Grazing incidence polarized neutron scattering in reflection geometry from nanolayered spintronic systems. **Pramana J. Phys.** 78: 1-58.

Paul, A., Buchmeier, M., Bürgler, D. E., Rücker, U., Brückel, T. and Schneider, C. M. (2008). Twisted magnetization state at the interface of an antiferromagnetically coupled Fe/Si multilayer as probed by apecular and off-specular polarized neutron scattering. **Phys. Rev. Lett.** 77: 184409.

Paul, A., Bürgler, D. E., Luysberg, M. and Grünberg, P. (2004). Enhancement of exchange bias through a spacer material. **Europhys. Lett.** 68: 233.

Paul, A., Kentzinger, E., Rücker, U. and Brückel, T. (2006). Magnetization reversal with variation of the ratio of the anisotropy energies in exchange bias systems. **Phys. Rev. B.** 74: 054424.

Paul, A., Krist, T., Teichert, A. and Steitz, R. (2011). Specular and off-specular scattering with polarization and polarization analysis on reflectometer V6 at BER II, HZB. **Physica B.** 406: 1598.

Paul, A. and Mattauch, S. (2004). Microscopic origin of training in exchange buas system. **Appl. Phys. Lett.** 95: 092502.

Paul, A., Paul, N., Jutimoosik, J., Yimnirun, R., Rujirawat, S., Höpfner, B., Lauermann, L., Lux-Steiner, M., Mattauh, S. and Böni, P. (2013). Change in interface magnetism of an exchange-coupled system due to the presence of nomagnetic spacers. **Phys. Rev. B.** 87: 014431.

Paul, A., Paul, N. and Mattauch, S. (2011). Magnetization reversal and domain correlation for a non-collinear and out-of-plane exchange coupled system. **New J. Phys.** 13: 063009.

Paul, A., Schneider, C. M. and Stahn, J. (2007). Reversal mechanism and suppression of training in an exchange-coupled system. **Phys. Rev. B.** 76: 184424.

Rehr, J. J., and Albers, R. C. (2000). Theoretical approaches to x-ray absorption fine structure. **Rev. Mod. Phys.** 72: 3.

Ravel, B. and Newville, M., (2005). ATHENA, ARTEMIS, HEPHAESTUS: Data analysis for X-ray absorption spectroscopy using IFEFFIT. **J. Synchrotron Radiat.** 12: 537.

Sakurai, J. J. (1967). **Advanced Quantum Mechanics.** Boston: Addison-Wesley.

Schmid, H. (1994). Multi-ferroic magnetoelectrics. **Ferroelectric.** 62: 317.

Shukla, D. K., Mollash, S., Kunar, R., Thakur, P., Chae, H. H., Choi, W. K. and Banerjee, A. (2008). Effect of Ti substitution on multiferroic properties of $BiMn_2O_5$. **J. Appl. Phys.** 104: 033707.

Singh, S. K., Ishiwara, H. and Maruyama, K. (2006). Room temperature ferroelectric properties of Mn-substituted $BiFeO_3$ thin films deposited on Pt electrodes using chemical solution deposition. **Appl. Phys. Lett.** 88: 262908.

Sosnowska, I., Schäfer, W., Kockerlmann, W, Andersen, K. H. and Troyanchuk, I. O. (2002). Crystal structure and spiral magnetic ordering of $BiFeO_3$ doped with manganese. **Appl. Phys. A.** 74: 1040.

Stacey, F. D. (1960). Thermally activated ferromagnetic domain wall motion. **Aust. J. Phys.** 13:599.

Stanton, A. (1896). On a new kind of rays. **Nature.** 53: 274.

Stern, E. A. and Heald, S. M. (1983). Basic principle and applications of EXAFS. **J. Synchrotron Radiat.** 10: 995.

Stilies, M. D. and McMichael, R. D. (1999). Model for exchange bias in polycrystalline ferromagnet-antiferromagnet bilayers. **Phys. Rev. B.** 59: 3722.

Stoner, E. C. and Wohlfarth, E. P. (1948). A mechanism of magnetic hysteresis in heterogeneous alloys. **Philos. Trans. London Ser. A.** 240: 599.

Tröger, L., Arvanitis, D., Baberschke, K., Michaelis, H., Grimm, U. and Zshech, E. (1992). Full correction of the self-absorption in soft-fluorescence extended X-ray absorption fine structure. **Phys. Rev. B.** 46: 3282.

Unruan, M., Sareein, T., Chandarak, S., Hunpratup, S., Thongbai, P., Maensiri, S. and Yimnirun, R. (2012). Aging and stress-dependent dielectric properties of multiferroic bismuth ferrite ceramics. **Mater. Lett.** 90: 185.

Wang, Y., Huang, H. and Wang, B. (2010). Effect of Mn substitution for Fe in multiferroic $BiFeO_3$: A First principle study. **Sci. Adv. Mater.** 2: 184.

Wang, Y., Jiang, Q. H., Xiaolu, L. and Nan, C. W. (2006). Multiferroic $BiFeO_3$ thin films prepared via a simple sol-gel method. **Appl. Phys. Lett.** 88: 142503.

Wang, Y. and Nan, C. W. (2006). Enhanced ferroelectricity in Ti-doped multiferroic $BiFeO_3$ thin films. **Appl. Phys. Lett.** 89: 052903.

Weiss, P. (1907). The hypothesis of the molecular field and the property of ferromagnetism. **J. de Phys. Rad.** 6: 661.

William, D. B. and Carter, C. B. (2009) **Transmission Electron Microscopy: A Textbook for Materials Science.** New York: Plenum Press.

Wolf, S. A., Awschalom, D. D., Buhrman, R. A., Roukes, M. L. and Treger, D. M. (2001). Spintronics: A spin-based electronics vision for future. **Science.** 294: 1488.

Yoneda, Y., Kitanaka, Y., Noguchi, Y. and Miyayama, M. (2012). Electronic and local structures of Mn-doped $BiFeO_3$ crystals. **Phys. Rev. B.** 86: 184112.

Zabel, H. (1994). X-ray and neutron reflectivity analysis of thin films and superlattices. **Appl. Phys. A.** 58: 159.

Zabel, H., Theis-Bröhl, K. and Toperverg B. P. (2007). **Polarized Neutron Reflectivity and Scattering from Magnetic Naostructures and Spintronic Materials** (Handbook of Magnetism and Advanced Magnetic Materials). New York: John Wiley & sons.

มหาวิทยาลัยเทคโนโลยีสุรนารี

APPENDIX

Abstract presented at the Joint IEEE International Symposium of ISAF-ISIF-PFM 2015, Singapore

Determination of Secondary Phase in Fe/$BaTiO_3$ Bilayers by Synchrotron X-ray Absorption Near-Edge Structure Spectroscopy

J. Jutimoosik[1*], A. Paul[2], S. Rujirawat[1] and R. Yimnirun[1]

[1]School of Physics, Institute of Science, and NANOTEC-SUT Center of Excellence on Advanced Functional Nanomaterials, Suranaree University of Technology, Nakhon Ratchasima 30000, Thailand
[2]Technische Universität München, Physik Department E21, Lehrstuhl für Neutronenstreuung,
James-Franck-Strasse 1, D-85748 Garching, Germany

*e-mail: jaru_tum@hotmail.com

Synchrotron X-ray Absorption Near-Edge Structure (SXANES) experiment was performed on Fe/$BaTiO_3$ (BTO) samples and compared with *ab initio* XANES calculation. The Fe *K*-edge and Ba L_3-edge XANES measurement was carried on Fe/$BaTiO_3$ bilayer samples with increasing thickness of the BTO layer grown on $SrTiO_3$ (STO). The measured XANES spectra were obtained in fluorescent mode and collected at ambient temperature with 4-element Si drift detector. The measured XANES spectra of Fe *K*-edge and Ba L_3-edge indicated the presence of few monolayers of antiferromagnetic FeO at the interface without the formation of any $BaFeO_3$. From the L_3-edge XANES result, it clearly showed the good agreement between measured and *ab initio* theoretical XANES spectra and confirmed the absence of any $BaFeO_3$. Our results also showed the ratios of each constituent of Fe oxide phases contained in Fe/BTO bilayers. We suggest that XANES measurement is a useful and reliable technique that can be applied to study the phase composition of thin film materials.

Abstract presented at the 3rd Southeast Asia Conference on Thermoelectrics 2014 (SACT 2014), Pakse, Lao PDR.

Determination of the secondary phase in Fe films on nano-porous TiO_2 templates by x-ray absorption near-edge structure spectroscopy

J. Jutimoosik[a,e1], A. Paul[b,e2], S. Rujirawat[a,e3] and R. Yimnirun[a,e4]

[a] *School of Physics, Institute of Science, and NANOTEC-SUT Center of Excellence on Advanced Functional Nanomaterials, Suranaree University of Technology, Nakhon Ratchasima 30000, Thailand*

[b] *Technische Universität München, Physik Department E21, Lehrstuhl für Neutronenstreuung, James-Franck-Strasse 1, D-85748 Garching, Germany*

[e1]jarutum@gmail.com, [e2]amitesh.paul@frm2.tum.de, [e3]saroj@sut.ac.th, [e4]rattikorn@sut.ac.th

We demonstrated that X-ray Absorption Near-Edge Structure (XANES) can be used as an unconventional characterization technique to determine the proportions of different crystal phases in thin film samples. The Fe *K*-edge XANES measurement was carried on Fe layers, which varied thickness from 5 nm to 100 nm, on a porous (nanostructured) TiO_2 template. The measured XANES spectra were obtained in fluorescent mode and collected at ambient temperature with 4-element Si drift detector. The features of Fe *K*-edge XANES spectra of thin film samples clearly showed that these spectra were thickness dependent. Our results also showed the ratios of each constituent of Fe oxide phases contained in the Fe layers of nanostructure samples. We suggest that XANES measurement is a useful and reliable technique that can be applied to study the phase composition of nanostructure thin film materials.

Abstract presented at the Joint Conference of 9th Asia Meeting on Ferroelectric & 9th Asia Meeting on Electroceramics (AMF-AMEC-2014), Shanghai, Chaina..

On Preferred Mn Site in Multiferroic $BiFeO_3$: A View by SynchrotronX-Ray Absorption Near Edge Structure Spectroscopy

Jaru Jutimoosik[1,*], Sitchai Hunpratub[2], Santi Maensiri[1], Saroj Rujirawat[1], and Rattikorn Yimnirun[1]

[1]School of Physics, Institute of Science, and NANOTEC-SUT Center of Excellence on Advanced Functional Nanomaterials, Suranaree University of Technology, Nakhon Ratchasima 30000, Thailand
[2]Department of Physics, Faculty of Science, Khon Kaen University, Khon Kaen 40002, Thailand
*Corresponding Author's E-mail: jaru_tum@hotmail.com

Abstract

Synchrotron X-ray Near Edge Structure (XANES) experiments were performed on Mn-doped $BiFeO_3$ samples and compared with *ab initio* XANES calculations. The Fe and Mn *K*-edge XANES measurements were carried out on Mn-doped $BiFeO_3$ powders (with 5-40 Mn mole%). Both XANES spectra were obtained in a fluorescent mode at ambient temperature with a Ge(111) double crystal monochromator and recorded after performing an energy calibration. From the XANES results, it was clearly identified that the oxidation state of both Fe and Mn ions in $BiFeO_3$ structure was +3. The features of the measured Mn *K*-edge XANES were consistent with *ab initio* XANES of Mn on the Fe site and inconsistent with Mn on other sites. The clear agreement between measured and *ab initio* theoretical XANES spectra was the strongest evidence of Mn substituting for Fe in $BiFeO_3$ structure for low Mn content. More interestingly, at higher Mn content, the presence of a second phase precipitation of $BiMnO_3$ and $BiMn_2O_5$ was evident. This clearly indicated the Mn solubility limit in the $BiFeO_3$ structure, while the two trace compounds could also be responsible for the relevant properties reported in Mn-doped $BiFeO_3$ materials.

Article published in Journal of Applied Physics

JOURNAL OF APPLIED PHYSICS 116, 104105 (2014)

On preferred Mn site in multiferroic $BiFeO_3$: A view by synchrotron x-ray absorption near edge structure spectroscopy

Jaru Jutimoosik,[1,a)] Sitchai Hunpratub,[2] Santi Maensiri,[1] Saroj Rujirawat,[1] and Rattikorn Yimnirun[1]

[1]*School of Physics, Institute of Science and NANOTEC-SUT Center of Excellence on Advanced Functional Nanomaterials, Suranaree University of Technology, Nakhon Ratchasima 30000, Thailand*

[2]*Department of Physics, Faculty of Science, Khon Kaen University, Khon Kaen 40002, Thailand*

(Received 29 May 2014; accepted 28 August 2014; published online 11 September 2014)

Synchrotron X-ray Near Edge Structure (XANES) experiments were performed on Mn-doped $BiFeO_3$ samples and compared with *ab initio* XANES calculations. The Fe and Mn *K*-edge XANES measurements were carried out on Mn-doped $BiFeO_3$ powders (with 5–40 Mn mole%). Both XANES spectra were obtained in a fluorescent mode at ambient temperature with a Ge(111) double crystal monochromator. From the XANES results, it was clearly identified that the oxidation state of both Fe and Mn ions in $BiFeO_3$ structure was +3. The features of the measured Mn *K*-edge XANES were consistent with *ab initio* XANES of Mn on the Fe site and inconsistent with Mn on other sites. The clear agreement between measured and *ab initio* theoretical XANES spectra was the strongest evidence of Mn substituting for Fe in $BiFeO_3$ structure for low Mn content. More interestingly, at higher Mn content, the presence of a second phase precipitation of $BiMnO_3$ and $BiMn_2O_5$ was evident. This clearly indicated the Mn solubility limit in the $BiFeO_3$ structure, while the two trace compounds could also be responsible for the relevant properties reported in Mn-doped $BiFeO_3$ materials. © *2014 AIP Publishing LLC*. [http://dx.doi.org/10.1063/1.4895474]

I. INTRODUCTION

Magnetoelectric or multiferroic materials have attracted enormous attention owing to their potential applications including data storage, spintronics, and microelectric devices.[1,2] Among all multiferroic materials studied so far, $BiFeO_3$ (BFO) that exhibits the simultaneous existence of ferroelectric (FE) and antiferromagnetic (AFM) orders has received great attention, due to its high Curie point ($T_C \sim 1103$ K) and Neél temperature ($T_N \sim 643$ K).[3–5] BFO has a distorted perovskite structure with rhombohedral symmetry, which belongs to the *R3C* space group (the hexagonal setting is used in the present report). The lattice constants determined at room temperature are $a_{hex} = 5.5810$ Å and $c_{hex} = 13.8757$ Å.[6] However, the small room temperature spontaneous polarization and magnetization, as well as large leakage current, are the obstruction of the commercial applications of BFO ceramics. Fortunately, the electrical and magnetic properties of BFO can be improved by doping of other ions or by making low-dimensional structures.

Interestingly, some research groups have modified BFO nanostructures by doping a small amount of impurities at *A* or *B* site (in ABO_3 perovskite structure), which offer great potential to enhance the physical properties of BFO. For example, the partial substitution of Tb at A-site can enhance both ferroelectric and magnetic properties of BFO.[7] On the other hand, some research groups have attempted B-site substitution by high valence state such as Zr^{4+} and Ti^{4+} to improve ferroelectric reliability.[8,9] Recently, One dopant that has been the subject of interest is Mn. Wang *et al.* reported the effect of Mn substitution for Fe in multiferroic BFO investigated via the first-principle calculation.[10] Interestingly, there has been no direct experimental determination of Mn-site in BFO structure. Since the site preference of Mn ions in BFO structure plays a critical role in determining the electric and magnetic properties of Mn-doped BFO materials as reported in prior theoretical and experimental investigations,[10–12] it is thus important to identify the exact local structure of Mn in BFO lattice.

The low energy region of X-ray absorption spectroscopy (XAS) called XA Near Edge Structure (XANES), which contains the information about the valence state and the local geometry of the selected elements, has been proven to be a powerful tool in resolving the local structures around the absorbing atoms.[13–15] In this work, the Fe and Mn *K*-edge XANES measurements and *ab initio* XANES calculations were used to determine the local structure of Mn in BFO structure. This letter will provide both experimental and theoretical evidences that Mn ions substitute for Fe in BFO structure.

II. EXPERIMENTAL PROCEDURES

The nominal $BiFe_{1-x}Mn_xO_3$ ceramic compositions (with $x = 0$, 0.05, 0.10, 0.20, 0.30, and 0.40) used in this study were prepared by a precipitation method. More details of the sample preparation and measurements are presented elsewhere.[11,12,16] X-ray diffraction (XRD) measurements were first carried out to verify the *global* crystal structure of the BFO and Mn-doped BFO samples. The *local* structure of the Mn in BFO structure was then determined by XANES technique. The XANES measurements of Fe and Mn *K*-edge were performed in fluorescent mode with 13-component Ge detector (Canbera) at the X-ray absorption spectroscopy

a)Author to whom correspondence should be addressed. Electronic mail: jaru_tum@hotmail.com

 © 2014 AIP Publishing LLC

beamline (BL-8) of the Siam Photon Source (electron energy of 1.2 GeV with electron currents between 120 mA and 80 mA), Synchrotron Light Research Institute, Thailand. The XANES spectra of all samples were collected at ambient temperature. Double crystal monochromator Ge(111) with an energy resolution ($\Delta E/E$) of 3×10^{-4} was used to scan the synchrotron X-ray with the photon energy step of 0.25 eV in the range of 7090 to 7190 eV and 6520 to 6620 eV, covering the XANES region of Fe and Mn *K*-edge, respectively.

III. RESULTS AND DISCUSSION

The measured Fe and Mn *K*-edge XANES spectra measured for BFO and Mn-doped BFO samples with different Mn contents are compared with standard Fe_2O_3 and Mn_2O_3 powders, as shown in Figures 1(a) and 1(b), respectively. For Fe *K*-edge, the position of absorption edge of all samples resembles that of the Fe_2O_3 standard, showing that the valence of Fe in BFO structure is +3, as expected. This observation also rules out the presence of the other bismuth ferrite secondary phases. Similarly, the Mn *K*-edge spectra of all samples and the Mn_2O_3 standard have similar positions of the absorption edge. This result indicates that the majority of Mn species in Mn-doped BFO is Mn^{3+}. Furthermore, both spectra contain the same main features, implying that the majority of Mn atoms assumes the same lattice locations in these samples. The main feature of the Mn *K*-edge XANES spectra are composed of two shoulders and three peaks labeled as s_1, s_2, p_1, p_2, and p_3 (as shown in inset of Fig. 1(b)). The pre-edge (s_1) absorption region around 6542 eV is attributed to the electric dipole forbidden transition of a 1*s* electron to an unoccupied 3*d* orbital, which is partially allowed because of electric quadrupole coupling and/or 3*d*–4*p* orbital mixing. The main absorption edge feature (s_2) was assigned to the purely dipole-allowed $1s \rightarrow 4p$ transition. Feature p_1, p_2, and p_3 results from the multiple-scattering contribution of absorbing Mn in MnO_6 octahedra surrounded by Bi. The features of Mn *K*-edge spectra of all the samples also look similar to those of Fe *K*-edge spectra, indicating that the local structure surrounding Mn atoms in Mn-doped BFO samples is similar to that of Fe atoms, which means Mn substituting for Fe in Mn-doped BFO samples. However, a small shift of the absorption edge to the higher energy and the broadening and increasing of p_1 and p_2 peaks can be observed when Mn concentration increases, as shown in inset of Fig. 1(b). These results can be attributed to the formation of secondary phase with $Bi_2Fe_4O_9$ or $BiMn_2O_5$ structure appeared in XRD pattern of high Mn-doped BFO samples (not shown here).

To further identify the lattice location of Mn atoms in BFO structure, *ab initio* XANES calculations of Mn at several lattice locations were carried out using FEFF8.2 code.[17,18] This code utilizes a full multiple scattering approach based on *ab initio* overlapping muffin-tin potentials. The muffin-tin potentials used in FEFF code were obtained using self-consistent calculations with Hedin-Lundqvist exchange-correlation functions. The sphere with 5.5 Å radius (containing approximately 50-atoms) around the absorber Mn atom was used for the self-consistent calculations. The full multiple scattering calculations included all possible paths within a large cluster radius of 7.8 Å (containing approximately 150-atoms). The electronic transitions associated with the XANES measurements must follow the dipole selection rule. An X-ray absorbance $\mu(\omega)$ is given by the Fermi's golden rule

$$\mu \propto \sum_f |\langle f|D|i\rangle|^2 \delta\langle E_i - E_f + \omega\rangle , \qquad (1)$$

where $|i\rangle$, $|f\rangle$, E_i, and E_f are the initial and final states and their energies, respectively. ω and D are the photon frequency and dipole operator.

In BFO perovskite structure, as shown in Fig. 2(a), there are three probable Mn sites: Mn substituting on the Bi site (Mn_{Bi}, Fig. 2(b)), Mn substituting on the Fe site (Mn_{Fe}, Fig. 2(c)), and Mn interstitial (Mn_i). The crystal structure of

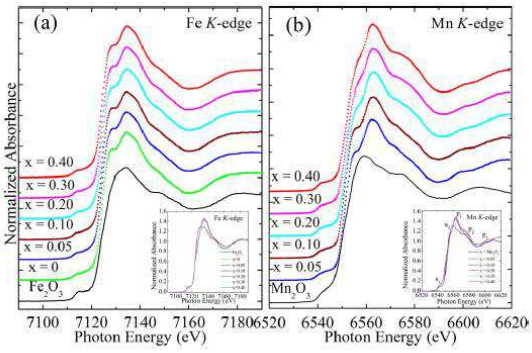

FIG. 1. (a) Normalized Fe K-edge XANES spectra of $BiFeO_3$ and Mn-doped $BiFeO_3$ ceramics with the different Mn concentrations with comparison to the Fe_2O_3 standard sample. (b) XANES spectra of Mn K-edge of Mn-doped $BiFeO_3$ ceramics with comparison to the Mn_2O_3 standard sample. Inset presents the broadening and increasing of p_1, and p_2 peaks.

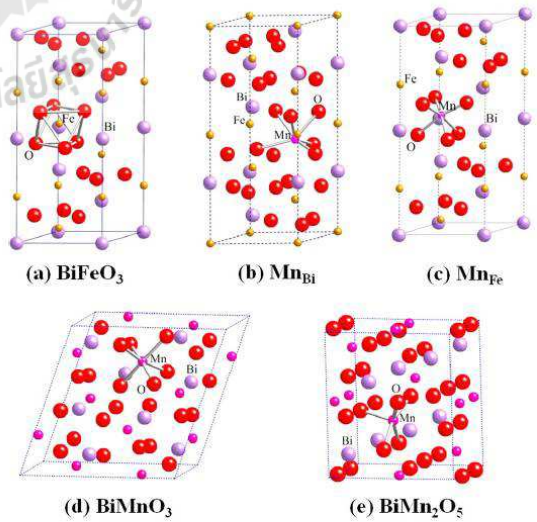

FIG. 2. (a) Perovskite crystal structure of $BiFeO_3$. [(b) and (c)] Schematic illustrations of Mn on Fe site, Mn on Bi site, and interstitial Mn. [(d) and (e)] show the crystal structure of $BiMnO_3$ and $BiMn_2O_5$.

$BiMnO_3$ and $BiMn_2O_5$ is also shown in Figs. 2(d) and 2(e), respectively. In these lattice settings, Mn_{Bi} and Mn_{Fe} are surrounded by O atoms, while Mn_i is surrounded by O and Bi atoms. The calculated XANES spectra of Mn_{Bi}, Mn_{Fe}, and Mn_i are shown in Fig. 3. It is clear that the features of calculated Mn_{Fe} XANES spectrum match very well with those of the measured ones. On the other hand, the calculated XANES spectrum of Mn_{Bi} can be clearly ruled out and the Mn_i calculation produces some features with slight similarity to the measured XANES spectra. The results intuitively indicate the lattice location of Mn atoms at B-site (Fe) in the BFO unit cell (Mn_{Fe}).

However, in order to clarify a small shift of the absorption edge to the higher energy and the broadening and increasing of p_1 and p_2 peaks, the Mn *K*-edge XANES spectra of pure $BiMnO_3$ and $BiMn_2O_5$ are compared qualitatively with those of Mn-doped BFO samples (as shown in Fig. 4(a)), as these spectra were obtained by extrapolating the spectra reported by Yoneda *et al.*[19] and Shukla *et al.*,[20] respectively. It can be clearly observed that the spectrum of low Mn-doped BFO sample ($x = 0.05$) certainly represents the features of pure $BiMnO_3$ XANES spectra, while the spectrum of the high Mn-doped BFO sample ($x = 0.40$) mostly represents the features of pure $BiMn_2O_5$ XANES spectra; an indication of the secondary phase formation. To estimate the quantitative constituent of the secondary phase, the Mn *K*-edge XANES spectra of $x = 0.05$ and $x = 0.40$ are considered as the parent component for creating the linear combination spectra. The fitted XANES spectra with various proportions of $BiMnO_3$ and $BiMn_2O_5$ are shown as a solid curves superimposed on top of the measured XANES spectra in Figure 4(a). To validate this interpretation, we also performed *ab initio* calculation.

The FEFF 8.2 code is used to calculate the Mn *K*-edge XANES spectra of $BiMnO_3$ and $BiMn_2O_5$ for ensuring all features of extrapolated XANES spectra. Similarly, the calculated Mn *K*-edge XANES spectra with various compositions can be simulated by using the linear combination of the proportion of $BiMnO_3$ and $BiMn_2O_5$, as shown in Figure 4(b). More importantly, the features of the calculated XANES spectra confirmed the accuracy of extrapolated XANES spectra and are in good agreement with the corresponding measured spectra obtained from Mn-doped BFO samples. This result supports that (1) Mn atoms certainly occupy B-site (Fe) in Mn-doped BFO samples and (2) a small shift of the absorption edge to the higher energy and the broadening and increasing of p_1 and p_2 peaks of Mn *K*-edge XANES spectra of Mn-doped BFO samples probably occur due to the increasing of the formation of $BiMn_2O_5$ as the Mn content are increased, which cannot be revealed by XRD measurement. Therefore, the combined XANES measurement and XANES calculation is a powerful technique to probe the local structure of Mn atoms within the BFO lattices and can be applied to examine the trace secondary phase formation, not detectable by a conventional XRD measurement.

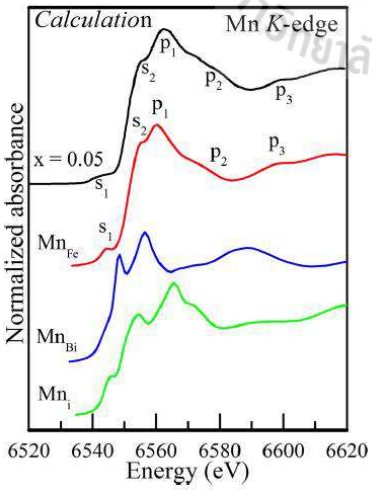

FIG. 3. The measured Mn *K*-edge XANES spectra of Mn-doped $BiFeO_3$ ceramics compared with the calculated Mn *K*-edge XANES spectra of the different Mn lattice locations (Mn_{Fe}, Mn_{Bi}, and Mn_i).

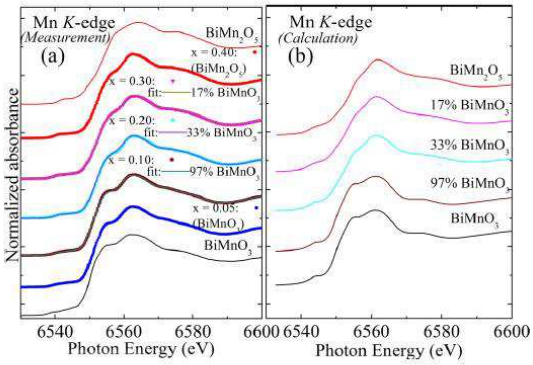

FIG. 4. (a) Comparison of the extrapolated $BiMnO_3$ and $BiMn_2O_5$ spectra (obtained from Yoneda *et al.*[19] and Shukla *et al.*,[20] respectively) and the measured Mn K-edge XANNES spectra of Mn doped BFO samples. Also included are the linear combination of Mn *K*-edge XANES spectra with various proportions of $BiMnO_3$ and $BiMn_2O_5$. (b) The calculated Mn *K*-edge XANES spectra of $BiMnO_3$ and $BiMn_2O_5$. The fitted linear combination XANES spectra are also plotted.

IV. CONCLUSIONS

In summary, Fe and Mn *K*-edge XANES measurement and *ab initio* XANES calculations are employed to determine the local structure of Mn atoms in Mn-doped $BiFeO_3$. Our measured Mn *K*-edge XANES spectrum clearly matches our XANES calculation of Mn atom substituting for Fe and inconsistent with that of Mn atom at other lattice locations, indicating that the majority of Mn atoms occupies the Fe site or B-site in BFO lattice. The calculated linear combination of Mn *K*-edge XANES with various proportion of $BiMnO_3$ and $BiMn_2O_5$ suggests that the increase of Mn content leads to the formation of $BiMn_2O_5$. The combination of XANES measurements and *ab initio* XANES calculations is demonstrated to be a very powerful tool for identifying local structure, oxidation state of a dopant in multiferroic $BiFeO_3$ materials. Finally, the technique reported here is also useful

in determining the formation of trace secondary phase(s), not detected by a conventional XRD technique, in BFO materials.

ACKNOWLEDGMENTS

Financial support for this work was provided by NANOTEC-SUT Center of Excellence on Advanced Functional Nanomaterials. J.J. and R.Y. also acknowledge SUT-Ph.D. Scholarship Program of Suranaree University of Technology through the Higher Education Research Promotion and National Research University Project of Thailand, Office of the Higher Education Commission.

[1]Y. Tokura, Science **312**, 1481–1482 (2006).
[2]M. Bibes and A. Barthélémy, Nature Mater. **7**, 425–426 (2008).
[3]S. V. Kiselev, R. P. Ozerov, and G. S. Zhdanov, Sov. Phys. Dokl. **7**, 742–744 (1963).
[4]C. Michel, J. M. Moreau, G. D. Achenbach, R. Gerson, and W. J. James, Solid State. Commun. **7**, 701 (1969).
[5]F. Kubel and H. Schmid, Acta Crystallogr.: Sect. E: Struct. Sci. **46**, 698 (1990).
[6]I. Sosnowska, W. Schäfer, W. Kockelmann, K. H. Andersen, and I. O. Troyanchuk, Appl. Phys. A **74**, 1040 (2002).
[7]V. R. Palkar, K. G. Kumara, and S. K. Malik, Appl. Phys. Lett. **84**, 2856 (2004).
[8]L. Hongri, L. Zuli, L. Xiaolu, and Y. Kailun, Physica B **400**, 252 (2007).
[9]Y. Wang, Q. H. Jiang, H. C. He, and C. W. Nan, Appl. Phys. Lett. **88**, 142503 (2006).
[10]H. Wang, H. Huang, and B. Wang, Sci. Adv. Mater. **2**, 184 (2010).
[11]S. Hunpratub, P. Thongbai, R. Yimnirun, and S. Maensiri, J. Supercon. Novel Magn. **25**, 1619 (2012).
[12]M. Unruan, T. Sareein, S. Chandarak, S. Hunpratub, P. Thongbai, S. Maensiri, and R. Yimnirun, Mater. Lett. **70**, 185 (2012).
[13]S. Limpijumnong, S. Rujirawat, A. Boonchun, M. F. Smith, and B. Cherdhirunkorn, Appl. Phys. Lett. **90**, 103113 (2007).
[14]J. T. Thienprasert, J. Nukeaw, A. Sungthong, S. Porntheeraphat, S. Singkarat, D. Onkaw, S. Rujirawat, and S. Limpijumnong, Appl. Phys. Lett. **93**, 051903 (2008).
[15]S. Limpijumnong, J. Jutimoosik, N. Palakawong, W. Klysubun, J. Nukeaw, M. H. Du, and S. Rujirawat, Appl. Phys. Lett. **99**, 261901 (2011).
[16]S. Hunpratub, R. Yimnirun, and S. Maensiri, "Effect of Mn doping on magnetic properties of $BiFeO_3$ Nanopowders," (unpublished).
[17]A. L. Ankudinov, C. E. Bouldin, J. J. Rehr, J. Sims, and H. Hung, Phys. Rev. B **65**, 104107 (2002).
[18]A. L. Ankudinov, B. Ravel, J. J. Rehr, and S. D. Conradson, Phys. Rev. B **58**, 7565 (1998).
[19]Y. Yoneda, Y. Kitanaka, Y. Noguchi, and M. Miyayama, Phys. Rev. B **86**, 184112 (2012).
[20]D. K. Shukla, S. Mollash, R. Kumar, P. Thakur, K. H. Chae, W. K. Choi, and A. Banerjee, J. Appl. Phys. **104**, 033707 (2008).

มหาวิทยาลัยเทคโนโลยีสุรนารี

Article published in Applied Physics Letter

APPLIED PHYSICS LETTERS **100**, 253102 (2012)

Direct manipulation of the uncompensated antiferromagnetic spins in exchange coupled system by GeV ion irradiation

Amitesh Paul,[1,a)] N. Paul,[2] C. Trautmann,[3] S. Mattauch,[4] Jaru Jutimoosik,[5] Rattikorn Yimnirun,[5] Saroj Rujirawat,[5] Britta Höpfner,[2] Iver Lauermann,[2] M. Lux-Steiner,[2] and P. Böni[1]

[1]*Technische Universität München Physik Department E21, James-Franck-Strasse 1, D-85748 Garching b. München, Germany*

[2]*Helmholtz-Zentrum Berlin für Materialien und Energie GmbH, Hahn-Meitner-Platz 1, D-14109 Berlin, Germany*

[3]*GSI Helmholtzzentrum für Schwerionenforschung GmbH, Planckstrasse 1, D-64291 Darmstadt, Germany*

[4]*Jülich Centre for Neutrom Science Forschungszentrum Jülich GmbH, Außenstelle am FRM-II c/o TU München, Lichtenbergstraße 1, D-85747 Garching b. München, Germany*

[5]*School of Physics, Institute of Science, Suranaree University of Technology and Synchrotron Light Research Institute, Nakhon Ratchasima, Thailand*

(Received 15 February 2012; accepted 29 May 2012; published online 18 June 2012)

Incident ion energy to matrix electrons of a material is dissipated within a narrow cylinder surrounding the swift heavy ion path. The temperature of the lattice exceeds the melting point and upon quenching causes nanometric modifications. We present here a unique *ex situ* approach in manipulating the uncompensated spins in antiferromagnetic layers of ferro-/antiferromagnetic exchange coupled systems on a nanometric scale. We use the impact of relativistic heavy ion (1–2 GeV) irradiation on such systems. We find an increase in the bias field and a restoration of the reversal via domain nucleation in the trained state. These are identified as plausible results of ion-induced antiferromagnetic ordering with little or no effect on the layer structure. This study demonstrates, therefore, the possibility of nanoscale tailoring of exchange coupled systems that survive even in the trained state. © *2012 American Institute of Physics*. [http://dx.doi.org/10.1063/1.4729472]

The passage of ions through matter has an interaction time $\sim 10^{-17}$ s (e.g., a 5 MeV/nucleon ion has a velocity $\approx$10% of the speed of light) and can create atomic point or extended defects within a hot cylindrical zone ($\sim$10 nm radius) of atoms in quasi-thermal equilibrium.[1] The slowing down of ions results from energy loss in solids. This can be either by inelastic collisions of the ions with electrons or by elastic collisions with the nuclei of the target atoms. A simple choice of the ion energies determines if it is in the regime of collision cascades or of electronic excitation with subsequent electron-phonon coupling. S_n [keV/nm] is the nuclear stopping power that dominates for the keV range of ions whereas S_e [keV/nm] is the electronic stopping power that dominates for the MeV range of ions.

It has been shown earlier that the coercive field and magnetic anisotropy of magnetic multilayers (MLs) can be accurately controlled by low energy irradiation in the elastic[2] or by high energy ions in the inelastic[3] regime. Particularly, local manipulations of magnetization in the inelastic regime are (a) confined to a few nanometers only (b) without significant modification of the interface structure, and (c) applicable for *ex situ* changes. Thus irradiation techniques offer means of magnetic-tailoring devices in information technology such as in exchange biased system.[4]

We have taken the example of ion irradiation in exchange bias systems which demands a complete understanding[5] of various other bias-related phenomena, such as coercivity enhancement,[6,7] asymmetric hysteresis loops,[8–10] and last but not the least the training effect.[11] An important issue has been the loss of magnetic memory upon repeated field cycling in exchange biased spin-valve systems. Direct manipulation of the antiferromagnetic (AF) spins in exchange biased systems enables us not only to tune the bias field but also to have a control over the coupled magnetization reversal mechanism.

In the low-energy ion regime, ballistic mixing causes atomic rearrangements, which subsequently modify the magnetic properties. It is possible to increase or decrease exchange bias field H_{eb} and also change its direction by *in-situ* irradiation.[12–14] The effect is due to orders of magnitude more energy as compared to thermal energy deposition (e.g., field cooling).[12,15] High energy heavy ions are liable to produce amorphization in a perturbed cylinder along the ion path beyond a threshold of energy transfer.

In this work, we demonstrate a unique way of affecting the uncompensated AF spins of an archetypical exchange coupled system as we irradiate it with GeV energy ions. The irradiations are done after deposition of the films in absence of any *in-situ* field. We show here that the irradiated samples have an increase in their H_{eb}. More interesting is the manipulation of the magnetization reversal mechanism that persists even in the trained state. Such unique manipulation of reversal mechanism has not been reported thus far.

We have investigated a ML of the composition $SiO_2/[Co(11.0\,nm)/CoO(5.0\,nm)/Au(22.5\,nm)]_{N=16}$. The usual pressure in the magnetron sputtering chamber was 3×10^{-3} mbar in Ar atmosphere during deposition with a base pressure of 1×10^{-7} mbar. We employ an ultra-violet light assisted oxidation at an O_2 pressure of 200 mbar at

a)Author to whom correspondence should be addressed. Electronic mail: amitesh.paul@frm2.tum.de. Tel.: 0049 89-28914717. Fax: 0049 89-28914713.

 © 2012 American Institute of Physics

50 °C for 1 h.[16] Irradiations were performed at GSI Helmholtzzentrum für Schwerionenforschung. Four $15 \times 15\,mm^2$ samples were cut from a single homogeneous piece ($30 \times 30\,mm^2$) for the irradiation. Thereby one can rule out any changes in their characteristics due to deposition conditions. The ion fluences used are 1×10^{12}, and 1×10^{13} ions/cm^2 for 8.4 MeV/amu of $197Au^+$ (1.6 GeV) and $238U^+$ (2 GeV) ions. Calculations using the transport of ions in matter (TRIM) code (J. P. Biersack TRIM91) indicate that GeV ions travel through the entire stack of our specimens.

Conventional in-plane magnetization loops are measured using a superconducting quantum interference device (SQUID) MPMS from Quantum design. Depth sensitive vector magnetometry was done using polarized neutron scattering at the TREFF reflectometer at FRM-2. We measure specular and off-specular intensities which contain significant information regarding the vertical and the lateral correlations of the layer structure and the magnetic structure. The neutron wavelength is fixed at $\lambda = 4.73$ Å. Details on the technique and a corresponding review can be found elsewhere.[17] In our experiment four different cross sections can be distinguished, namely, non spin-flip (NSF) (R_{++} and R_{--}) and spin-flip (SF) channels (R_{+-} and R_{-+}) measuring the respective longitudinal and transverse component of magnetization with respect to the guiding field. We use a cooling field $H_{FC} = +4.0$ kOe down to 10 K directed along an in-plane direction for all specimens. The K-edge Co x-ray absorption near-edge structure (XANES) measurements were performed in the fluorescent mode with a 13-compoment Ge detector at the x-ray absorption spectroscopy beamline (BL-8) of the Siam Photon Source (electron energy of 1.2 GeV, beam current 80–120 mA), Synchrotron Light Research Institute, Thailand. A double crystal Ge (220) monochromator was used to scan the synchrotron x-ray with a photon energy step of 0.30 eV. Additionally, at Berliner Elektronenspeicherring Gesellschaft für Synchrotronstrahlung GmbH (BESSY) in the CISSY end-station at the high-flux beamline U41-PGM, the photon energy is swept through the L3 (778 eV) and L2 (798 eV) edges of Co. The absorption cross-section is measured by collecting the energy selective fluorescence yield using a commercial XES300 spectrometer with an energy resolution of 0.43 eV. Microstructural characterization has been done using cross-sectional transmission electron microscopy (XTEM).

Figure 1(a) shows the hysteresis loops corresponding to the room temperature and the field cooled states of the as-

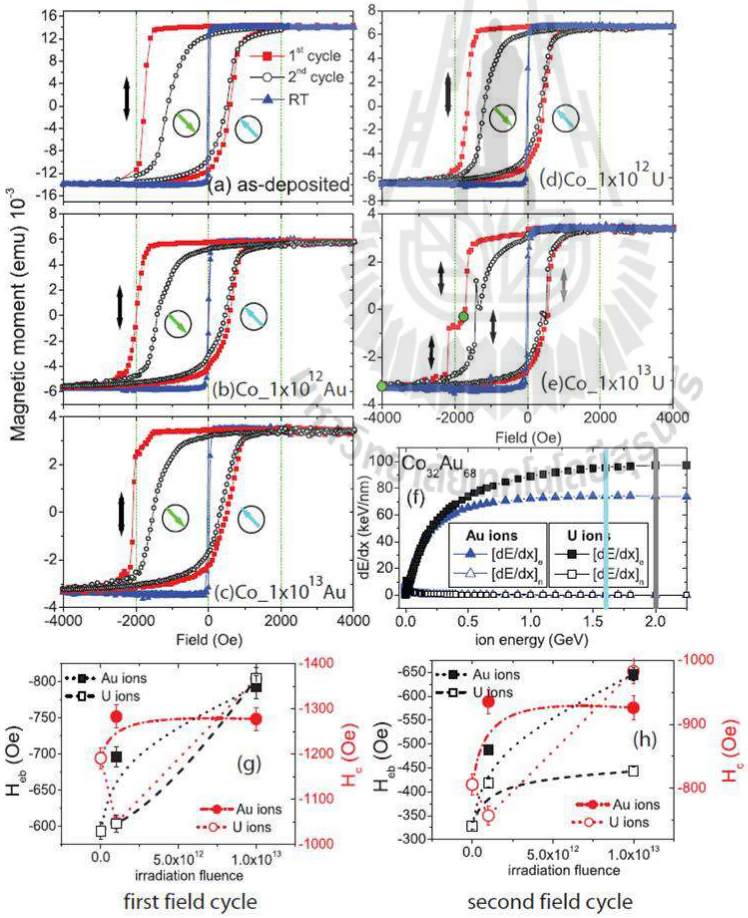

FIG. 1. SQUID magnetization hysteresis loops for the $[Co/CoO/Au]_{16}$ ML of (a) as-deposited specimen and for different fluences of (b–c) Au ion irradiation and (d), (e) U ion irradiation. The measurements are done at room temperature and at 10 K after cooling down at H_{FC}. The differently shaded arrows (vertical and rotating arrows) indicate the magnetization reversal mechanism along the respective branches of the loops. The green circles indicate the fields of neutron measurements shown later. (f) TRIM simulations on Co-Au target showing the electronic energy loss as compared to the nuclear energy loss with respect to the energies of Au and U ions. The ion energies used are indicated by lines. (g), (h) Plots of H_{eb} (squares) and H_C (circles) as a function of irradiation fluence of Au and U ions respectively during the first and second field cycles.

deposited specimen. A characteristic negative exchange bias and an asymmetric reversal: domain wall and nucleation (nonuniform reversal) in the decreasing (applied field opposite to the cooling field) branch is indicated by vertical arrows and coherent rotation (uniform reversal) in the increasing branch indicated by rotating arrows can be seen. This asymmetry disappears, as usual, during the second field cycling with a decrease in the bias field. Figures 1(b) and 1(c) and Figures 1(d) and 1(e) show similar hysteresis loops for the Au irradiated and U irradiated specimens, respectively. For the Au irradiated specimens and for the U 1×10^{12} ions irradiated specimen, even though one can see an increase in the H_{eb}, the magnetization reversal mechanism remain quite similar to that of the as-deposited specimen. The most interesting thing happens in the magnetization reversal mechanism for the U 1×10^{13} ions irradiated specimen. The loop is divided into two distinct parts. There are distinct steps at around 1650 and 1500 Oe (during the first and second field cycles, respectively) which are signatures of non-uniform reversal. While the upper part is fairly similar to that of the unirradiated (as-deposited) one, the lower part has undergone a significant shift. This extra shift leads to a distinct increase in exchange bias. Note that not only the first half of the first cycle (decreasing branch) shows the nonuniform reversal (indicated by vertical arrows) but also the second half of the first field cycle and also the increasing branch of the second field cycle. Henceforth we concentrate on the U 1×10^{13} ions irradiated specimen as it is most affected by the irradiation. The H_{eb} and H_{eb} are plotted with irradiation fluence of the ions in Figure 1(g) and 1(h).

Controlled columnar defects produced by swift heavy ions in high temperature superconducting materials have been shown to improve their properties.[18] However, in our system, GeV heavy ions could not produce any latent track damage visible by electron microscope since Co/Au system being metallic is not a good track-recording material. Figure 2 shows the XTEM pictures for the as deposited and the sample irradiated with 1×10^{13} ions/cm^2 U ions. Interesting, however, is that the layer structure remain pretty much unaffected after irradiation only the columnar Au grains in the as-deposited sample appear fractured in the sample irradiated with U ions.

Figure 3 shows the specular reflectivity data (NSF and SF) and the off-specular SF intensities corresponding to two different applied fields (H_a), indicated by circles in Figure 1(e) for the U 1×10^{13} ions irradiated ML. We also plot the spin asymmetry (SA) signals (difference in R_{--} and R_{++} divided by the sum of the two) as we compare it with the as-deposited specimen at saturation.[19] Relative variation of the multilayer Bragg peak intensities is quite evident here. Fits to the reflectivity data revealed a small increase in the AF layer (~1–2 nm) at the Co-CoO interface. The NSF intensity map shows vertically correlated multilayer interfaces added up in phase and forming the Bragg sheets in reciprocal space at the first Bragg peak position of 15 mrad. A small increase in the SF intensity at Q = 0.02 Å, measured during the first field cycle close to the coercive field (as compared to that in saturation), is only due to an increased instability induced in the system as the layers are on the verge of flipping and cannot be attributed to coherent rotation of the layers (a similar behavior is observed during the second field cycle as well). This is further corroborated by an increase in the off-specular SF intensities near the critical edge around the coercive field, a typical signature of random non-collinear arrangement of small scale (<1 μm) domains just before flipping.[19,20] Distorted wave Born approximation (DWBA) has been applied in simulating the corresponding SF intensity map.

The observed increase in H_{eb}, can be intuitively explained by intrinsic defects within the Co-Co_xO_y layers due to changes in oxidation atmosphere during the passage of high energy ions. This obviously can be related to stronger pinning of the domain walls at the defect sites. Figure 4(a) shows the measured Co K-edge XANES spectra of the samples and the reference spectra of CoO, Co_3O_4, and Co metal. By considering CoO, Co_3O_4, and Co metal as the parent components, the spectra of all the samples are fitted with varying proportion (indicated within the figure) using linear combination analysis (LCA) method in ATHENA.[21] The calculated spectra using the FEFF 8.2 codes[22] based on *ab initio* multiple scattering is also compared with the measured data. A very good agreement with the measured XANES spectra in both energy positions and shapes lead us to infer that all the MLs are composed of Co metal and CoO in phase-separated regions (Co_3O_4 content remains similar ≈2%).

We show the L-edge spectra from our U-irradiated MLs in Figure 4(b). One can see two broad peaks with broadened bases, a typical signature of localized character of the 3d states. We do not observe any shift in the absorption energies as they are separated by 15.3 eV for the MLs and also note

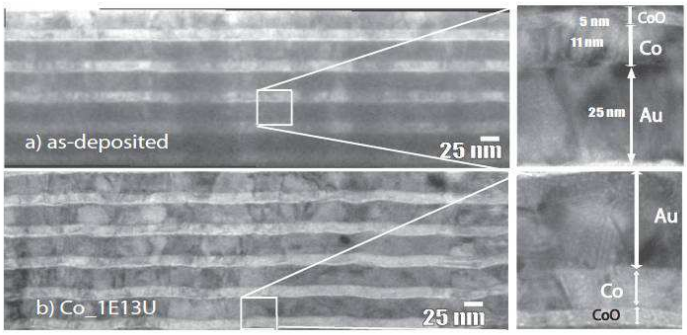

FIG. 2. XTEM micrographs of $[Co/CoO/Au]_{16}$ ML for (a) as-deposited and (b) U 1×10^{13} ion-irradiated sample.

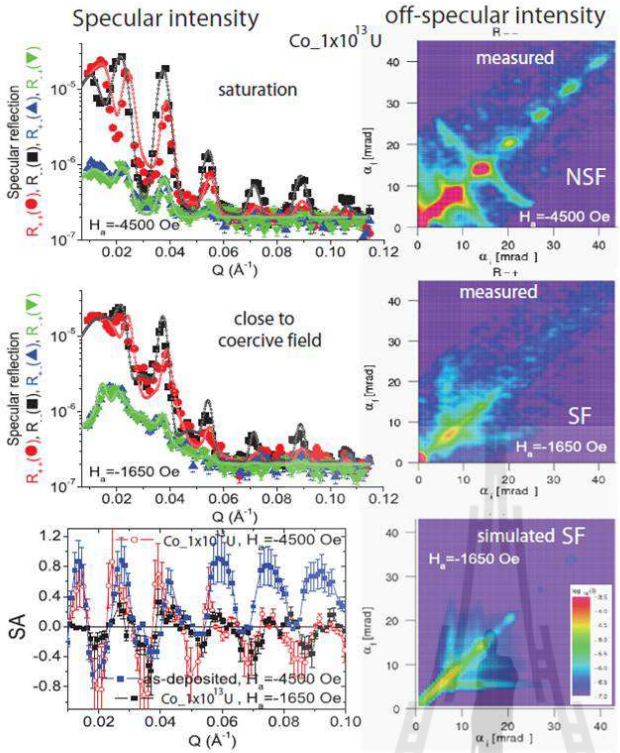

FIG. 3. Specular reflectivity patterns (solid symbols) along with their fits (open symbols) at two different applied fields, for the ML irradiated with U 1×10^{13} ions. The measurements were done during the first field cycle at field indicated in Fig. 1(e) after cooling the sample in field down to 10 K. $\vec{Q} = \frac{2\pi}{\lambda}[\sin(\alpha_i) + \sin(\alpha_f)]$, where $\alpha_{i,f}$ are the incident and exit angles. The SA signal is also plotted in the bottom panel for comparison with the as-deposited specimen. The right hand panels show the measured NSF and SF intensity maps along with DWBA simulated patterns at around the coercive field for the SF channel.

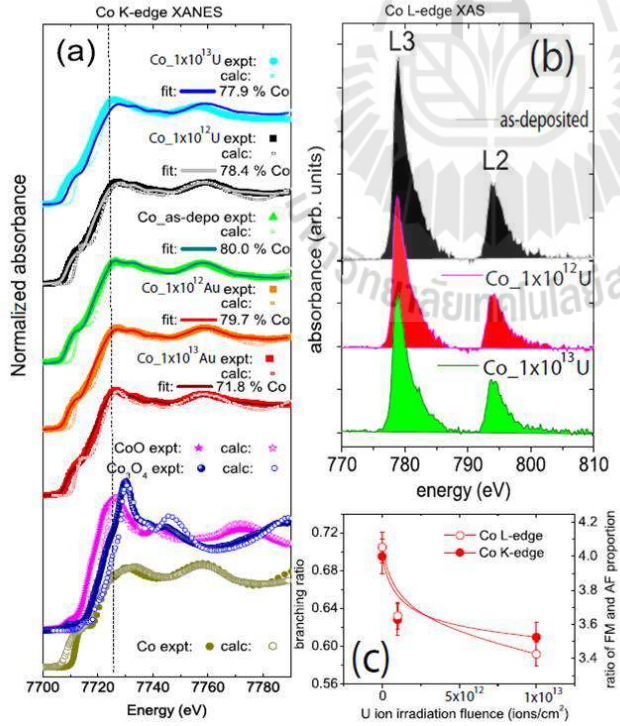

FIG. 4. (a) Comparison of the measured Co K-edge normalized XANES spectra of all the MLs along with their fits and compared with the calculated spectra. Also included are the reference spectra of CoO and Co metal. (b) L-edge XAS spectra for the U 1×10^{13} ions irradiated samples. (c) The intensity ratio (L-edge) and the AF-FM ratio (K-edge) for the same ML with fluence.

that the peak-to-peak distance of the $L_{2,3}$ absorption lines remains unchanged. The amount of core-hole screening by delocalized valence electrons is therefore negligible.[23] To avoid the lifetime broadening and the experimental broadening contributions it is helpful to opt for the so called branching ratio calculated as $I(L_3)/[I(L_2)+I(L_3)]$. The peak intensity ratio is shown in Figure 4(c).[24] The ratios are calculated from the area under the respective peaks using the IFEFFIT package.[25] The changes in the intensity ratio (transfer of the spectral weight between the two edges) is a measure of the angular part of the spin-orbit operator. It shows a decreasing trend with fluence of U ions which further corroborates with the increasing Co valency. Therefore, the increased H_{eb} in our samples can be attributed to the gradual decrease in the ferromagnet (FM)-AF proportion ratio with irradiation fluence as shown in Figure 4(c). Note that our AF thickness is below a typical critical AF thickness of $\approx$10 nm.[26]

In the electronic slowing-down regime, most of the energy of the incident ions is transferred to the host electrons, resulting in a high electronic ionization (ionic spike $\sim 10^{-14}$ s) and/or a high temperature increase of the electronic subsystem (thermal spike $\sim 10^{-12}$ s). Recently it has turned out that "coulomb explosion"/ion spike produces a "heat" spike and thus these are early and late aspects of the same process. According to the thermal-spike model, the energy locally deposited in matter is quickly shared among the electron gas by electron-electron interactions and then transferred to the neighboring atoms by electron-phonon (E-P) and phonon-phonon interactions.[27] The temperature along the ion path can be of the order of 5×10^4 K within a cylindrical range of 5–10 nm along the ion path which is followed by rapid quenching (10^{14} K s^{-1}) resulting in latent tracks. S_e induced defects can be created in Ti, Co, and Fe as they exhibit stronger electron-phonon coupling than in Ag, for example. The calculated threshold of defect creation induced by S_e for Co is about 28–34 keVnm^{-1} for 5–20 MeV/amu ions.[28] Figure 1(f) shows the dominance of electronic energy loss over nuclear energy loss for 1.6 GeV Au and 2 GeV U ions in a Co/Au system calculated by TRIM. For our system, the $S_e = \frac{dE}{dx}|_e$ is greater than 73 keVnm^{-1} and 97 keVnm^{-1} for Au and U, respectively ($\propto$ ion atomic number Z^2), which can give the latent track radius of about $\approx$2–10 nm.[3] The lattice temperature increase is proportional to S_e, which renders the related E-P coupling factor relatively higher for U ions than that for Au.

Ion-induced magnetic manipulation allows us to increase H_{eb} and recover untrained magnetization states in an otherwise trained exchange coupled system. The method demonstrated here is limited to nanometric scale with little influence on their interface structure. Such local manipulation holds promise for post production extrinsic treatment of integrated magnetic memory devices or sensors by choosing "specific" (energy/nucleon) ion energies.

This work was supported by the Deutsche Forschungsgemeinschaft via the Transregional Collaborative Research Centers TRR 80. We would also like to thank Ulrike Bloeck for the assistance in TEM measurements.

[1]B. E. Fischer and R. Spohr, Rev. Mod. Phys. **55**, 907–948 (1983).
[2]C. Chappert, H. Bernas, J. Ferr, V. Kottler, J.-P. Jamet, Y. Chen, E. Cambril, T. Devolder, F. Rousseaux, V. Mathet, and H. Launois, Science **19**, 1919 (1998).
[3]A. Paul and S. Mattauch, New. J. Phys. **12**, 103003 (2010).
[4]W. H. Meiklejohn and C. P. Bean, Phys. Rev. **102**, 1413 (1956).
[5]J. Nogués and I. K. Schuller, J. Magn. Magn. Mater. **192**, 203 (1999); A. E. Berkowitz and K. Takano, J. Magn. Magn. Mater. **200**, 552 (1999).
[6]M. D. Stiles and R. D. McMichael, Phys. Rev. B **59**, 3722 (1999).
[7]M. Gruyters and D. Schmitz, Phys. Rev. Lett. **100**, 077205 (2008).
[8]M. Gierlings, M. J. Prandolini, H. Fritzsche, M. Gruyters, and D. Riegel, Phys. Rev. B **65**, 092407 (2002).
[9]M. R. Fitzsimmons, P. Yashar, C. Leighton, I. K. Schuller, J. Nogues, C. F. Majkrzak, and J. A. Dura, Phys. Rev. Lett. **84**, 3986 (2000).
[10]A. Paul, E. Kentzinger, U. Rücker, and Th. Brückel, Phys. Rev. B **74**, 54424 (2006).
[11]A. Paul and S. Mattauch, Appl. Phys. Lett. **95**, 092502 (2009).
[12]A. Ehresmann, Recent Res. Dev. Appl. Phys. **7**, 401 (2004).
[13]D. Engel, A. Kronenberger, M. Jung, H. Schmoranzer, A. Ehresmann, A. Paetzold, and K. Roll, J. Magn. Magn. Mater. **263**, 275 (2003).
[14]J. Fassbender, D. Ravelosona, and Y. Samson, J. Phys. D: Appl. Phys. **37**, R179 (2004).
[15]A. Ehresmann, D. Junk, D. Engel, A. Paetzold, and K. Roll, J. Phys. D **38**, 801 (2005).
[16]A. Paul, D. Bürgler, M. Luysberg, and P. Grünberg, Europhys. Lett. **68**, 233 (2004).
[17]A. Paul, Pramana **78**, 1 (2012).
[18]D. Kanjilal, Curr. Sci. **80**, 25 (2001), http://www.iisc.ernet.in/currsci/jun252001/1560.pdf.
[19]A. Paul, N. Paul, and S. Mattauch, New J. Phys. **13**, 063008 (2011).
[20]A. Paul, E. Kentzinger, U. Rücker, D. Bürgler, and P. Grünberg, Phys. Rev. B **70**, 224410 (2004).
[21]B. Ravel and M. Newville, J. Synchrotron Radiat. **12**, 537 (2005).
[22]A. Ankudinov, B. Ravel, J. Rehr, and S. Conradson, Phys. Rev. B **58**, 7565 (1998).
[23]J. T. Lau, J. Rittmann, V. Zamudio-Bayer, M. Vogel, K. Hirsch, Ph. Klar, F. Lofink, and T. Möller, B. v. Issendorff, Phys. Rev. Lett. **101**, 153401 (2008).
[24]B. Thole and G. van Der Laan, Phys. Rev. B **38**, 3158 (1988).
[25]B. Revel and M. Newville, J. Synchrotron Radiat. **12**, 537 (2005).
[26]X. Y. Lang, W. T. Zheng, and Q. Jiang, Nanotechnology **18**, 155701 (2007).
[27]Z. G. Wang, C. Dufour, E. Paumier, and M. Toulemonde, J. Phys.: Condens. Matter **6**, 6733 (1994).
[28]A. Dunlop and D. Lesueur, Rad. Eff. Defects Sol. **126**, 123 (1993).

Article published in Physical Review B

Change in interface magnetism of an exchange-coupled system due to the presence of nonmagnetic spacers

Amitesh Paul,[1,*] N. Paul,[2] Jaru Jutimoosik,[3] Rattikorn Yimnirun,[3] Saroj Rujirawat,[3] Britta Höpfner,[2] Iver Lauermann,[2] M. Lux-Steiner,[2] Stefan Mattauch,[4] and Peter Böni[1]

[1]*Technische Universität München, Physik Department E21, Lehrstuhl für Neutronenstreuung, James-Franck-Strasse 1, D-85748 Garching b. München, Germany*

[2]*Helmholtz-Zentrum Berlin für Materialien und Energie GmbH, Hahn-Meitner-Platz 1, D-14109 Berlin, Germany*

[3]*School of Physics, Institute of Science, Suranaree University of Technology, Nakhon Ratchasima, and Thailand Center of Excellence in Physics (ThEP Center), Commission on Higher Education, Bangkok, Thailand*

[4]*Jülich Centre for Neutron Science Forschungszentrum Jülich GmbH, Außenstelle am FRM-II c/o TU München, Lichtenbergstraße 1, D-85747 Garching b. München, Germany*

(Received 27 April 2012; revised manuscript received 3 September 2012; published 28 January 2013)

We report on the effect of nonmagnetic spacer layers on the interface magnetism and the exchange bias in the archetypical $[Co/CoO]_{16}$ system. The separation of the magnetic bilayers by Au layers with various thicknesses $d_{Au} \geqslant 25$ nm leads to a threefold increase of the exchange bias field (H_{eb}). Reflectometry with polarized neutrons does not reveal any appreciable change in the domain population. This result is in agreement with the observation that the granular microstructure within the [Co/CoO] bilayers is independent of d_{Au}. The significant reduction of the magnetic moments in the Co layers can be attributed to interfacial disorder at the Co-Au interfaces. Element-specific x-ray absorption spectroscopy attributes part of the enhancement of H_{eb} to the formation of Co_3O_4 in the [Co/CoO] bilayers within the multilayers. A considerable proportion of the increase of H_{eb} can be attributed to the loss of magnetization at each of the Co-Au interfaces with increasing d_{Au}. We propose that the interfacial magnetism of ferro- and antiferromagnetic layers can be significantly altered by means of metallic spacer layers thus affecting the exchange bias significantly. This study shows that the magnetism in magnetic multilayers can be engineered by nonmagnetic spacer layers without involving the microstructure of the individual layers.

DOI: 10.1103/PhysRevB.87.014431 PACS number(s): 75.70.Cn, 75.60.Jk

I. INTRODUCTION

As new magnetic hard-disk-drive products are designed for higher storage densities in magnetic recording materials, the "superparamagnetic effect" has become increasingly important.[1] As the grains become smaller (50–100 nm), due to thermally activated fluctuations, the magnetization of the grains may become unstable. One approach to delay superparamagnetism is to increase the magnetic anisotropy or the unidirectional anisotropy.

The exchange bias phenomenon can be described as a form of a unidirectional magnetic anisotropy that arises due to the interfacial exchange coupling between a ferromagnet (FM) and an antiferromagnet (AF) and can effectively delay the superparamagnetic limit.[2] In most usual cases, the AF ordering temperature is lower than that of the FM, below which one observes a horizontal shift of the hysteresis loop. However, temperature-dependent competition between interfacial exchange and AF anisotropy energies can result in bias fields even for materials with higher AF ordering temperature.[3] Conventionally, a cooling field (H_{FC}) provides the unidirectional anisotropy while the shift is observed opposite to the applied field (H_a) direction. Over the last decade many salient features of the exchange bias effect have been clarified. It turns out that only a very small percentage of moments at the AF interface are pinned while the rest of the moments rotate rigidly with the FM. It also turns out that it is energetically favorable to form domains in the antiferromagnet. They account for the lowering of the energy cost associated with the reversal of the FM that determines the strength of the bias field (H_{eb}).[4–6] Exchange bias is also associated with many salient features such as coercivity enhancement,[7,8] asymmetric hysteresis loops,[9,10] and training effects.[11]

One of the interesting problems in multilayer physics is the influence of the interface between the magnetic film and the nonmagnetic spacer on kinetic, magnetic, and magnetooptical properties of thin-film systems. Information concerning effects of (a) an underlayer grain morphology and a grain crystallographic orientation (texture of the grains) on magnetic properties,[12] (b) induced magnetic moments via *s-d* hybridization,[13] (c) interface alloying,[14] and (d) canted magnetic structure are intrinsic to interfaces between magnetic-nonmagnetic magnetic layers.[15] These are highly relevant to systems that are used as magnetic field sensors, read heads, or memory devices.

It may be noted that exchange bias systems are often coated with a Au film, in order to protect them against further oxidation.[16] Moreover, Au is often used as metallic leads for spin-valve structures. Thus the Au/FM (or AF) interfaces and their effect on exchange bias cannot be ignored. In general, the introduction of a nonmagnetic (NM) metallic spacer such as Cu, Ag, or Au between the FM and FM/AF layers modifies the interface coupling between them. Therefore it is of great interest to obtain information about the spin directions in the vicinity of the interfaces. This aspect, however, remains largely unexplored. In fact, there are no studies on the impact of the

 ©2013 American Physical Society

AF/Au or FM/Au interface magnetism including the effects of roughness and interdiffusion on the exchange bias phenomena. The aim of this study is, therefore, to systematically investigate the magnetisation of exchange coupled bilayers of Co/CoO that are separated by nonmagnetic Au spacer layers.

Contrary to the expectations, we show here that the exchange bias field increases gradually with increasing thickness of the Au spacer layer. As expected, the magnetization reversal mechanism remains asymmetric for the two branches of the hysteresis loops, however, it shows significantly increased coerciveness along both branches with increasing thickness of the Au layers. These effects occur despite the fact that the diameter of the magnetic grains attains a similar size as the Au spacer thickness and that the FM domains show no significant variation in their size. It appears that the impact of the metallic Au spacer adjacent to an AF or FM is very significant for exchange bias systems in general as it can alter the interfacial magnetism.

II. SAMPLES AND MEASUREMENTS

A. Sample preparation

Over the years, Co/CoO has served as a prototypical exchange bias system, even though it is not actually technologically practical. In fact, very recent extensive investigations are on the same AF/FM combination.[16–19] It is ideal for investigation due to its large biasing field,[6] very distinct asymmetry of magnetization reversal,[5] large enough training effects,[11] and most interestingly, the AF moment configuration can be frozen-in in a variety of ways during the process of field cooling[20] without affecting the overall structure as the AF ordering temperature is far below room temperature (negligible interdiffusion at the interfaces).

We have investigated multilayers of the composition SiO_2/[Co(11.0 nm)/CoO(5.0 nm)/Au(25,30,50 nm)]$_{N=16}$ and compare them with SiO_2/[Co(11.0 nm)/CoO(7.0 nm)]$_{N=20}$/Au(50 nm). A schematic of the layer structure is shown in Fig. 1. During deposition, the Ar pressure in the magnetron sputtering chamber was 3×10^{-3} mbar. The process was started at a base pressure of 1×10^{-7} mbar. We employ an ultraviolet light assisted oxidation at an O_2 pressure of 200 mbar at 50 °C for 1 hour.[21]

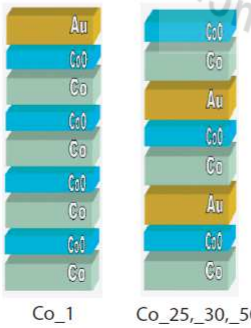

FIG. 1. (Color online) Schematic of the layer structures, namely, Co_1 having no spacer layer and Co_25, Co_30, and Co_50 having the bilayers separated by Au spacer layers.

B. Measurement techniques

1. Magnetometery

Conventional in-plane magnetization loops are measured using a superconducting quantum interference device (SQUID) MPMS and a physical property measurement system (PPMS) from Quantum design. We use a cooling field $H_{FC} = +4.0$ kOe within the sample plane for all specimens inducing an exchange bias as the system is cooled down to 10 K.

2. X-ray scattering and microscopy

X-ray diffraction patterns from the samples confirm the $[111]_{fcc}$ structure for the Au and Co layers. The microstructural characterization was performed using cross-sectional transmission electron microscopy (XTEM). Studies with transmission electron microscopy have been carried out on cross-sectional samples prepared by standard mechanical (diamond) polishing followed by Ar^+ ion milling at 4 kV for about 1 hour. A conventional bright-field imaging mode was used.

3. Polarized neutron scattering

Polarized neutrons are an excellent probe for investigating the in and out of plane correlations of the ferromagnetic domains. Depth-sensitive polarized neutron scattering measurements are performed at the neutron reflectometer TREFF at FRM II using polarization analysis. The specular as well as the off-specular data were measured. The neutron wavelength was fixed at $\lambda = 4.73$ Å. Details on the technique and a corresponding review can be found elsewhere.[23] In the experiment, four different cross sections are measured, namely, non-spin-flip (NSF) (R_{++} and R_{--}) and spin-flip (SF) (R_{+-} and R_{-+}) channels . Here, the subscripts + and − designate polarizations of the neutron beam parallel or antiparallel to the guide field, respectively. The specimens are field cooled in $H = 4.0$ kOe to 10 K inside a cryostat at the instrument. The NSF intensities provide the amplitude of the projection of the magnetization along the polarization direction of the neutrons ($M_{\parallel}$), while the SF intensities provide information about the magnetization components perpendicular to the polarization direction ($M_{\perp}$). The latter contributions are exclusively of magnetic origin.

4. X-ray absorption spectroscopy

An increase in the bias field H_{eb} can originate from the formation of defects within the antiferromagnetic Co_xO_y layer or from deviations in the stoichiometry during the course of the oxidation of Co to CoO[21] leading to a stronger pinning of the domain walls at the defect sites thus resulting in an increase of H_{eb}.[24] To verify the formation of such defect sites that can be inadvertently related to the degree of oxidation of the Co layer (few nanometers), it is necessary to investigate the proportion and stoichiometry of the CoO layers in the system. Such a detailed examination of the chemical species can be effectively done by x-ray absorption spectroscopy (XAS).

TABLE I. Samples and their saturation magnetization and exchange energy. The bilayers Co/CoO of sample Co_1 are not separated by Au spacer layers.

Composition	Label	M_{FM} (emu cm^{-3})	Magnetic moment μ_B/Co(FM)	E (erg cm^{-2})
[Co(11.0 nm)/CoO(7.0 nm)]$_{20}$/Au(50 nm)	Co_1	1694 ± 100	2.01 ± 0.2	0.75 ± 0.05
[Co(11.0 nm)/CoO(5.5 nm)/Au(25 nm)]$_{16}$	Co_25	1132	1.34	0.72
[Co(11.0 nm)/CoO(5.0 nm)/Au(30 nm)]$_{16}$	Co_30	992	1.18	0.73
[Co(11.0 nm)/CoO(5.0 nm)/Au(50 nm)]$_{16}$	Co_50	726	0.86	0.79

XAS is generally used to obtain information about the local arrangement of atoms around the absorbing atoms. In particular, the x-ray absorption near-edge structure (XANES) region corresponds to the excitation of core electrons to unoccupied bound states or to low lying continuum states. It thus turns out that the angular momentum and site projected partial density of empty states, with some broadening, resemble the XANES absorption spectra.

The Co K-edge XANES measurements were performed in the fluorescent mode with a 13-component Ge detector at the x-ray absorption spectroscopy beamline (BL-8) of the Siam Photon Source (electron energy of 1.2 GeV, beam current 120–80 mA), Synchrotron Light Research Institute, Thailand. A double crystal monochromator Ge (220) was used to scan the energy of the synchrotron x-ray beam with energy steps of 0.30 eV.

Further, we performed Co $L_{2,3}$ edge XAS measurements on the specimens. The XAS spectra result from Co $2p \longrightarrow 3d$ dipole transitions ($2p^{3/2}$ and $2p^{1/2}$ core-shell electrons to unoccupied $3d$ orbitals).[25] Comparing with the *ab initio* calculations of the L-edge and K-edge structure of Co, CoO, and Co_3O_4, it is possible to identify the individual constituents of magnetic species in the system.

The absorption cross section is measured by collecting the energy selective fluorescence yield using a commercial XES300 spectrometer with an energy resolution of 0.89 eV at the CISSY end station of the high-flux beamline U49/2-PGM1 installed at the Berliner Elektronenspeicherring Gesellschaft für Synchrotronstrahlung GmbH (BESSY). The photon energy is swept through the $L3$ (778 eV) and $L2$ (798 eV) edges of Co. The detector consists of a multichannel plate in conjunction with a resistive anode assembly. We integrate the x-ray emission spectroscopic signal to get the florescence signal.

In principle, x-ray magnetic dichroism (XMCD) can selectively probe the induced magnetic moment of Au in Co/Au multilayers and separate it into spin and orbital terms.[26] However, XMCD (sensitive to p, d, and f-electron polarization) is a surface sensitive technique as the probing depth in the soft x-ray regime is ∼5.0 nm in the electron yield (EY) mode and ∼100 nm in the fluorescence yield (FY) mode. FY dichroism measurements are extremely sensitive to saturation and self-absorption effects, complicating the evaluation. Thus it is almost impossible to investigate the interface of an ML with a thicker spacer at deeply buried interfaces (as in the present case).

Alternatively, by using the low-temperature nuclear orientation (LTNO) technique, one can detect the average magnitude and alignment of the nuclear spins which can be due to the induced nuclear polarization in the nonmagnetic Au spacer (s-moment polarization).[15] Canting of the induced Au magnetic moments was found to originate at the AF(FM)/Au/AF(FM) interface as well as canting of the Co moments (reducing the net moment of the uncompensated spins) was observed earlier in AF/Au/FM interfaces. However, a detailed inspection of the interface magnetization (depending upon the structure of the interface) was limited by the level of resolution available with the technique, and it also requires milli-Kelvin sample environment, which is not commonly available.

III. RESULTS AND DISCUSSION

A. Magnetization

The labeling of the samples along with the saturation magnetization per unit volume (M_{FM}) and the magnetic moment per Co (FM) atom is given in Table I. The exchange coupling energy[27] per unit surface area is usually given by

$$E = -J_E M_{AF} M_{FM} t_{FM} \cos\delta = -H_{eb} M_{FM} t_{FM} \cos\delta.$$

The *unidirectional* anisotropy energy is characterized by the exchange coupling constant J_E. The unidirectional anisotropy K_{ud} is included in $J_E M_{AF} M_{FM}$ in terms of the exchange field $H_{eb} = J_E M_{AF}$. Here, t_{FM} is the thickness of the FM layer and δ is the angle between M_{FM} and the easy axis of the FM. M_{FM} and M_{AF} are the respective magnetizations. We define the exchange bias shift $H_{eb} = (H_{C2} + H_{C1})/2$ and the coercive field $H_C = (H_{C2} - H_{C1})/2$, where H_{C1} and H_{C2} are the coercive fields on the decreasing and increasing branches of the hysteresis loop, respectively. Also given in Table I are the exchange coupling energy E as obtained from the respective FM layer thickness, the exchange bias field values and the saturation magnetizations for the MLs from the magnetization measurements.

1. Hysteresis loops

Figure 2(a) shows the hysteresis loops as measured with a SQUID for an in-plane cooling field and longitudinal magnetization measurements at 10 K for the sample Co_1. The results are reproduced from Ref. 32. For comparison, hysteresis loops for the samples Co_25, Co_30, and Co_50 are shown in Figs. 2(b)–2(d). Clearly seen is the usual asymmetry in the magnetization reversal and the disappearance of the asymmetry after the first field cycle. The room-temperature (RT) data [triangles in Figs. 2(b)–2(d)] show that the saturation field is around 100 Oe [for clarity, see the inset of Fig. 2(b)].

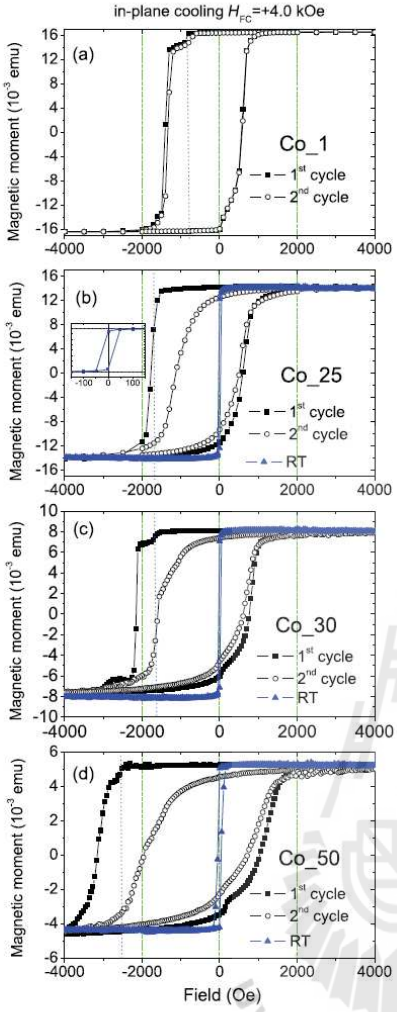

FIG. 2. (Color online) SQUID magnetization hysteresis loops for the (a) $[Co/CoO]_{20}$ ML (from Ref. 32) and for $[Co/CoO/Au]_{16}$ ML for Au layer thicknesses of (b) 25 nm: Co_25 (c) 30 nm: Co_30 and (d) 50 nm: Co_50. The measurements are done at room temperature (triangles) and at 10 K (after cooling down in $H_{FC} = +4$ kOe). The inset in (b) shows the RT data in lower field values. The blue dotted lines indicate the switching field $H_{C\text{-}O}$ during the first field cycle. The thin solid lines are guides to the eye.

For Co_25 and Co_30, the coercive fields at RT and the exchange bias fields at 10 K are approximately 20 Oe and ≈ -580 Oe/≈ -670 Oe, respectively. The corresponding RT data for Co_50 shows that the coercive field has increased to 40 Oe. Such a broadening of the hysteresis loop at RT can be generally attributed to defects within the magnetic layers. We point out that the exchange bias field along the cooling field axis is estimated to be around -1000 Oe for the 50 nm spacer ML, as compared to ≈ -400 Oe for the ML specimen with no spacer.

The hysteresis loops in Fig. 2(a) show at least three kinks near $-780, -1400$, and around -1676 Oe along the decreasing branch. These kinks are an indication for CoO layers having different oxidation levels. Similar kinks can also be seen during the first cycle in Figs. 2(b)–2(d). The last switching fields show an increasing magnitude with increasing thickness of the spacer layer.

In a previous work, Paul *et al.* have found very similar characteristics while varying the oxidation conditions for the bottom and top Co layer in a Co/CoO/Co based spin-valve system.[21] Note that similar subloops in oxidized Co dots were initially attributed to the effect of the aspect ratio for patterned samples,[28] even though they have been commonly observed in nonpatterned specimens as well. Intuitively, a varying stoichiometry of the Co_xO_y layers, that may also depend on the number of bilayers, affects the strength of the exchange coupling between the AF and FM layers. Therefore an optimized stoichiometry can lead to an enhancement of the switching fields. Of course, the grain size may affect the switching fields as well.

The net magnetization in the Co_1 ML (for example) shows a decrease of 5% after the first switching field along the decreasing branch of the hysteresis loop. This corresponds to 1 FM layer out of the 20 FM layers composing the ML, indicating that one of the 20 layers has already switched while the other 19 layers are on the verge of flipping. A similar argument can explain the magnetization data of the other samples, i.e., by a layer-by-layer flipping of the heterostructure.

2. *Magnetization versus temperature*

Figures 3(a) and 3(b) show the temperature dependence of the magnetization M of the samples Co_25 and Co_50 as

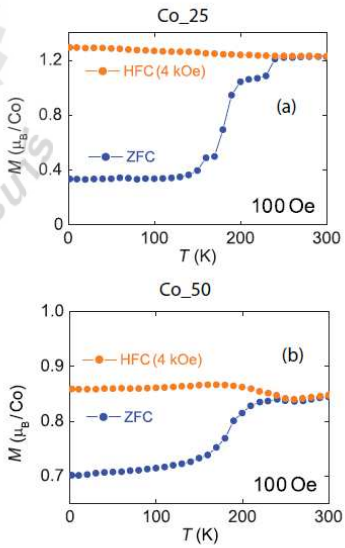

FIG. 3. (Color online) ZFC and HFC magnetizations as a function of increasing temperature (T) in a small external field of $H =$ 100 Oe for (a) Co_25 ML and (b) Co_50 ML.

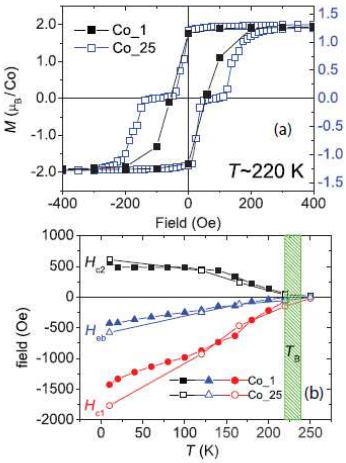

FIG. 4. (Color online) (a) SQUID magnetization hysteresis loops for the Co_1 and Co_25 MLs showing the sub-loops shifts. The measurements are done at 220 K (after cooling down in $H_{FC} = +4$ kOe). (b) The temperature variation of the coercive fields and the exchange bias fields for the two MLs.

measured at 100 Oe using a PPMS. The merging point of the zero field cooled (ZFC) and field cooled (HFC, $H = 4$ kOe) data provide the blocking temperature T_B of the system. T_B characterizes the onset of instabilities of the AF as thermal excitations creep in. The similar T_B of both polycrystalline specimens indicates that their grain sizes are very similar.[29] However, we find three distinct steps in Co_25 before the loops merge at $T_B = 240$ K. In Co_50, the steps are smeared out.

The samples show also a significant difference in the macroscopic magnetization during ZFC and HFC. The ZFC values at low T are smaller for Co_25 than for Co_50. The HFC values are larger for Co_25 than for Co_50. These results indicate that the anisotropy in the Co_50 sample is larger.

3. *Initial domain configurations due to Au spacer*

Apart from the local inhomogeneities (roughness, defects) due to variations in the AF crystallite/grain sizes and concomitant domain size distribution, a distribution of local T_B is typically observed. It is well known that a thicker AF layer leads to an increased stability of the AF domains.[29] Above a critical thickness (as in the present case), this may lead to splitting of the hysteresis loop into two subloops shifted in opposite directions when measured just around the blocking temperature. This subloop shifts and the temperature variation of the coercive fields can be seen in Figs. 4(a) and 4(b), respectively, for the Co_1 and Co_25 MLs. A marked difference is seen as we compare the MLs with and without the spacers. It is clear that the Co_1 ML does not show the subloop shifts. This clearly indicates that these shifts in the Co_25 ML are due to the presence of Co-Au and/or CoO-Au interfaces as they together are responsible for a FM imprint onto an AF. Thus there is a particular difference in the initial AF-FM domain configurations in such systems, which can

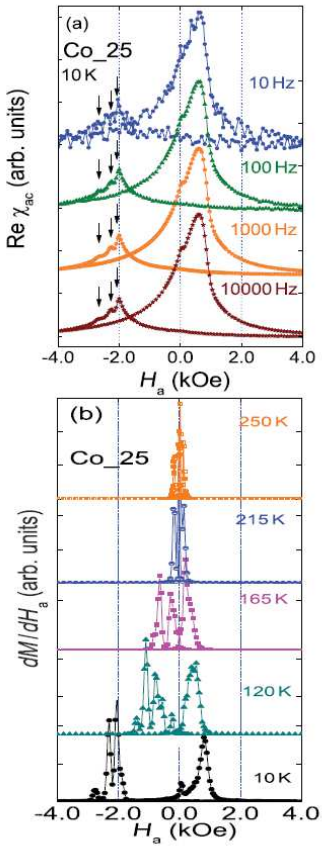

FIG. 5. (Color online) (a) Representative ac susceptibility measurements at different frequencies are shown for the Co_25 ML. (b) The field derivative of the magnetization as a function of field measured at various temperatures without applying an ac field is plotted for the Co_25 ML. They show the evolution of multiple switching with temperature along both branches of the hysteresis loop.

be a topic of future investigation. Usually, an imprint of the FM domain structure onto the AF during zero-field cooling procedure divides the AF into two types of regions locally oriented in opposite directions.[6] Note that in the present case, the cooling field is above the saturation field of the FM and the FM orders before the AF. Here, a proportion of the AF spins/domains (affected by the thermal activation) is aligned by the cooling field, while another proportion remains unaligned. After field sweeping, this proportion gets realigned along the direction opposite to that initially set during the first field cooling.

4. *Susceptibility*

Susceptibility data of Co_25 are shown in Fig. 5(a). The in-phase susceptibility ($\mathrm{Re}\chi_{ac} = dM/dH_a$) data measured at 10 K and at a driving field of 10 Oe (rms) after HFC from RT indicates also the occurrence of three reversal steps

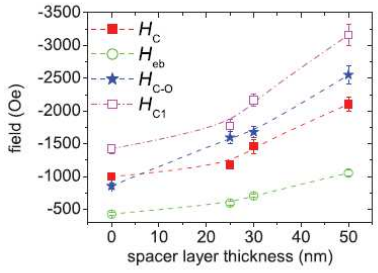

FIG. 6. (Color online) Dependence of H_{eb} and H_C on the thickness of the spacer layer as obtained from the SQUID magnetization hysteresis loops for [Co/CoO/Au] MLs. The coercive fields H_{C1} and the first switching fields $H_{C\text{-}O}$ show an increase with increasing thickness. The dotted lines are guides to the eye.

(indicated by arrows) along the decreasing branch and two reversal steps along the increasing branch. The response from the samples hardly shows any frequency (10 Hz–10 kHz) dependence. A much lower signal along the decreasing branch indicates that the domain dynamics along this branch is a slow process, at least slower than the response time corresponding to the 10 Hz of ac field. The reversal steps are more evident following the field derivative of the magnetization dM/dH_a as a function of field in Fig. 5(b) following the data measured at various temperatures without an ac field. The evolution of the switching fields with temperature is consistent with the data in Fig. 3(a). The behavior for all other samples is very similar and is therefore not shown.

5. H_{eb} and H_C with Au spacer thickness

The plot of H_{eb} and H_C versus the spacer layer thickness in Fig. 6 shows an increasing magnitude with increasing spacer layer thickness. Also plotted is H_{C1} and the first switching field $H_{C\text{-}O}$. While an increase in H_C can be associated with an increased number of nonpinned hysteretic AF grains, an increase in H_{eb} indicates an increase in the number of pinned domains or a stronger pinning by each domain in the polycrystalline specimens. Microstructural investigation could help in understanding such behavior further.

B. Microstructure

From the perspective of magneto-electronics, device characteristics are controlled by the magnetic evolution due to grain structure modulation. Each bit usually contains hundreds of grains. Magnetic recording relies on the statistical averaging over these grains to obtain a satisfactory signal to noise ratio. As the bit size continues to decrease, the grain size needs to be reduced too. The reduction can be achieved by controlling the surface properties of the coated and/or the noncoated substrate. However, eventually, the grains will become superparamagnetic. Thus a control over grain size is essential. Sputtered species have a high kinetic energy and surface mobility allowing rearrangements in the structure during film growth.

It was reported earlier that the exchange bias field can be increased with the number of bilayers with successive FM-AF interfaces. This is due to decreasing grain–size–mediated FM-AF exchange coupled domains stacked in successive layers with gradually smaller sizes.[12] For polycrystalline specimens, within the random anisotropy model, the exchange interaction averages over the anisotropy of the individual grains. This would, in general, increase the effective exchange length. However, with an increasing number of smaller grains (with an increase in the number of bilayers), as the exchange length is reduced to the order of individual grain sizes (≈50 nm in the present case), the random anisotropy model will break down. This will lead to the formation of individual exchange coupled grains—exchange coupled to the uncompensated AF moments preferably located at the grain boundaries. The spin alignment in individual FM domains is determined, domain by domain, by the spin directions in the AF grains. This is unlike the case of nanocrystallites where the grain sizes (⩽exchange length) concomitantly reduces the average anisotropy of the system and make them soft (lowered coercivity).[30] In exchange-coupled systems, the rotatable anisotropy field value is proportional to the magnetization of the small AF grains, it increases with the exchange coupling strength, which in turn increases the coercivity.[31] An increase in the coercivity with smaller AF grain sizes is basically due to an increase in the number of rotatable grains (proportional to the sum of the projections of these magnetizations along the bias direction).

Paul *et al.*[32] have reported earlier on the magnetization reversal for (i) a continuous sequence of successive FM-AF layers (no spacer layers) and that for (ii) a sequence of FM-AF bilayers that are separated by a nonmagnetic spacer layer (Au). The main difference in their magnetization reversal mechanisms is the following: the separated multilayers (ML) showed a usual asymmetric reversal—a nonuniform (domain wall motion and domain nucleation) reversal for the decreasing branch (H_{FC} anti–$\parallel$ H_a) of the hysteresis loop and a uniform (coherent rotation) reversal for the increasing branch (H_{FC} $\parallel H_a$). In contrast, the continuous multilayer showed symmetric and sequential reversal (nonuniform) for both branches of the hysteresis loop.

In this regard, it is interesting to note that in contrast to the unlike case of a *continuous* ML (case (i) above), in a sequence of bilayers Co-CoO that are interrupted by the presence of thick Au layers, the evolution of the grains may be interrupted depending on the thickness of the Au spacer layer, as the grain size is limited by the layer thickness.[33] For a thick enough Au layer, the grain structure of the underlayer is not propagated to the next Co layer. This is similar to a decoupling of the intergranular interactions.[34] It is therefore unlikely that the thickness of the nonmagnetic spacer will influence the magnetic grains as they are all nucleated on a similar spacer layer. Therefore one may speculate that the magnetic behavior does not change with an increasing thickness of the spacer layer. The aspect of grain structure evolution can be verified by cross-sectional TEM.

Figure 7 shows XTEM micrographs depicting repetitions of three layered structures with sharp interfaces for the MLs with (a) 25- and (b) 50-nm of spacer thickness. The thickness of the individual layers is in agreement with the nominal thickness. Magnifications of a trilayer interface show the existence of columnar grains with a width of ≈25 nm and ≈50 nm for the 25-nm and 50-nm sample, respectively.

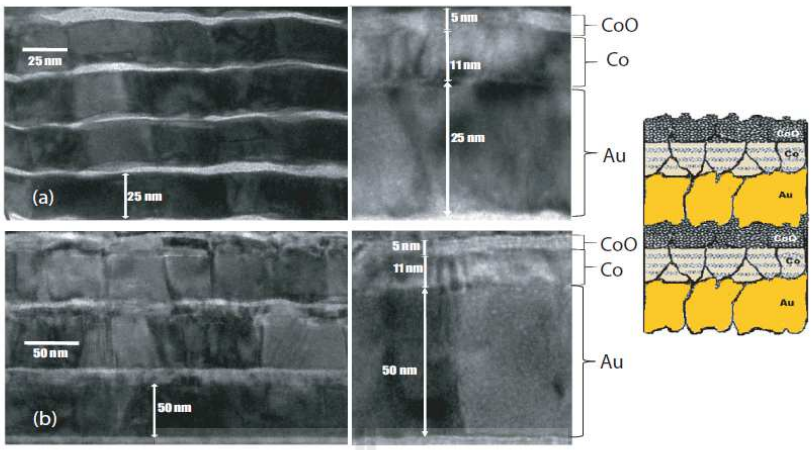

FIG. 7. (Color online) XTEM micrographs of $[Co/CoO/Au]_{16}$ ML for Au layer thicknesses of (a) 25 and (b) 50 nm. Vertically correlated Au grains are visible for both MLs. There are no visible differences for the Co-CoO grains, which are basically unaffected by the size of the underlying Au grains. A schematic of the granular layer structure is shown alongside.

Note that the almost square-shaped Au grains are vertically correlated. The results confirm the common observation in sputtered and evaporated thin films that the grain size is of the same order as the film thickness. The grains of the Co layer, however, are approximately 11×20 nm and are very similar for Co_25 and Co_50. A similar size of grains $d \sim 11.5$ nm is also estimated from the width of the Co peak from x-ray diffraction measurements. Therefore there is no visible microstructural difference in the Co layers.

An increased coercivity in exchange coupled systems is a clear indicator for a dominance of domain wall pinning, as the AF domain walls act as pinning sites for the neighboring FM domains.[22] Thus if we presume the grains to evolve (decrease) with increasing number of layers in a ML stack then an increase in the number of AF domain walls or increased grain boundaries is expected for those domain walls to form. In the case, that the evolution is interrupted (as in the present case), the number of AF domains will remain similar. In any case, this would concomitantly influence the FM domains.

When comparing the ML microstructures, particularly for Co_25 and Co_50, the enhanced coercivities of the FM layers do not appear to correlate in a systematic way with the AF grains. Due to a distribution of grain size, one can expect exchange decoupled AF grains (associated with individual grain spins) at the interface and exchange coupled FM grains. The FM and AF layer coupling can be via exchange and dipole-dipole interactions. However, the additional anisotropy giving rise to the enhanced coercivity can also have its origin within the bulk of the AF layer due to the grain structure that affects the AF magnetocrystalline anisotropy.[29] Hence the enhanced coercivity might be a combination of the effects in both the bulk and interfacial grain spins of the AF layers.

Since the XTEM pictures do not show a significant variation of the grain structures with an increase in the spacer layer thickness, the coupling of the interfacial grains can be considered to be responsible for the increase of the coercivity. It may be possible that due to the different oxidation states of the AF layer, i.e., CoO, Co_3O_4, and Co_2O_3, the individual grains are coupled differently to the FM grains. Such different oxidation states may originate from changes in the deposition conditions within the chamber while depositing a thicker spacer layer. CoO in a stoichiometric relationship Co : O = 1 : 1 is not the only binary oxide phase that forms under readily attainable oxygen partial pressures. The thermodynamically favored form of the cobalt oxide is often Co_3O_4. In contrast to the two cobalt oxides mentioned above, the metastable form Co_2O_3 may be difficult to form.

C. Specular and off-specular neutron scattering

1. Scattering geometry

The neutron scattering geometry is shown in Fig. 8. We define the ML surface in the x-y plane and the z axis along the surface normal. In the specular scattering geometry

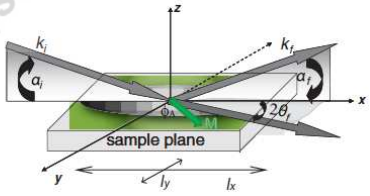

FIG. 8. (Color online) Schematic of the neutron scattering geometry. In reflection geometry, the beam is collimated in the reflection plane and relaxed along the y axis, whereas in the GISANS geometry scattering along the y axis is resolved. Here, $\vec{k}_i$ is the incident wave vector at an angle α_i. The scattered wave vector $\vec{k}_f$ makes an angle α_f and $2\theta_f$ along two different scattering planes. The grey shaded region represents the coherence ellipse covering several (or single) domains (shaded in green) and the mean magnetization making an angle ϕ_A with the polarization axis, which is along the y axis.

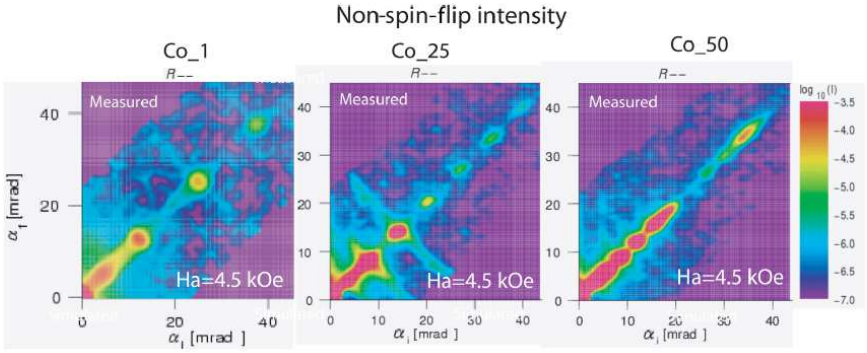

FIG. 9. (Color online) NSF intensity maps (R_{--}) from Co/CoO/Au MLs measured on HADAS/TREFF at saturating field along the decreasing branch of the hysteresis loops for Co_1 and Co_25 and Co_50 ML samples after field cooling at 4.5 kOe and measured at 10 K. The color bar encodes the scattered intensity on a logarithmic scale.

(i.e., angle of incidence α_i equal to the exit angle α_f), the reflectivities follow from energy and in-plane momentum conservation laws as normal wave-vector transfers $\vec{Q}_\perp$ are probed. However, when the in-plane translational symmetry is broken by interface waviness (roughness) or by magnetic domains on a length scale shorter than the in-plane projection of the neutron coherence length $l_\parallel$ along $\vec{Q}_\parallel(=\vec{Q}_x, \vec{Q}_y)$ then the off-specular scattering contributions along the in-plane momentum transfer vector ($\vec{Q}_\parallel$) arise.

At grazing incidence, there can be three scattering geometries: specular reflection, scattering in the plane of incidence (off-specular scattering), and scattering perpendicular to the plane of incidence (Grazing Incidence SANS). We can estimate the extent of correlation lengths from the three equations of momentum transfers along the three different axis owing to the scattering geometry for small angles:

$$\vec{Q}_z = \vec{Q}_\perp = \frac{2\pi}{\lambda}[\sin(\alpha_i) + \sin(\alpha_f)] \simeq \frac{2\pi}{\lambda}(\alpha_i + \alpha_f), \quad (1)$$

$$\vec{Q}_x = \vec{Q}_\parallel = \frac{2\pi}{\lambda}[\cos(\alpha_f)\cos(2\theta_f) - \cos(\alpha_i)] \simeq \frac{2\pi}{\lambda}\left(\frac{\alpha_i^2}{2} - \frac{\alpha_f^2}{2} - 2\theta_f^2\right), \quad (2)$$

$$\vec{Q}_y = \vec{Q}'_\parallel = \frac{2\pi}{\lambda}\cos(\alpha_f)\sin(2\theta_f) \simeq \frac{4\pi}{\lambda}(\theta_f). \quad (3)$$

Here, the incident wave-vector defined by $\vec{k}_i$, makes an angle α_i in the x-z plane with respect to the x axis, while the scattered wave vector $\vec{k}_f$ makes angle α_f in the x-z plane and also $2\theta_f$ in the x-y plane (relevant for diffuse scattering). Different length scales $\xi = \frac{2\pi}{Q}$ ranging from nanometers to micrometers can be accessed by using different scattering geometries in most practical cases. Specular scattering provides the scattering potential of the ML perpendicular to the film plane. The typical probed length scales are in the range 3 nm $< \zeta <$ 1 μm. Off-specular scattering scans provide the lateral correlations along $\vec{Q}_x$ (500 nm $< \xi <$ 50 μm), whereas grazing incidence SANS scans probe the surface (3 nm $< \xi <$ 100 nm) along $\vec{Q}_y$. From the above equations, one may also note that for a given geometry when $\alpha_i \sim \alpha_f \sim \theta_f \ll 1$, the projection $\vec{Q}_y \sim \vec{Q}_z \gg \vec{Q}_x$.

2. *NSF scattering*

The scattering-length densities (SLD) of a magnetic specimen are given by either the sum or difference of the nuclear (ρ_n) and magnetic (ρ_m) components. The $\pm$ signs refer to the spin-up and spin-down states of the incident neutron beam with respect to the magnetization of the sample. The non-spin-flip (NSF) scattering amplitude provides information about $\rho_n \pm \rho_m \cos\phi_A$, and the spin-flip (SF) channels measure $\rho_m^2 \sin^2\phi_A$, if the domain size is larger than the projection of the neutron coherence length along the sample plane ($l_\parallel$). Here, ϕ_A is the angle between the magnetization M and the applied field H_a, which corresponds usually to the neutron quantization axis.

a. Intensity maps. Next, we show the specular and off-specular NSF intensity maps in Fig. 9 for the Co_1, Co_25, and Co_50 samples corresponding to the channel R_{--}. The intensity along the diagonal $\alpha_i = \alpha_f$ is the specular reflection along the scattering vector $Q_\perp$. In the experimental geometry, only $\vec{Q}_x$ is resolved whereas the signal along $\vec{Q}_y$ is integrated because the collimation along the y axis is relaxed. The NSF intensities are shown at a saturating field along the decreasing branch of the respective hysteresis loops where the MLs are in the single domain state. The observed superlattice peaks from the specimens (see Fig. 9) confirm the periodicity of the multilayer structure. The off-specular scattering along the Bragg sheets occurs due to pronounced structural vertical correlation of each of the MLs.

b. Specular scattering. The neutron reflectivity does not only carry information on the mean magnetization direction but also on the layer-by-layer vectorial magnetization. In corroboration to the drop of the net magnetization at the first switching field ($H_a = 0.75$ kOe) along the hysteresis loop of the Co_1 ML, the fits to the neutron reflectivity data, indeed, show the switching of one out of the twenty FM layers at an applied field $H \simeq 1.0$ kOe. Similar to the Co_1 ML,[32] we find layer-by-layer flipping for the Co_25 and C0_50 MLs as well,

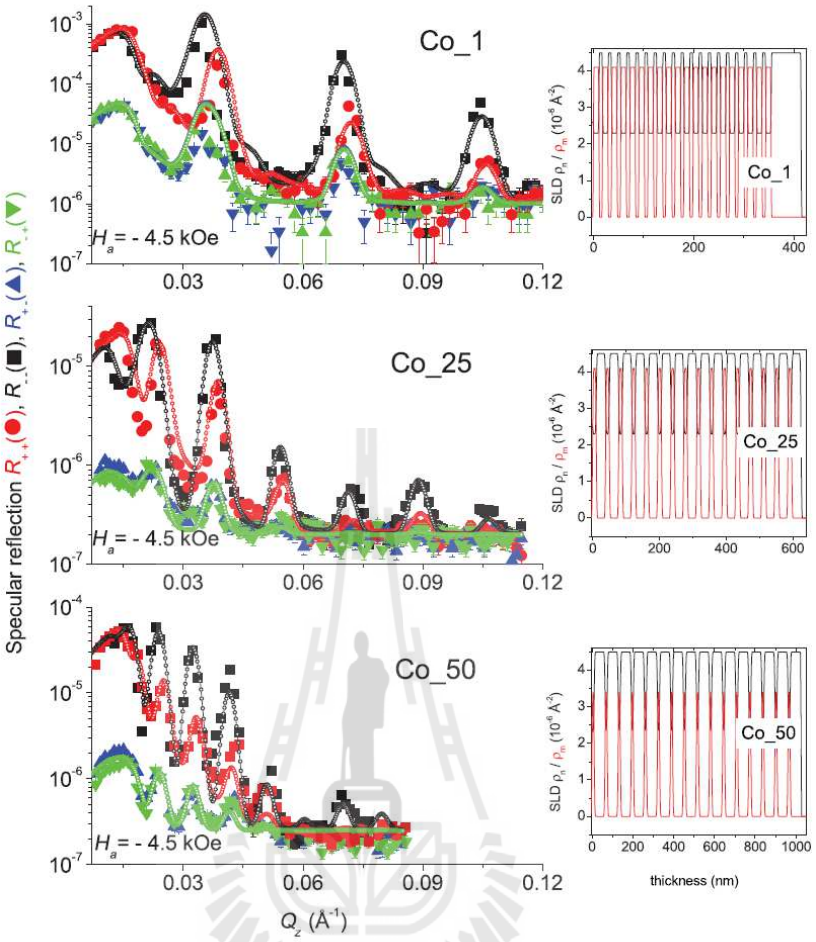

FIG. 10. (Color online) Specular reflectivity patterns (solid symbols) along with their best fits (open symbols) for the NSF [R_{++} (red) and R_{--} (black)] and SF [R_{-+} (green) and R_{+-} (blue)] channels measured at a saturation field, for the MLs with different spacer layer thicknesses. $\vec{Q}_z = \frac{2\pi}{\lambda}[\sin(\alpha_i) + \sin(\alpha_f)]$, where α_i and α_f are the incident and exit angles, respectively. The fits shown here are done by considering model A for the MLs Co_1 and Co_25 and model C for the ML Co_50. The corresponding nuclear (black) and magnetic (red) SLDs are shown alongside.

which is indicated by their multiple switching fields along the respective hysteresis loops.

Figure 10 shows the specular reflectivity data (NSF and SF) corresponding to the three MLs at a saturation field ($H_a = -4.0$ kOe) on a logarithmic scale. The relative variation of the multilayer Bragg peak intensities due to different periodicities of the MLs is quite evident here. Earlier, the layer magnetizations for Co_25, measured at their first switching field by Paul *et al.*,[20] revealed that at least four layers from the stack have flipped and the remaining twelve layers are at the onset of flipping. Here, we find the layer magnetizations for the Co_50 ML, also remain collinear at its first switching field, whereby nine of the sixteen layers have flipped with the field. The value of the mean magnetization angle ϕ_A for the individual layers in the stack (0° or 180° with respect to the field) are taken from the fitted values of the specular patterns (NSF and SF). We do not find any significant increase in the SF specular signals confirming their nonuniform reversal that is expected for these MLs, as we measure along the decreasing branch of the first field cycle. The best fits to the reflectivity data revealed a good agreement with the nominal thicknesses and the ρ_m and ρ_n values as listed in Table II. The other parameters such as interface roughness are kept similar for all samples. The respective nuclear and magnetic SLD values are plotted alongside.

Note that the bulk value of the Co moment is ~1.73 μ_B/atom, here μ_B designates the Bohr magneton.[35] The estimated magnetic moment from the corresponding values of ρ_m as obtained from the least square fit to the Co_1 ML neutron reflectivity profile measured at saturation is ~1.66 μ_B/atom

TABLE II. Fit parameters extracted from the PNR results. ρ_n and ρ_m designate the nuclear and magnetic scattering length densities, respectively. In sample Co_1, there are no spacer layers between the Co/CoO bilayers. Also given are the respective magnetic moments as calculated from the magnetic scattering length densities and the exchange energy E. The magnetic moments are calculated following model A: considering no dead layer, model B: considering 1.0 nm of dead layer, and model C: considering reduced moment for the entire magnetic layer. The Au layer in Co_1 protects the sample against oxidation.

Multilayer		Au	CoO	Co	Co-Au (dead layer)	error
Co_1	thickness (nm)	52.6	7.1	11.0	–	±0.2
(A)	ρ_n ($\times 10^{-6}$Å^{-2})	4.5	4.5	2.3	–	±0.2
	ρ_m ($\times 10^{-6}$Å^{-2})	0.0	0.0	4.1	–	±0.1
Co_1	thickness (nm)	52.6	7.1	10.0	1.0	±0.2
(B)	ρ_n ($\times 10^{-6}$Å^{-2})	4.5	4.5	2.3	2.3	±0.2
	ρ_m ($\times 10^{-6}$Å^{-2})	0.0	0.0	4.1	0.0	±0.1
	magnetic moment (μ_B/atom)			1.66		±0.1
	E (erg cm^{-2})			0.62		±0.1
Co_25	thickness (nm)	22.5	5.5	11.0		±0.2
(A)	ρ_n ($\times 10^{-6}$Å^{-2})	4.5	4.5	2.3		±0.2
	ρ_m ($\times 10^{-6}$Å^{-2})	0.0	0.0	4.1		±0.1
	magnetic moment (μ_B/atom)			1.66		±0.1
	E (erg cm^{-2})			0.92		±0.1
Co_50	thickness (nm)	48.0	5.0	11.0		±0.2
(A)	ρ_n ($\times 10^{-6}$Å^{-2})	4.5	4.5	2.3		±0.2
	ρ_m ($\times 10^{-6}$Å^{-2})	0.0	0.0	4.1		±0.1
Co_50	thickness (nm)	48.0	5.0	10.0	1.0	±0.2
(B)	ρ_n ($\times 10^{-6}$Å^{-2})	4.5	4.5	2.3	2.3	±0.2
	ρ_m ($\times 10^{-6}$Å^{-2})	0.0	0.0	4.1	0.0	±0.1
Co_50	thickness (nm)	48.0	5.0	11.0		±0.2
(C)	ρ_n ($\times 10^{-6}$Å^{-2})	4.5	4.5	2.3		±0.2
	ρ_m ($\times 10^{-6}$Å^{-2})	0.0	0.0	3.5	→ reduced	±0.1
	magnetic moment (μ_B/atom)			1.45		±0.1
	E (erg cm^{-2})			1.35		±0.1

±0.05. Note that this is 17.4% less when compared with the moment obtained from the magnetometric measurements using the SQUID/PPMS (see Table I). One may recall that $\rho_m = M_{\mathrm{FM}}\, 2.853 \times 10^{-9}$ Å^{-2}cm^{3}emu^{-1}. The magnetic moment for the Co_50 ML as obtained from the PNR data fits, is ∼1.45 μ_B/atom ± 0.05 (13% reduction from the Co_1 value). The reduced magnetic moment of the Co layers as obtained from the magnetometry measurements lead us to infer that there can be plausible magnetic dead layers at the Co-Au interfaces as we increase the Au spacer thickness. Such formation of dead layers on magnetron sputtered samples are commonly attributed to the interdiffusion that occurs during the deposition process.[36]

c. Models for fitting. In order to verify the formation of weakly coupled noncollinear domains at the interface, we compare the PNR profiles for the Co_1 and Co_50 specimens. These systems were chosen for comparison because the changes of the magnetic moment are maximum for these two MLs.

First, we compare the NSF simulated data (on a linear scale) over a certain range of $\vec{Q}_z$ where the changes are explicit, considering different probable models. The simulations in Fig. 11 are shown for both the MLs as we consider three models with (A) no magnetic dead layer (closed symbols), (B) 1.0 nm of magnetic dead layer (open symbols) at the Co-Au interfaces (see Table II), and a third model (C) with reduced moment throughout the entire Co layer thickness for the Co_50 ML (lines). The Co_1 ML obviously does not have Au spacers after each Co-CoO bilayer rendering model (C) irrelevant for it. One can clearly distinguish the impact of the models on the profiles and therefore our inferences from the fits can be considered unambiguous.

d. Spin asymmetry. Furthermore, the measured spin-asymmetry (SA) profile is plotted versus $\vec{Q}_z$ in Fig. 12. The spin asymmetry is expressed as the ratio of the difference and sum of R_{++} and R_{--} reflectivities measured at a saturation field of −4.5 kOe. This normalized difference is sensitive to the magnetization profile across the film and is less sensitive to interface roughness.

We follow the fit qualities in Figs. 11 and 12 for the Co_1 ML and Co_50 ML profiles using the model A, B, and C. Note the different ranges of the $\vec{Q}_z$ in Fig. 11 chosen for the two samples in order to compare the differences of model fits. One can see from both figures that the fit quality deteriorates for the case with model B (dead layer) in case of Co_1 ML. This confirms that there are no dead layers in this specimen. All Co layers (in each bilayer repetition) have an uniform magnetization throughout the entire thickness of the layer. A very similar situation is encountered for the Co_25 ML as well. However, from the Co_50 ML profile, one can see that a slight improvement in the fit quality has been achieved by using model C, i.e., by considering a 13% reduction in the moment for the entire Co layer (11.0 nm). No significant improvement in the fit quality can be achieved by using model B (dead layer at the Co-Au interface).

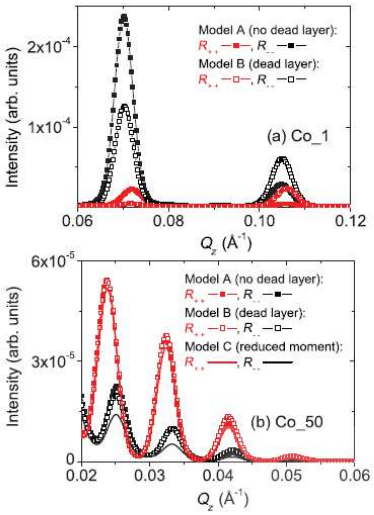

FIG. 11. (Color online) NSF simulations [R_{++} (red) and R_{--} (black)] with $\vec{Q}_z$ for the (a) Co_1 and (b) Co_50 MLs. The simulations are shown to compare for the models considering (A) no magnetic dead layer (closed symbols), (B) 1.0 nm of magnetic dead layer (open symbols) at the Co-Au interface, and a third model (C) with reduced magnetic moment throughout the entire Co layers for the Co_50 ML (lines). Note the different ranges of $\vec{Q}_z$ chosen for the two samples in order to show the differences in model fits distinctly.

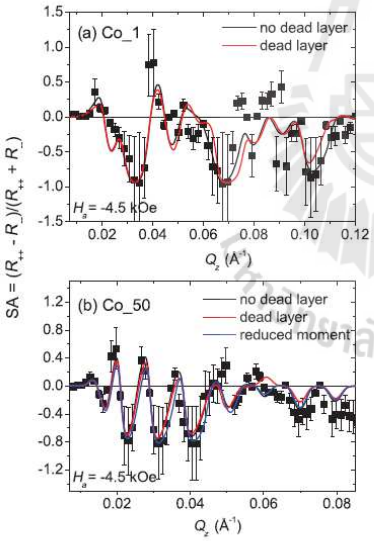

FIG. 12. (Color online) Spin asymmetry (SA) (black square) with $\vec{Q}_z$ in order to compare the magnetization in the (a) Co_1 and (b) Co_50 MLs. The simulations are shown for the models considering (A) no magnetic dead layer (black line), (B) 1.0 nm of magnetic dead layer (red line) at the Co-Au interface, and a third model (C) with reduced magnetic moment throughout the entire Co layers for the Co_50 ML (blue line).

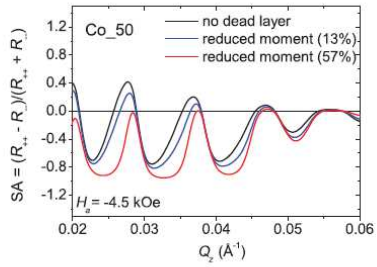

FIG. 13. (Color online) Simulated SA is plotted with $\vec{Q}_z$ for the Co_50 ML considering different degrees of reduction in magnetization of the Co layer as obtained from the PNR data and also from the PPMS data.

Figure 13 shows the simulated SA versus $\vec{Q}_z$ for various reductions of the magnetic moment of the Co layer in Co_50 ML. One can see that when the moment (or ρ_m) is reduced by 57% (which is estimated from the PPMS measurements) a strong deviation is encountered as compared to the best fit which is simulated considering only a 13% reduction in the magnetic moment. Note that these values are compared for the apparent saturation field measurements, thus one can rule out the possibility of canting in the film plane (however out-of-plane canting may be possible).

e. Discrepancies in magnetic moment. In the present case, from the changes in M_{FM} as obtained from PPMS (see Table I) and as obtained from PNR (see Table II), the exchange coupling E can be calculated. It turns out that $E \sim 0.75 \pm 0.05$ erg cm^{-2} is almost independent of the spacer layer thickness of the MLs as obtained from the PPMS measurements. The E values, as obtained from the PNR measurements however, show a two times increase for the Co_50 ($\sim 1.35 \pm 0.1$ erg cm^{-2}) ML as compared to the Co_1 ML. This of course follows from the respective difference in reduced magnetizations (particularly for the Co_50 ML) as obtained from the two techniques used.

Discrepancies in the estimates of the magnetic moment are commonly reported for SQUID based magnetometers and PNR measurements.[37] This becomes more visible, probably for oxidized layers, due to plausible inhomogeneities. Measurements at TREFF were done with a 2.0 mm beam diverging by $\sim 0.1^\circ$ at a distance of 1500 mm from the 15-mm sample along $\vec{Q}_x$. The neutron coherence lengths l_x (along $\vec{Q}_x$) and l_y (along $\vec{Q}_y$)[38] thereby turn out to be few micrometers and few angstrom, respectively, which can be estimated using the uncertainties in $\vec{Q}_x$ and $\vec{Q}_y$ as

$$l_x \sim \frac{1}{\Delta Q_x} \sim \frac{1}{\frac{\pi}{\lambda}\sqrt{(\alpha_i \Delta\alpha_i)^2 + (\alpha_f \Delta\alpha_f)^2}}, \tag{4}$$

$$l_y \sim \frac{1}{\Delta Q_y} \sim \frac{1}{\frac{2\pi}{\lambda}\Delta\theta_f}. \tag{5}$$

Here, l_x being $\ll$ than the illuminated sample area ($\sim$2.0–0.65 mm), the intensities on the detector are an incoherent sum of the coherently scattered intensities from the coherent ellipse. This can make a significant difference for samples with laterally and vertically inhomogeneous magnetic entities

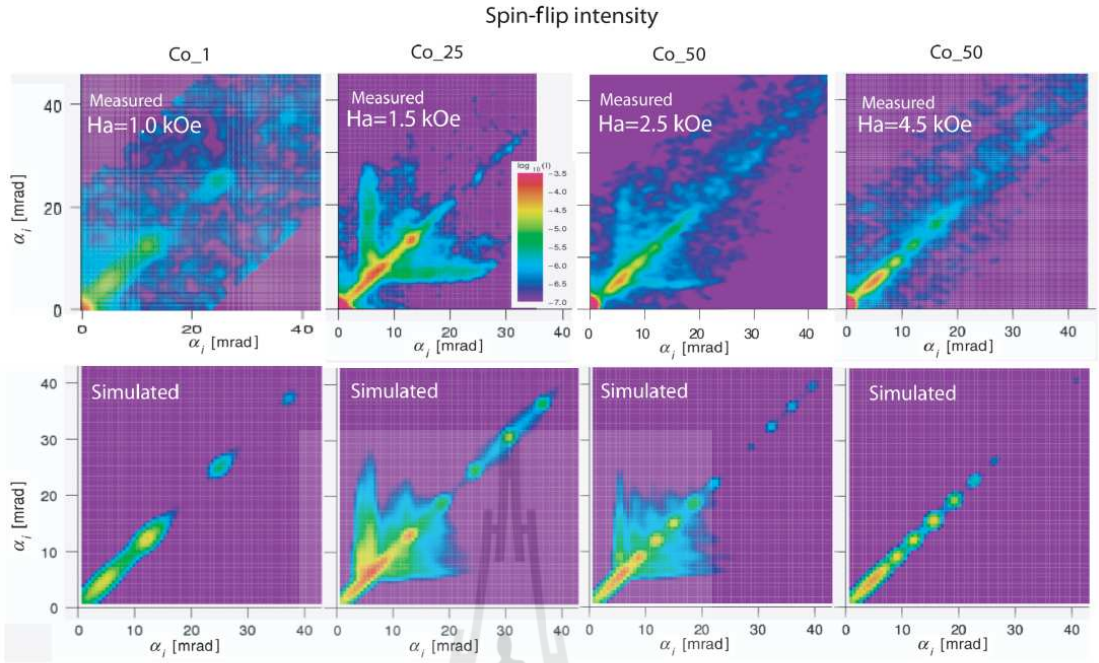

FIG. 14. (Color online) SF intensity maps (R_{+-}) along with their simulations within DWBA from Co/CoO/Au MLs measured on HADAS/TREFF at the first switching fields along the decreasing branch of the hysteresis loops for Co_1 and Co_25 and Co_50 ML samples after field cooling at 4.0 kOe and measured at 10 K. The color bar encodes the scattered intensity on a logarithmic scale.

varying from one coherence volume to the other. The PPMS measurements, on the other hand, are from a signal averaged over 5 t_{FM}-mm^3 sample volume.

3. SF scattering

a. Intensity maps. Figure 14 shows intensity maps for the Co_1, Co_25, and Co_50 samples corresponding to the channel R_{+-}. The SF intensities are shown at a field that is close to the first switching fields along the decreasing branch of the respective hysteresis loops. These intensities eventually disappear at saturation, demonstrating their magnetic origin. A small contribution from the NSF intensities appears in the SF channels due to a reduction of the efficiency of ≈5% of the polarizer and the analyzer components. Note that no Bragg sheets are visible in the SF channels unlike that in the NSF channels.

Here, we consider three possible scenarios for the Co_1 ML for fields close to the coercive field: (i) Paul *et al.*[32] have shown earlier that the reflectivity profile near coercivity is best simulated considering an almost equal number of layers oriented along the applied field direction and opposite to it. (ii) The magnetization is close to zero due to the formation of a multidomain state with random orientation of the domains, and (iii) the magnetization is oriented along an axis perpendicular to the polarization axis, corresponding to a coherent rotation of magnetization. In all these three cases, the projection of the longitudinal magnetization onto the neutron polarization axis (y axis) is proportional to $\langle \cos \phi_A \rangle$ (=0), while the projection of the transverse component with respect to the polarization axis onto the x axis is proportional to $\langle \sin^2 \phi_A \rangle$. However, in the case of a random distribution of domain magnetization directions, the dispersion is $\langle \cos^2 \phi_A \rangle - \langle \cos \phi_A \rangle^2 \neq 0$. For a coherent rotation this dispersion is essentially zero. Thus one can distinguish between a situation of random distribution of domains and that between a coherent rotation. In case of domains that are smaller than the neutron coherence length along the x axis, off-specular scattering is expected as well. The situation becomes more involved when an equal number of layer magnetizations is oriented along and opposite—but are strictly collinear—to the polarization axis. It is then difficult (or even impossible) to infer the domain size as there is no SF off-specular scattering in absence of fluctuations around the mean magnetization **M** direction even if the domains are smaller than the neutron coherence length.

The absence of well defined Bragg sheets in Fig. 14, in the off-specular scattering from Co_25 and Co_50 MLs indicates a lack of vertical correlations. In contrast to the Co_1 ML, both Co_25 and Co_50 MLs show a significant increase in the off-specular intensities. They occur due to fluctuations of the magnetization of the domains around the mean magnetization angle indicating an instability that is induced in the system at the onset of flipping of the magnetization of the layers. Flipping is likely when the size of the domains becomes comparable to the width of the domain walls.

b. DWBA simulations. The specular and the off-specular intensity is simulated within the distorted wave Born

approximation (DWBA).[38] The simulations are conducted by taking into account spin-dependent reflection and refraction. Finally, the cross section is convoluted with the instrumental resolution function (see Fig. 14). Inhomogeneities of the ML like magnetic roughness at the interfaces are taken into account to first order starting from an ideal multilayer with flat interfaces. We assume for all measurements that the mean magnetization is collinear with the neutron polarization axis, which is along the y axis. Note that the coherence area is substantially extended along the x axis (see Fig. 8). This area is restricted via the uncertainty in the momentum transfers ($\Delta\, Q_{x,y} \sim \frac{2\pi}{l_{x,y}}$) along the x and y directions. The uncertainties are a consequence of the angular divergences due to the beam collimation opted in the measurements.

The off-specular scattering gradually disappears when the field becomes larger than the first switching field (see Fig. 14). Within our model, we allow $\mathbf{M}$ to fluctuate from domain to domain around the mean angle by $\Delta\phi_A = 30^\circ$ averaged over the coherence volume for Co_25 and Co_50. These fluctuations can be longitudinal $\langle\cos(\delta\phi_A)\rangle$ ($\Delta\mathbf{M} \parallel \mathbf{M}$) as well as transverse $\langle\sin^2(\Delta\phi_A)\rangle$ ($\Delta\mathbf{M} \perp \mathbf{M}$). The structural parameters are obtained from the fits to the specular patterns.

Transmission and reflection amplitudes show singularities at the points of total reflection, i.e., at the critical edges. Figure 14 clearly shows these singularities, i.e., the Yoneda wings, which in turn are accompanied by an enhancement of the diffuse scattering. Such enhancements can be seen in the SF maps in cases when the domains are smaller than the neutron coherence length along the x axis, i.e., as and when the coherence ellipse covers several domains. One usually encounters an asymmetry of the scattered neutrons in the SF channels due to the inverse population of the incoming and the outgoing neutrons selected by the polarizer (different critical edges for up and down neutrons) and flipped by the spin flippers.[38] One can also see, particularly for the Co_50 data and its simulation, that the Yoneda wings are associated with streaks running parallel to the α_i and α_f axes. These streaks are commonly observed when the SLD values of one of the constituents of the ML form a shallow potential well (Co) with respect to a wider and higher SLD value (Au). The effect is related to the difference in the phases of the transmitted and reflected waves.

It is well known that a decreasing domain size leads to a concomitant increase in the number of grain boundaries (as domains can be associated with the grain size) and thereby an increase in the number of uncompensated spins in the AF as in the case of Co_1 type (nonseparated) MLs.[12,32] However, for the Co_1 ML, the magnetic correlation length cannot be properly estimated. This is because, at the reversal point, 50% of the layers are directed along the applied field and the remaining 50% are directed opposite to the applied field direction. Thus the net magnetization is close to zero. Furthermore, there are no indications of small scale variations around the mean magnetization angle close to the critical angle of total reflection (even at its reversal point) and also that these domains are either vertically uncorrelated (no Bragg sheets are observed in the SF channels) and/or larger than the neutron coherence length projected along $\vec{Q}_x$. Whereas, in the cases Co_25 and Co_50 ML specimens, the typical FM vertically uncorrelated domain sizes are of $\approx$1–2 μm (estimated from the observed enhanced SF scattering intensities around the total reflection edges in each of the specimens), which are consistent with previous measurements on similar samples.[39] Note that we could not observe any appreciable change in the domain size with the spacer layer thickness, at least not for the separated MLs.

Generally, as the grain sizes become small enough that they are comparable to the domain wall width, where domain walls can form within one grain, the magnetization direction corresponds to the anisotropy direction varying from grain to grain. For grain sizes below the critical size, one can opt for the random-anisotropy model, which takes into account the magnetic alignment between the grains that competes with the anisotropies of the individual grains. The spontaneous spatial magnetic correlations, extended over many individual grains, thus depend strongly on grain size.[40,41] Interestingly, nonevolving domain sizes in our separated MLs are in corroboration with the underlying grains (which are only of few nm in size) as they are also of very similar dimensions irrespective of the separation between the magnetic layers. This actually, in a way, confirms that the grain structure variation that was evident for the continuous multilayer was restricted in case of the separated multilayers. This information is significant enough as a variation in the domain sizes would have had an effect on the exchange bias as well.

D. X-ray absorption spectroscopy

1. K-edge spectroscopy

Figure 15(a) shows a comparison of the measured Co K-edge XANES spectra from the MLs (solid symbols) and the reference spectra from each of the possible constituents that can produce the absorption edge for example, CoO, Co_3O_4, and Co metal. By considering CoO, Co_3O_4, and Co metal as the parent components, the XANES spectra of the three Co MLs are fitted (lines) with a superposition of XANES profiles of the parent components using the linear combination analysis (LCA) method. The fitting was performed using the package ATHENA[42] with the LCA tool. The fits are shown in Fig. 15(a) together with the measured XANES spectra. In this way, we estimate the weighted proportions of Co_xO_y and Co layers.

Further, we calculate the Co metal, Co_3O_4 and CoO spectra (open symbols) using the FEFF 8.2 code, which is based on *ab initio* multiple scattering calculations.[43] The calculated spectra are shown along with the measured spectra for the MLs.

For Co metal (hexagonal), $a = 2.5074$ Å and $c = 4.0699$ Å are used as the lattice parameters. Whereas $a = 4.2667$ Å is used for the lattice constant of CoO (rocksalt) structures. For Co(CoO) metal, a cluster of 40(57) atoms [radius of 4.5(5.0) Å] is used to calculate the self-consistent field muffin-tin atomic potentials within the Hedin-Lundqvist exchange potential and a 80-atom cluster with a radius of 6.0 Å is used for full multiple scattering calculations. They include all possible paths within a larger cluster radius of 7.0 Å (147 atoms).

Next, we vary the proportions of each of the constituents in the calculated (*ab initio*) spectra according to the R ratio obtained from the proportional fits and compare them (open symbols) with measured XANES spectra. One can easily see

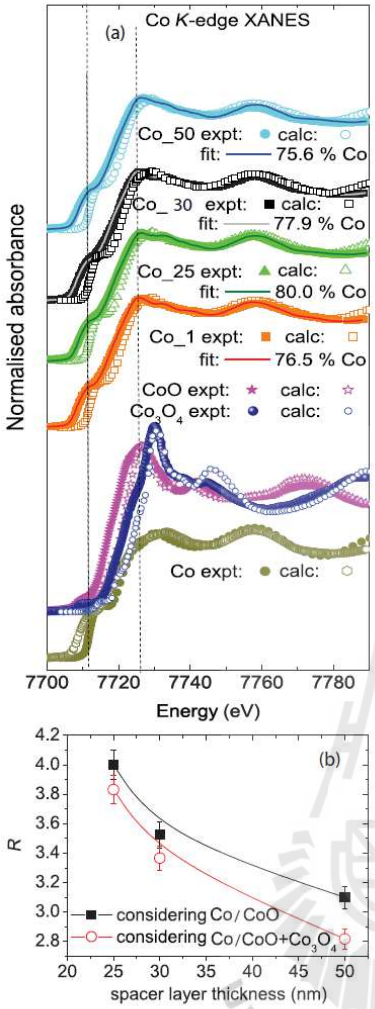

FIG. 15. (Color online) (a) Comparison of the measured Co K-edge normalized XANES spectra of the Co/CoO MLs (solid symbols) and their fits (lines) using the LCA method using the package ATHENA. Also included are the reference spectra for CoO, Co_3O_4, and Co metal. The *ab initio* calculated XANES spectra for the reference materials using the FEFF 8.2 code are also included. A weighted proportion of the species, with various proportions of Co metal, Co_3O_4, and CoO as obtained from the fits and are used to calculate the ML spectra, are also plotted (open circles). (b) The ratios R from the K-edge spectra are plotted for the total thickness of the MLs using two possible scenarios discussed in the text.

that the calculated XANES spectra are in very good agreement with the corresponding features in the measured spectra of the MLs in both energy positions and shapes. This confirms the presence of multiple constituents in the MLs from *ab initio* calculations.

The ratio of the signal, R is determined by evaluating the ratio between the Co-signal and the CoO- or the $CoO + Co_3O_4$ signal as obtained from the fits. Here, we have considered two possible scenarios for the AF layer in comparing the ratios (i) with $CoO + Co_3O_4$ content and (ii) only with CoO content. We have plotted these ratios in Fig. 15(b) as a function of the total ML thickness. In case of Co_1, the layer thicknesses being little different from the other MLs, the ratio cannot be strictly compared for the same thickness ratio. A better agreement with the data is obtained while considering scenario (i). The goodness-of-fit parameter (R factor) decreases by 5–30%. This indicates that the Co MLs are composed of phase-separated regions that differ in the proportion of their respective constituents (Co metal, Co_3O_4, and CoO).

From the ratio R in Fig. 15(b), it is interesting to note that the XANES spectra show an increasing proportion of oxide (AF) material, which is largely compensated by a decreasing proportion of Co in the Co_25, Co_30, and Co_50 MLs. A plausible change in the deposition pressure and temperature, with increasing deposition time (while growing thicker Au layers), might have caused an ≈4% increase in the Co_3O_4 content. Co_3O_4 has an ordering temperature ($T_N = 40$ K) lower than CoO, which can vary depending upon the FM layer in its proximity.[44] Coupling of the uncompensated AF spins within the Co_3O_4 proportion may be quite different from that within the CoO proportion, as they have different crystalline structures which can even lead to different anisotropy axes. Therefore the presence of multiple constituents with different magnetic ordering temperatures in a way corroborates with the magnetization loops and the multiple switching fields that has been discussed in the magnetization section.

Apart from the effect of the Co_3O_4 content, in general, an increase in the exchange bias field as has been observed here, may be associated with (a) an increase in the AF proportion (the AF thickness of our MLs is below a typical critical AF thickness of ≈10 nm),[45] (b) a decrease in the FM proportion (increasing the surface to volume effect), and (c) plausible formation of smaller AF domains[46] (domains are preferably stabilized at the grain boundaries) with an increase in the total film thickness.[12] A ≈30% change in the AF-FM thickness ratio corroborates well with the 35% change in the exchange bias field for the corresponding MLs. The XAS data definitely provide important clues to the fact that there are indeed changes in the magnetic layer thickness or proportions that have occurred due to the spacer layer. This information is also significant enough to proceed further with the investigation.

2. *L*-edge spectroscopy

L-edge spectra from the Co/CoO multilayers as measured at RT in the remanent state are shown in Fig. 16(a). As common for transition metals and transmission metal oxides, the spectra are dominated by two peaks separated by a few milli-electron-volts. The two main peaks $L_{2,3}$ arise from the spin-orbit interaction of the $2p$ core shell. The total intensity of the peaks is proportional to the number of empty $3d$ valence states above the Fermi level. While spectra from a metal show typically two broad peaks reflecting the width of the empty d bands, oxides exhibit a multiplet structure arising from the spin and orbital momentum of the $3d$ valence holes in the electronic ground state and from the coupled states formed

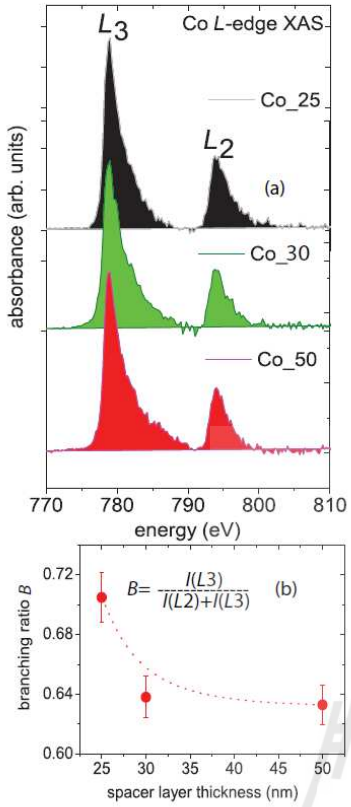

FIG. 16. (Color online) (a) Plot of the L-edge XAS for the multilayers. (b) Ratios of the area under the absorption peaks L_3 and L_2. The lines are guide to the eye.

after x-ray absorption between the $3d$ valence holes and the $2p$ core holes.[47]

In our MLs we observe two broad peaks with broadened bases, a typical signature of the localized character of the $3d$ states. We do not observe any fine structure (negating hybridization of the d orbitals with the s orbital of the Au spacer). We neither observe a shift in the absorption energies nor a change in separation of the peaks that amounts to 15.3 eV for the MLs investigated. Therefore the amount of core-hole screening by delocalized valence electrons is negligible.[48]

The branching ratios $B = I(L_3)/[I(L_2) + I(L_3)]$ (see Ref. 49) are calculated from the area under the L_2 and L_3 peaks as shown in Fig. 16(b) using the IFEFFIT package.[42] The advantage of using B is the minimization of the effects of line broadening by the finite lifetime of the transitions and experimental broadening contributions.

The changes in B being a measure for the amplitude of the angular part of the spin-orbit operator showing a 12% decrease with increasing spacer layer thickness which further partially corroborates with the increasing Co valency or changes of the local magnetic moment. Theoretical and experimental studies have shown that the ratio of a $3d$ transition metal atom generally increases with its magnetic moment. However, a clear relation, or a sum rule, relating these two quantities has not been established, and the absolute value of the magnetic moment cannot be obtained directly from this ratio.[50] Recently, XMCD spectra from Co-Au multilayers have demonstrated that changes in the neighborhood of the Co atoms can suppress its magnetism due to impurities and interdiffusion.[51] The increased thickness of the Au layers might have lead to an enhanced concentration of Au impurities around the Co atoms. The reduced magnetization of Co with the increasing thickness of the spacer layer is in agreement with the PPMS [see Figs. 3(a) and 3(b)] and PNR measurements [see Figs. 12(a), 12(b), and 13].

E. Interface magnetism

Furthermore, we discuss the various possibilities that can be responsible for the observed magnetic behavior with spacer thickness such as (a) exchange coupling across the spacer, (b) interfacial dilution, and (c) perpendicular anisotropy.

a. Exchange coupling. In the present scenario, the unusual thickness dependence of the spacer layer on exchange bias therefore raises the question of whether there is RKKY type coupling or magnetostatic coupling or any other mechanism that might determine the enhanced exchange coupling, besides the variations in relative proportion of AF-FM. In magnetic multilayers, magnetic moments can be looked upon as immersed in a sea of the conduction electrons of the spacer layer which gives rise to damped long-range oscillation of the interlayer *exchange coupling* as a function of the spacer thickness.[52,53] The magnetostatic interaction between two FM films, separated by a nonmagnetic spacer, is caused by the stray fields (*magnetostatic coupling*) with antiparallel magnetizations. However, following Néel's theory (in presence of a correlated roughness), an interlayer coupling can be induced that is ferromagnetic in nature and decreases exponentially.[54] In the possible coupling mechanisms discussed above, the coupling strength definitively dampens down at around 2.0–5.0 nm of spacer thickness, again ruling out such a possibility in our case.

Possible long-range interaction across a spacer layer is common in magnetic multilayers. For example, Gierlings *et al.*[13] investigated the effect of a Au spacer across a similar Co-CoO system where they could find induced magnetic moments in Au by local s-d hybridization with the d band of the nearest Co atoms. A canted magnetic structure in the film plane, thus realized at the interface across a Au spacer of $\leqslant$1.0 nm, reduces the exchange coupling. Very recently, Meng *et al.*[17] and Valev *et al.*[55] have reported an interlayer coupling between CoO and Fe separated by at least 4.0 nm (10 monolayers) of Ag and 3.5 nm of Cu spacer layer, respectively. The pinning centers deep inside the AF layer, contributing to the exchange bias field are also indicative of the long range aspect of it.[56] Note that in our case, the thickness of the Au spacers are at least an order of magnitude larger. Moreover, PNR shows that there is no in-plane canted spin structure. This may rule out spin-canting due to possible pin-hole formation between the two consecutive Co-CoO layers on either side of the Au layer.

b. Interfacial dilution. In this regard, it is natural to think of interfacial dilution for a magnetic/nonmagnetic interface. In an earlier case, a decrease of the thermal stability of the

AF was conjectured.[14] It was shown that the bias field can be slightly increased (only by around 100 Oe) by Cu dilution in IrMn based exchange biased system. Moreover, such a dilution effect affects the blocking temperature of the system as well. In the present case, we can rule out any dilution effect as we do not observe any significant change in the blocking temperatures for our multilayers. We may also rule out diffusion of Au impurities into the Co and CoO layers as Co and Au are immiscible (positive heat of mixing) at or below RT and we see no magnetic dead layers by PNR.

c. Perpendicular magnetic anisotropy. In ultrathin films, perpendicular magnetic anisotropy (PMA) effects may commonly result from interface and/or magnetoelastic effects apart from more intrinsic magnetocrystalline anisotropy. Magnetoelasticity is dominant with decreasing film thickness which can make PMA restricted to low thicknesses (typically 1 nm). Stöhr has shown that the orbital moment on a Co atom becomes anisotropic (below 10 monolayers or ∼2.5 nm) through quenching effects by the anisotropic ligand fields of the neighboring Au atoms (which can be as thick as 28.0 nm).[47] Recently, Paul *et al.* have also observed strong PMA in $[Co(2.0\ nm)/Au(2.0\ nm)]_{32}$ multilayers. Note that the Co layer thicknesses were restricted to 8 monolayers instead of usual range of 1–2 monolayers.[57]

The thickness of the Co layers in the present case are 11.0 nm (∼44 ML) thus one should not expect any PMA in this range. However, for the Co_50 ML, as compared to the Co_25 ML, we find ≈13% decrease in the magnetic moment (when measured along the sample plane, either by PPMS, PNR, or *L*-edge spectroscopy). The reduced magnetic moment indicates that there can be a relative increase in PMA. Schematics of possible scenarios for the magnetic structures of the layers are shown in Fig. 17. As an example, we have shown the cases for two the MLs namely, Co_25 and Co_50 at the FM- interfaces. From the *K*-edge spectroscopy, we observe the following. (i) For FM(Co)-Au interfaces: ≈30% decrease in the proportion of Co thickness (increase in the Au layer thickness can affect the interface with the Co layer). This will reduce the effective magnetic Co thickness from 11.0 nm to around 8.0 nm. Such a decrease can be due to canting of the Co moments at the interfaces. This would then obviously increase the probability of PMA. (ii) For AF($CoO + Co_3O_4$)-Au interfaces: ≈4% increase of the Co_3O_4 proportion within the AF layers. This can, on the other hand, increase the number of uncompensated spins within the AF. On the other hand, they can have increased un-oxidized proportions of Co (Co_xO_y). Since the absolute thickness of such an unoxidized layer is very small (below 10 monolayers), with increased possibility of Au at its neighborhood, the unoxidized Co magnetic moments can turn out of plane. Thus one can argue that the observed increase in the bias field can be attributed to the canting of the Co moments at the Co-Au interface (effective reduction in the FM layer thickness) and/or increased proportion of uncompensated moments within the CoO layers.

Presumably, the uncompensated AF moments within the CoO are located at approximately 1–2 nm from the interface and a canting of those spins would have reduced the bias field as a result of net reduction in the number of uncompensated spins. Similarly, with an induced magnetism in Au at the Co-Au (FM-Au) interface, there would have been a decrease in the bias field (effective increase of the FM layer). On the other hand, an induced magnetism within the AF, adjacent to a FM (AF-FM interface), can only reduce the bias field rather than increasing it.[58] However, the effect of an induced magnetism at the CoO-Au (AF-Au interface) interface would have been interesting to investigate. Thus we can rule out any induced moment either at the FM-Au or AF-FM interfaces or canting of the AF moments.

Paul *et al.* have recently reported that with the application of a perpendicular cooling field (perpendicular to the film plane) one can induce an exchange bias in Co/CoO/Au MLs which is directed out of plane.[20] This unconventional exchange biasing was possible mainly due to the difference in uniaxial anisotropy energies of the Co ($\sim 5 \times 10^5$ erg cm^{-3})[59] and the CoO ($\sim 25 \times 10^7$ erg cm^{-3})[60] layer apart from the possible intrinsic tendency of PMA at the Co-Au interfaces. In the present context, we performed similar measurements on our MLs. An increasing tendency of induced bias in the out-of-plane direction would essentially confirm the increasing out-of-plane canted proportion of the Co moments, with increasing spacer thickness. In other words, the larger the number of out-of-plane uncompensated moments is the larger the reduction of the moments in the film-plane will be.

Figure 18 shows the longitudinal magnetization measured at 10 K for an out-of-plane cooling field ($H_{FC} = +4.0$ kOe)

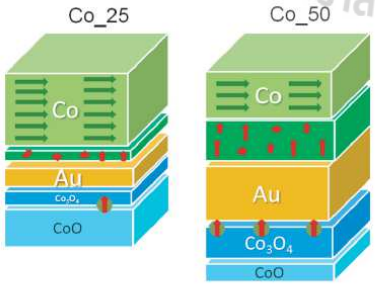

FIG. 17. (Color online) The schematics of the layer structures at the Co-Au and Au-CoO interfaces of the two MLs Co_25 and Co_50. The arrows represent the out-of-plane FM spins (red) and the in-plane FM spins (green).

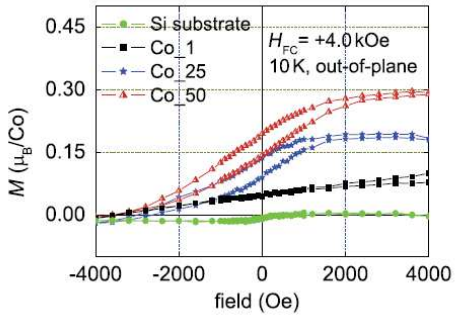

FIG. 18. (Color online) Magnetization loops for the substrate, Co_1, Co_25, and Co_50 MLs for out-of-plane cooling field.

for the Co_1, Co_25, and C_50 MLs. The signal can be compared with the background signal from a Si substrate measured with the same conditions in the PPMS, showing a typical linear paramagnetic slope. One may note that a hysteresis (opening up of the loop) is seen only for the Co_25 and Co_50 MLs and not for the Co_1 ML. This is expected since the Co_1 ML does not contain any Au spacer layer. This obviously indicates the increased tendency of PMA with increased spacer layer thickness. Out-of-plane canting of the Co moments have resulted in the net reduction in the moments in the film-plane. Additionally, we find a distinct but small vertical shift of the hysteresis loops for all of our MLs (and not for the substrate). Vertical shifts are related to uncompensated moments at the FM-AF interfaces or noncollinear magnetic structure at interfaces.[61] Depending upon their origin (which, however, remains unclear) that can be in the AF and/or in the FM, they can be, in principle, correlated or uncorrelated to the H_{eb} values. Thus nonmagnetic spacers are shown to affect the interface magnetism without changing the microstructure.

Canting of the Co moments or induced magnetism of the Au layer can be looked upon as due to *s-d* hybridization. However, whether the hybridization is at the Co-Au interface or at the CoO-Au interface is beyond the scope of the available techniques. We suggest that a deeper insight into the impact of the AF/Au or FM/Au interface magnetism including the effects of roughness and interdiffusion on the exchange bias phenomena has to be undertaken for a better understanding.

IV. CONCLUSION

We observe a systematic increase in the exchange bias fields and the coercive fields with increasing thicknesses of the Au layer that are immersed between the Co/CoO bilayers which may be an important route to improve future devices using the exchange bias. The structural evolution of the ferromagnetic grains as seen by XTEM measurements is interrupted by growing Au layers of appropriate thickness. The grains in the Au layers are of the order of the Au layer thickness. The Au layer decouples the structural and magnetic properties of the magnetic bilayers thus inhibiting the evolution of domains across the heterostructure. Evidence of this is provided by off-specular polarized neutron scattering. Interestingly, the magnetic moment per atom in the FM layers is seen to decrease with increasing thickness of the Au spacer layer. This is confirmed by PPMS and PNR measurements. Subloop shifts of the hysteresis around the blocking temperature indicates a different initial AF-FM domain configuration for samples with Au spacers (as compared to that without spacers).

The increase in the bias field, to some extent, accounts for the relative proportions of the FM and AF species as inferred from the XANES and the XAS measurements. However, a larger extent of the increment is owed to reduced magnetic moment of the Co layer as inferred from the magnetometry and PNR measurements. Such a reduction is plausibly owed to the out-of-plane orientation tendencies of the Co moments at the Co-Au interfaces. By performing perpendicular field cooling, we could demonstrate an increasing tendency of the Co moments to orient out-of-plane which effectively explains the in-plane decrease of the magnetic moment with increased Au spacer thickness. Perpendicular field cooling is thus seen as a novel way to characterize the uncompensated spins at the interface of such exchange coupled systems. Further detail on the interfaces, for example, hybridization at the AF/NM and FM/NM interfaces and changes in the AF-FM domain configurations (due to the NM) can be topics for future investigations.

ACKNOWLEDGMENTS

This work was supported by the Deutsche Forschungsgemeinschaft via the Transregional Collaborative Research Centers TRR 80. We would also like to thank Ulrike Bloeck and Andreas Bauer for the assistance in TEM and PPMS measurements, respectively.

*Corresponding author: amitesh.paul@frm2.tum.de

[1] A. Moser, K. Takano, D. T. Margulies, M. Albrecht, Y. Sonobe, Y. Ikeda, S. Sun, and E. E. Fullerton, J. Phys. D **35**, R157 (2002); D. Weller and A. Moser, IEEE Trans. Magn. **35**, 4423 (1999).

[2] W. H. Meiklejohn and C. P. Bean, Phys. Rev. **102**, 1413 (1956).

[3] M. G. Blamire, M. Ali, C.-W. Leumg, C. H. Marrows, and B. J. Hickey, Phys. Rev. Lett. **98**, 21702 (2007).

[4] J. Nogués and I. K. Schuller, J. Magn. Magn. Mater. **192**, 203 (1999); A. E. Berkowitz and K. Takano, *ibid.* **200**, 552 (1999).

[5] M. Gierlings, M. J. Prandolini, H. Fritzsche, M. Gruyters, and D. Riegel, Phys. Rev. B **65**, 092407 (2002).

[6] A. Paul, C. M. Schneider, and J. Stahn, Phys. Rev. B **76**, 184424 (2007).

[7] M. D. Stiles and R. D. McMichael, Phys. Rev. B **59**, 3722 (1999).

[8] M. Gruyters and D. Schmitz, Phys. Rev. Lett. **100**, 077205 (2008).

[9] M. R. Fitzsimmons, P. Yashar, C. Leighton, I. K. Schuller, J. Nogues, C. F. Majkrzak, and J. A. Dura, Phys. Rev. Lett. **84**, 3986 (2000).

[10] A. Paul, E. Kentzinger, U. Rücker, and T. Bruckel, Phys. Rev. B **74**, 054424 (2006).

[11] A. Paul and S. Mattauch, Appl. Phys. Lett. **95**, 092502 (2009).

[12] A. Paul, E. Kentzinger, U. Rücker, D. E. Bürgler, and P. Grünberg, Phys. Rev. B **70**, 224410 (2004).

[13] M. Gierlings, M. J. Prandolini, M. Gruyters, T. Funk, D. Riegel, and W. D. Brewer, Eur. Phys. J. B **45**, 137 (2005).

[14] M. Fecioru-Morariu, S. R. Ali, C. Papusoi, M. Sperlich, and G. Güntherodt, Phys. Rev. Lett. **99**, 097206 (2007).

[15] M. J. Prandolini, Rep. Prog. Phys. **69**, 1235 (2006).

[16] S. Laureti, S. Y. Suck, H. Haas, E. Prestat, O. Bourgeois, and D. Givord, Phys. Rev. Lett. **108**, 077205 (2012).

[17] Y. Meng, J. Li, P.-A. Glans, C. A. Jenkins, E. Arenholz, A. Tan, J. Gibbons, J. S. Park, C. Hwang, H. W. Zhao, and Z. Q. Qiu, Phys. Rev. B **85**, 014425 (2012).

[18] A. N. Dobrynin and D. Givord, Phys. Rev. B **85**, 014413 (2012).

[19] S. R. Ali, M. R. Ghadimi, M. Fecioru-Morariu, B. Beschoten, and G. Guntherodt, Phys. Rev. B **85**, 012404 (2012).

[20] A. Paul, N. Paul, and S. Mattauch, New J. Phys. **13**, 063009 (2011).

[21] A. Paul, D. Bürgler, M. Luysberg, and P. Grünberg, Europhys. Lett. **68**, 233 (2004).
[22] C. Leighton, J. Nogués, B. J. Jönsson-Åkerman, and Ivan K. Schuller, Phys. Rev. Lett. **84**, 3466 (2000).
[23] A. Paul, Pramana: J. Phys. **78**, 1 (2012).
[24] U. Nowak, K. D. Usadel, J. Keller, P. Miltenyi, B. Beschoten, and G. Güntherodt, Phys. Rev. B **66**, 014430 (2002).
[25] Y. Zhao, T. E. Feltes, J. R. Regalbuto, R. J. Mayer, and R. F. Klie, J. Appl. Phys. **108**, 063704 (2010).
[26] F. Wilhelm, M. Angelakeris, N. Jaouen, P. Poulopoulos, E. Th. Papaioannou, Ch. Mueller, P. Fumagalli, A. Rogalev, and N. K. Flevaris, Phys. Rev. B **69**, 220404(R) (2004).
[27] D. Mauri, E. Kay, D. Scholl, J. Kent, and J. Kent Howard, J. Appl. Phys. **62**, 2929 (1987).
[28] E. Girgis, R. D. Portugal, H. Loosvelt, M. J. Van Bael, I. Gordon, M. Malfait, K. Temst, C. Van Haesendonck, L. H. A. Leunissen, and R. Jonckheere, Phys. Rev. Lett. **91**, 187202 (2003).
[29] K. O'Grady, L. E. Fernandez-Outon, and G. Vallejo-Fernandez, J. Magn. Magn. Mater. **322**, 883 (2010).
[30] G. Herzer, J. Magn. Magn. Mater. **294**, 99 (2005).
[31] J. Geshev, L. G. Pereira, and J. E. Schmidt, Phys. Rev. B **66**, 134432 (2002).
[32] A. Paul, E. Kentzinger, U. Rücker, and Th. Brückel, Phys. Rev. B **73**, 092410 (2006).
[33] A. R. Modak, David J. Smith, and S. S. P. Parkin, Phys. Rev. B **50**, 4232 (1994).
[34] D. H. Wei, S. C. Chou, T. S. Chin, C. C. Yu, Y. Liou, and Y. D. Yao, J. Appl. Phys. **97**, 10N121 (2005).
[35] A. Ney, P. Poulopoulos, M. Farle, and K. Baberschke, Phys. Rev. B **62**, 11336 (2000).
[36] C. F. Majkrzak, J. D. Axe, and P. Böni, J. Appl. Phys. **57**, 3657 (1985); J. F. Ankner, C. F. Majkrzak, and H. Homma, *ibid.* **73**, 6436 (1993).
[37] J. Orna, L. Morellón, P. A. Algarabel, J. M. De Teresa, A. Fernández-Pacheco, G. Simón, C. Magen, J. A. Pardo, and M. R. Ibarra, Advances Science Technology **67**, 82 (2010).
[38] B. P. Toperverg, in *Polarized Neutron Scattering*, Matter and Materials Vol. 12 (Forschungszentrum Jülich, Germany, 2002), p. 247; H. Zabel *et al.* in *Handbook of Magnetism and Advanced Magnetic Materials*, edited by H. Kronmuller and S. Parkin (Wiley, NY, 2007), p. 1237.
[39] A. Paul and S. Mattauch, J. Appl. Phys. **108**, 053918 (2010).
[40] Jörg F. Löffler, Werner Wagner, and Gernot Kostorz, J. Appl. Crystallogr. **33**, 451 (2000).
[41] J. F. Löffler, H. B. Braun, and W. Wagner, J. Appl. Phys. **85**, 5187 (1999).
[42] B. Ravel and M. Newville, J. Synchrotron Radiat. **12**, 537 (2005).
[43] A. L. Ankudinov, B. Ravel, J. J. Rehr, and S. D. Conradson, Phys. Rev. B **58**, 7565 (1998).
[44] S. Gangopadhyay, G. C. Hadjipanayis, C. M. Sorensen, and K. J. Klabunde, J. Appl. Phys. **73**, 6964 (1993).
[45] X. Y. Lang, W. T. Zheng, and Q. Jiang, Nanotechnology **18**, 155701 (2007).
[46] J. A. Borchers, Y. Ijiri, D. M. Lind, P. G. Ivanov, R. W. Erwin, Aron Qasba, S. H. Lee, K. V. O'Donovan, and D. C. Dender, Appl. Phys. Lett. **77**, 4187 (2000).
[47] J. Stöhr, J. Magn. Magn. Mater. **200**, 470 (1999).
[48] J. T. Lau, J. Rittmann, V. Zamudio-Bayer, M. Vogel, K. Hirsch, Ph. Klar, F. Lofink, T. Mller, and B. V. Issendorff, Phys. Rev. Lett. **101**, 153401 (2008).
[49] B. T. Thole and G. vander Laan, Phys. Rev. B **38**, 3158 (1988).
[50] M. Koshinoa, H. Kuratab, S. Isodaa, and T. Kobayashia, Micron **31**, 373 (2000).
[51] O. Šipr, J. Minár, J. Vackář, and H. Ebert, Phys. Rev. B **75**, 134422 (2007).
[52] P. Grünberg, R. Schreiber, Y. Pang, M. B. Brodsky, and H. Sowers, Phys. Rev. Lett. **57**, 2442 (1986).
[53] N. N. Shukla, A. Sen, and R. Prasad, Phys. Rev. B **76**, 174417 (2007).
[54] J. Moritz, F. Garcia, J. C. Toussaint, B. Dieny, and J. P. Nozières, Europhys. Lett. **65**, 123 (2004).
[55] V. K. Valev, M. Gruyters, A. Kirilyuk, and Th. Rasing, Phys. Rev. Lett. **96**, 067206 (2006).
[56] R. Morales, Zhi-Pan Li, J. Olamit, Kai Liu, J. M. Alameda, and Ivan K. Schuller, Phys. Rev. Lett. **102**, 097201 (2009).
[57] A. Paul and P. Böni (unpublished).
[58] A. Paul, Appl. Phys. Lett. **97**, 032505 (2010).
[59] W. Wulfhekel, S. Knappmann, and H. P. Oepen, J. Appl. Phys. **79**, 988 (1996).
[60] W. L. Roth, Phys. Rev. **110**, 1333 (1958).
[61] E. C. Passamania, C. Laricaa, C. Marquesa, J. R. Provetia, A. Y. Takeuchib, and F. H. Sanchez, J. Magn. Magn. Mater. **299**, 11 (2006).

มหาวิทยาลัยเทคโนโลยีสุรนารี

Article published in Physical Review B

PHYSICAL REVIEW B **91**, 224428 (2015)

Recovery and nonrecovery of the untrained state in an exchange-coupled system

Jaru Jutimoosik,[1,2] Rattikorn Yimnirun,[2] Annette Setzer,[3] Pablo Esquinazi,[3] Jochen Stahn,[4] and Amitesh Paul[1,*]

[1]*Technische Universität München, Physik Department, Lehrstuhl für Neutronenstreuung, James-Franck-Strasse 1, D-85748 Garching b. München, Germany*

[2]*School of Physics, Institute of Science and NANOTEC-SUT Center of Excellence on Advanced Functional Nanomaterials, Suranaree University of Technology, Nakhon Ratchasima 30000, Thailand*

[3]*Division of Superconductivity and Magnetism, University of Leipzig, D-04103 Leipzig, Germany*

[4]*Laboratory for Neutron Scattering Paul Scherrer Institut, CH-5232 Villigen, Switzerland*

(Received 23 February 2015; revised manuscript received 6 May 2015; published 25 June 2015)

We report depth sensitive investigations of the magnetic interaction between exchange-coupled stacked CoO and ferromagnetic Co bilayers (separated by thick Au layers) as we explore the degree of recovery of the untrained state after the first two field cycles. Such a recovery is expected by field cycling a reorientation field (H_{RE}) along a direction (Ω_{RE}) away from the initial field cooling direction. Measurements as a function of Ω_{RE} and the strength of H_{RE} (along each direction) map the influence of Ω_{RE} on the reversal mechanism in the layers and thereby the degree of recovery. Our results are consistent with the earlier observations in similar systems that was realized with $\Omega_{RE} = 90^{\circ}$. We ascribe these partial and/or significant recoveries to the unchanged sense of rotation after initial field cooling of the ferromagnetic magnetization upon each field cycling. Furthermore, in our system, we find that this recovery can be regulated by choosing various other H_{RE} and Ω_{RE} values without changing the rotational sense. The best recipe for recovery is identified for $\Omega_{RE} = 45^{\circ}$, that can be achieved partially with $H_{RE} = 3.0$ kOe and remain significant even with $H_{RE} = 10.0$ kOe. In this study we not only understand the fundamental mechanism in the recovery of training, but also instigate its technological prospects by lifting the directional restrictions of the reorientation field.

DOI: 10.1103/PhysRevB.91.224428 PACS number(s): 61.05.fj, 75.70.Cn, 75.60.Jk

I. INTRODUCTION

Interfacial exchange coupling between a ferromagnet (FM) and an antiferromagnet (AF) can "lock" the magnetization into the FM in a well-defined direction. This effect, which in a phenomenological picture takes the form of a unidirectional magnetic anisotropy, is known as exchange bias [1]. A cooling field H_{FC} (cooling below the ordering temperature of AF) essentially determines the state of the FM which in-turn determines the strength of the bias field H_{EB} [2–4].

We focus on a polycrystalline Co (ferromagnet)/CoO (antiferromagnet) exchange bias system. It is ideal for the investigation due to its large biasing field [5], very distinct asymmetry of magnetization reversal [2], large enough training effects [6], and most interestingly the AF moment configuration can be frozen-in in a variety of ways during the process of field cooling [7] without affecting the overall structure as the AF ordering temperature is far below room temperature (leading to negligible interdiffusion at the interfaces). The difference between subsequent (partial) magnetization reversal loops is called the "training effect." The training effect can be linked to a deviation of the average interfacial magnetization vector of the AF CoO grains with respect to the initial field cooling direction. Even though the microscopic origin of the training effect is still under debate, it is generally agreed to be due to some initial nonequilibrium arrangement leading to such a metastable state of the AF spins [5,8–11]. Therefore, it is perceived that the metastable state can somehow be rearranged to reinduce the original state.

Brems *et al.* [11] attempted to restore the untrained state, i.e., the untrained state with its pronounced asymmetry was largely reinduced by a moderate magnetic field, applied perpendicular ($\perp^r$) to the initial cooling field in a Co/CoO bilayer system. In fact a very similar phenomenon was reported earlier by the same group on stripes of CoO/Co as well [12]. The only difference being the strength of the cooling field that may determine the degree of asymmetry in reversal in the latter version. Very recently, Brems *et al.* [13] have reported of tracking the average rotation sense of the magnetization vector of a 20 nm Co layer upon magnetization reversal in a similar CoO/Co bilayer system. Their inference on the rotational sense relied upon the anisotropic magnetoresistence (AMR) signal measured along 45° with respect to the cooling field and also the $\perp^r$ field directions.

It may be noted that the AMR measurements rely on the current distribution within the sample and are difficult to infer on any reinduction of the untrained state within a multilayered system, particularly when domains are involved. AMR values are weak when a sample consists of different domains of equal proportions that can rotate clockwise or counterclockwise. Moreover, the direction of the reorienting magnetic fields (with different magnitudes) in the works of Brems *et al.* were always restricted along or opposite to the direction $\perp^r$ to the initial cooling field.

Using depth sensitive polarized neutron reflectivity (PNR), Paul *et al.* [14,15] reported earlier that such a partial restoration of the untrained state was indeed possible even within a Co/CoO/Au multilayer. Since the bilayers of the multilayer was separated by a thick nonmagnetic Au layer at each AF-FM interface, it was expected to behave as a repeated stack of independent Co/CoO bilayers. Interestingly, the PNR data showed that the $\perp^r$ field cycling has inflicted an additional

*Corresponding author: amitesh.paul@frm2.tum.de

 ©2015 American Physical Society

modification at the Co/CoO interface magnetization. One may note that PNR is sensitive to each and every interface along the depth of the whole multilayer stack and to the direction of the parallel magnetic moment (though not to the directional sense of the perpendicular magnetic moment). However, such a conclusion on interface magnetism in the work of Paul *et al.* suffered from two shortcomings. First, the PNR data were limited to a relatively low value of the accessible scattering vector (0.05 Å^{-1}) and second, the particular specimen was subjected to a single field value along the $\perp^r$ direction.

In this paper we report on the investigation of reinduction of the untrained state in a Co/CoO/Au multilayer using different values of the reorientation field (H_{RE}) and along three different orientations (Ω_{RE}) with respect to the cooling field direction. Simulations have indicated earlier that the reinduction of the untrained state depends on the amplitude and direction of the reorientation field. We have done a detailed investigation of the phenomena by measuring the parallel component of magnetization using a superconducting quantum interference device (SQUID). Furthermore, using PNR we have investigated the parallel as well as the perpendicular components of magnetization for each representative case identified in the SQUID data.

II. SAMPLES AND MEASUREMENTS

We have investigated multilayers of the composition SiO_2/[Co(13.0 nm)/CoO(5.0 nm)/Au(20.0 nm)]$_{16}$ prepared by dc magnetron sputtering [10]. During deposition, the Ar pressure in the magnetron sputtering chamber was 3×10^{-3} mbar. The process was started at a base pressure of 1×10^{-7} mbar. We employ an ultraviolet light assisted oxidation at an O_2 pressure of 200 mbars at 50 °C for 1 h [4].

Microstructural characterization has been done using cross-sectional transmission electron microscopy (XTEM). The samples were prepared by standard mechanical (diamond) polishing followed by Ar^+ ion milling at 4 kV for about 1 h. A conventional bright-field imaging mode was used.

Conventional in-plane magnetization loops are measured using a SQUID, MPMS from Quantum Design. All SQUID measurements were done after the sample was cooled down to 10 K from room temperature (RT) in the presence of a well defined cooling field of $H_{\text{FC}} = +10.0$ kOe (along the $-y$ axis) provided by a cryomagnet and then it was subjected to two consecutive field cycling (first and second). After the second hysteresis loop we have completed a third hysteresis loop (which starts and ends in the Ω_{RE} directions) before measuring the hysteresis loop along the fourth (and fifth) field cycle (which is along the same direction as the first and second field cycles). Thus, expect for the third field cycle, all measurements were along the y axis.

The sample was raised to room temperature and cooled again each time we opt for a different amplitude of the reorientation field H_{RE} and also along a different orientation Ω_{RE} in measuring along the third field cycle. The purpose of the third field cycle is merely to reorient the spin configuration after the first field cooling. The orientation angles were made possible by using a precision sample rotator attached to the SQUID.

The neutron scattering experiments were performed at the polarized neutron reflectometer with polarization analysis AMOR in a time of flight (TOF) mode at SINQ, Paul Scherrer Institute in Switzerland. The neutron measurements were done following the very same procedure as described for measuring the SQUID data which enabled us to measure along the decreasing branch (applied field opposite to the cooling field). The different orientation angles of the sample with respect to the initial cooling field direction were made possible by using a unique precision sample rotator within the cryomagnet at the sample position of AMOR.

Depth sensitive neutron scattering under grazing incidence with polarization analysis (PNR) [16–18] were used for our investigation on a *microscopic* scale. A detailed description of the PNR technique and measurements can be found in Refs. [16,19]. The reflectivity was recorded as a function of scattering vector,

$$\vec{Q} = \vec{k_i} - \vec{k_f}, \tag{1}$$

$$Q_z = Q_\perp = \frac{2\pi}{\lambda}[\sin(\alpha_{\text{i}}) + \sin(\alpha_{\text{f}})] \simeq \frac{2\pi}{\lambda}[\alpha_{\text{i}} + \alpha_{\text{f}}], \tag{2}$$

$$Q_x = Q_\parallel = \frac{2\pi}{\lambda}[\cos(\alpha_f) - \cos(\alpha_i)]. \tag{3}$$

Here the incident wave vector defined by $\vec{k_i}$, makes an angle α_{i} in the x-z plane with respect to the x axis while the scattered wave vector $\vec{k_f}$ makes angle α_{f}. In specular scattering geometry, the normal wave vector transfers $Q_\perp$ are probed while off-specular scattering contributions along the in-plane momentum transfer vector $Q_\parallel$ arise, when the in-plane translational symmetry is broken by interface waviness (roughness) or by magnetic domains on a length scale shorter than the neutron coherence length ($l_\parallel$) along $Q_\parallel$.

The nonspin flip (NSF) scattering amplitude provides information about $\rho_{\text{n}} \pm \rho_{\text{m}} \cos\phi_{\text{A}}$, and the spin flip (SF) channels measure $\rho_{\text{m}}^2 \sin^2\phi_{\text{A}}$, if the domain size is larger than the projection of the neutron coherence length along the sample plane ($l_\parallel$). Here, ρ_{n} is the nuclear and ρ_{m} is the magnetic scattering length density (SLD). We designate ϕ_{A} as the angle between the direction of FM magnetization ($\mathbf{M_{FM}}$) and the neutron spin quantization axis. The neutron polarization vector is guided by the field applied to the sample (H_{a}) along the y axis.

With spin analysis of the reflected neutron beam, it is possible to measure independently the NSF and SF reflectivities. PNR is sensitive to the directions of the parallel ($\mathbf{M_{FM\parallel}}$) and perpendicular ($\mathbf{M_{FM\perp}}$) components of the magnetic moment. In the experiment three different cross sections were distinguished, namely NSF channels : (R_{++} and R_{--}) and SF channel : (R_{-+}). Here $+$ and $-$ signs are used to distinguish the intensity contributions R representing the polarization component $\parallel$ and anti-$\parallel$ to the guiding field, respectively. $R_{++/--}$ contains the sum/difference between ρ_{n} and ρ_{m}, whereas the SF signal contains only the magnetic information via ρ_{m}.

The NSF reflectivities involve squares of the combinations of $(1 - \cos\phi_{\text{A}})$ and $(1 + \cos\phi_{\text{A}})$ terms while SF reflectivities involve $(\sin^2\phi_{\text{A}})$ term. Thus, within the one dimensional

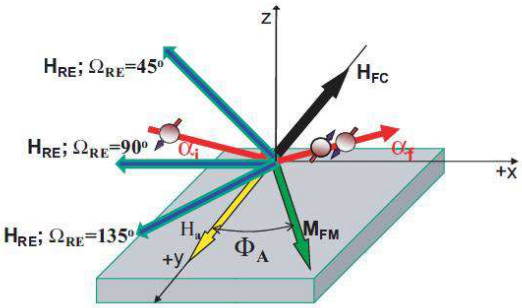

FIG. 1. (Color online) Illustration of the neutron scattering geometry. H_a along the $+y$ axis is shown to be antiparallel to H_{FC}. M_{FM} is the FM magnetization making an angle Φ_A with respect to the field axis. The reorientation field H_{RE} along the $-x$ axis (for $\Omega_{RE} = 90°$) is also shown along with two other orientations ($\Omega_{RE} = 45°$ and $135°$) in the sample plane.

analysis of the polarization vector (for noncollinear structures) it is not possible to discriminate the tilt angle ϕ_A from $(\phi_A + \pi)$ [16].

Figure 1 shows a sketch of the neutron scattering geometry. Here the applied field H_a along the y axis is shown to be antiparallel to the cooling field H_{FC}. $\mathbf{M}_{FM}$ is making an angle Φ_A with respect to the field axis. The reorientation fields H_{RE} are shown along different orientations Ω_{RE} in the sample plane.

III. RESULTS AND DISCUSSIONS

A. Microstructural measurements

Figure 2 shows the XTEM micrographs of the sample. A multilayer structure with three different interfaces can be seen. The sample has a repeated sequence of around 21 nm of Au, 11 nm of Co and 3.5 nm of CoO layers in the stack. These thicknesses are close to their nominal values.

B. Magnetization measurements

Figures 3, 4, and 5 show the SQUID hysteresis loops measured at 10 K for an in-plane cooling field. The parallel component of magnetizations ($\mathbf{M}_{FM\|}$) were measured for different strengths of the H_{RE} values and for three different orientation angles Ω_{RE}.

Clearly seen is the usual asymmetry in the magnetization reversal during the first field cycle (black curve) and the disappearance of the asymmetry during the second field cycle (red curve). We point out that the exchange bias field along the cooling field axis is estimated to be around -630 and -430 Oe for the first and second field cycles, respectively. This decrease in the bias field is due to commonly observed training. The first hysteresis loop shows a kink around -1500 Oe along the decreasing branch and at around $+100$ Oe along the increasing branch. These are typical indications of different oxidation levels in the CoO layers in the stack. Such a variation of oxidation affects the exchange coupling that results in a decrease in the switching fields along the respective branches [17].

After the first two field cycles the third hysteresis loop (magenta curve) shows the magnetization for different values of H_{RE} while completing a field cycle along $\Omega_{RE} = 45°, 90°$, and $135°$ in Figs. 3, 4, and 5, respectively. At $\Omega_{RE} = 135°$ the magnetization goes negative for $H_{RE} = 0.5$ kOe since it changes its direction. After each third field-cycling process, it was followed by two other consecutive hysteresis loop measurements along the fourth (blue curve) and fifth (green curve) field cycles, respectively.

Comparing the coercive fields for the second and fourth field cycles, one can find that there is indeed a reinduction of the untrained state. During the fifth field cycle, however, the revival is completely lost. The degree of reinduction of course varies with the strength of the H_{RE} values and with the angle Ω_{RE}.

Next we plot the derivative of the magnetization $\chi_{mag} = dM/dH_a$ as a function of field corresponding to the different loops as shown in Fig. 6 for $H_{RE} = 0.5$ kOe, as an example. The two peaks on either branch of the hysteresis loops indicate multiple switching fields. We neglect the smaller peak and

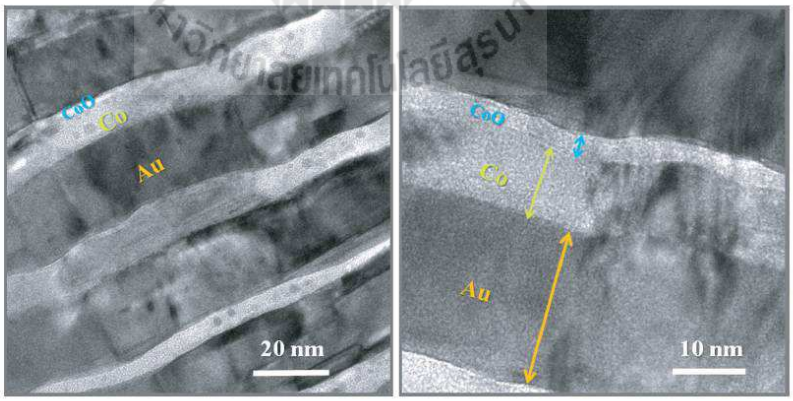

FIG. 2. (Color online) XTEM micrographs of the $[Co/CoO/Au]_{16}$ multilayer.

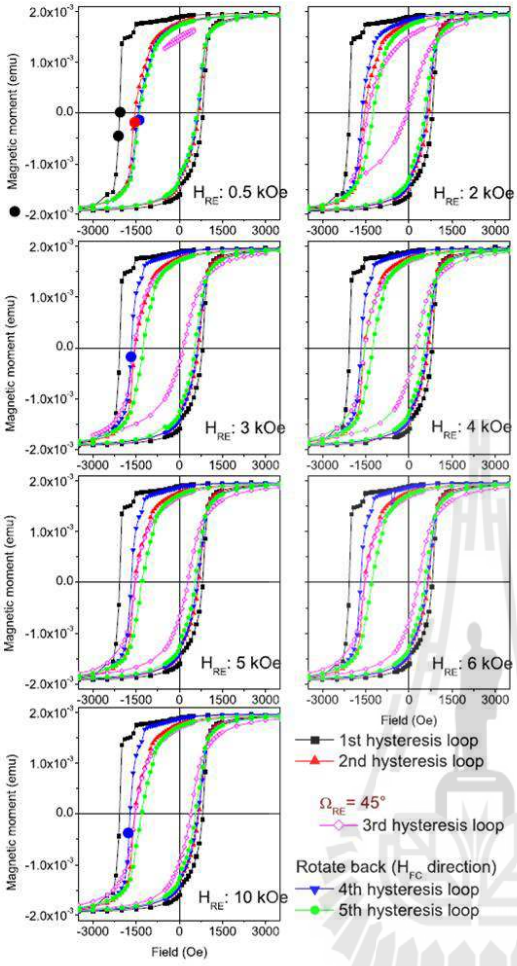

FIG. 3. (Color online) SQUID magnetization hysteresis loops for different field cycles measured at 10 K and for various reorientation fields H_{RE} along $\Omega_{RE} = 45°$ in the sample plane. The black, red, and blue circles mark the applied field values H_a for the neutron measurements along the respective branch of the loops.

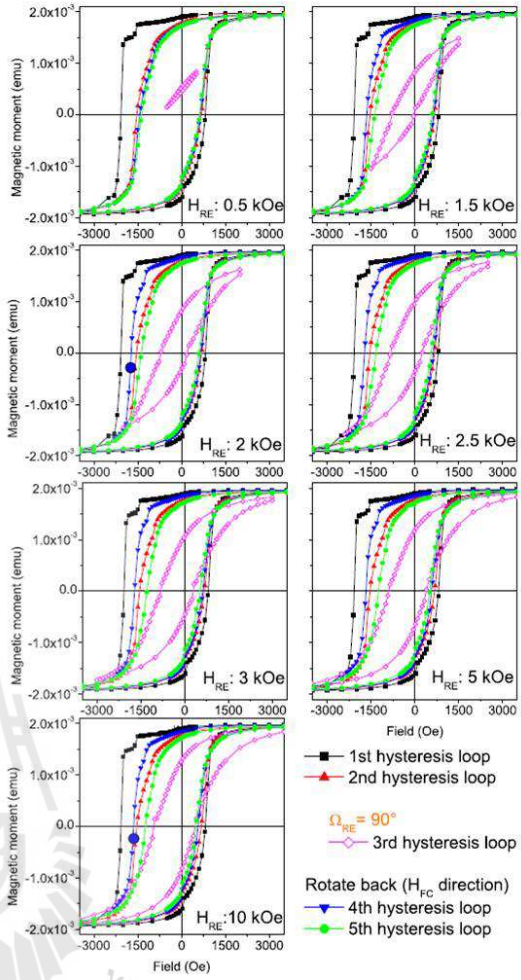

FIG. 4. (Color online) SQUID magnetization hysteresis loops for different field cycles measured at 10 K and for various reorientation fields H_{RE} along $\Omega_{RE} = 90°$ in the sample plane. The blue circles mark the applied field values H_a for the neutron measurements along the respective branch of the loops.

concentrate on the main peaks A1 and A2 on the decreasing and the increasing branch, respectively, which represents most of the magnetization (from majority of the layers) within the layer stack.

In order to quantify the degree of reinduction of the untrained state, we have taken the following path. Firstly, we calculate the integrated areas under each peak from a Gaussian fit to each and every peak A1 and A2 for each field cycle shown in Fig. 6. Secondly, we estimate the degree of asymmetry by defining a parameter X1 for the first hysteresis loop as $X1 = Hys1_{A1}/Hys1_{A2}$. A similar procedure was opted for the second, fourth, and fifth hysteresis loops as we estimate $X2 = Hys2_{A1}/Hys2_{A2}$, $X4 = Hys4_{A1}/Hys4_{A2}$, and $X5 = Hys5_{A1}/Hys5_{A2}$. Here $Hys1_{A1,A2}$, $HSY2_{A1,A2}$, $HSY4_{A1,A2}$, and $HSY5_{A1,A2}$ are the integrated areas under the peaks corresponding to the derivatives of the first, second, fourth, and fifth hysteresis loops, respectively. Finally, we plot in Fig. 7 the ratio of the integrated areas under each peak as $C12 = X1/X2$, $C14 = X1/X4$, and $C15 = X1/X5$. Thus C12 (red up-triangles) lies close to unity and defines the initial degree of training with respect to the state where $H_{RE} = 0$ Oe and $\Omega_{RE} = 0°$. This is compared with the case every time we heat the sample up to RT and cool down again to 10 K in $H_{FC} = +10$ kOe as we set for a different value

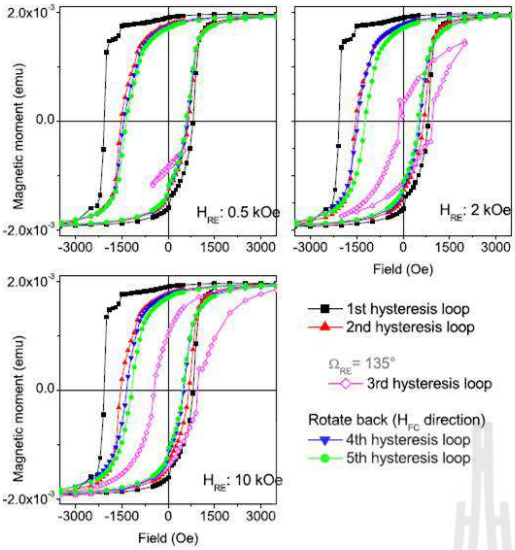

FIG. 5. (Color online) SQUID magnetization hysteresis loops for different field cycles measured at 10 K and for various reorientation fields H_{RE} along $\Omega_{RE} = 135°$ in the sample plane.

of H_{RE} and Ω_{RE}. The slight deviation of C12 from unity with increasing H_{RE} redefines the initial trained state.

Let us now look into some specific cases. It may be noted that on the one hand while C14 (blue squares) is distinctly higher than C12, C15 (green circles) is always lower. This is true for $\Omega_{RE} = 45°$ and $\Omega_{RE} = 90°$ and for all H_{RE} with an exception for $H_{RE} = 0.5$ kOe, where C14 is also lower. On the other hand, for $\Omega_{RE} = 135°$, C14 and C15 are always lower than C12. Following these plots one can infer on the fact that a reinduction of the training has plausibly taken place where C14 is higher than C12. The C15 plot indicates that the reinduction of training is eventually lost after such a revival.

To drive the point on the degree of reinduction/recovery further, we summarize our findings in Fig. 8 where we plot the ratio of the normalized integrated areas C14 with respect to C12 for the three Ω_{RE} values. Here one can see that the reinduction is most efficient (∼42%) for $\Omega_{RE} = 45°$ and attains a fairly constant value after $H_{RE} = 3.0$ kOe. For $\Omega_{RE} = 90°$, one can see that a maximum of the reinduction is reached around $H_{RE} = 2.0$ kOe. Note that this is very similar to the value reported by Brems *et al.* as well for the $\Omega_{RE} = 90°$ case. This is in a way a vindication of our estimation procedure. Moreover, it agrees with their observation that the amplitude of the reorientation (⊥) field needs to be sufficiently large (∼1.9 kOe) in order to realize a maximum in reinduction [13]. Interestingly, unlike that in the $\Omega_{RE} = 45°$ case, here we find a decrease (from 35% to 10%) in the reinduction for any further increase in H_{RE}. In the case when $\Omega_{RE} = 135°$, however, there is no indication of reinduction.

C. Neutron scattering measurements

1. First and second field cycles

We show the specular NSF and SF scattering signals measured at 10 K in Figs. 9(a)–9(d) after the system has been cooled down in the presence of $H_{FC} = +10.0$ kOe. The data show at least four orders of magnitude drop in intensity at $Q_z = 0.11$ Å^{-1}. Note that we have measured up to a high

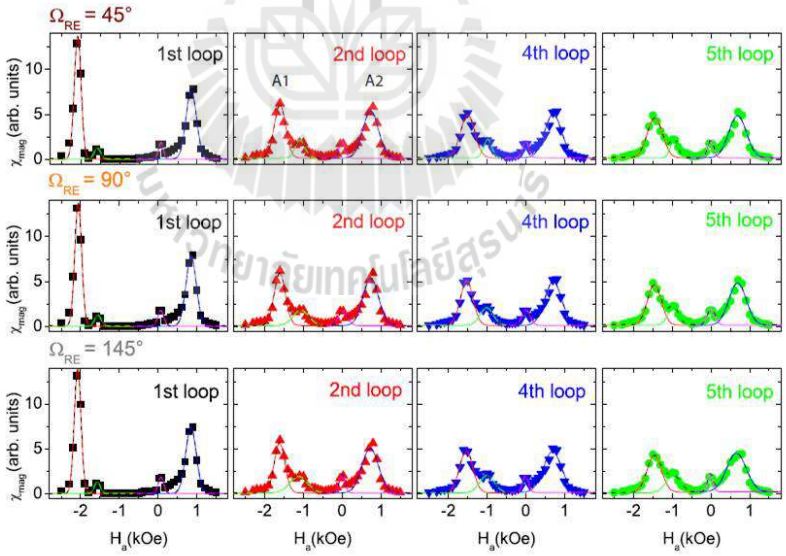

FIG. 6. (Color online) The field derivative of magnetization χ_{mag} as a function of field measured at a reorientation field $H_{RE} = 0.5$ kOe and along different orientations Ω_{RE} in the sample plane. The Gaussian fits to the peaks are shown in lines.

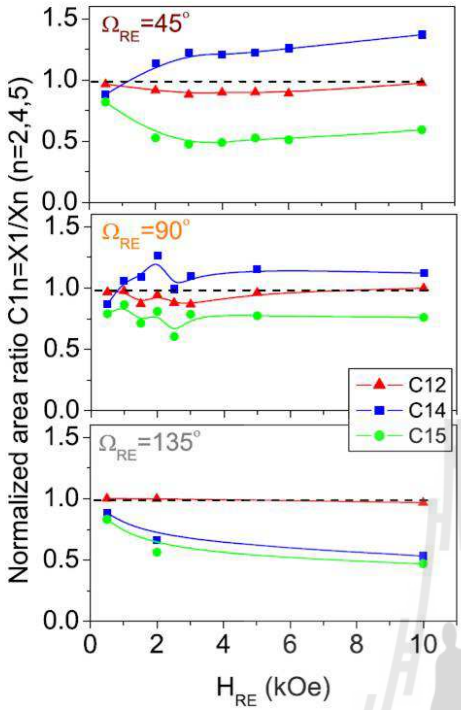

FIG. 7. (Color online) The normalized integrated area ratios $C1n = X1/Xn$ ($n = 2,4,5$) with respect to the initial training for various reorientation field H_{RE} and along different orientations Ω_{RE} in the sample plane. Here n is the number of loop cycle. The symbol sizes are typical of their error bars.

value (0.11 $Å^{-1}$) of the scattering vector which is expected to reduce the possible ambiguities in the data analysis.

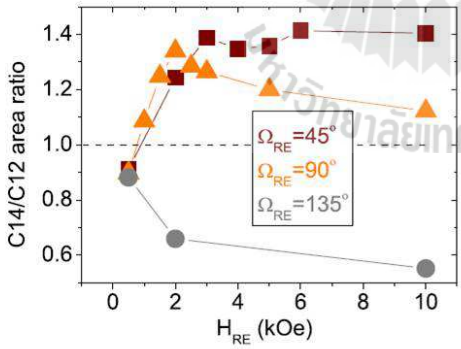

FIG. 8. (Color online) The ratio of normalized integrated area corresponding to the fourth field cycle with respect to the trained state during the fourth field cycle (C14/C12) for various reorientation field H_{RE} and along different directions Ω_{RE} in the sample plane. The symbol sizes are typical of their error bars.

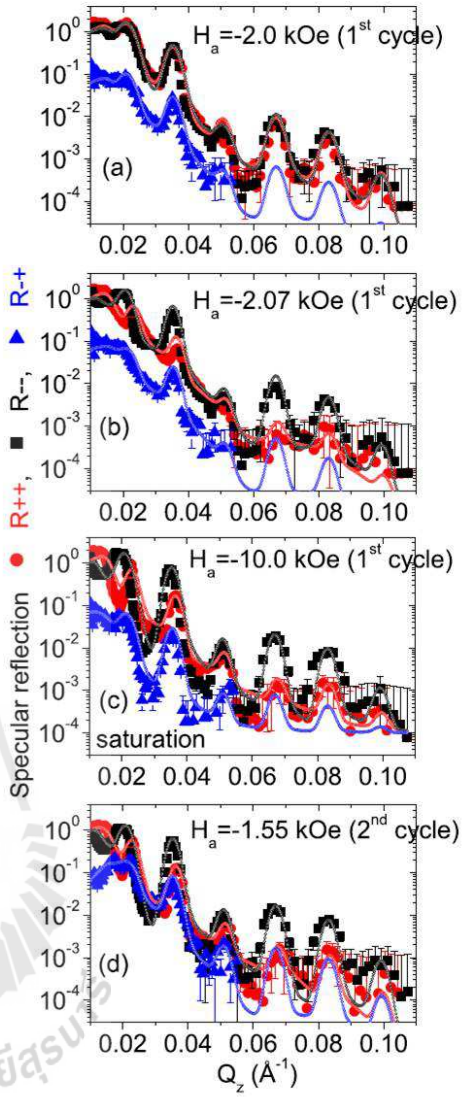

FIG. 9. (Color online) Specular reflectivity patterns (solid symbols) along with their best fits (open symbols) as a function of Q_z for the NSF [R_{--} (black) and R_{++} (red)] and SF [R_{-+} (blue)] channels measured at (a) close to the coercive field $H_a = -2.0$ kOe, (b) a slightly higher field $H_a = -2.07$ kOe, (c) a saturation field of $H_a = -10.0$ kOe during the first field cycle, and (d) at $H_a = -1.55$ kOe during the second field cycle.

Let us first concentrate on the data that was measured at a saturation field of $H_a = -10.0$ kOe [Fig. 9(c)] during the first field cycle. The black circles in Fig. 3 show the fields of measurements. Since the data were measured at saturation we do not expect any SF signal to be present. The intensities

TABLE I. Fit parameters extracted from the PNR results at saturation. Here ρ_n and ρ_m designate the nuclear and magnetic scattering length densities, respectively.

Multilayer	Au	CoO	Co	Co-Au	Error
Thickness (nm)	20.0	5.1	10.5	2.7	± 0.2
ρ_n ($\times 10^{-6}$ Å^{-2})	4.5	4.5	3.0	4.0	± 0.2
ρ_m ($\times 10^{-6}$ Å^{-2})	0.0	0.0	3.0	1.0	± 0.1

in the SF channel are therefore from the small contribution of the NSF intensities which appears in the SF channels due to nonideal efficiencies of the polarizer and analyzer which amounts to a polarization efficiency factor $P \approx 94\%$.

From the fits to the saturation data we get the informations on $\rho_n \approx 3.0 \times 10^{-6}$ Å^{-2} and $\rho_m \approx 3.0 \times 10^{-6}$ Å^{-2} for the Co layers in the stack. For the Au and CoO layers, $\rho_n \approx 4.5 \times 10^{-6}$ Å^{-2} was obtained. Additionally, we find a reduced magnetic layer $t_{\text{Au-Co}} \approx 2.7$ nm with $\rho_n \approx 4.0 \times 10^{-6}$ Å^{-2} and $\rho_m \approx 1.0 \times 10^{-6}$ Å^{-2} at the Co-Au interface possibly due to canting as has been reported earlier in similar systems [17]. The thicknesses and the SLD values of the individual layers in the multilayer are found to be close to their nominal values and they are tabulated along with the nuclear and magnetic SLDs in Table I. Note that since $R_{--} > R_{++}$ (as H_a is negative), we expect a complete alignment of the Co moments along the field direction at -10.0 kOe, i.e., $\phi_A = 0°$.

Next we inspect the data measured at $H_a = -2.0$ kOe [Fig. 9(a)] and $H_a = -2.07$ kOe [Fig. 9(b)] during the first field cycle (marked by the black circles in Fig. 3). The fits to the data set reveal that the magnetization reversal is via domain wall and/or nucleation (DW) process when measured at a coercive field of $H_a = -2.0$ kOe. The identification of the reversal process via DW or rotational reversal from the SF signals was demonstrated more than a decade earlier [2]. Here in our model we have considered eight of the Co layers to have flipped ($\phi_A = 0°$) along the field direction while the other eight layers have not ($\phi_A = 180°$). The error bars in the turn angles are not more than ±5°. The rotational sense of the magnetically weak intermediate layers ($t_{\text{Co-Au}}$) has been always kept similar to that of the Co layers in the stack. However, due to the fact that the net magnetization in the system at this field is close to zero ($R_{++} \simeq R_{--}$ since $\overline{\mathbf{M}_{\text{FM}}} \neq \mathbf{0}$) it is not possible to determine the preferential directional sense of the $\mathbf{M}_{\text{FM}}$ with respect to the H_{FC} direction.

This scenario becomes somewhat different when the sample is measured at a slightly higher field. Then the directional sense of the FM layers can be clearly sensed. This is due to the imbalance in the torque on the magnetic layers that would be exerted on the layers at a field higher than the coercive field. Here at $H_a = -2.07$ kOe [Fig. 9(b)], since $R_{--} > R_{++}$, one can infer from the fit to the data that more numbers of the FM layers (14 out of the 16 layers) have flipped ($\phi_A = 0°$) towards the H_a direction while the bottommost layer ($\phi_A = 180°$) has not. The top/bottom FM layer ($\phi_A = 17°$) has a different turn angle which can be attributed to a loosely coupled state of the FM layer. The variation in coupling strength is due to the asymmetric sequence of the layers in the stack. A distinction between the top or bottom layer upon their interchange in magnetization angle is not very clear thus the references to the top or bottom layers are merely for the sake of identification. It may be noted that the SF signals at the two measuring fields ($H_a = -2.0$ and -2.07 kOe) did not show significant differences due to negligible variations in the perpendicular components of the respective layer magnetizations.

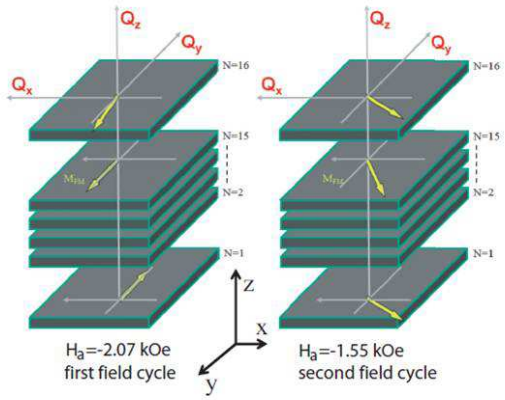

FIG. 10. (Color online) FM layer switching sequence during the first field cycle at $H_a = -2.07$ kOe and during the second field cycle at $H_a = -1.55$ kOe. The arrows indicate the $\mathbf{M}_{\text{FM}}$ orientations in the respective layers. The applied field H_a is along the $-y$ axis.

Next we inspect the data measured at $H_a = -1.55$ kOe [Fig. 9(d)] during the second field cycle. The red circle in Fig. 3 shows the field of measurement. In this case we find from the fits to the data that almost all the FM layers (14) in the stack are undergoing a simultaneous rotational reversal process with $\phi_A = 30°$. Here again the topmost and the bottommost layer have slightly different turn angles ($\phi_A = 50°$) from the rest.

In Fig. 10 we show the layer switching sequences for $H_a = -2.07$ kOe during the first field cycle and $H_a = -1.55$ kOe during the second field cycle. The reversal is dominated by the DW process and by the rotational reversal process, respectively. The rotational senses of $\mathbf{M}_{\text{FM}}$ for all the layers are seen to be preserved. Here the rotational senses of the layers are indicated towards the H_a direction as $R_{--} > R_{++}$. One may recall that apart from a decrease in the coercive field, rotational reversal process of the layers is also a strong signature of training in Co/CoO systems where the untrained-state reversal mechanism during the first field cycle is usually via a DW reversal process.

In Fig. 11(a) we compare the measured SF scattering signals (perpendicular component of M_{FM}) measured at 10 K and at a field of $H_a = -2.07$ and -10.0 kOe (at saturation) during the first field cycle and -1.55 kOe during the second field cycle. The corrected SF signals in Fig. 11(b) is the subtracted-off SF signal (due to the inefficiencies of the optical elements) at saturation. This can be approximated as the net SF signal assuming no SF signal to be present at saturation (neutron polarization is collinear with the magnetization direction).

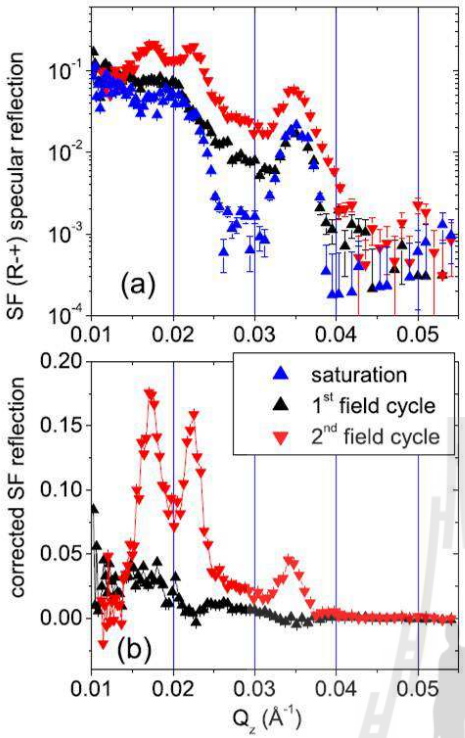

FIG. 11. (Color online) (a) SF specular reflectivity $[R_{-+}]$ patterns as a function of Q_z measured during the first field cycle at $H_a = -2.07$ and -10.0 kOe and during the second field cycle at $H_a = -1.55$ kOe. (b) Plot of the corresponding corrected SF signals as a function of Q_z.

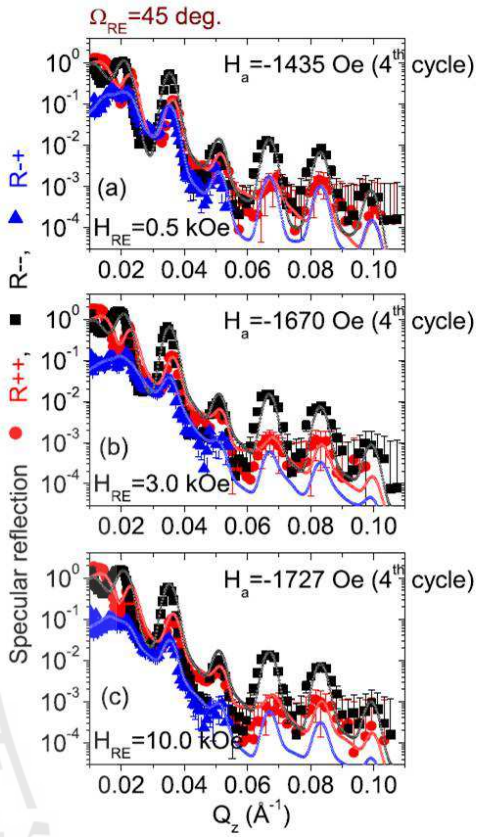

FIG. 12. (Color online) Specular reflectivity patterns (solid symbols) along with their best fits (open symbols) as a function of Q_z for the NSF $[R_{--}$ (black) and R_{++} (red)] and SF $[R_{-+}$ (blue)] channels measured at (a) $H_a = -1.43$ kOe, (b) $H_a = -1.67$ kOe, and (c) $H_a = -1.73$ kOe during the fourth field cycle for different H_{RE} (= 0.5, 3.0, and 10.0 kOe, respectively) values when $\Omega_{RE} = 45°$.

The small increase in the corrected SF signal (black curve) during the first field cycle, which is unexpected during a DW reversal process, is due to some instability within one of the unflipped layers in the stack of 16 layers [18,20]. During the second field cycle (red curve) we find a significant increase in the corrected SF intensity. This increase is related to a rotational reversal process and thereby leads to training [2].

2. *Fourth field cycle with* $\Omega_{RE} = 45°$

PNR measurements during the fourth field cycles were performed keeping $\Omega_{RE} = 45°$. The blue circles in Fig. 3 show the fields of measurements. In Figs. 12(a)–12(c) we show the data measured at 10 K and at $H_a = -1.44$, -1.67, and -1.73 kOe, respectively during the fourth field cycles. The respective H_a values were chosen slightly higher than the coercive fields which are corresponding to the three different representative values of H_{RE} (= 0.5, 3.0, and 10.0 kOe). Note that each time we chose to opt for a different H_{RE} value during the third field cycle, we have used a different H_a value during the fourth field cycle. This was done in accordance with the measured SQUID data.

When $H_{RE} = 0.5$ kOe, the fits to the data reveal magnetization reversal via rotation of the FM magnetization for majority of the layers with $\phi_A = 35°$. Here also we could find that almost all layers (14 out of the 16 layers) in the stack are rotating simultaneously with the exception of the top ($\phi_A = 55°$) and the bottom ($\phi_A = 65°$) layers which have different turn angles. The rotational senses of $\mathbf{M_{FM}}$ for all the layers are seen to be preserved since ϕ_A lies in between 0° and 180°.

In the case of $H_{RE} = 3.0$ kOe, the fits to the data reveal magnetization reversal process of the multilayer is via a DW (flipping) or a rotational process within the individual layers. In this case, we find 12 out of the 16 layers with $\phi_A = 0°$ have flipped while the bottommost layer did not flip ($\phi_A = 180°$). Two layers from the top (with $\phi_A = 25°$) and a layer above the bottommost layer (with $\phi_A = 40°$) are found to be

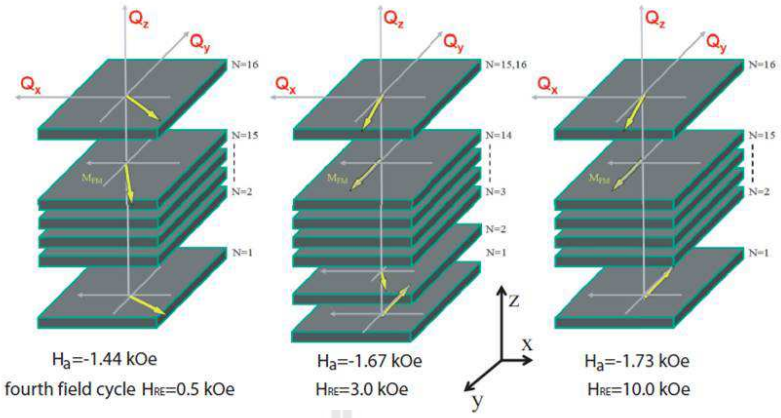

FIG. 13. (Color online) FM layer switching sequence during the different fourth field cycles at $H_a = -1.44$ kOe ($H_{RE} = 0.5$ kOe), -1.67 kOe ($H_{RE} = 3.0$ kOe), and -1.73 kOe ($H_{RE} = 10.0$ kOe) when $\Omega_{RE} = 45°$. The arrows indicate the $\mathbf{M_{FM}}$ orientations in the respective layers. The applied field H_a is along the $-y$ axis.

rotating. Thus, we have a combination of rotation and flipping, depending upon the degree of coupling of the layers.

For $H_{RE} = 10.0$ kOe we find a distinct layer-by-layer flipping scenario. The scenario is close to the case during the first field cycle. Here 13 out of the 16 layers have flipped ($\phi_A = 0°$), while the bottommost layer remain unflipped ($\phi_A = 180°$). The top layer has a turn angle of around $\phi_A = 25°$.

In Fig. 13 we show the layer switching sequences for $H_a = -1.44$, -1.67, and -1.73 kOe during the respective fourth field cycles. Here we can see a gradual transition of the reversal process from being dominated by a rotational reversal process followed by a mixed process of rotational and DW reversal and finally taken over by a pure DW process.

In Fig. 14(a) we compare the measured SF scattering signals (perpendicular component of M_{FM}) measured at 10 K and at fields of $H_a = -1.44$, -1.67, and -1.73 kOe and during the respective fourth field cycles and compare them with $H_a = -10.0$ kOe (at saturation) during the first field cycle. The corrected SF signals in Fig. 14(b) is the subtracted-off SF signal at saturation.

We find a gradual decrease in the corrected SF signals (brown, dark yellow, and pink curves) with increasing H_{RE}. The significant decrease in ϕ_A ($= 0°$ or $180°$) for a majority of the layers in the case of $H_{RE} = 3.0$ and 10.0 kOe as compared to that ($\phi_A = 35°$) for $H_{RE} = 0.5$ kOe, is mainly responsible for the decrease in the respective corrected SF signals.

One may note that in the case of $H_{RE} = 0.5$ kOe, there is no flipping of the layers. Thus one cannot attribute this to reversal via a DW process. Since the rotational reversal process is a signature of training, one can readily infer that in this case there is no revival of the untrained state. This was also expected following the analysis of the SQUID data (Fig. 8).

When $H_{RE} = 3.0$, the decrease in the SF signal is due to the flipping of the layers which indicates a DW reversal mechanism for a majority of the layers. The remaining SF intensities, however, are due to the rotation of one or two top and bottom layers. Even though the reversal mechanism for

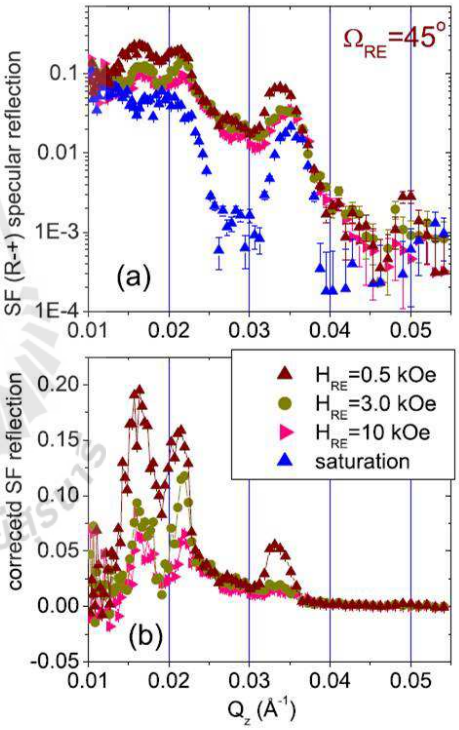

FIG. 14. (Color online) (a) SF specular reflectivity [R_{-+}] patterns as a function of Q_z measured during the fourth field cycle for $\Omega_{RE} = 45°$ at $H_a = -1.44$, -1.67, and -1.73 kOe for $H_{RE} = 0.5$, 3.0, and 10.0 kOe, respectively. (b) Plot of the corresponding corrected SF signals as a function of Q_z.

the majority of the layers is via a DW process, for the minority of the layers it is identified with rotation. Thus one can infer that the sample has signatures of mixed reversal processes. In other words, there is only partial revival of the untrained state.

Interestingly, in the case of $H_{RE} = 10.0$ kOe, the reversal process is fully dominated via the DW process. Here one can infer that a significant revival of the untrained state has indeed taken place. One may also note that the orientations of the $\mathbf{M_{FM}}$ do not depend upon the strength of H_a, but upon the H_{RE} strength. Thus the degree revival of the untrained state has been shown to depend upon the H_{RE} strength.

3. *Fourth field cycle with* $\Omega_{RE} = 90°$

PNR measurements during the fourth field cycles were performed keeping $\Omega_{RE} = 90°$. The blue circles in Fig. 4 show the fields of measurements. In Figs. 15(a)–15(c) we show the data measured at 10 K and at $H_a = -1.73$ and -1.65 kOe, respectively, during the respective fourth field cycles corresponding to the two different representative values of H_{RE} (=2.0 and 10.0 kOe). Here also each time we chose to opt for a different H_{RE} value during the third field cycle, we have used a different H_a value during the fourth field cycle. This was done again in accordance with the measured SQUID data.

In Fig. 16 we have shown the layer switching sequences for $H_a = -1.73$ and -1.65 kOe during the respective fourth field cycles. Here one can see that for $H_{RE} = 2.0$ kOe the situation is typical of a magnetization reversal via the DW process.

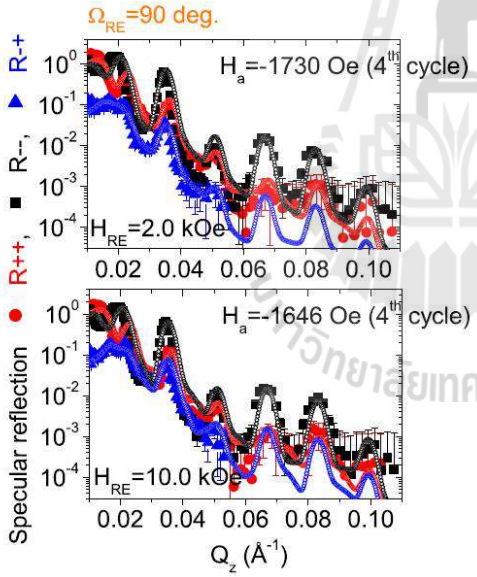

FIG. 15. (Color online) Specular reflectivity patterns (solid symbols) along with their best fits (open symbols) as a function of Q_z for the NSF [R_{--} (black) and R_{++} (red)] and SF [R_{-+} (blue)] channels measured at (a) $H_a = -1.73$ kOe and (b) $H_a = -1.65$ kOe during the fourth field cycle for different H_{RE} (= 2.0 and 10.0 kOe, respectively) values when $\Omega_{RE} = 90°$.

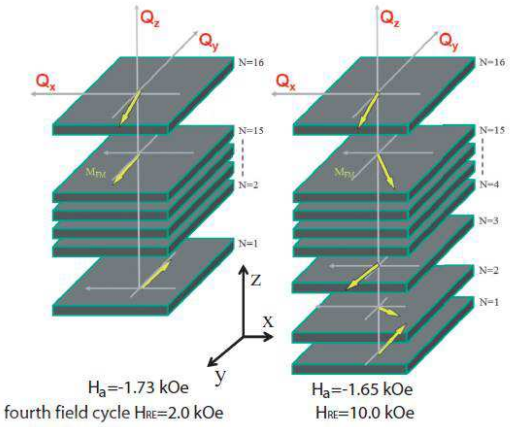

FIG. 16. (Color online) FM layer switching sequence during the different fourth field cycles at $H_a = -1.73$ kOe ($H_{RE} = 2.0$ kOe) and -1.65 kOe ($H_{RE} = 10.0$ kOe) when $\Omega_{RE} = 90°$. The arrows indicate the $\mathbf{M_{FM}}$ orientations in the respective layers. The applied field H_a is along the $-y$ axis.

For $H_{RE} = 10.0$ kOe, however, the situation is far more complicated. There is a mixture of DW and rotational reversal process. This is consistent with the earlier observations in similar systems by Brem *et al.* [11] as we can see that with further increase in the H_{RE} strength, the recovery of the untrained state is reduced.

In Fig. 17(a) we compare the measured SF scattering signals (perpendicular component of M_{FM}) measured at 10 K and at fields of $H_a = -1.73$ and -1.65 kOe during the respective fourth field cycles and at $H_a = -10.0$ kOe (saturation) during the first field cycle. The corrected SF signals in Fig. 17(b) is the subtracted-off SF signal at saturation. The corrected SF signals can also be regarded as signatures of recovery or nonrecovery of the untrained state.

4. *Discussion on the rotational sense*

We can explain our experimental observations within the extended Fulcomer-Charap model [21], where a single ferromagnetic domain (FM magnetization) exchange couples with multiple AF grains with rotatable (responsible for training) and/or nonrotatable (responsible for bias field) moments but without any direct exchange coupling between the grains [22–24].

Brems *et al.* [13] have shown the consequences of changing the sense of direction during field cycling, for example, along $+x$ and $-x$ directions. The recovery of the untrained state depends upon the direction of the average uncompensated magnetization vector $\vec{m}_{AF}$ of the antiferromagnetic grains. The directional sense of $\vec{m}_{AF}$ was related to the directional sense of the FM magnetization. The whole sample magnetization was found rotating in the negative direction during the initial hysteresis loop which was accounted for in the initial negative direction of $\vec{m}_{AF}$ as well [23,24].

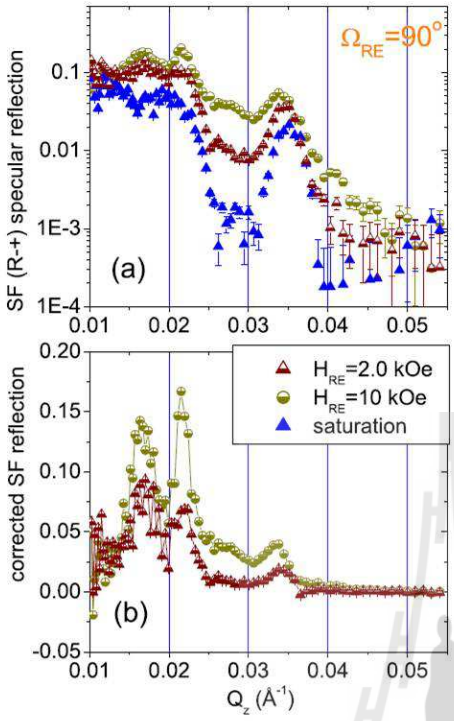

FIG. 17. (Color online) SF specular reflectivity [R$_{-+}$] patterns as a function of Q_z measured during the fourth field cycle for $\Omega_{RE} = 90^\circ$ at $H_a = -1.73$ kOe, and -1.65 kOe for $H_{RE} = 2.0$ kOe and 10.0 kOe, respectively. (b) Plot of the corresponding corrected SF signals as a function of Q_z.

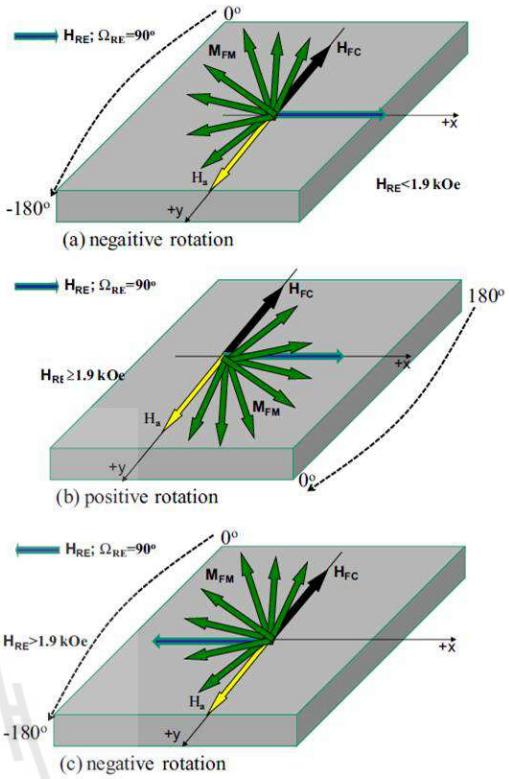

FIG. 18. (Color online) Sketch showing the rotational sense of $\mathbf{M}_{FM}$ under different conditions as $\Omega_{RE} = 90^\circ$ lies in the sample plane. The reorientation field H_{RE} can be either along the $+x$ axis (a) and (b) when the $\mathbf{M}_{FM}$ rotational senses are sensitive to the strength of H_{RE} or along the $-x$ axis (c) when they are insensitive.

The rotational sense of magnetization can be determined by following the trend of the angle ϕ_A with respect to the cooling field direction along the $-y$ axis for increasing measurement fields along the $+y$ axis. When the angle is positive (negative), the system undergoes a positive (negative) rotational sense. In a generic way, more is the angular direction of $\vec{m}_{AF}$ oriented away from the cooling field direction, more is the torque acting on the FM moments. The torque in turn triggers magnetization reversal via rotation instead of the DW reversal process.

Let us now consider the case when H_{RE} is along the $+x$ axis ($\Omega_{RE} = 90^\circ$) following the work of Brems *et al.* [13]. We show a sketch in Fig. 18, the direction of FM magnetization for $\Omega_{RE} = 90^\circ$ (started and ended in the $+x$ direction). Note that a maximum recovery of the untrained state was reported for $H_{RE} \leqslant 1.9$ kOe (experimentally observed) only when the rotational sense (from 0° to -180°) remained unchanged with respect to the state realized after the initial field cooling. This was valid as long as $H_{RE} \leqslant 1.9$ kOe [Fig. 18(a)]. For a $H_{RE} \geqslant 1.9$ kOe, the recovery was less pronounced since the rotational sense of the magnetization changed from negative to positive (i.e., from 180° to 0°) with respect to the initial state after field cooling [Fig. 18(b)]. The recovery was also reported considerably less pronounced as the perpendicular field started and ended in the $-x$ direction [Fig. 18(c)] and was insensitive to the value of H_{RE}. Note that this was in spite of the fact that the rotational sense of the FM magnetization remained unchanged from the initial field cooled state.

The rotational sense of $\vec{m}_{AF}$, which remains unknown from our experimental data, can be evaluated in principle by energy minimization of the total energy in the system. The total energy is given by

$$E = \sum A^i k_{AF} t_{AF} \sin^2(\phi^i - \alpha) - J_{int} A^i \cos(\theta - \phi^i) - H_a M_{FM} t_{FM} \cos(\chi - \theta) \sum A^i. \quad (4)$$

Here the uniaxial anisotropy energy constant of CoO and Co are $k_{AF} = 2.5 \times 10^8$ erg/cm^{-3} and $k_{FM} = 1.5 \times 10^6$ erg/cm^{-3}, respectively. J_{int} is the interfacial exchange energy which involves the coupling constant between the FM and AF grains and t_{FM} (t_{AF}) is the FM (AF) thickness. The angles are the respective angles made by $\vec{m}_{AF}(\phi^i)$, AF easy axis (α), FM magnetization (θ), and $H_a(\chi)$ with H_{FC} along the $-y$ axis.

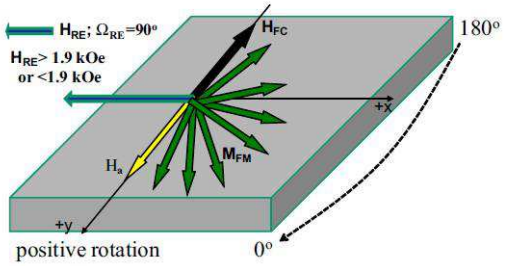

FIG. 19. (Color online) Sketch showing the rotational sense of $\mathbf{M}_{\mathrm{FM}}$ in the present geometry as $\Omega_{\mathrm{RE}} = 90^\circ$ lies in the sample plane. The reorientation field H_{RE} is along the $-x$ axis when the $\mathbf{M}_{\mathrm{FM}}$ rotational sense is insensitive to the H_{RE} strength.

A^i is the area of every noninteracting AF grain coupled to a single FM domain $\sum A^i$. We have considered 100 such AF grains coupled to one FM grain. We have neglected the term corresponding to k_{FM} as it is smaller by 2 orders of magnitude when compared with the value of k_{AF}. From the value of ρ_{m} we estimate $M_{\mathrm{FM}} = 1051$ emu/cm^3 or 1.25 μB/atom, which gives $J_{\mathrm{int}} (= H_{\mathrm{eb}} M_{\mathrm{FM}} t_{\mathrm{FM}}) = 0.86$ erg/cm^2.

For the first field cycling case, we can consider $\alpha = 0^\circ$ assuming the AF easy axis to be coinciding with the H_{FC} axis after field cooling. Using the stability conditions $dE/d\phi^i = 0$ and $dE/d\theta = 0$ we are lead to a system of two equations:

$$k_{\mathrm{AF}} t_{\mathrm{AF}} \sin 2(\phi^i) + J_{\mathrm{int}} \sin(\theta - \phi^i) = 0, \tag{5}$$

$$H_{\mathrm{a}} M_{\mathrm{FM}} t_{\mathrm{FM}} \sin(\chi - \theta) + J_{\mathrm{int}} \sin(\theta - \phi^i) = 0. \tag{6}$$

In our case, since we always measure along the axis of H_{FC}, we can consider $\chi = 0^\circ/180^\circ$ ($\|$/anti-$\|$ to the cooling axis). For finding the coercive fields we have used $\theta = \chi + \pi/2$, considering the magnetization of the FM is zero across the easy axis which gives $\sin\phi^i = \frac{-J_{\mathrm{int}}}{2k_{\mathrm{AF}} t_{\mathrm{AF}}}$ or $\phi^i = -0.33^\circ$ from Eq. (5) during the first field cycle. Note that using a similar model, the average magnetization vector was calculated to be at -0.6° away from the cooling field direction by Brems *et al.* [11], signifying a negative sense of rotation.

In our case, using PNR alone, we cannot discriminate the rotational sense of the FM magnetization. In other words situations depicted in Fig. 18(c) cannot be discriminated from the situation depicted in Fig. 19. However, following the systematic variation of the magnetization directions (during the fourth field cycles) with applied fields H_{a}, we could figure out that the rotational sense has not changed with the change in the H_{RE} values along a particular Ω_{RE} direction. This unchanged FM rotational sense can be due to the fact that H_{RE} in our case always starts and ends in the $-x$ direction (at least for $\Omega_{\mathrm{RE}} = 90^\circ$). This implies that in spite of an unchanged rotational sense of the FM magnetization, a well pronounced recovery of the untrained state is possible.

IV. SUMMARY AND CONCLUSION

Antiferromagnetic-ferromagnetic exchange bias systems are known to suffer from training effect after the first field cycle. It has been shown that field cycling along a direction perpendicular to the field cooling direction can recover the untrained state, partially with different degrees of recovery. Here in this paper we have investigated a prototypical exchange − coupled multilayer in exploring the degree of recovery of the untrained state. We apply field cycling with various amplitudes (H_{RE}) and different orientation angles (Ω_{RE}) with respect to the initial cooling direction. Systematic magnetization measurements by SQUID magnetometery along with depth-sensitive vector magnetometry by PNR have been combined in our experiments.

Parallel component of magnetization measurements by SQUID indicate recovery of the untrained state for two orientation angles, namely $\Omega_{\mathrm{RE}} = 45^\circ$ and 90° along the $-x$ direction. PNR measurements, which simultaneously involve parallel as well as perpendicular components of magnetization, reveal that it is necessary to apply at least $H_{\mathrm{RE}} = 3.0$ kOe to achieve a significant recovery. For a higher value of H_{RE} (up to $\approx$10.0 kOe), the recovery saturates while for a lower value, we could only achieve a partial recovery. For $\Omega_{\mathrm{RE}} = 90^\circ$, we could reach a peak in the recovery even with $H_{\mathrm{RE}} = 2.0$ kOe. However, with higher fields, the recovery gradually decreases and only a partial recovery is possible. For any other higher angles of orientation (e.g., $\Omega_{\mathrm{RE}} = 135^\circ$), no recovery of the untrained state is possible.

Our results are consistent with the earlier observations in similar systems [13] where a small degree of rotation with positive rotational sense (opposite to the sense after initial field cooling) of the AF magnetization vector—related to the FM magnetization direction—was attributed to partial recovery of the untrained state for $\Omega_{\mathrm{RE}} = 90^\circ$. In our case we always observe an unchanged sense of the FM magnetization, irrespective of the strength and orientation of field cycling. The partial and/or significant recoveries can therefore be related to the directional sense of the AF magnetization vector. Contrary to the earlier observations, the degree of recovery is well pronounced in the present case, particularly for $\Omega_{\mathrm{RE}} = 45^\circ$. Moreover, they can be regulated not only with the H_{RE} values but also with the Ω_{RE} values below 90°. Thus we provide a deeper insight into understanding the fundamental mechanisms involved in the recovery of training. By lifting the directional restrictions of the field for the recovery of the untrained state, our work also opens up its technological prospects for such exchange biased systems, which remain coupled at room temperature.

ACKNOWLEDGMENTS

We would like to thank M. Braendlein for helping in the SQUID measurements and S. Mukherjee for his assistance during the PNR measurements. We would also like to thank N. Paul and U. Bloeck for their assistance in the TEM measurements. This work is based on experiments performed at Amor at the Swiss spallation neutron source SINQ, Paul Scherrer Institute, Villigen, Switzerland. A.P. prepared the sample. A.S. did the SQUID measurements, and J.J. assisted A.P. in analyzing the data. J.J., J.S., and A.P. did the PNR measurements. All authors including P.E. and R.Y. read the manuscript. Discussions with Professor P. Böni are gratefully acknowledged. A.P. conceived and designed the work, analyzed the data, coordinated the work, and also wrote the manuscript.

CURRICULUM VITAE

Name Mr. Jaru Jutimoosik

Date of Birth 21 July 1980

Place of Birth Nakhon Si Thamarat, Thailand

Education:

1999-2003	Kasetsart University, Bangkok, Thailand Bachelor of Science (Physics)
2008-2010	Suranaree University of Technology, Nakhon Ratchasima, Thailand Master of Science (Physics)
2011-2016	Suranaree University of Technology, Nakhon Ratchasima, Thailand Doctor of Philosophy in Physics

Academic Experience:

1. Ph.D. Research at Technical University of Munich, Germany
2. Teaching Assistant at Laboratory, School of Physics, Suranaree University of Technology, Thailand.